TYPE IV CRACK CHARACTERISATION AND MODELLING OF

HIGH CHROMIUM FERRITIC STEEL WELDMENTS

By

BEN SHUANG SUN

A Doctoral Thesis

Submitted in partial fulfillment of the requirements for the award of Doctor of

Philosophy of Loughborough University

July 2005

ABSTRACT

In this thesis, the heat affected zone (HAZ) of Gleeble simulated welds, the weldments and the creep specimens for several types of 9%-12% Cr ferritic steels were studied by focusing on the Type IV cracking in the fine grained zone (FZ). The field emission gun transmission electron microscopy (FEGTEM) and scanning electron microscopy (SEM) were used to measure the phosphorus segregation on the grain boundary (GB) and the creep fracture morphologies respectively. Meanwhile the well-developed grain boundary segregation and precipitation (GBSP) model was applied to simulate the experimental results.

The experimental results have showed that the HAZ zone was characterised by softening and Type IV cracking. All the high Cr ferritic steel welds gave a microstructure of mainly tempered martensite and $M_{23}C_6$ precipitates after the post weld heat treatment (PWHT). There was no δ-ferrite observed in the HAZ.

The Type IV cracking exhibited a mixed cracking mechanism in which the intergranular grain boundary separation is dominant due to the crack initiation by voids and the faster $M_{23}C_6$ growth with the service time. A new model on the mechanism of the Type IV cracking is established.

The FEGTEM research has also showed obvious non-equilibrium phosphorus segregation at the grain boundaries, which is affected significantly by the quenching temperature. The phosphorus GB segregation deteriorates the weak grain boundaries.

The experimental results were well in agreement with the GBSP modelling.

Key words: High Cr ferritic steels, Gleeble simulation, Weldments, HAZ, Type IV crack, Creep fracture, P segregation, GBSP model.

DEDICATION

To my wife

"For being a continuous love, encouragement and support in everything I do"

ACKNOWLEDGEMENTS

I would like to express sincere thanks to my supervisor, Professor Roy G. Faulkner for his kind encouragement, excellent advice and guidance throughout the course of this project.

Thanks also go to Dr. David Allen for his supervision on doing experiments at Powergen Technology Centre.

I would like to give my appreciation to the academic and technical staff both from the university and the company, especially Mr. Stuart Turnbull, without their assistance, it would not have been possible for me to have completed this work in time.

I shall say thanks to my colleagues, whose discussion, criticism and help have been very useful.

My special thanks go to my wife and son for their love and constant support during my stay in Loughborough.

Finally acknowledgements go to EPSRC and Powergen for the financial support.

TABLE OF CONTENTS

CHAPTER 1:

CHAPTER 2:

Review of High Cr Ferritic Heat Resistant Steels and Weldments......5

CHAPTER 3:

Modelling of Grain Boundary Microstructure in Alloys (I)—

Grain Boundary Segregation Model.................................40

CHAPTER 4:

Modelling of Grain Boundary Microstructure in Alloys (II)—

Grain Boundary Precipitation Model.................................54

CHAPTER 7:

Determination of Phosphorous Segregation on the Grain Boundary

CHAPTER 8:

Type IV Crack Failure Examination on The Creep Specimens......168

CHAPTER 9:

Overall Discussion, Conclusions and Future Work.....................219

ABBREVIATIONS

AC	Air Cooling
Ac_1	The temperature at which austenite starts to form
Ac_3	The temperature at which austenite formation is complete
ASME	American Society of Mechanical Engineers
AW	As-Welded
AWS	American Welding Society
CCT	Continuous Cooling Transformation diagram
COST	European Cooperation in the field of Scientific and Technical Research
CRS	Creep Rupture Strength
CZ	Coarse Grained Zone
DBTT	Ductile-Brittle Transition Temperature
EBW	Electron Beam Welding
EPRI	Electric Power Research Institute
ES	Equilibrium Segregation
FEGSEM	Field Emission Gun Scanning Electron Microscopy
FEGTEM	Field Emission Gun Transmission Electron Microscopy
F/M	Ferritic and Martensitic
FZ	Fine Grained Zone
GB	Grain Boundary
GBP	Grain Boundary Precipitation
GBS	Grain Boundary Segregation
GBSP	Grain Boundary Segregation and Precipitation
GMAW	Gas Metal Arc Welding
GP	Guinier-Preston
GTAW	Gas Tungsten Arc Welding
HAZ	Heat Affected Zone
HV	Vickers Hardness
ID	Inner Diameter
IG	Inter-Granular
IPS	Inter-Particle Spacing

LF	Life Fraction
MAW	Metal Arc Welding
MAG	Metal Arc Gas welding
MCS	Monte Carlo Simulation
MCW	Metal Cored Wire
NES	Non-Equilibrium Segregation
OD	Outer Diameter
PC	Pulverised Coal
PFZ	Precipitate-Free Zone
PM	Parent Metal
PS	Precipitation of the Secondary Phase
PWHT	Post Weld Heat Treatment
RSD	Relative Standard Deviation
SAW	Submerged Arc Welding
SCL	Solute Concentrated Layer
SDL	Solute Deleted Layer
SEM	Scanning Electron Microscopy
SGTE	Scientific Group Thermodata Europe
SH/RH	Superheater and Reheater
SMAW	Submerged Metal Arc Welding
SSS	Solid Solution Strengthening
TEM	Transmission Electron Microscopy
TIG	Tungsten Inertial Gas Welding
TS	Transformation Strengthening
USC	Ultra Supercritical
WM	Weld Metal

LIST OF SYMBOLS

a	the lattice parameter
A	a constant determined by the temperature, the GB diffusion coefficient of the solute, the GB width and the fraction of the boundary face covered by precipitates
A_{mi-1}	the mean collector plate area at the (i-1)th stage
A_{mn}	the mean collector plate area after ageing for a time t at ageing temperature T
$A_m(t)$	the mean collector plate area after ageing for a time t at ageing temperature
A_v	the mean collector plate area
b	absorption constant
B	the grain size
C_0	the concentration in the adjacent matrix
C_b	the concentration of the solute on GB
$C_{be}^i(0)$	the boundary solute concentration at time = 0
$C_{be}^i(t)$	the grain boundary concentration of solute i after time t
$C_{bn}^i(t)$	the concentration of solute i at the concentrated layer as a function of holding time at temperature T
$C_{bn}^i(T)$	the maximum non-equilibrium segregation level of solute i at temperature T
C_c	the carbon content of the alloy being considered
C_C^0	the binding energies of C with the boundary
C_g	the bulk solute concentration
C_g^i	the bulk concentration of solute i in the matrix
C_g^{Mo}	the concentrations of Mo in solution
C_g^P	the concentrations of P in solution
C_{Mo}^0	the binding energies of Mo with the boundary

C_N	the concentration of the non rate controlling element
C_P^0	the binding energies of P with the boundary
C_r	the solute concentration at the surface of a particle with radius of curvature of r
$\overline{C_t}$	average solute concentration at time t
C_∞	the equilibrium solute concentration
$C_\infty^i(T)$	the maximum equilibrium segregation level
$C(y, t')$	the solute concentration distribution at this time, $t' = i\delta t$
$c(\lambda', t)$	the solute concentration distribution function in the solute depleted area
d	the grain size
d_0	the thickness of the concentrated or segregation layer
d_{gb}	the GB width
d_s	the mean inter-particle spacing
D	the diffusivity
D_b	the grain boundary diffusion pre-exponential term
D_{bnuc}	the GB diffusion coefficient of the solute atoms at temperature T_{nuc}
D_c	the diffusion coefficient of the vacancy-solute complexes in the matrix at the ageing temperature
D_c^i	the diffusion coefficient of solute i-vacancy complexes in the matrix
D_{ci}	the diffusion coefficient of the vacancy-solute complexes at the solution treatment temperature
D_I	the volume diffusion coefficient of the impurity at ageing temperature
D_{oc}^i	the pre-exponential constant for diffusion of solute i-vacancy complex
D_{oi}	the pre-exponential constant for diffusion of solute atoms
D_s^i	the diffusion coefficient of solute i in the matrix
D_{V0}	the volume diffusion pre-exponential term
E	elastic module
E_A	the activation or migration energy for diffusion of solute i-vacancy

complexes in the matrix

E_b	the solute-vacancy binding energy
E_b^i	the solute i-vacancy binding energy
E_f	the formation energy
E_f^0	the formation energy of vacancy when $\sigma = 0$
E_f^v	the vacancy formation energy
E_f^σ	the formation energy of vacancy when the stress is present
E_g^i	the matrix concentration of solute i
$E_{m(i)}^c$	the migration energy for diffusion of solute i-vacancy complexes in the matrix
$f(\psi)$	the morphological factor
g	the concentration gradient in the vicinity of the surface of a particle
H_v	the enthalpy of vacancy formation in the bulk
I	nucleation rate
J	the diffusion flux
J_{1c}	the fracture toughness on elastic/plastic condition
k	Boltzmann's constant
K_j	precipitate shape factor
K_{1c}	the fracture toughness on linear condition
L	the precipitate radius
L_g	the mean radius of the precipitates at the time of the onset of coarsening
L_{i-1}	the precipitate size determined for the previous time
L_j	precipitate shape factor
L_n	the mean precipitate radius
m	the moment of inertia
M_s	martensite transformation temperature
n_0	the distribution density function of GB precipitate nuclei
N	the number of atom sites at the GB
N_0	the nucleation site density

N_A	Avagadro's number
$N_{A_{\min}}^{4L_n^2}$	the number of all these precipitates which have collector plate areas smaller than $4L_n^2$
N_g	the number of the precipitates at the time of the onset of coarsening
N_i	the atomic fraction of the ith component in the matrix
N_i^s	the atomic fraction of the ith component on the boundary
N_{mi}	the number of precipitate per unit area of GB
N_{n-1}	the number of the precipitates after time, $(n-1)\delta t$
N_r	the number of rate controlling atoms in the precipitate molecule
$N(t)$	the number of the precipitates at the grain boundary after ageing for a time t
N_v	the vacancy concentration in the bulk
N_v^{eq}	the equilibrium thermal vacancy concentration
N_v^0	the number of lattice sites
Q^i	the ES binding energy of solute i with GB
Q_b	the grain boundary diffusion activation energy
Q_c	the activation energy term for the calculation of the diffusion coefficient of the vacancy-solute complexes
Q_C	the equilibrium segregation energies of C
Q_{Mo}	the equilibrium segregation energies of Mo
Q_P	the equilibrium segregation energies of P
Q_P^0	the binding energy P with the boundary
Q_V	the volume diffusion activation energy
r	the particle radius
r^*	the critical nucleus size
r_a	the radius of the angular motion
R	the gas constant
R_1	the radius of the precipitate
R_2	the radius of an allotriomorph

S	the surface area of the nucleus or particles
s_0	the unit area
S_v	the entropy of the solution
T	the absolute temperature
T_0	the room temperature
T_{age}	the aging temperature
T_{eff}	the effective quenching time
T_i	the isothermal holding temperature at the ith step of the stepped curve
T_{mp}	the melting point of the alloy
T_{nuc}	the nucleation temperature
t	the ageing time
t_c	a critical time for NES
t_{cc}	the critical time when the growth stops and coarsening begins
t_e	the effective time of complex diffusion
t_i	the isothermal holding time at the ith step of the stepped curve
$t_{8/5}$	the cooling time from 800°C down to 500°C
V	the volume of the nucleus
V_{Cu}^{α}	the partial molar volume of Cu in the precipitate phase
V_f	the volume fraction of precipitates
V_{α}	the molar volume of the matrix
V_{θ}	the molar volume of the precipitate phase
w_{pfz}	the width of precipitate-free zone
x	intragranular precipitate size
x_b	GB solute concentration modified to account for the segregation parameter of the material, which is taken to be equal to C_b
X_E	the ratio of the number of non rate controlling to rate controlling atoms in the precipitate phase
x_{α}	the solute concentration in matrix
$x_{\alpha T_{nuc}}^{\alpha\theta}$	the equilibrium solute concentration at the interface between the

	nucleated precipitate phase and the matrix at temperature T
$x_{\alpha i}$	the average concentration of the solute in the region from the GB to a distance δl into the grain
x_θ	the solute concentration in precipitate phase
y	the distance from the GB
Z	the concentration of impurity absorption sites on the boundary
α	the lattice parameter of the matrix phase
α_a	the half length of the crack
$\alpha_{e(i)}$	the maximum equilibrium enrichment ratio of solute i
$\alpha'_{i_2 P}$	the i_2-P chemical interaction coefficient
σ	the GB surface tension
σ_c	critical stress
σ_d	the standard deviation of the collector plate area
$\sigma_{\alpha\theta}$	the matrix/precipitate interfacial energy
σ_1	the equilibrium GB surface tension
θ	the cooling rate between temperatures T_i and T_0
ρ	the atomic densities in the matrix
ρ^s	the atomic densities on the boundary
ρ_α	the molar density of the matrix
ρ_θ	the molar density of the precipitate phase
ω	the angular velocity
ϖ	the half width of SCL
γ	the surface energy of the material
γ_I	the interfacial energy
γ_ρ	elastic deformation work
$\gamma_{\rho P}$	elastic deformation work or intergranular work-of-fracture required to overcome the precipitates
$\gamma_{\rho S}$	elastic deformation work or intergranular work-of-fracture required to overcome the impurities
$\gamma_{\rho V}$	elastic deformation work or intergranular work-of-fracture required to

	overcome the voids
λ	the GB thickness
δ	a numerical constant as 0.05
μ_i	the chemical potentials of the components in the bulk of the grain
Γ	the vacancy absorption
Γ_i	absorption of ith component
ψ	an angle decided by the particle shape
τ	the incubation time for nucleation
Ω	the atomic volume
Σ	a measure of the disordered state of the boundary
$\Delta G^{\bullet}$	the Gibb's free energy of critical GB nucleus formation
ΔG_v	the driving force for the solid state transformation
ΔH	the enthalpy of solution of the precipitate
ΔS	the entropy of solution of the precipitate
ΔV	the increase of the volume of a particle
ΔV_v	the volume of a void

LIST OF FIGURES

LIST OF TABLES

CHAPTER 1:

Introduction

1.1 Research Background

The growth in world population and living standards continues to make increasing demands on energy supplies, particularly electricity. There is some growth in the use of renewable sources, such as wind power, and a new interest in nuclear power in some countries. However, for the foreseeable future, there will be major reliance on electricity generated by fossil fuels with efficiency and minimum environmental damage.

The efficiency of conventional boiler/steam turbine fossil power plants, and ultra supercritical (USC) power plants is a strong function of the steam temperature and pressure. The goal of improving efficiency has been pursued worldwide and for many decades. The key components whose performance is critical for ultra supercritical plants are high-pressure steam piping and header, super-heater tubing and waterwall tubing. All of them have to meet creep strength requirements. In addition, pipes and headers, being heavy section components, are subject to fatigue induced by thermal stresses. High Cr (9%-12%Cr) ferritic/martensitic steels are preferred because of their lower coefficient of thermal expansion and higher thermal conductivity compared to austenitic steels. Many of the early problems in the USC plants were traceable to the use of austenitic steels which were very prone to thermal fatigue. Research during the last decades has, therefore, focused on developing cost-effective, high-strength ferritic steels that could be used in place of austenitic steels. This has resulted in ferritic steels capable of operating at higher temperature, with good weldability and fracture toughness.

Ferritic steel developments are mostly aimed at their use for thick section pipes and headers. Among the 9%Cr steels fully commercialised, the P91 steel has the highest allowable stress and has been extensively used all over the world as a material for

headers and steam pipes in USC plants operating at steam temperatures up to 593°C. Alloy NF616 (P92), developed by substituting part of the Mo in P91 by W, has an even higher allowable stress and can be operated up to steam temperature of 620°C. E911 is a European alloy similar in composition to P92 with similar capabilities. Beyond 620°C, the 9%Cr steels become limited by oxidation resistance and 12%Cr steel has to be used.

Among the 12%Cr steels, HT91 has been widely used for tubing, headers and piping in Europe. Use of the steel in Japan and US has been limited due to their poor weldability. HCM12 is an improved version of HT91 with 1%W and 1%Mo, having a duplex structure of δ -ferrite and tempered martensite with improved weldability and creep strength. Further increases in creep strength by substituting more of the Mo with W and addition of Cu has resulted in the alloy HCM12A (P122), which can be used for header and piping up to 620°C.

The welding is one of the most essential fabrication processes for component manufacture. The thick sections of these steels need to be welded. The welding could exhibit all types of crackings, of which the Type IV cracking is a crack occuring in the fine-grained heat-affect-zone. The principal Type IV cracking mechanism affecting large CrMoV steel welds has still not clearly been identified.

1.2 Aims of the Project

The research contents and objectives in the project for the weld metals of high Cr ferritic steels are:

(1) **To study the weld simulation (Gleeble testing) of the P91 ferritic steel.**
This is a valuable and an easy way to simulate the actual welding situation and to allow convenient weld HAZ zone exploration.

(2) **To characterize the microstructures of high Cr ferritic steel weldments.**
This will be done mainly by optical microscopy, scanning electron microscopy (SEM), transmission electron microscopy (TEM), and field emission gun SEM (FEGSEM)

techniques etc. to examine the phase transformation, precipitate type, size and distribution, main and trace elements distribution, etc. The materials to be investigated will include P91, P92, P122 and E911 weldments and creep specimens.

(3) To apply modelling to microstructures (grain boundary).

The grain boundary segregation and precipitation (GBSP) model will be used to validate its application in the ferritic steel materials and the weldments in particular. The model for the weld HAZ zone will be modified.

(4) To analyse the Type IV crack in the weldments.

This will be based on the research on the HAZ zone to gain a fundamental understanding of why the weld HAZ zone is susceptible to "Type IV" cracking in high temperature service, how its susceptibility is related to steel composition and heat treatment, and consequently, how advanced steels can be best selected and developed to minimize these risks.

(5) To determine phosphorus segregation on the grain boundaries.

The high-resolution field emission gun TEM (FEGTEM) will be used to determine the phosphorus segregation on the grain boundaries.

In combination with experimental work on the weld simulation, Type IV crack weld characterization and Type IV crack creep specimen failure examination, the aim is to explain the Type IV cracking in the high Cr ferritic steel weldments by using a GBSP model.

1.3 Thesis Layout

There are **9 chapters** in this thesis as follows:

Chapter 1 is the **Introduction.**

Chapter 2 is a literature **Review of High Cr Ferritic Heat Resistant Steels and Weldments**

Chapter 3 introduces the **Grain Boundary Segregation Model.**

Chapter 4 introduces the **Grain Boundary Precipitation Model.**

Chapter 5 describes the **Weld Simulation of P91 Materials with the Gleeble**

Testing Machine.

Chapter 6 describes the **Microstructure Characterisation of High Cr Ferritic Steel Weldments.**

Chapter 7 describes the **Determination of Phosphorus Segregation on Grain Boundaries.**

Chapter 8 describes the **Type IV Cracking Mechanism of High Cr Ferritic Steels.**

Overall Discussion, Conclusions and future work appear in **Chapter 9.**

Appendices include the partial reports on the **Type IV crack Creep Specimen Failure Examination** and the **Phosphorus Determination.**

CHAPTER 2:

Review of High Cr Ferritic Heat Resistant Steels and Weldments

2.1 Development of High Cr Ferritic Heat Resistant Steels

High chromium ferritic heat resistant steels, usually referred to the ferritic-martensitic (F/M) steels, are widely used in high temperature environments, combining high strength at both ambient and elevated temperatures with adequate toughness[1-5]. Based on basic crystal structure of materials, the heat resisting steels include pearlitic, bainitic and martensitic types. These steels contain chromium contents up to 12% with usually about 1%Mo. They were used in the oil and processing industry as early as the 1930s[6,7]. Since then a series of integrated standards concerning chemical compositions, heat treatment procedure and mechanical properties have been established. These steels have also been widely used for tubing or piping in the power generation industry.

The energy crisis in mid 70's and subsequent sharp increase in fuel prices re-kindled interest in the development of more efficient pulverised coal (PC) power stations. Electric Power Research Institute (EPRI) initiated a study of the development of more economic coal-fired power plants in 1978[8]. This study led to a number of research and development activities involving US, Japanese and European manufacturers. These activities focused on developing further the existing high-temperature-resistant ferritic-martensitic 9%Cr and 12%CrMoV steels for the production of rotors, casings and chests, pipes and headers capable of operating at inlet steam temperatures of up to 650 ℃. One of the early conclusions from this project was that the construction of power plants with a 593℃/31MPa steam condition would be feasible with only minor evolutionary improvements in materials technology. This has in fact proved to be correct as evidenced by the spate of power plants built in Japan and Europe over the last decade. In Japan, nearly 16 plants, most of them with typical main steam temperature of about 593 ℃ and pressure of

24MPa, are operational. In Europe, nearly a dozen plants are operational with main steam temperature/pressure of 583°C/30MPa.

Ferritic steel development is mostly aimed at their use for thick section pipes and headers. Masuyama[9], as shown in Fig. 2.1, has reviewed the systematic evolution of these materials. Headers and pipes have traditionally been made from low alloy steels such as P11 and P22 in the USA. Even in conventional boilers, such headers can fail due to thermal fatigue cracking, caused by load and thermal cycling. A common failure mode is the cracking of the ligament between the tube boreholes[10]. The use of higher temperatures and pressures can only increase the problem. Previous attempts to use austenitic steels have not been successful due to high thermal expansion of these steels.

10^5h Creep Rupture Strength at 600°C

	First Generation	Second Generation	Third Generation	Fourth Generation
35 MPa	60 MPa	100 MPa	140 MPa	180 MPa

2.25Cr-1Mo → +V → 2.25Cr-1MoV → -C +W -Mo +Nb → 2.25Cr-1.6MVNb

ASME T22 (STBA24) +Mo → 9Cr-2Mo   HCM2S (ASME T23 STBA24J1)

+Mo +V → HCM9M (STBA 27)

9Cr-1Mo   +Nb → 9Cr-2MoVNb

ASME T9 (STBA26)   EM12 (NFA 49213)   V, Nb Optimized

+V +Nb → 9Cr-1MoVNb   Tempaloy F-9 → 9Cr-1MoVNb (ASME T91 STBA28)   -Mo +W → E 911   9Cr-0.5Mo-1.8WVNb   NF616 (ASME T92 STBA29)

12Cr   +Mo → 12Cr-0.5Mo   → 12Cr-0.5Mo-1.8WVNb   TB12   +W +Co → 12Cr-WCo-NiVNb   NF12

AISI 410

+Mo +V → 12Cr-1MoV   +W → 12Cr-1MoWV   -C +W +Nb → 12Cr-1Mo-1WVNb   -Mo +W +Cu → 12Cr-0.5Mo-2WCuVNb   +W +Co → 12Cr-WCoVNb

HT91 (DINX20Cr MoV121)   HT9 (DINX20Cr MoWV121)   HCM12 (SUS410J 2TB)   HCM12A (ASME T122 SUS410J3TB)   SAVE12

Fig. 2.1. Evolution of ferritic steels for boilers[9]

Several candidate ferritic steels have emerged succeeding low Cr ferritic steels, such as the P11 (1.25Cr-1Mo) and P22 (2.25Cr-1Mo), which are capable of operation up to 593℃.These include HT9, HT91, HCM9M, HCM12 and P91. Alloys HT9 and HT91 are well-established steels with an extensive stress-rupture database which exceeds 10^5 h at temperatures in the range 500 to 600℃ for all product forms. There is also extensive operating experience (>20years) in Germany, Belgium, Holland, South Africa, and Scandinavia for steam temperatures up to 540℃ and some limited experience on a few small units with steam temperature from 560 to 580℃.This experience generally has been satisfactory. Difficulties have, however, been reported during fabrication and particularly during welding and post-weld heat treatment (PWHT). This arises because the relatively high carbon content of the steel (0.2%) and the correspondingly low M_s temperature promoting the possibility of austenite retention after welding, high residual stresses, and cracking prior to and during stress relief. It is reported that these problems have been overcome by careful control of preheat treatment and PWHT backed up by vigorous quality control. Difficulties have also been reported when the material has been given inadequate solution heat treatment. Due to these concerns, these alloys have not found much favour in the United Kingdom, the United States, or Japan. Alloys with improved weldability characteristics, such as HCM12M have been adequately characterized for tubing and large-diameter, thick-wall pipes.

With regard to the 9Cr-2Mo steel (HCM9M), the feasibility of fabrication of large-diameter, thick-wall piping and its application to in-plant header and main steam piping was first demonstrated in 1985[11]. The practical use of this material has been easy because its simple composition provides fabricability and weldability comparable to those of low-alloy steels. The critical strain of large-diameter pipes has been found to be over 102J/cm^2 at 0℃. Allowable stresses are comparable to those for the HT9 alloy, but lower than those for P91. Service experience of nearly 25 years has been accumulated since the alloy was developed with about 2000 tons having been produced specifically for superheater -reheater (SH/RH) tubes and steam pipes.

The modified 9Cr alloy, P91, appears to be quite superior to HT9, HT91 and to HCM9M in terms of creep-rupture strength and is, hence, the most promising candidate for use in header and steam piping for temperatures up to 595°C. One of the early applications was by the Chubu Electric Power Company (Kawagoe Power Station, Units 1 and 2) for 565°C steam conditions as headers and steam pipes. A majority of the recent European supercritical plants have utilized P91 as main steam and reheat piping. Numerous retrofit applications have also been carried out for headers/steam pipes. The alloy was approved by the ASME Boiler Code Committee for various uses between 1983 and 1986 as T91, P91, F91[8]. Since that time, the alloy has found applications worldwide and is available from many sources, since the composition is not proprietary. It is especially popular in Europe, where it proved superior in creep strength as well as weldability, compared to the well-known HT91 steel, used in supercritical boilers.

The high creep strength of grade 91 steel is due to small additions of V, Nb and nitrogen in addition to Cr, which lead to precipitation of $M_{23}C_6$ carbides and (Nb, V) carbonitrides, and solution strengthening by Mo. Very extensive studies were made worldwide to evaluate the suitability of P91 for heavy section components. These included manufacturing studies, welding trials, and various mechanical tests, on both virgin and aged samples[12, 13]. The net result of all these tests is that P91 is now the preferred heavy section materials for supercritical boilers worldwide. However, most designs using P91 will probably be limited to steam conditions of about 593°C/25MPa.This is especially the case in Europe, where the allowable creep strength is about 10% lower than in Japan and the USA.

Fortunately, Fujita in Japan discovered that the creep strength of 9-12Cr, Mo, V, Nb steels could be raised by about 30% through partial substitution of Mo by W [14]. This has spawned another round of intensive alloy development and evaluation worldwide[15]. ASME has approved two of these steels, a 9Cr steel developed by Nippon Steel NF 616(P92) and a 12Cr steel HCM12A developed by Sumitomo Metal (P122) for use in boiler heavy section components. Another W containing steel E911 is in advanced development in Europe. The allowable strength of the new steels at 600°C is about 25%

higher than that of P91. Thus these steels should allow steam temperature up to 620°C
and pressures up to 34 MPa.

A sample list of European installations using the most advanced steels NF616 (P92),
HCM12A (P122) and E911 is shown in Table 2.1[16]. There is considerable interest in
using these alloys for outlet headers and main steam and reheat pipe work. The Danish

Table 2.1. Application of advanced ferritic steels in European power stations[16]

Power Station	Material Grade	Size	Component	Steam Condition[※]	Installation
Vestkraft Unit 3	P92 (NF 616)	ID 240x39	Straight PipeMain Steam	560/25	1992
Nordjyllandsvaerket	P92 (NF 616) P122 (HCM12A)	ID 160x45	Header	582/29	1996
Schkopau Unit B	E911	ID 550x24	Induct.BenHot Reheat	560/7	1996
Staudinger Unit 1	E911	ID 201x22	Induct.BenMain Steam	540/21.3	1996
Staudinger Unit 3	E911	ID 230x60	Induct.BenMain Steam	582/29	1996
GK Kiel	P92	ID 480x28	Header	545/5.3	1997
VEW	E911	OD 31.8x4	Superheater	650	1998
Westfalen	E911	ID 159x27	Steam Loop	650/18	1998
Westfalen	P92	ID 159x27	Steam Loop	650/18	1998

※   °C/MPa

Utility, ELSAM, has installed full-scale headers in a 415MW supercritical plant under construction. Headers using P92 and P122 have been constructed and installed. Two of the headers will be tested under accelerated high-temperature conditions in a high-pressure cell operated by Mitsubishi Heavy Industries.

2.2 Microstructures and Mechanical Properties of High Cr Ferritic Steels

2.2.1 Fe-Fe$_3$C Diagram

Phase changes and solidification are best shown in an iron-carbon phase diagram (Fig.2.2). The temperature range can also be obtained from the equilibrium diagram when the iron carbon alloy is slowly heated. The Fe-Fe$_3$C diagram presents the structure, composition and percentages of the equilibrium phase that are shown for various Fe-C alloys with different compositions at specified temperature. It can show the phase transformations occurring during slow heating and cooling.
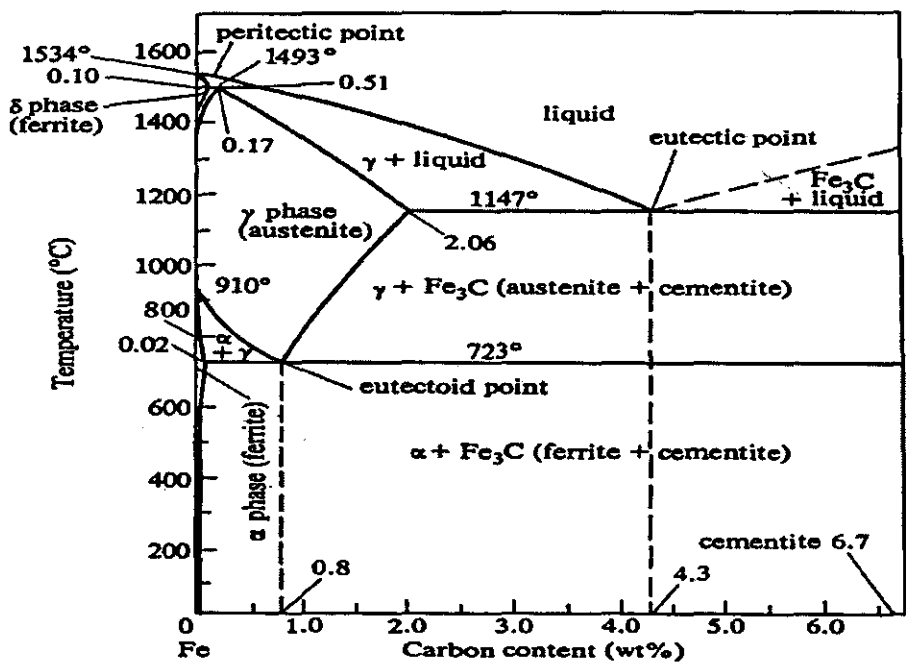
Fig. 2.2. Fe-Fe$_3$C phase diagram[17]

10

Steels are an important range of commercial alloys. It is essential for successful steel welding to understand the phase transformations taking place during this process. Based on the Fe-Fe$_3$C diagram, a eutectoid steel with pearlite structure and a hypo- or hyper-eutectoid steel with proeutectoid ferrite (α-ferrite) are heated to above the Ac$_3$ temperature (the temperature at which austenite formation is complete); all eutectoid and proeutectoid are changed into austenite with a face-centred cubic structure.

During cooling, the austenite subsequently transforms back to a body-centred cubic structure around 910°C known as α- iron or α-ferrite. When the temperature is below 723°C austenite transforms to ferrite and an intermetallic compound of iron and carbon which is called cementite. Ferrite and cementite form a laminated eutectoid structure which is called pearlite.

2.2.2 Composition Design

The typical composition of high Cr ferritic steels is given in Table 2.2[17, 18]. As the 9% Cr-1% Mo steel is used in high temperature environment (>500°C), the chemical composition of the steel should be designed to obtain a high temperature strength and oxidation resistance. Standard 9%Cr-1%Mo steel mainly contains 9%Cr and 1%Mo. Although it can be used at higher temperature, both the dispersion effect and the creep strength of the steel are poor due to the carbides mainly from the Cr, such as Cr$_{23}$C$_6$, Cr$_7$C$_3$, and the corresponding lower carbide stability under long duration of high temperature and stress. The modified 9%Cr-1%Mo steel has the 9% Cr and 1% Mo, and modified V, Ti, Nb, W and also trace alloying elements, e.g. N, added to form nitrides. The elements V, Ti, Nb etc. in the steel have strong tendency to form MX type (V,Nb,Ti)(C,N) carbides, which possess higher stability. Hence the matrix is further strengthened and higher creep strength performance and resistant to oxidation result[4, 19-22].

Table 2.2. Composition of high Cr ferritic heat resistant steels

wt%

Alloy *	Cr	C	Mn	Si	Ni	Mo	W	Nb	V	B	N	Co	Cu
T9	9.0	0.12	0.45	0.60	--	1.0	--	--	--	--	--	--	--
HCM9M	9.0	0.07	0.45	0.30	--	2.0	--	--	--	--	--	--	--
T91	9.0	0.10	0.45	0.40	--	1.0	--	0.08	0.20	--	0.05	--	--
P91	9.0	0.12	0.66	0.29	0.51	1.05	0.01	0.03	0.18	--	0.03	--	0.03
P92	9.0	0.11	0.51	0.32	0.24	0.45	1.80	0.06	0.20	--	0.04	--	0.05
E911	9.0	0.12	0.51	0.20	0.20	0.94	0.90	0.06	0.20	--	0.06	--	--
HT91	12.0	0.20	0.60	0.40	--	1.0	--	--	0.25	--	--	--	--
HT9	12.0	0.20	0.60	0.40	--	1.0	0.5	--	0.25	--	--	--	--
HCM12	12.0	0.10	0.55	0.30	--	1.0	1.0	0.05	0.25	--	0.03	--	--
TB12	12.0	0.08	0.50	0.05	--	0.50	1.8	0.05	0.20	0.30	0.05	--	--
HCM12A	12.0	0.11	0.60	0.1	--	0.40	2.0	0.05	0.20	0.003	0.06	--	--
NF12	11.0	0.08	0.50	0.2	--	0.2	2.6	0.07	0.20	0.004	0.05	2.5	--
SAVE12	11.0	0.10	0.20	0.3	--	--	3.0	0.07	0.20	--	0.04	3.0	--
TAF650	10.5	0.18	0.50	0.3	--	1.5	--	0.15	0.20	--	--	--	--

* weld metal, PWHT = 750°C×2hr

The functions of all types of alloying elements in steels are as follows:

Cr The corrosion resistance and oxidation resistance will depend on the Cr content. More Cr in the steel gains stronger corrosion resistance. The characteristics of Cr make it one of the most important alloying elements in steels. Cr can also improve the hardenability of steel. Cr is a strong ferrite formation element, which can stabilize the ferrites, so δ ferrites can often be seen at ambient temperature in high Cr steels[4]. The Cr-strengthening mechanism to steel includes solid solution and precipitation. Using a different composition and heat treatment condition, Cr can be formed as $M_{23}C_6$, M_7C_3, M_2X (where the M is a metallic element, X is the carbon or nitrogen) and other carbides or nitrides. These carbides and nitrides have the effect of precipitation strengthening in

steels. More importantly they will keep the microstructures of the steel stable at high temperature and enhance their creep and fatigue strengths[8].

Mo, W [23-28] Mo and W have similar effects in steels: both are ferrite stabilization elements. Mo can restrain eutectoid transformation and proeutectoid precipitation and increase the steel's hardenability. Both Mo and W can improve steel's anti-temperability, which is attributed to the solid solution and precipitation strengthening mechanism. Mo and W can be formed as MC, M_2C or M_6C in different M/C ratio and heat treatment conditions. For Mo, M_2C is the commonest carbide while M_6C is more common for W. Both Mo and W can promote the formation of the δ ferrite.

V, Nb, Ti [29, 30] The addition of V, Nb, and Ti is needed for the formation of the secondary phase precipitation strengthening and stabilization of the high temperature properties of the steel. MC carbides rich V or Nb will be precipitated in the form of fine particles, and dispersed in the matrix steel. MC is a very stable phase and plays a very important role in high temperature strengthening in steels. The V enriched M_2C carbide may also precipitate in steels. The effect of Ti on the high temperature properties of steels is similar to V and Nb. However Ti is easily oxidized. Hence it is very difficult to control the Ti content in steels, particularly during welding. When N exists in steels, V and Nb will react with it to produce nitrides, V and Nb can also accelerate the formation of residual δ ferrite and restrain transformation of the austenite.

Ni Ni is an austenite stabilizer, which can increase the hardenability of steels and strengthen steels in the form of solid solution hardening. However Ni cannot improve the high temperature creep strength. Usually the addition of Ni in high Cr steels is to balance the quite high Cr content and reduce residual δ ferrite[30]. Ni can also decrease the Ac_1 temperature of steels and the stability of carbides. These effects of Ni will lead to the degradation of resistance to temperability of steels.

Co Co is an austenite stabilizer too[31]. Co is known to delay recovery on tempering of martensitic steels. Co also promotes nucleation of finer secondary carbides on tempering.

This is attributed both to its effect on recovery and its effect on the activity of carbon. Co also slows coarsening of alloy carbides in secondary hardening steels. This was suggested to be the result of cobalt increasing the activity of carbon and its insolubility in alloy carbides. Furthermore Co has a positive effect on creep rupture stress.

C C has a strong strengthening effect in steels, but it can reduce the toughness and ductility. C is an austenite-stabilizing element and it forms carbide in heat resistant steels, which can block the dislocation and grain boundary (GB) movement in high temperature[32], resulting in the stabilization of the microstructure at high temperature. However C is a harmful element in welding because it will increase the susceptivity to cracking. Normally C content in high Cr steels should be controlled to under 0.2%.

N N is a strong austenite formation element whose effect is 20 times stronger than that of Ni[33]. Meanwhile N can replace the C in carbides to produce nitride precipitation. Nitrides are very stable precipitates. The disadvantage of N is its limited solubility in ferrites.

B A small amount of B will enhance the creep rupture strength of heat resistant steels. In ordinary steels B is usually segregated on GB hence the grain growth is restrained[31]. Studies[34] showed that B will be dissolved in $M_{23}C_6$ precipitates. B in carbides may have influence on the stability, distribution and size of carbides so that the creep strength is enhanced.

Cu Cu is also an austenite stabilizer. The addition of copper to ferritic steels produces alloys that can be precipitation hardened to higher strength and hardness.

Due to the different effects and the interactions of all kinds of alloying elements, a balance must be sought in steels, in order to optimize the composition to develop high Cr heat resistant steels.

2.2.3   Microstructural Evolution

Modified 9%-12% Cr steels are commonly used in "normalized and tempered" or "quenched and tempered" conditions. Austenitizing treatment dissolves the majority of secondary phases (nitrides, carbides or carbo-nitrides). Austenite transforms to martensite after air-cooling or oil and water quenching.

Tempering of martensite in 9%-12% Cr steels results in precipitation of $M_{23}C_6$ carbides (especially on subgrains and lath boundaries) and particles of nitrogen rich phases (especially inside subgrains).The type of nitrogen rich phases depends on the chemical composition of steels and the temperature of tempering. At tempering temperatures below 700 ℃, M_2X phases, which is isomorphous with Cr_2N, is preferred while at higher temperatures the MX phases is formed. This phase is often designated as the secondary MX phase in order to distinguish it from undissolved NbX particles. The secondary MX phase is almost pure nitride containing vanadium, chromium and a small amount of niobium.

$M_{23}C_6$ carbides precipitate during tempering with a chromium concentration very close to equilibrium, but in the course of the subsequent creep exposure at lower temperatures the redistribution of chromium towards new equilibrium takes many thousands of hours. It is proposed that boron can reduce the coarsening of $M_{23}C_6$ particles. The amount of boron in $M_{23}C_6$ particles after tempering corresponds in most cases to between 50% to 100% of the total boron in the alloy. It is worth noting that microstructural investigations of boron containing steels indicate that dislocation density during creep is significantly higher than in the boron free steels[35]. In niobium and nitrogen containing steels, the secondary MX phase is not thermodynamically stable. It dissolves due to precipitation of a more stable nitride that is called Z-phase[36]. The particles of this phase form thin plates that grow fast and do not contribute to the precipitation strengthening. The formation of Z-phase is accompanied by dissolution of both MX and M_2X phases. To avoid this microstructural instability, the content of niobium in 9%-12% Cr steels has to be kept very low.

Precipitation of Laves phase particles can significantly reduce the content of molybdenum and /or tungsten in solid solution. Laves phase particles usually precipitate during creep exposure, but in the steel TAF650 containing about 2.6wt.% W Laves phase of Fe_2W type was found to precipitate during tempering at 750℃[37]. Particles of Laves phase usually nucleate at $M_{23}C_6$/matrix interface possibly because this interface is enriched in silicon and phosphorus[38]. Preferential nucleation of Laves phase at $M_{23}C_6$ /matrix interface diminishes its contribution to the precipitation strengthening.

2.2.4 Phase Transformation

The addition of Cr to heat resistant steels is not only to improve the corrosion resistance, but also to increase the effectiveness of Cr in gaining the right mechanical properties. The effect of Cr on the microstructures of F/M steels can be seen in the Fe-Cr-0.1%C equilibrium microstructure transformation diagram, (Fig. 2.3)[17, 39].
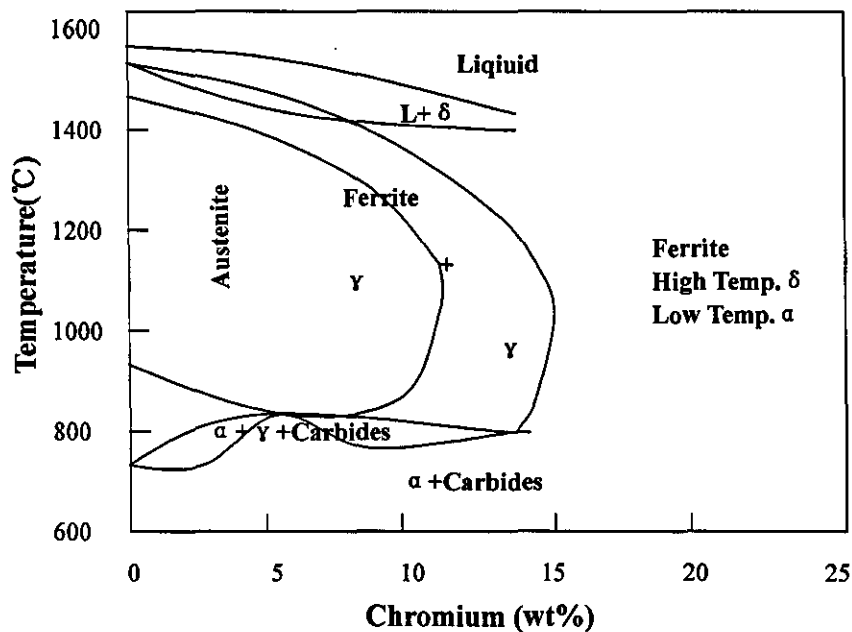
Fig. 2.3. Fe-Cr-0.1%C equilibrium microstructure transformation diagram[17]

It can be seen that, in different ranges of temperatures, 9%-12%Cr can form several types of phases. In multi component systems it is more reasonable to use an equivalent to Cr than Cr content. For Cr equivalent the following equivalent equation is defined[18, 40, 41].

$$Cr_{eq} = Cr + 1.37Mo + 1.5Si + 2Nb + 3Ti$$

The diagram Fig. 2.3 shows that ferrite content increases as Cr_{eq} (Mo or Nb content) increases. When the steel is heated to above austenite temperature followed by continuous cooling, it is observed that there is a close relationship between the microstructure transformation and the cooling rate. As high Cr austenite has high hardenability, fast-cooled austenite will be changed to martensite, which can be seen in
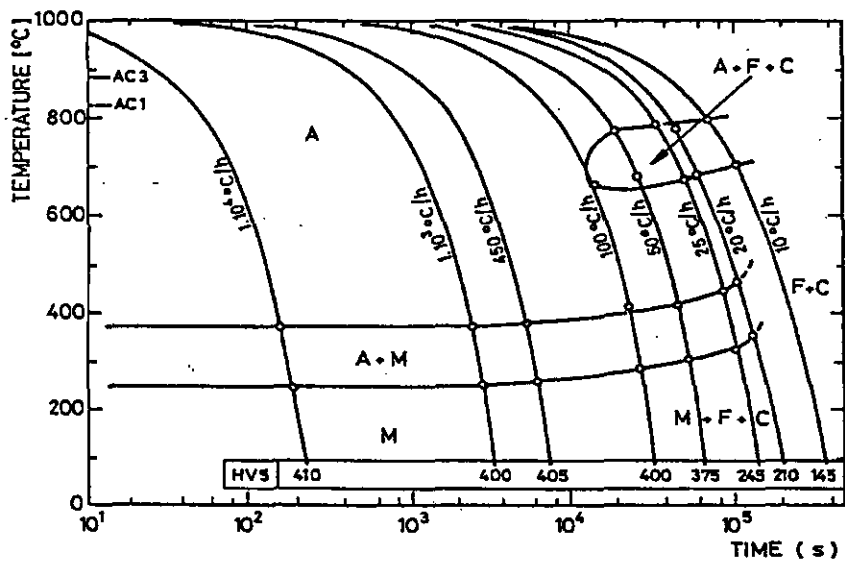
Fig. 2.4. 9%Cr-1%Mo steel CCT diagram[42]

the 9%Cr-1%Mo steel continuous cooling transformation diagram (CCT diagram) (Fig.2.4)[42]. When the cooling rate is below the critical value, proeutectoid ferrite is produced in the transformation. The larger the Cr_{eq} is, the slower the critical cooling speed for ferrite formation.

2.2.5 Strengthening Mechanism

The most potential strengthening mechanisms operating during high temperature service in modified chromium steels are precipitation of the secondary phases (PS), solid solution strengthening (SSS) and transformation strengthening (TS) as the effect of dislocation strengthening is usually limited to short time.

2.2.5.1 Precipitation strengthening

The precipitation strengthening of chromium steels containing 9%-12% Cr and about 1% Mo is effected predominantly by $M_{23}C_6$ carbides. It was shown that with decreasing interpaticle spacing (IPS) of $M_{23}C_6$ carbides the proof stress at room temperature and creep rupture strength (CRS) at high temperature increases, while the creep rate decreases.

Microstructural analyses of chromium modified steels containing vanadium revealed precipitation of very fine particles during creep exposure. The beneficial effect of vanadium on the creep resistance of chromium steels is explained by the precipitation of VN in the course of the creep process. The creep rate and CRS respectively are then controlled by the mean effective IPS of $M_{23}C_6$ and VN particles[44]. When the volume fraction of VN increases, the creep resistance increases[45]. With increasing Al and /or Nb content in the steel, creep resistance decreases due to a reduction in nitrogen content available for formation of vanadium nitride.

2.2.5.2 Solid solution strengthening

In order to assess how the creep strength of ferritic steel depend on Mo and/or W content, the reduction of these elements in solid solution in the course of creep must be taken into account. When the creep strength of Cr modified steels is defined by the stress leading to the creep rate $10^{-8}s^{-1}$ at 600°C, the beneficial effect of increasing Mo content can be set to 2.64% and W content to 4%. When assessing how the creep strength of modified Cr steels depend on the Mo and/or W contents, we must consider how the concentration of

these elements in the solid solution changes in the course of creep. Precipitation of Laves phase should be expected especially in steels with a Mo equivalent (%Mo+0.5%W) higher than about 1%.

Fe_2Mo and M_6C deplete the Mo content from the solid solution and weaken the SSS. The solubility limit of Mo at 600°C is well below 1%, therefore there is no advantage to increase the Mo content of modified Cr steels above 1%. Similarly, we can expect the decrease of W content in the solid solution during creep exposure. This assumption was confirmed on the Nippon W-bearing steel NF616 (9%Cr-0.56%Mo-1.8%W) [46].

The amount of W in precipitates increased with prolonged time of isothermal ageing or creep exposure at 600°C. After 20,000 hours' exposure at 600°C only one third of total W content in the steel remained in the solid solution and could contribute to the SSS.

2.2.5.3 Transformation strengthening

A quenched martensite phase is produced from austenite through diffusionless transformation by quenching from high temperature. Therefore, the alloying elements are dissolved in the γ-phase remain in the martensite phase, resulting in strengthening[44].

2.2.6 Mechanical Properties

2.2.6.1 Conventional mechanical properties

The conventional mechanical properties of the high Cr ferritic steels include the creep and fatigue strength, yield strength and tensile strength at a high temperature. Compared with other standard steels, e.g. T9, the properties of the modified 9%Cr-1%Mo steel are better, as shown in Fig. 2.5[1, 20]. An advantage of the 9%Cr-1%Mo steel is its lower ductile-brittle transition temperature (DBTT) and higher impact toughness (Fig. 2.6) [43].
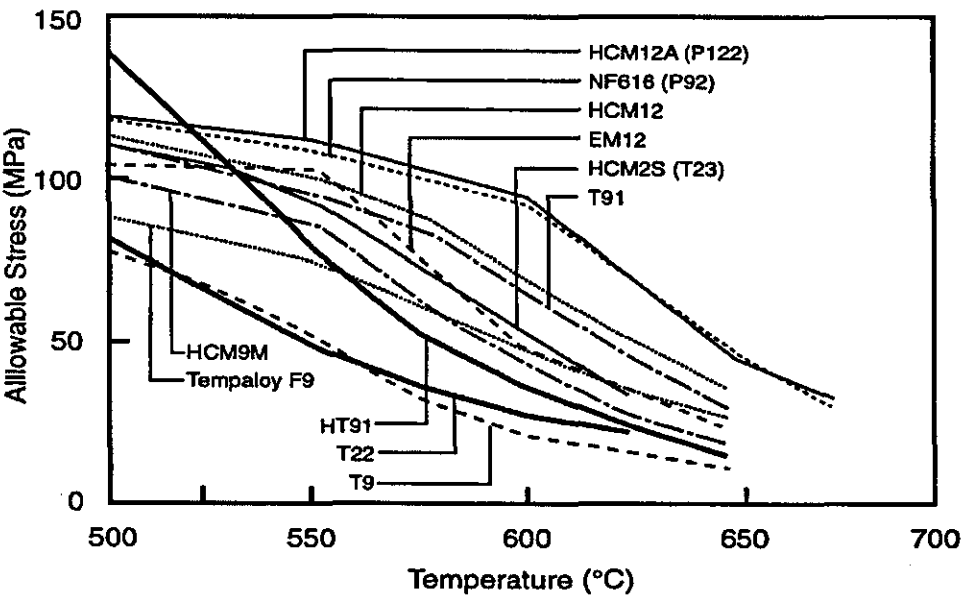
Fig. 2.5. Variation of nominal stress intensity with temperatures for different materials[20]
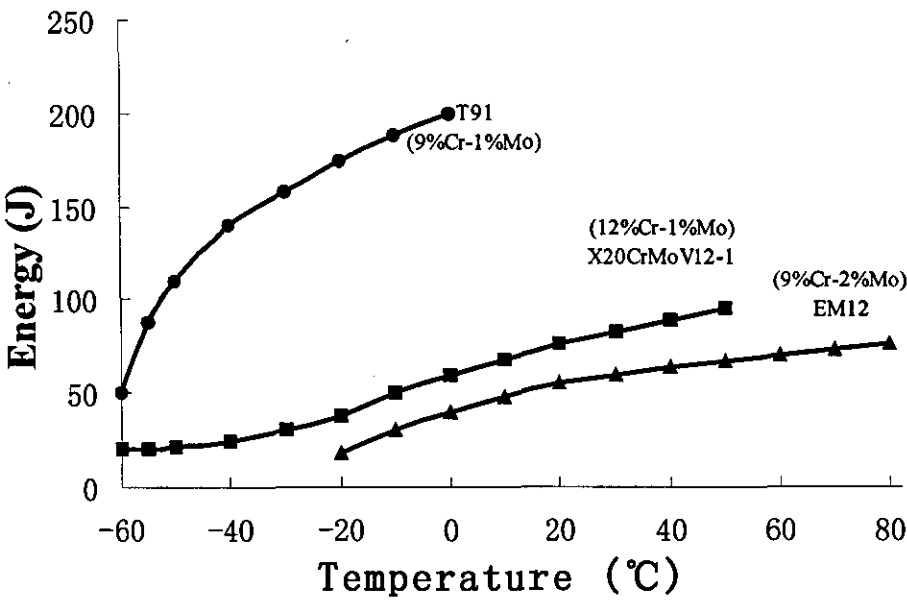
Fig. 2.6. Comparison of Charpy impact curves for different high Cr steels[43]

Although heat resistant steel structures are mostly used at high temperature, for pipes and pressure vessels, the toughness should be maintained both at high and ambient temperature to withstand the varied stress. These structures will also be tested under water pressure, and the equipment handling, debugging and repairing will also stand impact or cold initiation impact. Hence this kind of steel and weld should be ductile. On this point, there is no doubt that the 9%Cr-1%Mo steel has great potential[46, 47].

As well known, the mechanical properties and microstructures cannot be considered separately, and the microstructures are related closely to the chemical compositions. In order to increase the mechanical properties of a material, the microstructure and the final alloy composition must be optimized and controlled[19, 48]. The compositions of heat resistant steels have been described above. The microstructural aspects connected to mechanical performance include: lath martensites, original austenite grain size, precipitate size and distribution, and amount of residual δ ferrites. A large amount of well-dispersed fine precipitates will be beneficial to the steel's strength and toughness; a fine grain size will also improve the overall properties. Generally it is known that the smaller the lath martensite is, the better is the toughness of material. The effect of residual δ ferrite is more complex and contradictory. It was thought that the small amount of residual δ ferrite would not be harmful to the steel's properties.

Studies show that small amount of δ ferrite (e.g. <10%) form intergranularly in the heat resistant steel and help to prevent austenite grains from growing. For example in weld metal, δ ferrite can reduce welding solidification cracking because of its better toughness. Otherwise a certain amount of Ni must be added to remove all δ ferrite. If a small amount of δ ferrite were allowed to exist, which could reduce the properties of materials in a short period of time; however because there is no huge amount of Ni addition, the creep strength will be improved in a long run[49].

2.2.6.2 Fracture toughness

Fracture toughness is the ability of materials to resist the crack propagation. Similar to other toughness indices, the fracture toughness generally reflects the strength and plasticity of materials. Different types of crack sources (gas pores, inclusions, microcracks, etc) exist in practical structures, and fracture mechanics can be used to quantify this. The relationship between the crack size in the structures and the working stress of structure and the ability to crack materials (fracture toughness) can be evaluated quantitatively by using fracture mechanics, which can be used to assess the safety and the longevity of structures with cracks. At present the safety design of engineering structures based on fracture mechanics has been widely used, such as K_{1c}, J_{1c}, etc[50-59].

2.3 Welding of High Cr Ferrite Heat Resistant Steels

2.3.1   Welding Processes and Applications

Welding technology has been used widely in the manufacturing of almost all metal material structures, including the high Cr ferritic heat resistant steels. The typical applications of welding for turbine parts are given in Table 2.3[4]. The welded joint is always the weak area in welded structures. Therefore the welding effect is the key to controlling the quality of products.

Apart from the metal arc welding (MAW) and the submerged metal arc welding (SMAW) electrodes, there is also a strong need for consumables for other welding processes, such as GTAW (gas tungsten arc welding), GMAW (gas metal arc welding) and SAW (submerged arc welding) [60, 61].

Table 2.3. Applications of welding in gas turbine parts[4]

Type of Welding	Material	Welding Procedure	Reason for Welding	Main Problem
Fabrication Welding of Castings	12%CrMoV, 2.25%CrMoV 1%CrMoV, 2.25%MoCMn	MAW SMAW	Repair of casting defects	Creep and mechanical properties of weld region
Construction Welding Casting to casting, similar material Casting to forging /pipe, similar mat.	as above	MAW SAW SMAW	Design and /or fabrication	as above
Casting to casting, dissimilar material Casting to forging/pipe, dissimilar mat.	as above 9-12%CrMoV (Nb) 2.25%Cr1%Mo 1.25%Cr1.1%MoV 0..5% MoC, CMn	MAW SAW SMAW	Design and /or fabrication	Selecting weld metal compromise in PWHT temperature Diffusion in fusion region
Forging to forging-rotor shaft welding	3%-12% NiCrMoV 2%Cr1%NiMo 1%CrMoV 12%CrMoV	SMAW SAW	Design and /or fabrication Service behaviour	NDT Mechanical properties
Overlay welding of casting on Forging/piping	Ni-base alloys Hardfacing material Martensitic Cr steel	MAW, SAW SMAW	Wear, corrosion and erosion prevention Filler wire	Dissimilar materials Heat treatment Hot cracking
Rotor Forgings	3.25%NiCrMoV 2%Cr1%NiMo 1%CrMoV 1%CrMo	MAW SAW SMAW	Prolongation of service-time by repairing of failures caused by creep exhaustion, fatigue cracks, distortion, grazing erosion, corrosion.	Properties of base material Local heat treatment
Turbine blades Castings	12%Cr steels 12%Cr steels	MAW, SMAW MAW, SMAW	Prolongation of service life-time by repair of erosion-corrosion failures Prolongation of service life-time by repairing of creep, creep-fatigue and fatigue damage	Stability of shape, residual stresses Properties of base material, heat treatment

2.3.1.1 SMAW

Owing to its adaptability, the SMAW process is still widely used for both new fabrications and upgrades or repairs. The electrodes used for welding CrMo creep resisting steels such as P91 and P92 employ low hydrogen basic flux systems. These are designed to satisfy demanding all-positional operability for fixed pipework welding and excellent metallurgical integrity is required for critical applications. The all-weld metal composition closely matches the major alloying of the relevant base materials although there is usually some minor variations to optimise weld metal properties (e.g. the impact property).

2.3.1.2 GMAW

As a process of potentially high productivity, interest in GMAW for welding type 91 materials is increasing. Of the wires available for GMAW process, because of its flexibility in alloying and low cost, MCW (Metal Cored Wire) is attracting more attention and is now being used in real applications. The operability of the GMAW process using a MCW is strongly influenced by the type of the shielding gas.

2.3.1.3 GTAW

There is a need for consumables for the GTAW process for various applications in welding type 91 materials where other processes are either not practicable or too costly. Solid wires with or without nickel additions are available but relatively expensive and offer little flexibility in alloying content for some of the new highly alloyed steels[62]. Metal-cored wire, on the other hand, offers a viable alternative particularly where continuous consumables are required for auto-GTAW or for spool-on-gun manual GTAW.

2.3.1.4 SAW

For applications where mechanized welding is practically convenient, SAW is undoubtedly preferred and more productive than SMAW[63]. Welding 9Cr material with the MCW using SAW was investigated. Five fluxes of different levels of basicity were employed.

2.3.2   Weldability

Because the martensite will be formed in wide range of cooling rates for high Cr ferritic steels, more obvious hardenability and cool-cracking tendency will be obtained during high temperature welding followed by air cooling. If the hydrogen has emerged in the meantime, there will be a greater chance of cool-cracking[64].

Preferential welding crack sensitivity index formula is used as follows,

$$P_{cm} = C + \frac{Mn}{20} + \frac{Si}{30} + \frac{Ni}{60} + \frac{Cr}{20} + \frac{Mo}{15} + \frac{V}{10} + \frac{Cu}{20} + 5B$$

The P_{cm} of high Cr ferritic steels is more than 0.6, which shows larger hardenability. Furthermore, as large amounts of ferrite stabilizing elements exist in the high Cr steels, a certain amount of δ ferrite occurs in the welds and the heat affected zone (HAZ). This remains at room temperature, and will affect the properties of welded joint. Because of the different welding and PWHT processes, different structures and carbide precipitates will be formed in the welding resulting in welding joints with very different properties. Therefore an appropriate welding process should be adopted to control the weld quality. Typically, the processes chosen for the high Cr ferritic heat resistant steels welding include following aspects[65, 66]:

2.3.2.1 Selection of welding materials

To ensure the welded joint and the parent material perform properly at high temperature, it is necessary to select welding materials with the same composition as the parent materials. As the property of weld metals is poor, some alloying elements should be added to it to improve the weld performance.

2.3.2.2 Electrode drying and slope crater treatment

These two measures can reduce penetration of harmful hydrogen during welding. The temperature for drying electrodes should be about $350^{\circ}C$. Before welding, electrodes should be placed in an oven with a temperature of about $80^{\circ}C$.

2.3.2.3 Preheating

Preheating can extend the cooling time of welds from peak temperature to room temperature and will allow the diffused hydrogen in welds to have enough time to diffuse out and prevent the cool cracking. Preheating can also make the temperature distribution of weldments more uniform and reduce internal stress. Hence preheating is a very important process for preventing the cool cracking and improving the weld properties. The preheating temperature chosen depends on the plate thickness, weld type and input energy. Normally the preheating temperature is suggested to be $150\sim250^{\circ}C$[67].

2.3.2.4 Interlayer temperature

The proper interlayer temperature (the temperature between the welding pass) is also a very important measure to prevent welds from quenching crack or cooling crack; it is usually chosen by minimum preheating temperature.

2.3.2.5 Critical cooling temperature

Because the preheating and interlayer temperatures of high Cr heat resistant steels are high, austenite exists in both the welds and the HAZ zone. If the treatment is carried out once welding is finished, austenite may be decomposed or changed to nontempered martensite during cooling, resulting in deteriorating properties of the welds. Therefore PWHT should be employed till cooling to below the critical temperature has occurred. The critical cooling temperature is based on the temperature of austenite to martensite transformation under the condition of no crack appearance.

2.3.2.6 Post weld heat treatment

PWHT is a very important heat treatment process to high Cr steels. Excellent fatigue and creep strength of high Cr steels at high temperature are attributed to well dispersed carbide particles and high-density dislocation sub-microstructures in the steels. Fine carbo-nitride compounds (Nb, V)(C, N) with sizes less $0.1\mu m$ in tempering are obtained with the addition of elements such as Nb, V. The formation of $M_{23}C_6$ can prevent the grain growth at high temperature and improve the stability of microstructures. In order to form these carbides it is necessary to have enough time at the right temperature for the diffusion of alloying elements. For example, Cr can only diffuse effectively above 500°C, and equivalent temperature for Mo, V and Ti are at 550°C, 575°C and 600°C respectively, so an efficient tempering temperature should be above 600°C[68].

For the high Cr steel weldments, PWHT is additionally important as high temperature tempering can not only stabilize microstructures but also remove welding residual stress and improve the toughness of welds. If the temperature is too low or the time is too short, heat treatment effects can not be achieved; on the other hand, tempering at too high a temperature or for too long might produce serious recrystallization of martensite and precipitate growth resulting in the deterioration of the performance of welds. Generally PWHT temperature cannot be higher than the tempering temperature of parent material. The tempering temperature of the modified 9%Cr-1%Mo steel is at 680~780°C,

depending on the compositions and service conditions of the steel. As a general rule, the low temperature limit is chosen when the creep and fatigue strength are important, and the upper limit should be taken if corrosion and resistance to hydrogen embrittlement are of great concern [69].

2.3.3   Characteristics of Microstructure Transformation of Weld Metal

As weld materials are chosen by the principle of equivalent composition, the high Cr ferritic steel, weld metals should be similar to parent materials in composition. However the welding process is different to common heat treatments, the cooling rate is quite high and far away from the equilibrium. Even though they have the same composition, the microstructures of the welds and parent metals will not be completely the same, which will lead the weld metals to have quite high strength but very low toughness and plasticity which is not beneficial for either crack resistance or the practical performance of welds.

The microstructures of weld metal microstructures after welding and PWHT consist mainly of tempered martensites, precipitates, and small amounts of δ ferrite. Tempered martensites and precipitates are similar to parent materials while δ ferrite is a non-equilibrium phase formed in high temperature welding followed by rapid cooling, as shown in Fe-Cr-C equilibrium diagram (Fig. 2.3). The δ ferrite is the first phase produced after solidification, and will be transformed to martenite at a lower temperature. However there are many ferrite-stabilizing elements such as Cr and Mo in welds, and the cooling rate of welds is fast; δ ferrites may therefore remain at room temperature. Therefore in weld composition design the amount of austenite stabilizing elements should be considered to resist the formation of non-equilibrium δ ferrite. Ni and Cr equivalent [18, 19] can show the influences of ferrite and austenite formation elements on the microstructures in relation to the Schaeffler diagram (Fig. 2.7) [70]:

$Cr_{eq} = Cr + 1.37Mo + 1.5Si + 2Nb + 3Ti$

$Ni_{eq} = Ni + 0.81Mn + 22C + 14.2N + Cu$
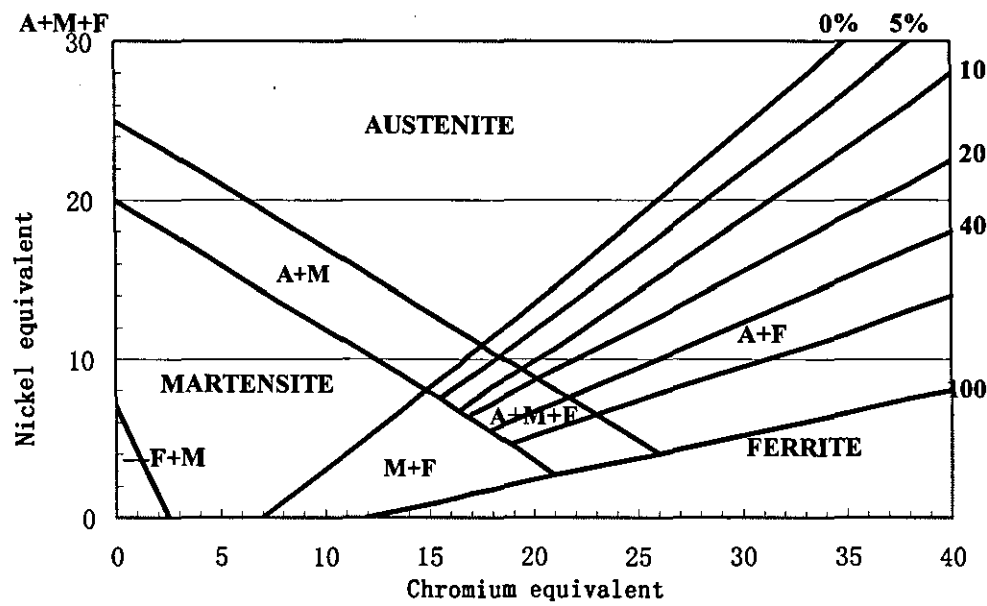
Fig. 2.7. Schaeffler diagram of Fe-Cr-Ni weld metals

2.3.4   Type IV Crack

2.3.4.1 Weld crack classification

The typical weld damage includes creep, fatigue, thermal fatigue and creep-fatigue types that can occur in different locations (e.g. outer diameter: OD, mid-wall and inner diameter: ID; base metal, HAZ and weld metal).

The identification of weld zone and the weldment defects are commonly classified in terms of their location in the joint according to the scheme reproduced in Fig. 2.8 [71, 72].

● Type I – Oriented transverse or longitudinal, located in the weld, and remains in the
        weld
● Type II – Similar to Type I but grow out of the weld
● Type III – Located in the coarse-grained HAZ
● Type IV – Located in the fine-grained HAZ
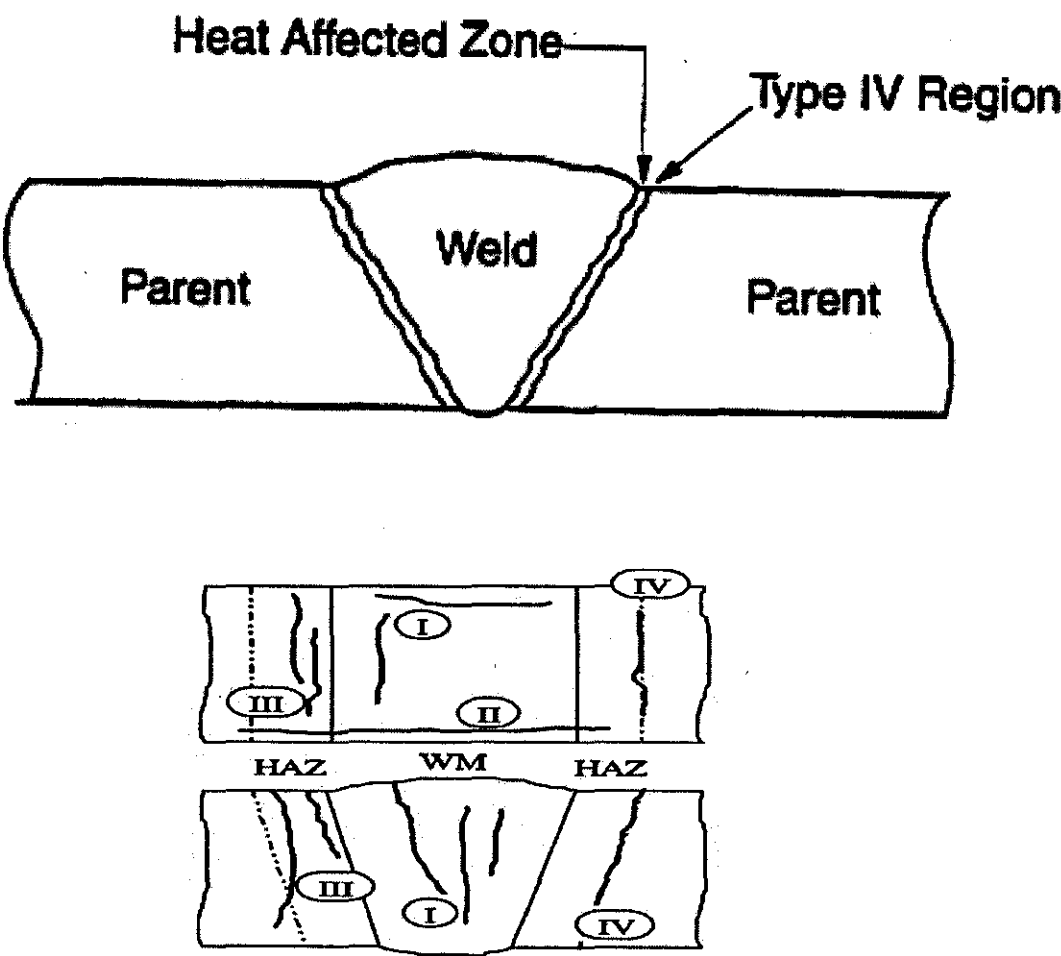
Fig. 2.8. Identification of assessment zones and classification of weldment defects[71]

2.3.4.2 Type IV crack characteristics

The intricate nature of damage accumulation associated with a growing creep crack in HAZ of a 9CrMo-pipe joint is illustrated in Fig. 2.9[73].
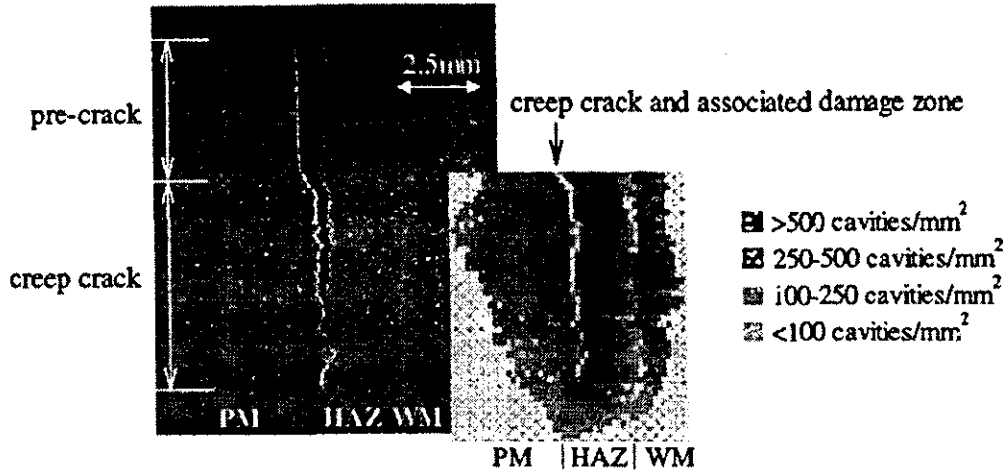
Fig. 2.9. Creep crack growth in the Type IV region of a 9CrMoVNb pipe joint at 600°C[73]

The Type IV failure location is at the outer boundary of the HAZ. This region is partially re-austenitised by reheating within the intercritical temperature range during the welding thermal cycle and most of the carbon and nitrogen are precipitated from solution. Further recrystallisation of the transformed microstructure during PWHT produces a relatively soft martensite, which lacks the carbo-nitride grain strengthening essential for creep resistance. This weakened zone where "Type IV" creep failure occurs is characteristic of all creep resisting CrMo steels.

The Type IV crack are also characterized as follows:
- Initiates at subsurface
- Cracking occurs very early in component life
- Only creep cavitation present to 70%-80% life fraction (LF)
- Once a crack initiates, growth is very rapid through highly damaged material
- Cracking grows along the grain boundaries

2.3.4.3 Type IV crack susceptibility

- Material and process considerations
  --Welding process

31

--PWHT

--Inclusions

--Carbide former elements (Cr, Ti, V)

● Stress considerations

--multiaxial stresses

--Piping system axial stresses

--Higher susceptibility at terminal connections (header outlets, Tees, Valves)

--Damage is greatest along planes that are closest to being purely radial

2.3.5 Fracture Toughness of Weld Metal

The weld metal toughness may be thought to be irrelevant in assemblies designed for operation in the temperature range of 500-600 °C, since this is definitely far in excess of the temperature range at which brittle fracture could occur. However, the components may very well also be stressed at ambient temperature during testing or start-up, for example. To minimise the risk of brittle fracture in these situations, some authorities considered that the weld metal should satisfy a minimum toughness value at +20°C. The American Welding Society (AWS) specification does not specify impact requirements, but the non-mandatory appendix to A5.5-96 proposes that the purchaser and supplier should agree a suitable test criterion. On the other hand, the recently introduced European specification EN1599: 1997 requires a minimum average of 47J and a minimum single value of 38J at 20°C. These values appear to be rough and values in the range 35-50J at 20°C after a prescribed PWHT are typical. However, it is difficult to justify the need for toughness >41J specified for parent material, or indeed higher than that specified for X20 weld metal, with minimum of 34J average and 22J single values[10, 31].

There are four factors which have a major influence on toughness of weld metal:

(1) **Composition** Normally, the elements which are beneficial in improving creep performance, are detrimental in terms of toughness. These elements include niobium, nickel, vanadium and silicon. For the modified 9%Cr-1%Mo steel, adjustments to the Nb

and Ni content are crucial to obtain acceptable toughness values. Compared with the parent steel, the Nb content has to be lowered. However, as stated above, the Nb is essential for satisfactory creep resistance and cannot be totally excluded. The Ni content, on the other hand, is higher in the weld metal than in the parent material. The addition of Ni lowers the Ac_1 temperature. This can have both a positive and a negative effect on the toughness, depending on how much it is lowered. The positive aspects include the fact that an Ac_1 temperature that is closer to the PWHT temperature improves the response to tempering, and thus has a beneficial effect on the toughness. It also minimises the risk of residual δ ferrite. δ ferrite is thought to lower the creep resistance and may also have a detrimental effect on toughness. However, an excessive amount of Ni may lower the Ac_1 to a level that is exceeded by the upper end of the PWHT temperature range, causing austenite to form, which will in turn be transformed into untempered martensite. Untempered martensite has a negative effect on the impact toughness. Hence a balanced composition to restrict δ ferrite and to give a fully martensitic microstructure[74] helps to contribute both optimum toughness and creep performance to the steel

(2) **PWHT** Effective tempering of the martensitic microstructure is essential to obtain a reasonable level of toughness. In practice this involves selecting both an appropriate temperature and time. The AWS specification requires PWHT of 730-760°C for 1h. This is considered insufficient for normal fabrication procedures and a minimum of 2-3h at a temperature range 750-760°C is usual, or longer for thicker sections.

(3) **Welding process** The choice of welding process can have a dramatic influence on the toughness of weld metal because of the effects of fluxes and shield gases. The highest toughness at + 20°C after PWHT is normally achieved with solid wire and MCW using GTAW with pure argon, while flux processes such as MMW (Manual Metal Welding) and SAW produce lower toughness values. It has been suggested that the reason for this is varying oxygen content. Oxygen content of less than 100-200ppm may be reached with GTAW procedures, while MAW and SAW will produce typical oxygen contents in the range of 400-800ppm[75].

(4) **Microstructural refinement** This is influenced by heat input or bead size. The sequence can also vary the toughness, as is the case generally for weld metals, which undergo transformations during cooling and reheating in multipass welding. The fracture toughness of welds will always be a problem in engineering. Studies indicate that the crack propagation behavior is related closely to the stress field distribution near the crack tip. However in weldments the crack tip stress distribution is more complicated because of the influences of non-uniform weld microstructures, stress concentration and welding residual stress, where severe inhomogeneity appears to change the fracture toughness of welds distinctly from that of the parent materials.

References to Chapter 2

1. G.W. Cunningham, Ferritic Steels as Alternate Structural Materials for High-temperature Applications, Proc. Of Conf. on Ferritic Steels for High-temperature Applications. Ed. By A. K. Khare, ASM, New York, 1981, 3-6.

2. D. Christian,The Development on Heat Resistant Steels, Metal Materials, 3, 1988,1-8

3. S. Kjaer, Advances in PF Plant, 1990-2010, PARSONS 2003, Proceedings of the Sixth Intern. Charles Parsons Turbine Conf., 16-18 Sept. 2003, Trinity College Dublin, Ireland, 2003, 57-67.

4. M. Abe, M. Igarashi, N. Fujitsuna, K. Kimura and S. Muneki, New Ferritic Heat Resistant Steels for 650°C USC Boilers, 3rd EPRI Conf., Swansea, UK, 1-6 Apr. 2001, 1-10.

5. M. Hattestrand and H. O. Andren, Mater. Sci. Eng., A270, 1999, 33-37.

6. H.D. Newell, Met. Progr., Feb. 1936, 51-58.

7. B. Rotenstein, Metallurgia, 23(5), 1971, 314-321.

8. M. Gold and R. I. Jaffee, Materials for Advanced Steam Cycles, ASM J. of materials for Energy System, 6(2), 1984, 130-145.

9. F. Masuyama, New Developments in Steels for Power Generation Boilers, in Advanced Heat Resistant Steels for Power Generation, Ed. By R. Viswanathan and J. W. Nutting, IOM Communications Ltd., London, 1999, 33-48.

10. R. Viswanathan, Damage mechanisms and Life Assessment of high-Temperature components, ASM International, Metals Park, OH, 1989.

11. H. Haneda, I. Sakaguchi, S. Hishida, T. Ishigaki and T. Mitsuhashi, Proceedings of the Third International Conference on Steel Rolling, Tokyo, September 2-6, 1985, 669-676.

12. T. Topoda, Development of Thick Walled Pipes and Headers of Modified 9Cr Steel, Proc. of the Second International Conference on Improved Coal-Fired Power Plants, 2-7 Nov. 1988, Palo Alto, CA, EPRI Report GS –6422, 36-1.

13. B.W. Roberts, F. V. Ellis and J. F. Henry, Thick Section Welding of Modified 9Cr-1Mo (P91) Steel, EPRI Report TR –101394, September 1992.

14. T. Fujita and K. Oda, Development of a 9Cr Steel, in EPRI Report, CS –5581- SR, 5-201.

15. E. Metcalfe, Ed., Proc. New Steels for Advanced Power Plants, EPRI Report TR – 104952, 1995.

16. W.Bendik, New 9-12% Cr Steels for Boiler Tubes and Pipes: Operating Experiences and Future Developments, in Advanced Heat Resistant Steels for Power Generation, R. Viswanathan and J.W. Nutting, Ed.; IOM Communications Ltd., London, 1999, 133-142.

17. C. Willby and J. Walser, Material Choices for the Commercial Fast Reactor Steam Generators, Inter. Conf. On Ferritic Steels for Fast Reactor Steam Generators, 30 May-2 June 1977, British Nuclear Energy Society, London, 160-163.

18. S.J. Sanderson, Mechanical Properties and Metallurgy of 9%Cr-1%Mo Steel, Ferritic Steels for High-Temperature Applications, Ed. By A. K. Khare, ASM, New York, 1981, 85-100.

19. J.F. Lancaster, Metallurgy of Welding, Fourth Edition, London, 1987, 28-35.

20. R. Viswanathan and W. Bakker, Materials For Boilers In Ultra Supercritical Power Plants, 2000 International Joint Power Generation Conference, Miami Beach, Florida, July 23-26, 2000.

21. K.Hamada, A.Okada, H. Maeda and I. Ishida, Nucl. Eng. And Design, 139, 1993, 277.

22. A. Orlova, J. Bursik, K. Kucharova and V. Sklenicka, Mater. Sci. and Eng., A245, 1998, 39-48.

23. E. Cerri, IBID., A245, 1998, 285.

24. A. Strang and V. Vodarek, Mater. Sci and Tech., 12, 1996, 552.

25. A. M. Barnes, The Effect of Composition on Microstructural Development and Mechanical Properties of Modified 9%Cr-1%Mo Weld Metals, Microstructural Stability of Creep Resistant Alloys for High Temperature Plant Applications, Ed. By A. Strang, The Institute of Materials, 1998, 339-359.

26. V. K. Sikka, Development of Modified 9%Cr-1%Mo Steel, 7th Annual Conf. Material for Coal Conversion and Utilisation, National Bureau of Standards, Gaithersburg, Maryland, USA, Nov. 1982, 411-437.

27. P. Patriarca, US Advanced Materials Development Programme for Steam Generators, Nucl. Tech., 1976, 28(3), 516-536.

28. R.G. Faulkner, The Influence of Cobalt, Copper and Tungsten on the Microstructure of 9% Chromium Weld Metals, Mater. Sci. and Tech., 19(3), 2003, 347-354.

29. L. Lundin, Material Sci. and Tech., 13, 1997, 223.

30. H. Cerjak, V. Foldyna, P. Hofer and B. Schaffernak, Microstructure of Advanced High Chromium Boiler Tube Steels, The Institute of Materials, 1997, 145-158.

31. W. Garrison and R.F. Buck, An Overview of the Development of Advanced 9-12% Cr Steels, In ASM Symposium on Materails for Rotating Machinery, Oct. 1999, Cincinnati.

32. H. Cerjak, P. Hofer and B. Schaffernak, The Behaviour of Weldings in Large 9% Cr Alloy Castings, Parsons 2000 Conference, Advanced Materials for 21st Century Turbines and Power Plant, Book 736,S.386-398, ISBN 1-86125-113-0,The University Press Cambridge.

33. H. Nickel, Y. Wouters, M. Thiele and W.J. Quadakkersthe, Creep Rupture Properties of 9% Chromium Steels and the Influence of Oxidation on Strength, Min.Pro.Ext.Met.Rev.,Vol.22,181-195.

34. A.C. Filemonnwicz and K. Bryla, The Role of Boron in the 9% Chromium Steels for Steam Power Plants, PARSONS 2003, Proceedings of the Sixth Intern. Charles

Parsons Turbine Conf., 16-18 Sept. 2003, Trinity College Dublin, Ireland, 2003, 365-377.

35. V. Foldyna and A. Jakobova, Proc.5th Conf. on Materials of Advanced Power Engineering 1994,C.R.M., Liege, Belgium, October, 1994,453.

36. A. Strang and V. Vodarek, Materials Sci. and Techn., 12, 1996, 552.

37. V. Foldyna and Z. Kubon, Steel Research, 67, 1996, 375.

38. H. Andren and L. Lundin, Proc. of Parsons 2000 Advanced Materials for 21st Century Turbines and Power plant, IOM, London, England, 2000, 603.

39. S.H. Ryo, Effects of Alloying Elements on the Creep Rupture Strength of 9-12%Cr Steels, PARSONS 2000, Advanced Materials for 21st Century Turbines and Power Plant, Ed. By A. Strang et al., The Institute of Materials, 2000, 472-484.

40. R. Kaneko, Y.Tanaka and T. Fujita, The Thermal and Nuclear Power, 46(9), 1995, 968.

41. F.B. Pickering and A.D. Vassiliou, Effect of austenitizing temperature on constitution, transformation, and tempering of 9Cr-1Mo steel, Met. Technol., 7(10), 1980, 409-413.

42. A Alamo, J.C. Brachet, A. Castaing and C. Foucher, Effect of Austenitizing and Tempering Conditions on Structure and Mechanical Properties of 9Cr-1Mo Martensitic Alloy, Microstructure and Mechanical Properties of Aging Materials II, the 1995 TMS Annual Meeting in Las Vegas, Nevada, Feb., 12-12, 1995, 121-134.

43. W.B. Jones and J.A. Van Den Avyle, Met. Trans. A, Vol.11A, 1980, 1275.

44. V. Vodarek and A. Strang, Scripta Materialia, 38, 1998, 101.

45. S.J. Sanderson, Metal Science, 12, 1978, 220.

46. B.B. Argent, J. Iron and Steel Inst., 208, 1970, 830.

47. P.J. Alberry, Weld. Fab. Metal., 54, 1986, 33-34

48. K. Kimura, K. Sawada, T. Ohba, and H. Kushima, PARSONS 2000, Advanced Materials for 21st Century Turbines and Power Plant, Ed. By A. Strang et al, The Institute of Materials, 2000, 590-602.

49. G.Y. Lai, Metall. Trans., 5, 1974, 1663-1675.

50. E.R. Parker, Eng. Frac. Mech., 7, 1975, 371-375.

51. M. Sarikeya, Metall. Trans. A, 11A, 1982, 227-2237.

52. K.H. Khan, Metall. Trans. A, 9A, 1978, 839-907.

53. M.F. Carlson, Metall. Trans. A, 10A, 1979, 1273-1284.

54. R.O. Ritchie, Metall. Trans. A, 7A, 1976, 831-888.

55. R.O. Ritchie, Metall. Trans. A, 9A, 1978, 331-341.

56. S. Lee, Metall. Trans. A, 16A, 1985, 1633-1648.

57. W.M. Garrision, Metall. Trans. A, 17A, 1986, 669-678.

58. Y. Tomita, Metall. Trans. A, 19A, 1988, 2513-2521.

59. S.J. Sanderson, Metal Sci., 10, 1977, 490-492.

60. G. Dai, NDT & E International, 6, 1990, 17-26.

61. J. Arndt, TheT23/T24 Book, New Grades for Waterwalls and Superheaters, Vallourec and Mannesmann Tubes, 1998.

62. N. Komai,and F. Masuyama, Advanced Heat Resisting Steels for Power Generation, ISIJ Inter., 42(12), 2002, 1364-1370.

63. C. Shiga, A. Gotoh, T, Kojima, Y. Horii, Y. Fukada, K. Ikeuti and F. Matuda, State of the art review on the effect of PWHT on properties of steel weld metal, Welding in the World/Le Soudage dans le Monde, 37(4), 1996, 163-176

64. H. Fujii, D.J.C. MacKay, H.K.D.H. Bhadeshia, H. Harada and K. Nogi, J. of the Japan Institute of Metal, 63(7), 1999, 905-911

65. I.A. Shibli, Creep and fatigue crack growth in P91 weldments, 9th Int. Conf. On Creep and Fracture of Engineering Materials and Structures, Swansea, Wales, UK, 1-4th April 2001, Vol 769, 777-787.

66. H. Heuser and R. Fuchs, Properties of Weldments in the Creep Resistant CrMo-Steels T23/T24 and P91/P92 and E911 Made with Matching Filler Metals, 4th International EPRI Conference on Welding and Repairing Technology for Power Plants, Marco Island, Florida, 2000.

67. A.N.R. Hunter, E.J. MacDonald and E.G. Taylor, Specification, Development and Optimization of the Welding and Post-Weld Heat Treatment Procedures, Boiler Shell Weld Repair, ImechE, ISSN 1357-9193, 25 October 1999,ImechE HQ, London, UK.

68. A. Zielinska-Lipiec, F. Czerwinski, J.A. Szpunar, The influence of heat treatments on the microstructure of 9% chromium steels containing tungsten, J. of Mater. Proc. Technol., 64, 1997, 397-405.

69. A.L. Schaeffler, Metal Progr. 55(6), 1949, 680-680B.

70. N. Parvathavarthini, S, Saroja and R.K. Dayal, Influence of microstructure on the hydrogen permeability of 9%Cr-1%Mo ferritic steel, J. Nucl. Materials, 264, 1999, 35-47.

71. G.C. Bodine, C. Chakravarti, C.M. Owens, B.W. Roberts, D.M. Vandergriff and C.T. Ward, The Development of a Cr Steel with Improved Strength and Toughness, Inter. Conf. On Ferritic Steels of Fast Reactor Steam generators, 30 May-2 June 1997, British Nuclear Energy Society, London, 160-163.

72. S.R. Holdsworth, Proc. Inter. Conf. on Integrity of High-Temperature Welds, Suffolk, UK, 1998, 155-166.

73. H. Cerjak and F. Schuster, Weldability and Behavior of Welding of New Developed Cr Steel, PARSONS 2003, Proceedings of the Sixth Intern. Charles Parsons Turbine Conf., 16-18 Sept. 2003, Trinity College Dublin, Ireland, 2003, 275-286.

74. Z. Zhang, A.W. Marshall and J.C.M. Farrar, Proc. Inter. Conf. On Integrity of High-Temperature Welds, Suffolk, UK, 1998, 77.

75. A. Barnes, Microstructural Stability of Creep Resistant Alloys for High Temperature Plant Applications (Conference), Sheffield, UK, March, 1997.

CHAPTER 3:

Modelling of Grain Boundary Microstructure in Alloys (I)— Grain Boundary Segregation Model

3.1 The Development on the Grain Boundary Segregation Modelling

The research on grain boundary segregation (GBS) can be dated back to 1957, when D. Mclean first studied the segregation of elements on the grain boundaries[1]. His work led to the establishment of first boundary segregation criteria based on the equilibrium thermodynamics of segregation. Later Mclean and Seah[2] studied the kinetic process of equilibrium segregation (ES), as well as the effect of temperature and time on the temper brittleness of boron-containing steels. Aust[3] and Anthony[4] developed the non-equilibrium segregation theory. The mechanism is different from that of the equilibrium segregation, and is dependent on the combined diffusion of vacancy-solute complexes. Recently, based on the complex diffusion mechanism, Faulkner[5]and T. Xu[6] both have carried out the detailed mathematical derivation on the grain boundary non-equilibrium segregation (NES) thermodynamics and kinetics. Their research confirmed that the grain boundary non-equilibrium segregation can be classified into two stages: segregation and de-segregation. They put forward the concept of a critical time. Currently the research on segregation has extended from the grain boundaries to varied surfaces of phase boundaries. The research methods have also been developed from original radioactive tracer methods (which was done by Mclean) to many modern approaches such as Auger electron spectroscopy, field ion microscopy, neutron activation, and field emission gun transmission electron microscopy (FEGTEM), etc. Up to now, boundary segregation has become an important branch of metallic physics and surface science. It has also been developed into an interdisciplinary subject which involves the knowledge of crystallography, thermodynamics and mechanical properties.

3.1.1   Equilibrium Segregation

The segregation of elements on the boundaries is determined by thermodynamics. The tendency of the segregation of elements on the boundaries is to cause the overall free energy to be reduced. Although there are many different boundary segregation equations, they are all related to the thermodynamic dimension and can be characterized to contain minus index relationship of energy/temperature, which is the reflection of equally partial mole free-enthalpy. Hence it is called equilibrium segregation. This includes: (a) the mechanism: Gibbs internal absorption; (b) driving force: the reduction of boundary free energy; (c) Characteristics: significant segregation, but with narrow range (1~2 or several atomic layers); (d) Other affecting factors: (1) temperature: when solute concentration is constant, a certain equilibrium segregation exists at a temperature. When temperature rises to a higher value, the segregation will tend to disappear. If temperature is too low, although the equilibrium segregation level will be higher, because of difficult diffusion, it is hard to reach the equilibrium value. (2) Solute concentration: grain boundary segregation increases as solute concentration within the grain increases. (3) Maximum solid solubility: the lower the maximum solid solubility, the more difficult for the solute is inside the grains; this will promote the segregation. (4) Time: time has no influence on the equilibrium segregation levels.

3.1.2   Non-Equilibrium Segregation

The history of research on the non-equilibrium segregation is that of research on the boron segregation. From early 1970s, people had been trying to use the equilibrium segregation of boron on grain boundaries to explain the segregation behaviour of boron in the steels[7]. Hence, many unexplained phenomena were met later. After 1973 Ueno and Gladman[7] found during their research on the isothermal bainite transformation that the boron segregation on the grain boundaries could not be seen when the boron-containing steel was heated and quenched. The segregation could only be observed when slow cooling prevailed or a period of time at lower temperature was maintained. Therefore in order to understand the segregation, the process should start from the heating stage, as pointed out by Grange. More importantly, Williams et al.[8] studied the segregation of boron in the 316 stainless steel.

They found that (i) as solid solution temperature increases, the segregation level of boron on the grain boundaries after quenching increases, and (ii) the segregation is dependent on cooling rate. Further research showed that segregation occurs during slow cooling, whereas fast cooling will not result in segregation. Thus the segregation mechanism is put forward as follows: solute atoms, vacancies and their complexes are equilibrium both on the boundaries and within the grains when at the solid solution temperature. During cooling, a part of loss of vacancies along the grain boundaries will happen to maintain equilibrium at a lower temperature. This will lead to a reduction in complex concentration in the vicinity of grain boundaries associated with vacancy concentration, i.e., some of complexes have been changed into isolated vacancy atoms. Because a complex concentration gradient appears on the grain boundaries and within the grains, this causes   diffusion in which more complexes migrate towards the grain boundaries and dissociate. When the vacancies disappear, the solute atoms are preserved. When the diffusion rate of complexes towards the grain boundaries is greater than the rate of reverse diffusion of atoms on the grain boundaries induced by enrichment, there will be an enrichment of solute atoms, i.e., segregation.

In 1979, Hwang et al.[9] added traces of boron to Fe-12Mn steel leading to significant improvement in the low temperature toughness due to segregation of boron on the grain boundaries. Later the segregation of Cr in the 2.25%Cr1%Mo steel was found by Doig and Flewitt[10]. It was explained by the diffusion of a vacancy-solute complex to the grain boundaries. Subsequently an analytical model was formulated in which the segregation amount would be dependent on the austenitising temperature, cooling rate and complex binding energy. A higher temperature and lower cooling rate would lead to an increased amount of segregation. Increasing the complex binding energy would also improve the segregation. Doig and Flewitt also stated that if other vacancy sinks exist, such as dislocation networks, dislocation substructures and secondary precipitates exist, the theoretically calculated segregation curve would be affected seriously. The research represented a systematic approach.

X. He et al.[11] studied the non-equilibrium segregation of boron and found that a boron depleted zone existed on both sides of the segregated boundaries. When the quenching temperature increases, the width of the boron depleted zone increases. The

width is inversely proportional to the square root of the cooling rate, which means that the segregation increases as the width extends.

Faulkner[5] presented a thermodynamic differential equation on the non-equilibrium segregation. It was concluded that larger misfit atoms and larger grain size lead to significant segregation. A very important concept of critical time was defined in this theory. When the cooling time is longer than the critical time, the de-segregation of segregated atoms is dominant. It can be seen in this model that concentration of segregated atoms on the grain boundaries is constant. Adding the time will only lead to a widen segregated zone. Furthermore in order to obtain maximum segregation, the aging operation after quenching should be avoided. In another study[12], typical vacancy-atom complex binding energies based on elastic strain energy arguments were calculated at around 0.2~0.3eV.

X. He et al.'s studies[13] also showed that non-equilibrium of boron in the low carbon Mn-Mo steel and Fe-Ni steel was a type of kinetic phenomena. When it is treated at a fixed temperature under certain conditions, the non-equilibrium segregation on the grain boundaries will be many times greater than the equilibrium segregation. However as holding time extended, this excess segregation will disappear. The change of the segregation peaked being related with the temperature-holding time was an important feature of this type of non-equilibrium segregation. Doig and Flewitt[14] discovered the segregation of Cr in the 316 stainless steel in 1987.

S. Song and T. Xu[15] did some research on determining the critical time and cooling rate of the equilibrium segregation of boron. They considered the holding time as the critical time when segregation was transferred to de-segregation. In other words, when the cooling rate is faster than this value, the segregation would be dominant; otherwise de-segregation would be the main mechanism.

Faulkner and S. Song[16] studied the equilibrium and non-equilibrium segregation of elements such as C, Mo and P etc in ferritic steels in 1998.

Having considered the history of the non-equilibrium segregation, we can see that the non-equilibrium segregation is a type of temporary kinetic phenomena and can be

significant for a certain period of time. However as time prolongs, the de-segregation will take place or the segregation will disappear. Thus this type of segregation is phrased as non-equilibrium segregation. The driving force of this segregation is the interaction of solute atoms and vacancies or solute concentration gradient. Therefore, as a result, the segregation is related with the starting temperature and the cooling rate.

The cause for non-equilibrium segregation could be summarised as follows:

- During grain boundary precipitate growth, enrichment of the solute atoms was at the phase interface
- Quenching induction
- Radiation induction
- Stress induction

3.2 The Model Details

3.2.1 Equilibrium Segregation

The equilibrium segregation for the solute was initially developed by McLean[1], which was based the statistical thermodynamics of Gibbs. The approach states that for a solute atom with a binding energy to the matrix Q^i, at any temperature T, there will be an increased concentration of that solute on the boundaries or interfaces. The driving force for segregation in this instance is the reduction of energy, associated with the solute on reaching a strain-free environment at the grain boundary. The maximum equilibrium segregation levels at a certain temperature T, $C_{bn}^i(T)$, is given by

$$C_{bn}^i(T) = \frac{\beta C_g^i \exp(Q^i / kT)}{1 + \beta C_g^i \exp(Q^i / kT)}$$

(1)

where i is defined as the solute; C_g^i is the concentration of the solute i in the solution; β is a constant representing the vibrational entropy of the grain boundary region; and k is Boltzmann's constant.

When complex alloys (solute i_1, i_2 and i_3) are considered, and it is assumed that the sites available at the grain boundary are all the same type, these solutes will compete with each other for the sites in the segregation process. This is called site competition. Their maximum equilibrium segregation levels, $C_\infty^i(T)$, in the approximation that all possible sites at the grain boundary are available for segregation of solute atoms, are given respectively by [16]

$$C_\infty^i(T) = \frac{C_g^i \exp\left(Q^i/kT\right)}{1 + \sum_i C_g^i \exp\left(Q^i/kT\right)} \qquad i = i_1, i_2, \text{and } i_3 \qquad (2)$$

In the research, the phosphorus segregation is focused, in which the i_1 is assumed to be the P. Hence the prediction can be made of solute segregation in many dilute ternary P containing alloys, e.g. Fe-B-P, Fe-C-P and Mo-C-P etc. through consideration of solute-solute competition for segregation sites on the grain boundary. Then the competition effect for P, C and Mo can be evaluated by

$$C_\infty^P(T) = \frac{C_g^P \exp(Q_P/kT)}{1 + C_g^P \exp(Q_P/kT) + C_g^C \exp(Q_C/kT) + C_g^{Mo} \exp(Q_{Mo}/kT)} \qquad (3)$$

$$C_\infty^C(T) = \frac{C_g^C \exp(Q_C/kT)}{1 + C_g^P \exp(Q_P/kT) + C_g^C \exp(Q_C/kT) + C_g^{Mo} \exp(Q_{Mo}/kT)} \qquad (4)$$

$$C_\infty^{Mo}(T) = \frac{C_g^{Mo} \exp(Q_{Mo}/kT)}{1 + C_g^P \exp(Q_P/kT) + C_g^C \exp(Q_C/kT) + C_g^{Mo} \exp(Q_{Mo}/kT)} \qquad (5)$$

where C_g^P, C_g^C and C_g^{Mo} are the concentrations of P, C and Mo   in solution, respectively; Q_P, Q_C and Q_{Mo} are the equilibrium segregation energies of P, C and Mo respectively.

Because of the high concentration of all types of solutes encountered in grain boundaries, the chemical interactions between atoms cannot be neglected. The chemical interactions between the P and other solutes are complex. Some interactions are obvious, but may not make a contribution to the solute segregation on the grain boundaries, whereas some interactions are still unknown. If the P-solute (i_2) chemical interaction effect is taken into consideration[17, 18], the equilibrium segregation energy of P, Q_P, may be acquired from

$$Q_P = Q_P^0 + \alpha'_{i_2 P} C_\infty^{i_2}(T) \tag{6}$$

where Q_P^0 is the binding energy of P with the boundary; and $\alpha'_{i_2 P}$ is the i_2-P chemical interaction coefficient.

The kinetics of equilibrium grain boundary segregation of site-competition at temperature T are given by [1,19]

$$\frac{C_{be}^i(t) - C_{be}^i(0)}{C_\infty^i(T) - C_{be}^i(0)} = 1 - \exp(\frac{4D_s^i t}{\alpha_{e(i)}^2 d_0^2}) erfc(\frac{2\sqrt{D_s^i t}}{\alpha_{e(i)} d_0}) \qquad i = i_1, i_2, \text{ and } i_3 \tag{7}$$

where $C_{be}^i(t)$ is the grain boundary concentration of solute i after time t, $C_{be}^i(0)$ is the boundary solute concentration at time = 0, D_s^i is the diffusion coefficient of solute i in the matrix, d_0 is the thickness of the concentrated layer, and $\alpha_{e(i)}$ is the maximum equilibrium enrichment ratio of solute i given by

$$\alpha_{e(i)} = C_\infty^i(T) / C_g^i \tag{8}$$

3.2.2 Non-Equilibrium Segregation

The non-equilibrium segregation mechanism relies on the formation of sufficient quantities of vacancy-solute complexes. Solute atoms, vacancies and their complexes are in equilibrium with each other at a given temperature. When a material that is properly maintained at a high temperature is quickly cooled to a lower temperature, it will exhibit a loss of vacancies along grain boundaries, i.e., at vacancy sinks, whereby it achieves the equilibrium vacancy concentration corresponding to the lower temperature. The decrease in vacancy concentration brings about the dissociation of the complexes into vacancies and solute atoms. This in turn leads to a decrease in complex concentration in the neighbourhood of grain boundaries. Meanwhile, in regions remote from the grain boundary, where no other vacancy sinks are present, the vacancy concentration, which is nearly equal to the equilibrium vacancy concentration corresponding to the high temperature, always remains. As a result, a complex concentration gradient appears between the grain boundary and the adjacent grains. The concentration gradient of the complexes causes their migration leading to an excess solute concentration in the vicinity of grain boundaries. It is obvious that the larger the super-saturation level of vacancies induced by cooling from the high temperature, the larger the segregation level of solute atoms resulting at the boundary.

Non-equilibrium grain boundary segregation can be classified into segregation and desegregation. When a sample is quickly cooled from a high temperature to a lower temperature and then maintained at this lower temperature, there is a critical holding time at which the non-equilibrium segregation level will be maximum. If the holding time of the sample is shorter than the critical time, the diffusion of solute-vacancy complexes to the grain boundary will be dominant and the process is termed a segregation process; if the holding time is longer than the critical time, the process in which the diffusion of solute atoms from the boundary to the adjacent grains is dominant will also take place. This is termed a desegregation process.

The non-equilibrium grain boundary segregation model[20, 21] is utilised to depict the process. The model states that when a sample is quickly cooled to a lower temperature T_0, from a high one, such quenching temperature T_s and then maintained at the lower

temperature, the maximum concentration of non-equilibrium grain boundary segregation of solute i induced during holding at this lower temperature, $C_{bn}^m(T)$, is given by

$$C_{bn}^m(T) = C_g^i \frac{E_b^i}{E_f^v} [\frac{C_g^i \exp(\frac{E_b^i}{kT_s})}{\sum_i C_g^i \exp(\frac{E_b^i}{kT_s})}] \exp(\frac{E_b^i - E_f^v}{kT_s} - \frac{E_{b(SI)} - E_f^v}{kT_0}) \quad i = i_1, i_2 \text{ and } i_3 \quad (9)$$

Where E_b^i is the solute i-vacancy binding energy, C_g^i is the matrix concentration of solute i, and E_f^v is the vacancy formation energy, T_0 can be considered as the half of the absolute melting point of the matrix (T_m).

When a sample is quickly cooled from a high temperature T_s to a lower temperature T_0 so that no mass transfer occurs in the sample during cooling and held at temperature T_0, the non-equilibrium segregation kinetics are given by[20, 22]

$$\frac{C_{bn}^i(t) - C_g^i}{C_{bn}^m(T) - C_g^i} = 1 - \exp(\frac{4D_c^i t}{\alpha_{n(i)}^2 d_0^2}) erfc(\frac{2\sqrt{D_c^i t}}{\alpha_{n(i)} d_0}) \quad i = i_1, i_2 \text{ and } i_3 \quad (10)$$

where $C_{bn}^i(t)$ is the concentration of solute i at the concentrated layer as a function of holding time at temperature T_0, D_c^i is the diffusion coefficient of solute i-vacancy complexes in the matrix, $C_{bn}^m(T)$ is the maximum non-equilibrium segregation level of solute i at temperature T_0, d_0 is the thickness of the concentrated layer, and $\alpha_{n(i)}$ is the maximum non-equilibrium enrichment ratio of solute i, which is given by

$$\alpha_{n(i)} = C_{bn}^m(T) / C_g^i$$

Equation (10) is an isothermal kinetic relationship of non-equilibrium segregation for the segregation process. It describes the non-equilibrium segregation concentration of

solute atoms at grain boundaries as a function of holding time at temperature T, from Equations (9) and (10), one may predict the non-equilibrium segregation level of solute i in the sample quenched from a higher temperature and then tempered at tempering temperature.

As mentioned above, a critical time, t_c, exists at a certain temperature. When the critical time is longer than the effective time of complex diffusion corresponding to the cooling process, t_e, the process in which segregation is dominant takes place alone; nevertheless, when t_c is shorter than t_e, desegregation is dominant.

For solute i, the critical time, t_c, is given by[5]

$$t_c = \frac{\delta B^2 \ln(D_c^i / D_s^i)}{4(D_c^i - D_s^i)} \tag{11}$$

where δ is a numerical constant (quoted by Faulkner) as 0.05^5 and B is the grain size, D_s^i and D_c^i are the diffusion coefficient of solute i atoms and solute-vacancy complex, respectively. The D_c^i and D_s^i are given by the following relations:

$$D_c^i = D_{oc}^i \exp\left(-\frac{E_m^i}{kT}\right)$$

$$D_s^i = D_{oi} \exp\left(-\frac{E_i}{kT}\right)$$

where D_{oi} and D_{oc}^i are the pre-exponential constant for diffusion of solute atoms and solute i –vacancy complex, respectively; E_i and E_m^i are the activation or migration energies for the diffusion of solute atoms and solute-vacancy complex, respectively.

As discussed elsewhere[22], any continuously cooling curve for a sample may be replaced by a corresponding stepped one, each step of which is set up by a horizontal segment with a vertical one so as to calculate an effective time at a given temperature

for this cooling process so long as the step is small enough. For solute i, the effective time of a stepped cooling curve consisting of n steps at temperature T, t_e, is given by[22]

$$t_e = \frac{RkT_s^2}{\theta E_A}$$

(12)

where E_A is the activation or migration energy for diffusion of solute i-vacancy complexes in the matrix, θ is the cooling rate, R is the gas constant.

When the effective time is longer than the critical time at temperature T, the process in which desegregation is dominant may take place after the critical time. In such an instance, the grain boundary segregation level of solute atoms, $C_{bn}^i(t)$, is given by[22]

$$C_{bn}^i(t) = C_g^i + \frac{1}{2}[C_{bn}^i(t_c) - C_g^i]erf[(\frac{d/2}{[4D_s^i(t-t_c)]^{1/2}}) - erf(\frac{-d/2}{[4D_s^i(t-t_c)]^{1/2}})]$$

$$i = i_1, i_2 \text{ and } i_3$$

(13)

where t is the isothermal holding time at temperature. Segregation is two different processes in nature. Non-equilibrium segregation is a kinetic process whereas equilibrium segregation is a thermodynamic process. As a consequence, it may be envisaged that these two processes are independent of each other. In the calculations, the segregation level is taken to be the sum of the non-equilibrium and equilibrium segregation levels minus the matrix concentration.

3.2.3 Site Competition and Co-segregation

Site competition between impurities during segregation is dealt with by the following methods: the impurity atoms first segregation to the grain boundary by site competition assisted solute drag (co-segregation) to obtain the segregation level C_{bn}^i

in Equation (1), and then redistribute there in proportion to their binding energies with grain boundary Q^i. The redistribution effect can then be evaluated by [20, 24]

$$C_{bn}^{i*} = C_{bn}^i \left(\frac{C_g^i \exp(Q'/kT)}{C_g^i \exp(Q^i/kT) + C_g^j \exp(Q^j/kT)} \right) \qquad (14)$$

It should be noted that the vacancy is regarded as the main transporter of impurity due to its lower migration energies and higher binding energies.

3.2.4 Free Carbon Concentration

It is well known that carbon plays an important role in thermally induced phosphorus segregation. Free carbon is one of key input parameters in model. The concentration of free carbon is determined using the following rules:

(1) For the quenching, starting at temperatures usually over 1000K, nearly all carbon is dissolved in the matrix. Therefore it is assumed free carbon concentration equals to the carbon concentration in material.

(2) For tempering or PWHT, usually carried out between 600°C and 700°C, the equilibrium carbon concentration in materials is used and determined by Gibbs energy minimisation calculations performed using the multiphase module of MTDATA in conjunction with the SGTE (Scientic Group Thermodata Europe) solution plus database [25].

3.3. Conclusions

(1) The GBSP models for both ES and NES segregation on GB in alloys are:

$$\text{ES: } C_\infty^i(T) = \frac{C_g^i \exp\left(Q^i/kT \right)}{1 + \sum_i C_g^i \exp\left(Q^i/kT \right)}$$

and $\dfrac{C_{be}^{i}(t)-C_{be}^{i}(0)}{C_{\infty}^{i}(T)-C_{be}^{i}(0)}=1-\exp(\dfrac{4D_{s}^{i}t}{\alpha_{e(i)}^{2}d^{2}})erfc(\dfrac{2\sqrt{D_{s}^{i}t}}{\alpha_{e(i)}d})$

NES: $C_{bn}^{m}(T)=C_{g}^{i}\dfrac{E_{b}^{i}}{E_{f}^{v}}[\dfrac{C_{g}^{i}\exp(\dfrac{E_{b}^{i}}{kT_{s}})}{\sum_{i}C_{g}^{i}\exp\left(\dfrac{E_{b}^{i}}{kT_{s}}\right)}]\exp(\dfrac{E_{b}^{i}-E_{f}^{v}}{kT_{s}}-\dfrac{E_{b(SI)}-E_{f}^{v}}{kT_{0}})$

and $\dfrac{C_{bn}^{i}(t)-C_{g}^{i}}{C_{bn}^{m}(T)-C_{g}^{i}}=1-\exp(\dfrac{4D_{c}^{i}t}{\alpha_{n(i)}^{2}d^{2}})erfc(\dfrac{2\sqrt{D_{c}^{i}t}}{\alpha_{n(i)}d})$

(2) The GBSP model gives prediction of GB segregation behavior.

References to Chapter 3

1. D. Mclean, Grain Boundaries in Metals, Oxford University Press, London, 1957, 123-129.

2. M.P. Seah, Acta Metall., 25, 1977, 345.

3. K.T. Aust and S.J. Armijo, et al., Trans. ASM, 60, 1967, 360.

4. T.R. Anthony, Acta Metall., 17, 1969, 603.

5. R.G. Faulkner, J. of Mater. Science, 16, 1981, 373.

6. T.D. Xu, J. Mater. Sci. 22, 1987, 337.

7. Ueno and Gladman, Metal Trans., 1973, 338-345.

8. T.M.Williams, L. Liang and J.F. McCarthy, Metal Science, 10, 1976, 14-20.

9. S.W. Hwang and J.W. Morris, Metal. Trans., 11A, 1980, 1197.

10. P. Doig and P.E.J. Flewitt, Acta Metall., 29, 1981, 1831.

11. X. He, J. Herz and J.M. Guenet, J. Appl. Phys., 16, 1983, 1145.

12. R.G. Faulkner, Materi. Sci. and Tech., 1, 1985, 442.

13. X. He, Metal Bull., 3, 1986 ,65.

14. P. Doig and P.E.J. Flewitt, Metall. Trans., 18A, 1987, 399-406.

15. S. Song and T. Xu, Wuhan Iron and Steel University Bull., 13, 1991, 258.

16. R.G. Faulkner and S. Song, Defect and Diffusion Forum, 143, 1997, 149.

17. M. Guttmann, Suf. Sci., 53, 1975, 213.

18. M. Guttmann, Metall. Trans., 13A, 1982, 1693.

19. T.D. Xu and S.H. Song, Acta Metall., 37, 1989, 2499.

20. R.G. Faulkner, S.H. Song, P.E.J. Flewitt, M. Victoria, P.J. Marmy, Nucl. Mater., 225, 1998, 189-209.

21. R.G. Faulkner, Acta Metall., 35, 1987, 2905.

22. S.H. Song and T.D. Xu, J. Mater. Sci., 29, 1994, 61.

23. S.H. Song, R.G. Faulkner and P.E.J. Flewitt, Acta Metall., 37, 1989, 319.

24. P. Maier, R.G. Faulkner and P. Spellward, Grain Boundary Segregation of Phosphorus, Manganese, and Carbon in Boiler Shell Weld Material, Materials Science and Technology, 17(11), 2001, 1377-1384.

25. Z. Lu, P.E.J. Flewitt, and R.G. Faulkner, Acta Metall., 52, 2002, 290-313.

CHAPTER 4:

Modelling of Grain Boundary Microstructure in Alloys (II)—
Grain Boundary Precipitation Model

4.1 Introduction

The microstructure especially the grain boundary (GB) structure play a very important role in alloys, such as aluminum, copper, magnesium, zinc alloys and steels. The GB structure in alloys is determined by misorientation, composition, and heat treatment, the resultant GB precipitation and segregation, the size and distribution of precipitates and also inclusions and pores on GB will affect the properties of alloys e.g. creep strength, stiffness, resistance to stress corrosion, and oxidation. Meanwhile some failures often occur because of the flaws on GB; therefore, it is very important to be able to modify the GB structure in order to control the final properties. Recently it has become more important to realize that modelling of GB structures can provide useful information for GB engineering.

4.2 Development on Modelling of Grain boundary Microstructure in Alloys

Modelling of the GB precipitation (GBP) behaviour was carried out first for Al-Cu alloy by Aaron and Aaronson in 1969[1,2] who pointed out that one of the most common precipitate morphologies formed during solid-solid transformations is that of grain boundary allotriomorph-crystal which nucleate at grain boundaries and grow preferentially and more or less smoothly along them, and both the rate of thickening and the rate of lengthening of allotriomorphs are considered to be controlled by the volume diffusion of solute toward or away from the growing crystals. They put forward square "collector plate" mechanism for lengthening of allotriomorphs, illustrated in Fig. 4.1, in which each grain boundary is considered as completely to be filled by a set of square

"collector plates" of length d_v on a side, and of area A_v, where $A_v >> A_0 = \pi R_1^2$, where R_1 is the radius of the precipitate. Each square is taken to be centered on a single θ allotriomorph. Initial approximations show that the composition at the grain boundary can be estimated to be $x_{\alpha(r)}^{\alpha\theta}$, essentially independent of time; it was found that lengthening is proceeded by volume diffusion of solute to the α:α grain boundaries, followed by grain boundary diffusion to the advancing edges of the allotrimorphs. $x_{\alpha(\gamma)}^{\alpha\theta}$ is

Plane of grain boundary
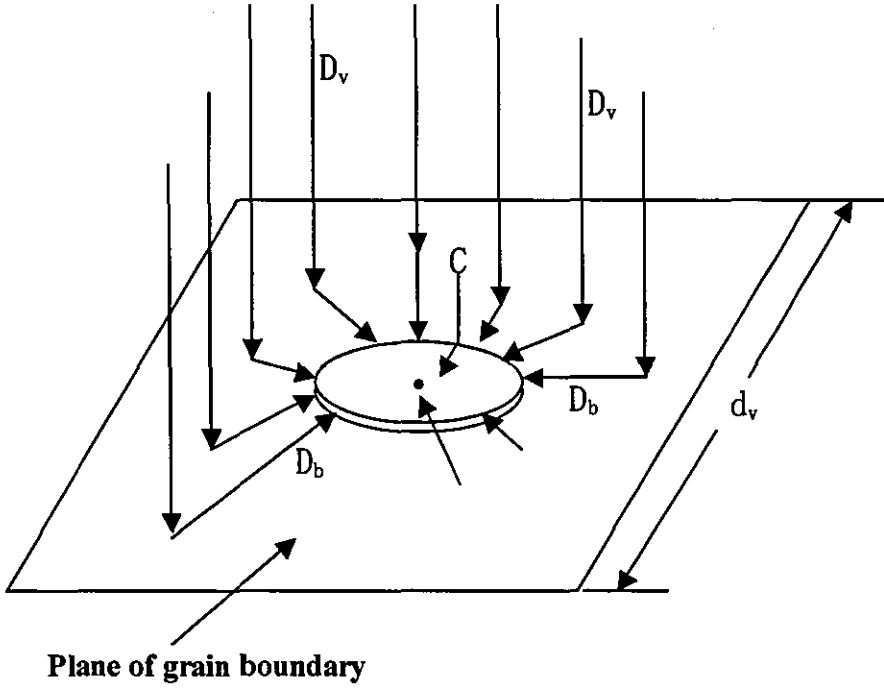
Fig. 4.1. The collector plate model

defined as the mole fraction of Cu in α at the edges (of radius R_2) of an allotriomorph. It is related to $x_{\alpha(T)}^{\alpha\theta}$ by the Gibbs-Thompson equation:

$$x_{\alpha(r)}^{\alpha\theta} = x_{\alpha(T)}^{\alpha\theta} \left[\exp\left(\frac{\sigma_{\alpha\theta} V_{Cu}^\alpha}{RTR_2} \right) \right]$$

(1)

where $x_{\alpha(T)}^{\alpha\theta}$ is the solute concentration in equilibrium with the precipitate phase and matrix at temperature, T; $\sigma_{\alpha\theta}$ is the specific interfacial free energy of the interface, V_{Cu}^{α} is the partial molar volume of Cu in the precipitate phase, R is the gas constant and T is the absolute temperature. Finally the model of lengthening is given by the following equation:

$$L = [\frac{2A_v D_I^{\frac{1}{2}}(x_{\alpha i} - x_{\alpha T}^{\alpha\theta})\rho_\alpha}{\pi^{\frac{3}{2}}(x_\theta - x_{\alpha T}^{\alpha\theta})\rho_\theta r} + L_{i-1}^3]^{\frac{1}{3}}$$ (2)

It was noticed that the thickening kinetics were controlled by the diffusion of solute over the broad face of a growing precipitate through interfacial diffusion, and that it determined that the $\alpha{:}\alpha$ interface boundary diffusion coefficient is

$$D_{\alpha\theta} = 0.23\exp(-12{,}800/RT)$$ (3)

It has been suggested that the lengthening of proeutectoid ferrite allotriomorphs in steel may be expedited by preferential diffusion of carbon along prior austenite grain boundaries. However this has not been supported by either a preliminary growth kinetics measurements or by the unsuccessful attempts which have been made to find evidence of preferential diffusion of carbon along austenite grain boundaries.

Faulkner and Caisley[3] introduced a modified "collector plate" theory which assumed a aspect ratio for the GB precipitates, and established a GB carbide precipitation model for Nimonic PE16, which worked satisfactorily with experimental observations.

In 1981 Faulkner and Carolan[4-7] modelled of carbide precipitation in steel; the simple precipitation kinetics have been well developed and the models have been generated to predict the growth rate of grain boundary precipitates. It has been noticed that segregation can influence grain boundary precipitation by altering the driving force for grain

boundary precipitation nucleation, which will strongly influence the mean initial size of the collector plates. Segregation also alters the solute flux arriving at the grain boundaries. The size of the collector plates and the solute flux strongly affect the grain boundary precipitate growth rate.

By the 90's the modelling studies of grain boundary precipitation in alloys by the Faulkner group were intensified and widened. In 1992, Faulkner and Jiang[8-10] put forward a combined model which took into account solute segregation behavior and precipitate growth kinetics by linking the fluxes expected at grain boundaries from both segregation and precipitation mechanisms. This model was based on Faulkner and Carolan's model for grain boundary precipitation and segregation. The numerical model for constant square collector plate control was used in predicting $MgZn_2$ grain boundary precipitate growth in 7150-aluminum alloy with reasonable success. The combined model has been further developed to predict the inter-particle spacing by relating the spacing to the density of grain boundary precipitate nuclei. Furthermore the model has modified the NES model for the segregation process. In this way the combined model can predict nucleation, the precipitate free zone (PFZ) behavior, the dispersion of precipitates on the grain boundaries and the onset of coarsening.

Faulkner, Meade and Goodwin[11, 12] studied inter-and intra-granular $Cr_{23}C_6$ in type 316 austenitic stainless steels. It was pointed out that mass transfer to assist growth was assumed to take place by a combined lattice and grain boundary diffusion controlled mechanism. Nucleation was also included in the kinetics appraisal and for the case of $M_{23}C_6$ in an austenitic steel matrix the nucleation kinetics were lattice diffusion controlled. The results for $M_{23}C_6$ in 316 steel showed that carbon content and precipitate-matrix interfacial energy are sensitive parameters when considering the overall isothermal precipitation behavior, and inter-granular precipitation rates exceeded those of inter-granular precipitation when ageing times exceed 1000 hours at 650°C.

Faulkner's GBSP model has also been successfully used for the heat resistant high Cr ferritic steels. Further development of models is the Monte Carlo simulation (MCS)

method successfully used for Fe-Cr steels by Y. Yin and Faulkner[7]. This new simulation approach is based on the Monte Carlo random sampling technique, time-dependent nucleation theory, and diffusion laws.

4.3 The GBSP Model[8]

4.3.1 Segregation During Quenching

The model begins by describing the amount of the NES[13, 14] of solute (e.g. Cr in steels) created around the GB during quenching. The effective quenching time is calculated assuming that the quenching is performed at a constant temperature. The quenching conditions set the solute concentration expected on the boundary as a result of non-equilibrium segregation, which can be given by[11]

$$C_b = C_g \exp\left(\frac{E_b - E_f}{kT_i} - \frac{E_b - E_f}{k0.50T_{mp}}\right)\frac{E_b}{E_f} \tag{4}$$

where C_g is the bulk solute concentration, E_b is the solute-vacancy binding energy, E_f is the vacancy formation energy, k is Boltzmanns constant, T_i is the solution treatment temperature and $0.50T_{mp}$ is the temperature below which no more segregation is assumed to take place since complexes are insufficiently mobile, taken as 0.50 times the melting point of the alloy. Two regions, the solute concentrated layer (SCL) and the solute depleted layer (SDL), are created near to the boundary (see Fig. 4.2). These originate from solute being taken into the SCL by solute-vacancy complex diffusion during the quenching time.

During quenching from solute treatment temperature, or during high temperature aging where the aging temperature, T_{age}, is greater than $0.50T_{mp}$, Equations (5a)-(5c) govern the NES segregation behavior[15].

$$C(y,t_{eff}) = C_b \exp(-\alpha y^2) \qquad\qquad \text{if } y \le w_1 \qquad\qquad (5a)$$

$$C(y,t_{eff}) = C_b \exp(-\alpha y^2) + \frac{y-w_1}{w} C_g \qquad \text{if } w_1 \le y \le w \qquad (5b)$$

$$C(y,t_{eff}) = C_b \exp(-\alpha y^2) + C_g \qquad\qquad \text{if } y \ge w \qquad\qquad (5c)$$
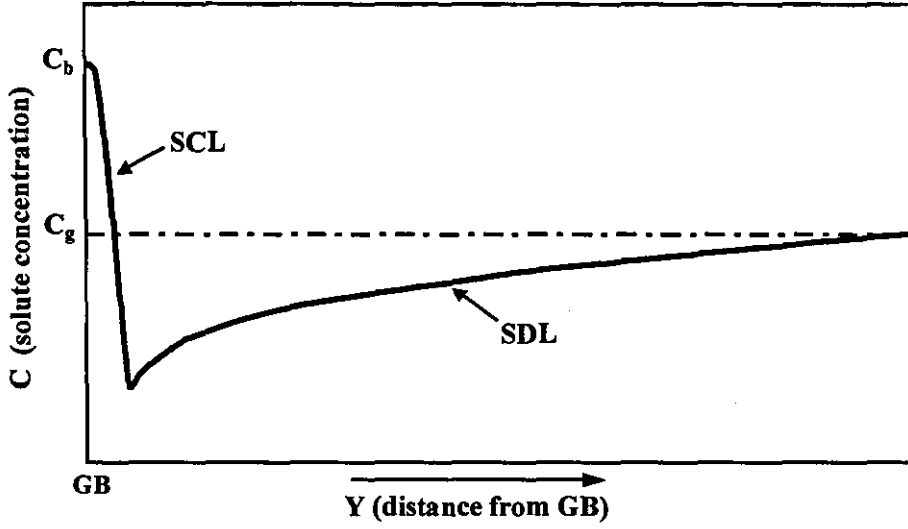
Fig. 4.2. Segregation profile during quenching

where y is the distance from the GB, w and w_1 are the width of the solute depleted and concentrated layers respectively:

$$w_1 = \frac{C_g \sqrt{2D_{ci}t_{eff}}}{C_b}, w = \frac{2w_1(C_b - C_g)}{C_g}, \alpha = \frac{\pi C_b^2}{8D_{ci}t_{eff}C_g^2} \qquad (6)$$

where t_{eff} is the effective quench time and D_{ci} is the diffusion coefficient of the vacancy-solute complexes at the solution treatment temperature, T_i.

$$t_{eff} = t_{T_0}^{T_i} e\left(\frac{-Q_c(T_i - T_0)}{kT_iT_0}\right)$$ (7)

$$t_{T_0}^{T_i} = \frac{(T_i - T_0)}{\theta}$$ (8)

where T_0 is room temperature, θ is the cooling rate between temperatures T_i and T_0, Q_c is the activation energy term for the calculation of the diffusion coefficient of the vacancy-solute complexes.

However, quenching processes generally have different cooling rates at different temperatures, so this approach will only give an approximate value.

4.3.2 Precipitate Nucleation

Nucleation is important for two reasons. First, it defines the nucleation site density on the GB which is crucial to predict the inter-particle spacing and hence the collector plate area at the onset of growth. Second, it is important for determining the nucleation time, which is needed to describe the total time necessary to grow a precipitate to a given size.

4.3.2.1 The nucleation site density

The nucleation site density i.e. the number of the critical precipitate nuclei per unit area of GB, N_0, is given by Russell's equation [14, 16]:

$$N_0 = \frac{N}{x_\theta} \exp\left(\frac{-\Delta G*}{kT_{nuc}}\right)$$ (9)

where x_θ is the solute concentration in the nucleus phase, T_{nuc} is the temperature of the environment where nucleation takes place, $\Delta G*$ is the Gibb's free energy of critical GB nucleus formation and N is the number of atom sites at the GB, which is given by:

$$N = s_0 d_{gb} \rho_\alpha N_A \qquad (10)$$

where s_0 is the unit area, d_{gb} is the GB width, ρ_α is the molar density of the matrix phase and N_A is Avagadro's number.

Hence, the driving force, ΔG^*, to produce the critical nucleus size can be determined by:

$$\Delta G^* = \frac{4\pi \sigma_{\alpha\theta}^3}{3\Delta G_V^2}(2 - 3\cos\psi + \cos^3\psi) \qquad (11)$$

$$\Delta G_v = \frac{RT_{nuc}}{2V_\theta}\ln\left(\frac{x_b}{x_{\alpha T_{nuc}}^{\alpha\theta}}\right) \qquad (12)$$

where $\sigma_{\alpha\theta}$ is the matrix/precipitate interfacial energy, V_θ is the molar volume of the precipitate phase, x_b is GB solute concentration modified to account for the segregation parameter of the material, which is taken to be equal to C_b, ΔG_v is the driving force for the solid state transformation, ψ is the angle between the surface of nucleus and the grain boundary, $x_{\alpha T_{nuc}}^{\alpha\theta}$ is the only unknown factor which is the equilibrium solute concentration at the interface between the nucleated precipitate phase and the matrix at temperature T_{nuc}. The calculation of $x_{\alpha T_{nuc}}^{\alpha\theta}$ is described by Faulkner and Caisley[2]:

$$x_{\alpha T_{nuc}}^{\alpha\theta} = \left[\frac{1}{C_c}\exp\left(\frac{-28800}{RT_{nuc}} - 0.9\right)\right]^{\frac{6}{23}} \qquad (13)$$

where R is the gas constant, and C_c is the carbon content of the alloy being considered.

4.3.2.2 Nucleation time

The equation of incubation time for a cap shape particle presented by Van der Velde et al.[16, 17]:

$$\tau \simeq \frac{32kT_{nuc}a^4\sigma_{\alpha\theta}^2\ N_A^2}{D_{bnuc}d_{gb}x_bV_\theta^2\Delta G_v^3\sin\psi}\tag{14}$$

where k is Boltzmann's constant, a is the lattice parameter of the matrix phase, D_{bnuc} is the GB diffusion coefficient of the solute atoms at temperature, T_{nuc}, and $\sigma_{\alpha\theta}$ is the matrix-precipitate interfacial free energy.

4.3.2.3 Size distribution density

The distribution density function of grain boundary precipitate nuclei, n_0, is given by a normal distribution function of mean collector plate area (A_v):

$$n_0 = \frac{N_0}{2\sqrt{\pi}\sigma_d}\exp\left[-\frac{(A_v - A_{m0})^2}{2\sigma_d^2}\right]\tag{15}$$

where A_v is defined as an area of GB that has a precipitate nucleus at its center, and all such plates together fill up a unit area of GB, σ_d is the standard deviation of the collector plate area and is taken as:

$$\sigma_d = (A_{m0} - A_{min})/3\tag{16}$$

A_{m0}, is given by:

$$A_{m0} = \frac{1}{N_0}\tag{17}$$

where

$$A_{min} = 16D_{bnuc}\tau\tag{18}$$

4.3.3   Segregation During Ageing

The width of the SCL increases with time until the temperature drops below the temperature at which non-equilibrium segregation is expected to cease, usually about $0.50\,T_{mp}$, where T_{mp} is the absolute melting point of the material. After this time no more non-equilibrium segregation is expected to occur and the SDL is gradually filled up by solute diffusion down the concentration gradient formed by the NES process (Fig. 4.2). During ageing where the ageing temperature, T_{age}, is less than $0.50\,T_{mp}$. The solute concentration profile due to ES can be described as follows:

$$C(y,t) = C_b \exp(-\alpha' y^2) \quad \text{if } y < w_1 \tag{19a}$$

$$C(y,t) = C_b \exp(-\alpha' y^2) + C_I(y,t) + C_{II}(y,t) + C_{III}(y,t) + C_{IV}(y,t) \quad \text{if } y \geq w_1 \tag{19b}$$

where:

$$\alpha' = \frac{\pi C_b^2}{8 D_{ci} t_{eff} C_g^2} \tag{20}$$

$$C_I(y,t) = C_g + \frac{(y-w_1)C_g}{w} erf \frac{y-w_1}{2\sqrt{D_c t}} + \frac{2\sqrt{D_c t}\,C_g}{\sqrt{\pi}w} \exp \frac{-(y-w_1)^2}{4D_c t} \tag{21a}$$

$$C_{II}(y,t) = -\frac{C_g}{2}\left(erf \frac{w+y-w_1}{2\sqrt{D_c t}} + erf \frac{w-y+w_1}{2\sqrt{D_c t}}\right) \tag{21b}$$

$$C_{III}(y,t) = -\frac{2\sqrt{D_c t}\,C_g}{\sqrt{\pi}w}\left[\exp \frac{-(w+y-w_1)^2}{4D_c t} + \exp \frac{-(w-y+w_1)^2}{4D_c t}\right] \tag{21c}$$

$$C_{IV}(y,t) = -\frac{yC_g}{2w}\left(erf \frac{w+y-w_1}{2\sqrt{D_c t}} - erf \frac{w-y+w_1}{2\sqrt{D_c t}}\right) \tag{21d}$$

where t is the ageing time, $w_1 = \dfrac{C_g \sqrt{2D_{ci} t_{eff}}}{C_b}$ and D_c is the diffusion coefficient of the

vacancy-solute complexes in the matrix at the ageing temperature.

4.3.4   Precipitate Growth

Assumptions are made that the precipitates have a cap shape and a constant morphology throughout the early stage of precipitate growth occurs. The mean half volume of a precipitate can then be written as, $V = \pi f(\psi) L^3$, where L is the mean radius of the precipitate along the GB after ageing at a given temperature for a time of t. The model is expected to give the prediction of precipitate size, L with time, t, during an isothermal process.

Modelling starts by dividing the time, t, into intervals of δt such that $t = n\delta t$. Where n is an integer. δt is chosen to be so small that within which the solute concentration, the mean size of collector plate area and the mean radius of the precipitate can be considered as constants. Thus the solute concentration at the GB, the mean collector plate area and the mean radius of the precipitate change with time in increments of δt.

At the ith stage ($1 \leq i \leq n$), the solute concentration in the vicinity of the GB is described by $x_{\alpha i}$; the mean collector plate area is described by A_{mi} which is given by $A_{mi} = \dfrac{1}{N_{mi}}$

where N_{mi} is the number of precipitate per unit area of GB at this time; and the mean radius of the precipitate is described by L_i.

L_i is calculated by Faulkner and Carolan's model for a constant collector plate condition. In the model, the increase of the precipitate size, dL during the increase of time, dt, at a given temperature, T, is given by equation:

$$dL = \frac{(x_\alpha - x_{\alpha T}^{\alpha\theta}) A_v D_i^{\frac{1}{2}} \rho_\alpha t^{-\frac{1}{2}}}{3\pi^{\frac{3}{2}} \rho_\theta (x_\alpha - x_{\alpha T}^{\alpha\theta}) L^2 f(\psi)} dt \qquad (22)$$

Replacing x_α (the solute concentration in the matrix) and A_v in equation (22) with $x_{\alpha i}$ and A_{mi-1}, then integrating from

$t^* = (i-1)\delta t$ to $t' = i\delta t$ yields

$$L_i = \{\frac{2A_{mi-1}D_I^{\frac{1}{2}}(x_{\alpha i} - x_{\alpha T}^{\alpha\theta})[t'^{\frac{1}{2}}-(t'-\delta t)^{\frac{1}{2}}]\rho_\alpha}{\rho_\theta \pi^{\frac{3}{2}} f(\psi)(x_\theta - x_{\alpha T}^{\alpha\theta})} + L_{i-1}^3\}^{\frac{1}{3}} \tag{23}$$

where $x_{\alpha T}^{\alpha\theta}$ is the solute concentration in equilibrium with the precipitate and matrix at the ageing temperature, T; x_θ is the solute concentration in precipitate phase; D_I is the volume diffusion coefficient of the impurity at the ageing temperature; A_{mi-1}, is the mean collector plate area at the (i-1)th stage; ρ_α is the molar density of the matrix; ρ_θ is the molar density of the precipitate phase, $f(\psi)$ is the morphological factor; $x_{\alpha i}$ is the solute concentration term which is modified according to the segregation parameter.

$x_{\alpha i}$ is taken as the average concentration of the solute in the region from the GB to a distance δl into the grain. δl is the diffusion distance of the solute in the matrix with time t'.

$$\delta l = \sqrt{2D_I t'} \tag{24}$$

$$x_{\alpha i} = \frac{1}{\delta l}\int_0^{\delta l} C(y,t')dy \tag{25}$$

$$x_{\alpha i} = \frac{A_{mi-1}\int_0^{\sqrt{2D_I i\delta t}} C(y,t'_{eff})dy - \pi f(\psi)L_{i-1}^3(x_\theta - x_{\alpha T}^{\alpha\theta})}{\sqrt{2D_I i\delta t}A_{mi-1}} \tag{26}$$

65

where $C(y,t')$ is the solute concentration distribution at this time, $t' = i\delta t$.

The iteration carries on from $i = 1$ till $i = n$, at which point, L ($L = L_n$), the mean radius of the precipitate after ageing for a time of t at ageing temperature T. Thus,

$$L = \{\sum_{i=1}^{i=n} \frac{2A_{mi-1}D_i^{\frac{1}{2}}(x_{\alpha i} - x_{\alpha T}^{\alpha\theta})\{(i\delta t)^{\frac{1}{2}} - [(i-1)\delta t]^{\frac{1}{2}}\}\rho_\alpha}{\rho_\theta \pi^{\frac{3}{2}} f(\psi)(x_\theta - x_{\alpha T}^{\alpha\theta})} + L_0^3\}^{\frac{1}{3}}$$

(27)

4.3.5 During Coarsening

After the coarsening begins, there is no more flux of the solute atoms from the grain center to supply the growth of the grain boundary precipitates. Driven by the requirement of a small surface to volume ratio, the precipitates coarsen on the grain boundaries. The mean radius of the GB precipitate, $L(t)$, increases with the increase in ageing time according to the following relationship[18, 19]:

$$L(t) = [A(t - t_{cc}) + L_g^4]^{\frac{1}{4}}$$

(28)

where, L_g is the initial mean radius of GB precipitates before the start of coarsening; A is a constant determined by the temperature, the GB diffusion coefficient of the solute, the GB width and the fraction of the boundary face covered by precipitates; t is the ageing time; t_{cc} is the critical time when the growth stops and coarsening begins. t_{cc} is taken as the time when no flux of solute atoms to the GB occurs. t_{cc} = g δt, where g is an integer. Bringing g into Equation (24) to replace i, we will have $x_{\alpha g}$ which satisfies the condition:

$$x_{\alpha g} \cong x_{\alpha T}^{\alpha \theta} \tag{29}$$

A program is written which leads the computer to carry out iteration from $i = 1$ until the relation $x_{\alpha g} \leq x_{\alpha T}^{\alpha \theta}$ is satisfied. Such a time is the critical time of the onset of coarsening.

4.3.6 Mean Collector Plate Area

4.3.6.1 Before the onset of growth

This is the situation that $i = 0$. The mean collector area is:

$$A_{m0} = \frac{1}{N_0} \tag{30}$$

Where N_0 is the number of the equilibrium precipitate nuclei in a unit area of the GB. N_0 is given by Equation (9) where $T_{muc} = T$, the ageing temperature. This is because the quenching is assumed to be so fast that there is no nucleation until ageing occurs.

4.3.6.2 During growth

During the growth of the precipitates, i.e. before coarsening, the mean collector plate area will not change with time unless coalescence occurs. The change of the mean collector plate area is caused by a reduction in the number of precipitates.

The reduction in the number of precipitates after ageing for a time of t ($t = n\delta t$) at the ageing temperature is ΔN_n given by

$$\Delta N_n = N_{A_{min}}^{4L_n^2} \cdot \frac{N_{A_{min}}^{4L_n^2}}{N_{n-1}}$$

(31)

where $N_{A_{min}}^{4L_n^2}$ is the number of all these precipitates which have collector plate areas

smaller than $4L_n^2$; $\dfrac{N_{A_{min}}^{4L_n^2}}{N_{n-1}}$ is the probability of coalescence happening to one of those

precipitates; N_{n-1} is the number of the precipitates after time, $(n-1)\delta t$; L_n is the mean

precipitate radius given by Equation (34).

The mean collector plate area (A_m) after ageing for a time of t ($t = n\delta t$) at ageing

temperature is to give A_{mn} as in

$$A_{mn} = \frac{1}{N_0 \prod\limits_{i=1}^{i=n} \left\{ 1 - 0.25 \left[erf\left(\frac{A_{mi-1} - A_{min}}{\sqrt{2}\sigma_d} \right) - erf\left(\frac{A_{mi-1} - 4L_i^2}{\sqrt{2}\sigma_d} \right) \right]^2 \right\}}$$

(32)

where A_{mi-1} is the previous collector plate area.

A computer program is generated to iterate the calculations of L_i, N_i and A_{mi} from $i = 1$

to n. At this time, A_{mn} is the mean collector plate area after ageing for a time t at ageing

temperature T.

4.3.6.3 During coarsening

Once the coarsening begins, the concentration of the solute atoms at the grain boundaries

does not change with time. This can be expressed as:

$$N(t)\pi f(\psi)L(t)^3 = N_g \pi f(\psi)L_g^3$$

(33)

where L_g and N_g are the mean radius and the number of the precipitates at the time of the onset of coarsening respectively; $L(t)$ and $N(t)$ are the radius and the number of the precipitates at the grain boundary after ageing for a time t at the ageing temperature, respectively.

$A_m(t)$, the mean collector plate area after ageing for a time t ($t \geq t_{cc}$, $t_{cc} = g\delta t$) at ageing temperature is

$$A_m(t) = \frac{1}{N(t)} \tag{34}$$

which can be written as

$$A_m(t) = A_{mg}\left[\frac{L(t)}{L_g}\right]^3 \tag{35}$$

where A_{mg} and L_g can be obtained from Equations (32) and (27) respectively by replacing index n with g; $L(t)$ is given by equation (28).

4.3.7 Mean Inter-Particle Spacing

In principle, the model can be used not only to calculate precipitate size as a function of quenching and ageing treatments, but also to calculate inter-particle spacing. In the modelling, the mean inter-particle spacing is taken as the square root of the mean area of collector plate, i.e.

$$d_s = \sqrt{A_{mn}} \tag{36}$$

4.3.7.1 The initial size of the GB inter-particle spacing

The initial size of the GB inter-particle spacing is defined as the square root of the inverse of the number of the equilibrium precipitate nuclei per unit GB area. Russell's equation for the number of critical nuclei per unit volume[13] is adopted (see Section 4.3.2.1). The number of the critical precipitate nuclei per unit area of GB is taken as the number of the precipitate nuclei in volume of a unit area multiplied by the thickness of the GB. The misorientation of the GB, the temperature at which the nucleation takes place and the solute concentration at the GB strongly affects the initial inter-particle spacing. The solute concentration at the GB is determined by the segregation concentration. The limitations of the segregation model used could influence the reliability of the value of this concentration.

4.3.7.2 The critical time for the onset of coarsening

The inter-particle spacing changes with time during the ageing. The change of the inter-particle spacing is caused by coalescence before the coarsening begins.

The critical time for the onset of coarsening is taken at the time when there no longer exists supersaturation of solute atoms in the areas adjacent to the grain boundaries and hence no flux of solute atoms to the GB appears, i.e. when the average solute concentration in the region from the GB to a distance δl becomes equal to or less than $x_{\alpha T}^{\alpha\theta}$. The model predicts that as the ageing time increases, the growth rate decreases and eventually approaches zero. The relation $x_{\alpha} \leq x_{\alpha T}^{\alpha\theta}$ exists only after a very long time ($t \rightarrow \infty$). This is under the situation when the precipitation in the matrix is ignored.

Further ageing after the critical time leads to precipitate coarsening driven by the minimization of interfacial free energy between the precipitate and the matrix-the process known as Ostwald ripening. Increasing inter-particle spacing occurs with increasing ageing time and is due to the reduction of the number of the precipitate in unit GB area.

4.3.8 Intragranular Precipitation

The Zener model[2] is used for this type of growth. It simply applies a spherical diffusion field around the precipitate, controlled by the lattice diffusion coefficient for the solute. In one dimension the amount of solute supplied from a right angled triangle of composition-distance space whose height is $(x_\alpha - x_{\alpha T_{nuc}}^{\alpha\theta})$ and length is $2(Dt)^{\frac{1}{2}}$ is used to grow a particle whose area in composition-distance space is $(x_\theta - x_\alpha) \times$ (particle radius). With certain approximations, the particle grows with a power law relationship with time of $t^{\frac{1}{2}}$ using the following equation

$$x = \sqrt{\frac{2D_I\left(x_\alpha - x_{\alpha T_{nuc}}^{\alpha\theta}\right)t}{x_\theta}} \qquad (37)$$

where x_α is the solute concentration in the matrix and x_θ is the solute concentration in the precipitate phase.

4.3.9 Width of Precipitate-Free Zone

The width of the precipitate-free zone (PFZ) after ageing for a time t at the ageing temperature is defined by w_{pfz}

$$w_{pfz} = 2y_0 \qquad (38)$$

where

$$y_0 = \varpi + \lambda' \qquad (39)$$

where λ' should satisfy the condition:

$$c(\lambda',t) = x_{\alpha T}^{\alpha\theta} \tag{40}$$

$c(\lambda',t)$ is the solute concentration distribution function in the solute depleted area, ϖ is the half width of SCL.

The PFZ is formed for two reasons. The first is the depletion of the solute due to the ready diffusion of the solute atoms into the boundary where relatively large particles of precipitate are subsequently formed. The second is the depletion of vacancies to levels below that needed to assist with nucleation of precipitates at the particular ageing temperature. The vacancy depleted part of a PFZ may be absent in some alloys aged at temperatures below the Guinier-Preston (GP) zone solvus as GP zones can form homogeneously without the need of vacancies[20-22]. The modelling of width of PFZ here considers only the depletion of solute atoms in the area adjacent to the grain boundaries caused by segregation.

Solute depletion in the PFZ is caused by NES during quenching from high temperature and subsequent growth of GB precipitates. In such areas it is difficult or impossible for the precipitate nucleation to take place. Vacancy depletion profiles have not been considered as a cause of the PFZ here.

4.4 The MCS Approach

A different approach is the Monte Carlo Metropolis sampling simulation (MCS)[23,24]. The simulation starts with assigning energies to the matrix and the precipitate phase and then sampling the phase transformation using the Metropolis sampling algorithm. Detailed information of precipitation, including particle size distribution may be obtained.

4.4.1 Basic Theories

The theories on which the new simulation approach is based are briefly reviewed below.

4.4.1.1 Grain boundary segregation

Segregation of solute atoms to grain boundaries results in the redistribution of solute atoms in the material, and this affects the nucleation site density. The segregation mechanism is based on the model in section 4.3.1.

4.4.1.2 Nucleation

The nucleation rate, that is the nuclei formed per unit time, can be described by the following equation [25, 26]:

$$I = Z\beta * \left(\frac{N}{x_\theta}\right) \exp\left(-\frac{\Delta G *}{kT}\right) \exp\left(-\frac{\tau}{t}\right) \tag{41}$$

where N is the number of a particular type of atomic sites, x_θ is the molar fraction of solute atoms in the nucleus phase, k the Boltzmann constant, T the absolute temperature, $\Delta G*$ the energy required to form the critical nucleus given by Equation (11), t the time and τ the incubation time for nucleation. The two coefficients Z and $\beta*$ are as follows

$$Z = \frac{V_\theta (\Delta G_V)^2}{8\pi\sqrt{kTK_j}\sigma_{\alpha\theta}^3} \tag{42}$$

$$\beta* = \frac{16\pi\sigma_{\alpha\theta}^2 D x_\alpha L_j}{a^4 (\Delta G_V)^2} \tag{43}$$

where V_θ is the volume occupied by one atom in the nucleus, ΔG_V given by Equation (12) the free energy change per unit volume of nucleus, $\sigma_{\alpha\theta}$ the interfacial free energy, D the diffusivity, x_α the solute concentration in the matrix, a the lattice parameter, L_j and K_j are precipitate shape factors and are defined by

$$V = \frac{4}{3}\pi r^3 K_j \tag{44}$$

$$S = 4\pi r^2 L_j \tag{45}$$

In these two equations, V and S are volume and surface area of the nucleus respectively and r the radius or a characteristic length parameter of the particle. The incubation time

$$\tau = \frac{8kT\sigma_{\alpha\theta}a^4}{V_\theta^2(\Delta G_V)^2 Dx_\alpha} \tag{46}$$

is usually very small, so that the term $\exp\left(-\frac{\tau}{t}\right)$ in Equation (41) can be assumed as unity.

4.4.1.3 Growth and coarsening

The formed nuclei can either grow or dissolve depending on the size of the nuclei and the solute concentration in the matrix. The growth and coarsening mechanisms are shown in Fig. 4.3. At early stages of precipitation, the solute concentration in the matrix is high and it is probable that the average solute concentration in the matrix is higher than the solute concentrations at surfaces of all precipitates despite their different size. Therefore, all precipitates will grow. However, as the concentration gradient in the vicinity of the smaller particles is lower than that of the larger particles, smaller particles grow at lower rates. This process is commonly called growth. As the precipitates grow, the solute concentration in the matrix decreases. When the concentration in the matrix decreases to

such a level that the average concentration in the matrix is higher than some large particles but lower than some smaller particles, then there is a concentration gradient between small and large particles as shown in Fig. 4.3. In such circumstances, the larger particles continue to grow at the cost of the dissolution of small particles. This is referred to as coarsening. The driving force for coarsening is that larger particles have lower surface to volume ratio and therefore a lower free energy.
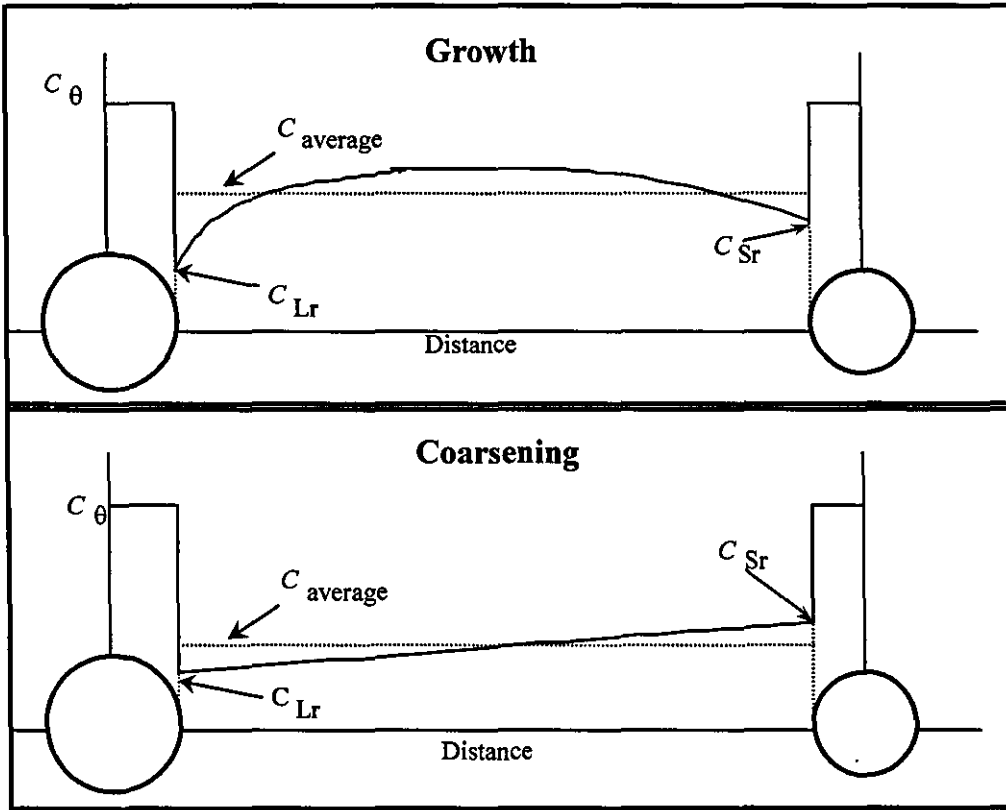
Fig. 4.3. Growth and coarsening mechanism of precipitation[27]

The solute concentration at the surface of a particle with radius of curvature of r, C_r can be described by the Gibbs-Thomson equation:

$$C_r = C_\infty \exp\frac{2\sigma_{\alpha\theta}V_\theta}{RTr} \tag{47}$$

where C_∞ is the equilibrium solute concentration, $\sigma_{\alpha\theta}$ the interfacial free energy, V_θ the molar volume of the precipitate phase, R the universal gas constant and T the absolute temperature. The equilibrium solute concentration is determined using the following equation[8]

$$C_\infty = \left[\frac{1}{C_N}\exp\left(\frac{-\Delta H}{RT}+\frac{\Delta S}{R}\right)\right]^{X_E} \tag{48}$$

where C_N is the concentration of the non rate controlling element, X_E the ratio of the number of non rate controlling to rate controlling atoms in the precipitate phase. ΔH and ΔS are the enthalpy and entropy of solution of the precipitate.

When the solute concentration gradient in the vicinity of a particle surface is known, the rate of its growth or dissolution can be calculated using Fick's first law of diffusion:

$$J = D\frac{dC}{dZ} \tag{49}$$

where J is the diffusion flux, D the diffusivity and $\frac{dC}{dZ}$ is the concentration gradient in the direction normal to the particle interface.

4.4.2 The Simulation Approach[27-29]

4.4.2.1 The simulation cell

The previous section reviews the basic theories necessary for the simulation of precipitation kinetics in alloys. This section presents the details of the new approach.

As in all Monte Carlo simulations, the process is simulated in a simulation cell. The cell can be a single grain or contain a number of grains, so that it contains both the matrix and grain boundaries and can be regarded as the basic unit of the material. One of the simplest forms of simulation cell is shown in Fig. 4.4. The material then can be
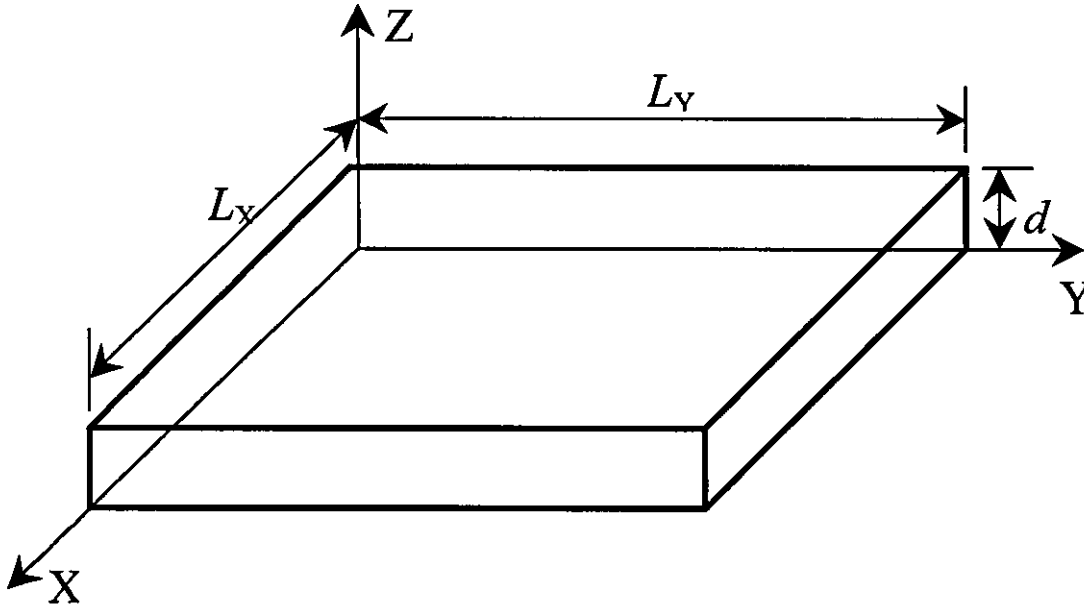
Fig. 4.4. The simplest simulation cell (the surface of the cell is the grain boundaries)

constructed with the periodic boundary conditions applicable to the cell, *i. e.* the cell is imaged all over the space in three dimensions. In this way, the structure and properties of the cell can be taken as representative of the structure and properties of the real material. The cell can be regarded as a grain and the surface of the cell is the grain boundary, though it is acknowledged that the actual grain may have totally different and irregular shape. The size of the grain is characterised by its length in X, Y and Z directions, namely L_X, L_Y and d as shown in Fig. 4.4. In ferritic steels, d is taken as a measure of the grain size and L_X, L_Y are much larger than d.

4.4.2.2 Segregation

Segregation of solute atoms to grain boundaries is considered in the new approach in two ways. (1) As most power plant steels are solution heat treated or normalised at

temperatures around 1060°C and then either quenched or air cooled, the non-equilibrium segregation model (Equation (19a)) is employed to predict the segregation effects during quench. This gives the initial solute concentration distribution in grain boundaries and the matrix within the simulation cell. (2) The time-dependent segregation model is employed to give solute distributions during subsequent tempering and ageing of the alloys of concern. In other words, the solute concentration at any time, t, during ageing is obtained using Equation (19b).

4.4.2.3 Nucleation

Two types of nucleation sites are considered. One is the intra-granular precipitate. In this case, homogeneous nucleation and spherical particles are assumed. In the case of inter-granular or grain boundary precipitates, cap shaped particles are assumed (Fig. 4.5.). In both cases, the critical nucleus size and the driving force can be determined using the following equations:

$$r^* = -\frac{2\sigma_{\alpha\theta}}{\Delta G_V} \tag{50}$$

$$\Delta G^* = \frac{16\pi\sigma_{\alpha\theta}^3}{3\Delta G_V^2} K_j \tag{51}$$
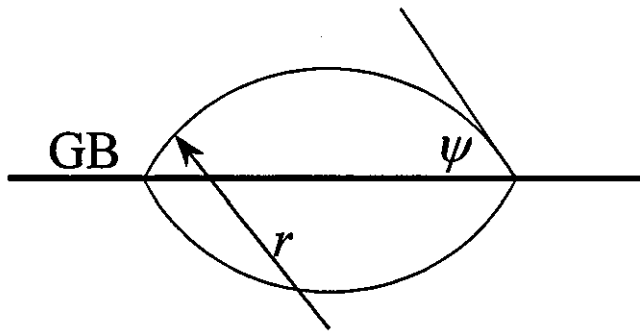
Fig. 4.5. Grain boundary cap shaped precipitate (GB stands for grain boundary, ψ is the contact angle and r is the radius of the sphere from which the cap is cut)

For spherical particles, r is the radius and thus K_j and L_j in Equations (44)-(45) and (51) are unity. For cap shaped particles, r is the radius of the cap, and K_j and L_j are related to the contact angle by:

$$K_J = \frac{1}{2}\left(2 - 3\cos\psi + \cos^3\psi\right) \tag{52}$$

$$L_J = 1 - \cos\psi \tag{53}$$

Here it is assumed that $\psi = 57°$, as in reference 5 for $M_{23}C_6$ particles in austenitic steels. Therefore, $K_j = 0.2638$ and $L_j = 0.4554$, which are the same as Saito used for Nb carbide[30]. It is found that the simulation results fit the experimental observations well when the interfacial energy, $\sigma_{\alpha\theta}$, equals 0.51 J m^{-2}. This value is a little lower than that used by Saito for Nb carbides.

ΔG_V in Equations (42), (43), (50) and (51) is determined as a function of temperature and matrix composition using MTDATA[31,32]. The equilibrium solute concentration in Equations (47) and (48) is also determined using MTDATA.

The simulation treats the tempering and ageing of the steel consecutively. The whole tempering and ageing process is divided to many small time intervals, Δt. At each time interval $t \sim t + \Delta t$, sets of random numbers (x, y, z) are generated to locate the critical nucleus both in the grain boundaries and in the matrix. At present, we assume nucleation is successful when the generated nucleus does not overlap with others. The total number of nuclei accepted at any time interval $t \sim t + \Delta t$ is controlled by Equation (41), i. e.,

$$\Delta N(t) = Z\beta * \left(\frac{N}{x_\theta}\right)\exp\left(-\frac{\Delta G*}{kT}\right)\Delta t \tag{54}$$

where $\Delta N(t)$ is the number of nuclei generated in the simulation cell during the time interval. The numbers of nuclei generated in the matrix and in grain boundaries are different due to the differences both in the solute concentration and the driving force for nucleation. No particular size distribution of the nuclei is introduced here. Note that the nucleation rate described by Equation (54) changes with time because solute concentration in the matrix decreases due to the formation of precipitates. β^*, the rate of arrival of solute at the nucleus, also decreases with time. N in Equation (54) is taken to be the total atomic sites in the matrix and grain boundary for intra- and inter-granular precipitation. The grain boundary width is assumed to be 1 nm.

4.4.2.4 Growth and coarsening

When the number of generated nuclei at any time interval $t \sim t + \Delta t$ reaches the value determined by Equation (54), generation is stopped. When the next time interval is considered and the appropriate number of new nuclei are generated according to Equation (54), with adjusted parameters for β and ΔG^* because of the changed matrix composition. All particles generated before this time interval are assumed to be in the growth/coarsening regime.

The average solute concentration at any time t can be determined from the initial composition of the material and the volume fraction of precipitates. Assuming that the initial concentration of solute is C_g and the volume fraction of precipitates at any time t is V_f, then the average solute concentration at time t will be:

$$\overline{C}_t = 1 - \frac{V_f \rho_\theta N_r}{\rho_\alpha C_g} \tag{55}$$

where ρ_α and ρ_θ are molar density of the matrix and the precipitate phase respectively and N_r is the number of rate controlling atoms in the precipitate molecule.

From Equations (44) and (55), the concentration gradient in the vicinity of the surface of a particle of radius of curvature r at any time t can be estimated using a mean field approximation

$$g = \frac{\overline{C_t} - C_r}{d_s}$$ (56)

where d_s is the average inter-particle spacing. If $g>0$ the particle grows and if $g<0$ the particle dissolves. The rates of both growth and dissolution are determined using Fick's first law of diffusion. Thus, the increase of the volume of a particle, ΔV, in time interval $t \sim t + \Delta t$ is

$$\Delta V = DSg \frac{\rho_\theta}{C_\theta \rho_\theta - C_r \rho_\alpha} \Delta t$$ (57)

Where $S = 4\pi r^2$ is the surface area of the spherical particle. For inter-granular particles, S is divided into two parts: one within the matrix and the other in the grain boundary to allow both volume and grain boundary diffusion of solute atoms to or from the formed precipitates. The latter is determined by the precipitate size and the grain boundary width. The average solute concentration along grain boundaries is taken as the segregation factor, C_b / C_g times $\overline{C_t}$ calculated using Equation (55). In any time interval $t \sim t + \Delta t$ during the simulation, all the particles, including the nuclei generated in this time interval and all others generated before time t, are allowed either to grow or to dissolve. That is, at each time step, concentration gradient and the volume increase are calculated for each individual particle. The average concentration in the matrix is re-calculated when any one of the particles changes its volume. To ensure a random sample particle, a random number with values between one and the number of particles in the cell is generated to pick up the first particle. Then the volume change of this particle is calculated according to Equation (57) and consequently the average concentration in the matrix is calculated

according to Equation (55). This process is repeated in each time interval for all existing particles.

4.4.2.5 The simulation loop

The simulation process is summarized in Fig.4.6. After the establishment of the simulation cell, the inter-granular segregation models are used to calculate the initial solute distribution within the cell (section 4.4.2.2). Then the heat treatment time is

```
┌─────────────────────┐
│  Simulation  Cell   │
└─────────────────────┘
          │
          ▼
┌─────────────────────┐
│       N E S         │
└─────────────────────┘
          │
          ▼◄──────────────────────────┐
┌─────────────────────┐               │
│    Segregation      │               │
└─────────────────────┘            L  │
          │                        O  │
┌─────────────────────┐            O  │
│    Nucleation       │            P  │
└─────────────────────┘               │
          │                           │
┌─────────────────────┐               │
│      Growth/        │               │
│    Coarsening       │───────────────┘
└─────────────────────┘
          │
          ▼
┌─────────────────────┐
│      Results        │
└─────────────────────┘
```
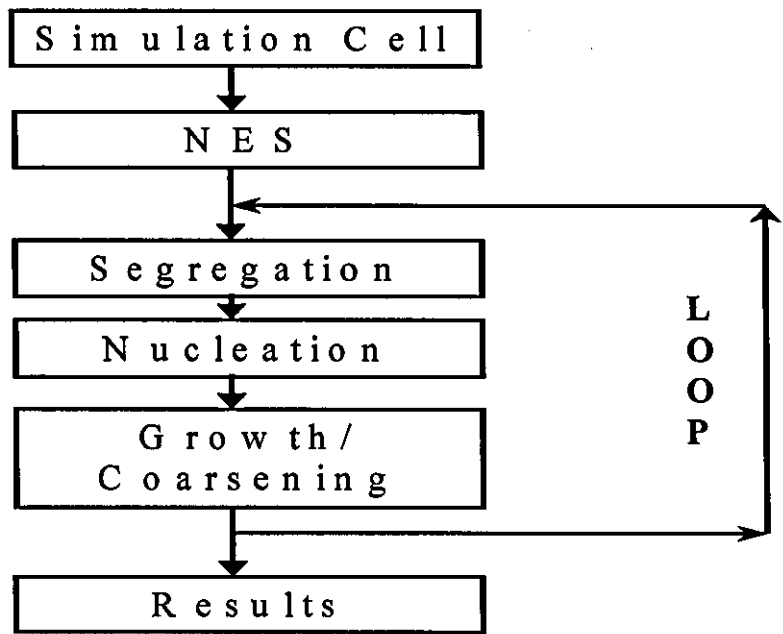
Fig. 4.6. The simulation loop shows the main steps in the simulation.

divided into tens of thousands of small time intervals. Within each time interval, segregation model is used to calculate solute concentration distribution (section 4.4.2.2), then positions of a certain number of nuclei are generated randomly (section 4.4.2.3) and all particles are individually allowed to either grow or dissolve (section 4.4.2.4). The process is looped until the required ageing time is reached and simulation results are then

written to a file. Particle size distribution data can be saved to a file at the end of tempering and then at time intervals set at the start of the simulation.

4.5 Conclusions

(1) The GBSP model for precipitate growth on GB in alloys is:

$$L = \{\sum_{i=1}^{i=n} \frac{2A_{mi-1}D_i^{\frac{1}{2}}(x_{\alpha i} - x_{\alpha T}^{\alpha\theta})\{(i\delta t)^{\frac{1}{2}} - [(i-1)\delta t]^{\frac{1}{2}}\}\rho_\alpha}{\rho_\theta \pi^{\frac{3}{2}}f(\psi)(x_\theta - x_{\alpha T}^{\alpha\theta})} + L_0^3\}^{\frac{1}{3}}$$

The GBSP model for precipitate coarsening on GB in alloys is:

$$L(t) = \left[A(t - t_{cc}) + L_g^4\right]^{\frac{1}{4}}$$

(2) The GBSP model gives a good description of the trend in which solute atoms are drawn to and concentrated at the grain boundary and the vicinity based on "collector plate" theory.

(3) The GBSP model gives prediction of GB precipitation and segregation behavior, and inter-particle spacing and PFZ width.

(4) The GBSP model can be widely used in different type of alloys for predicting the GB microstructures.

(5) The MCS approach to the modelling of precipitation kinetics of chromium carbide in ferritic steels based on Monte Carlo random sampling technique can automatically predict the transition from growth to coarsening.

References to Chapter 4

1. H.B. Aaron and H.L. Aaronson, Acta Metall., 16, 1968, 789.

2. H.B. Aaron, D. Fainstein and G.R. Kotler, J. Appl. Phys., 41, 1970, 4404.

3. R.G. Faulkner, J. Caisley, Met. Sci., 11, 1977, 200.

4. R.G. Faulkner, J. Mater. Sci., 16, 1981, 373.

5. R.A. Carolan and R.G. Faulkner, Acta Metall., 36(2), 1988, 257.

6. R.G. Faulkner Mater. Sci & Tech., 1, 1985, 442.

7. R.G. Faulkner and H. Jiang, Mater. Sci & Tech., 9, 1993, 665.

8. H. Jiang and R.G. Faulkner, Acta Mater., 44(5), 1996, 1857.

9. H. Jiang and R. G. Faulkner, Acta Mater., 44(5), 1996, 1865.

10. R.G. Faylkner, Acta Metall., 35(12), 1987, 2905.

11. R.G. Faulkner, S.H. Song and P. E. J. Flewitt, Met. Trans., 27A, 1996, 3381.

12. R.G. Faulkner, D. Meade, C.C. Goodwin and M. Spindler, Microstructure of High temperature materials, 2, 2000, 431.

13. T.R. Anthony, Acta. Metall. 18, 1970, 307.

14. K.C. Russell, Acta. Metall, 17, 1969, 1123.

15. R.G. Faulkner, Inter. Materil. Review, 41(5), 1996, 198.

16. K.C. Russell, Acta Metall, 17, 1969, 1123

17. G. Van der Velde, J. A. Velasco, K. C. Ressell and H. I. Aaronson, Metall. Trans, 7A, 1976, 1472.

18. R.G. Faulkner, D. Meade and R. Hales, Acta Mater., 42(5), 1994, 345.

19. J.W. Martin, in Micromechanisms in Particle-Hardneed Alloys, 1980, 23-26.

20. I. J. Polmear, in Light Alloys, Chapter 2.1.3, Edward Arnold Ltd., 1981, 19.

21. P.R. Sperry, Metall. Trans., 1, 1970, 2650.

22. W.F. Smith and N. I. Grant, ASM Trans. Quart., 62(3), 1969, 72.

23. Y. Saito, Materials Science and Engineering A, 1997, 223(1-2), 125.

24. J.M. Liu, Materials Science and Engineering A, 1998, 254(1-2), 45.

25. K.C. Russell, Acta Metallurgica, 1969, 17, 1123.

26. W.C. Johnson, M.B. Berkenpas and D.E. Laughlin, Metallurgical Transactions A, 1975, 6A, 911.

27. Y.F. Yin and R.G. Faulkner, Simulations of Precipitation in Ferritic Steels, Materials Sci. and Techn., 19, 2003, 91-98.

28. Y.F. Yin and R.G. Faulkner, A New Modelling Approach to Microstructural Evolution in Ferritic Steels, Power Techn., J. Lecomte-Beckers, et al., eds., 19(2), 2002, 1247-1256.

29. Y.F. Yin and R.G. Faulkner, PARSONS 2003, Engineering Issues in Turbine Machinery, Power Plant and Renewables, Proc. Of the Sixth Inter. Charles Parsons Turbine Conf., 16-18 Sept. 2003, Trinity College Dublin, Ireland, 457-471.

30. Y. Saito, Materials Science and Engineering A, 1997, 223(1-2), 134-145.

31. R.H. Davies, A.T. Dinsdale, J.A. Gisby, S.M. Hodson and R.G.J. Ball, Proc. Conf. ASM/TMS Fall Meeting on 'Applications of Thermodynamics in the Synthesis and Processing of Materials', Rosemont, IL, USA, Oct 1994, 371.

32. R.H. Davies, A.T. Dinsdale, S.M. Hodson, J.A. Gisby, N.J. Pugh, T.I. Barry and T.G. Chart, High Temperature Sci., 1990, 26, 251.

CHAPTER 5:

Weld Simulation of P91 Materials with the Gleeble Testing Machine

5.1 Introduction

5.1.1 Determination of Weldability by Simulation Techniques

In principle there are several methods which can be applied for the assessment of the weldability. These are as follows:

- Investigations of real, full scale weldments
- Welding simulation, e.g. using a Gleeble machine
- Determination of welding CCT diagrams
- Hardness measurements across the heat affected zone (HAZ)[1]
- Special weldability tests
- Data bases on results of cracking tests
- Empirical or parametric equations
- Knowledge based systems
- Mathematical models concerning fundamental microstructural phenomena involved during welding

First of all, experimental investigations are used to understand the fundamentals and further on to optimize the material or the welding conditions. Due to the difficulties involved during full scale testing, it consumes on time and cost, produces many troublesome secondary effects, and it results in a very small critical zone width, therefore weldability tests have been developed to evaluate the cracking susceptibity, mainly on the base material, to cracking[2]. These tests are of following types:

- Cold cracking tests
- Hot cracking tests
- Stress-relief cracking tests

● Lamellar tearing tests

The basic idea of all these tests is that the most important parameters are taken into account and measured, whereas disturbing parameters are eliminated as far as possible. Besides the many advantages of these tests, the negative side is that the test conditions have to be standardized and kept constant, so that the "system results" are in most of the cases just an indicator and not a physical or metallurgical measure of a phenomenon. A further disadvantage is that most of these procedures are limited to special cases, material groups and perspectives.

In order to get a full understanding, a sound fundamental approach is necessary, which separates effects which can be treated separately and linked together as appropriate. From this physical point of view, weldability issues are accumulated or linked phenomena. It is essential to separate this complex subject into its basic components.

These components comprise the following key elements:
● Changes in the mechanical properties or any defect appearance in weldments caused by the effect of the thermal history combined with mechanical loading/deformation or chemical reactions during and after welding[3].
● Most of the microstructural changes in the weld metal or in the heat-affected zone are thermally activated and can be described by metallurgical models[4], which are fully developed for isothermal conditions.

In any case, the most reliable procedure that should be applied is the sound investigation of the underlying fundamental processes. One of the most promising and most reliable ways to simulate weldability is the Gleeble simulation, which will be considered below in more detail.

5.1.2 Gleeble Welding Simulation

Weldability testing by the Gleeble machine is nowadays accepted worldwide and recommended[3]. Because it follows directly the above mentioned philosophy i.e. separation of the individual phenomena and accurate measurement of the effects of the most relevant parameters by simultaneous elimination of disturbing factors, it can be used for studies of

- Microstructural evolution
- Hot ductility
- Mechanical properties of the HAZ
- Welding continuous cooling transformation diagrams
- Precipitation kinetics in the HAZ
- Basic weldability
- Strain age cracking
- Strain age embrittlement
- Constitutional liquation
- Liquid metal embrittlement
- Solidification cracking of austenitic stainless steels

In general, the Gleeble system permits simulations of virtually any thermomechanical process. It is a fully interfaced system, readily programmed to provide reference signals for closed loop control of both thermal and mechanical operations. Heating is accomplished by the flow of low-frequency alternating current in the specimen with heating rates up to 10000 K/s. The feedback signal necessary for closed-loop control is normally obtained from a fine wire thermocouple percussion welded to the specimen surface.

In order to determine the specific properties of a particular region in the HAZ, one needs to know only the weld thermal cycle, which can be predicted as a function of the welding process, welding parameters, weldment form, thickness and preheating temperature. In Europe, the cooling time ($t_{8/5}$) concept is applied as standardized in SEW-088[5]. In

computerized form, the HAZ-Calculator[6] provides the input data of the thermal cycle for the Gleeble weldability simulation. Depending on the distance from the fusion line, the temperature history can then be programmed into the Gleeble machine and applied to a cylindrical or square sample.

The advantages of Gleeble weldability testing can be summarized as follows[7, 8]:

- Accurate application and measurement of the thermal cycle for a predefined location in the HAZ
- After simulation, an enlarged volume for further metallographic investigation or mechanical tests is available compared to the limited size in a real weldment
- Due to the larger volume and higher homogeneity of the simulated microstructure, there is a reduced scatter of the HAZ properties
- Phase transformations during welding can be measured by thermal analysis or dilatometric measurement of the C-strain
- In addition, mechanical stresses during the cooling phase can be superimposed in order to simulate any contraction of the surrounding material
- The mechanical material properties during cooling from high temperatures can be directly measured for input in finite element calculations
- Other combined thermomechanical tests can be applied, like reheating relaxation test, hot ductility test, partly melting and afterwards cooling to simulated the behavior of the weld metal

Some pitfalls are as follows[9, 10]:

- The temperature profile in longitudinal direction causes some experimental problems
- Effects of local gradients on microstructure, properties and residual stresses are not taken into account when using the HAZ simulation technique

In order to be able to investigate sufficiently the HAZ, simulated microstructures were produced using the Gleeble technique. Specimens, machined from a bar 110 mm in width and 10 mm in diameter, were heated to a peak temperature in the centre of the gauge section, held for a while and cooled with $t_{8/5}$ = 22 second which is comparable to a

manual arc welding. The HAZ zone can be enlarged from about 2 mm wide in the real welds to 15 mm, so it will be easier to observe in detail the phase transformation and microstructure changes across the whole HAZ region. Therefore the Gleeble testing method is an ideal and also practical way for the HAZ analysis of ferritic steel weldments.

5.2 Experimental Procedure

5.2.1 Materials

P91 pipe material (Table 5.1) was supplied from KA series cast by Powergen in a solution heat treated and tempered condition (1040°C/1.5h/AC; 780°C/1.5h/AC).

Table 5.1. Chemical composition of P91 material (balance Fe)

	C	Si	Mn	P	S	Cr	Mo	Ni	Al	Nb	V	N
wt. %	0.09	0.31	0.46	.010	.002	8.68	0.92	0.12	.008	0.09	0.21	.05
At. %	0.41	0.62	0.46	.018	.003	9.25	0.54	0.11	.016	0.06	0.21	.05

5.2.2 Gleeble Testing

The Gleeble 1500 simulator (Fig. 5.1) at Powergen was used to apply resistance heating to cylindrical threaded specimens held unstrained at each end in water-cooled jaws. The thermal cycle at the specimen center was controlled by a feedback loop. Diametral expansion during the cycle was measured by dilatometry.

Simulated welding thermal cycles were applied to each specimen with peak temperatures of 850°C, 900°C and 950°C. Simulated weld pre-heat was applied by heating to 200°C in 5 seconds followed by holding at 200°C for 10 second. Heating rates in each case to peak temperature were 150°C/sec followed by a 5 second hold at the peak temperature. Cooling from the peak temperature to 500°C was controlled at 15°C/sec^2. The Gleeble

a)   b)
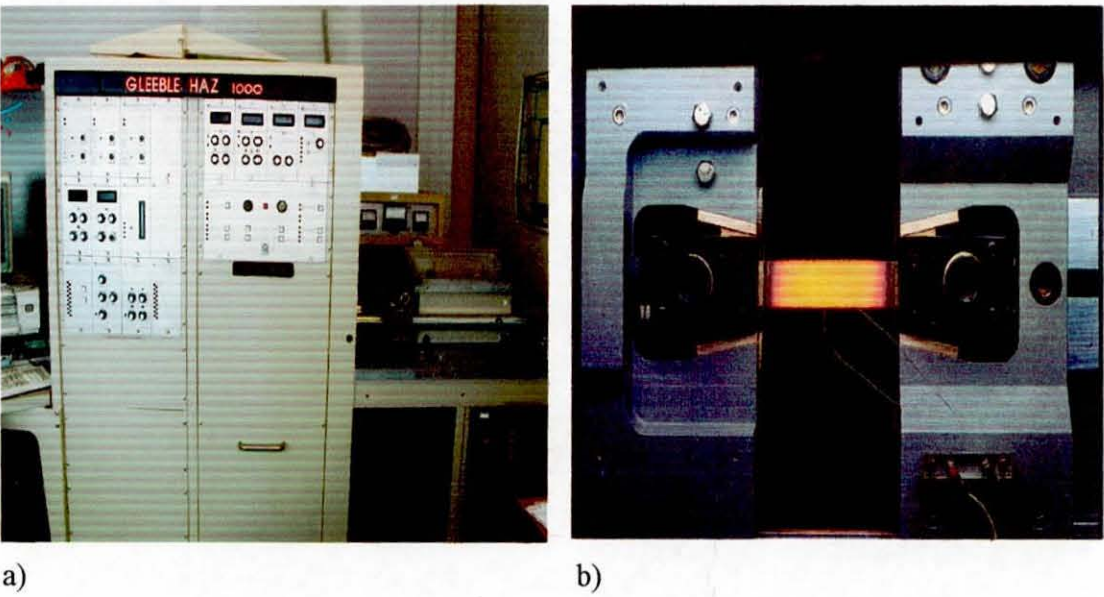
Fig. 5.1. The Gleeble testing machine

    a) Control panel, b) Jaws

control cycle was then set to 0°C such that a condition of free cooling continued. Details of the thermal cycles are shown in Fig. 5.2.
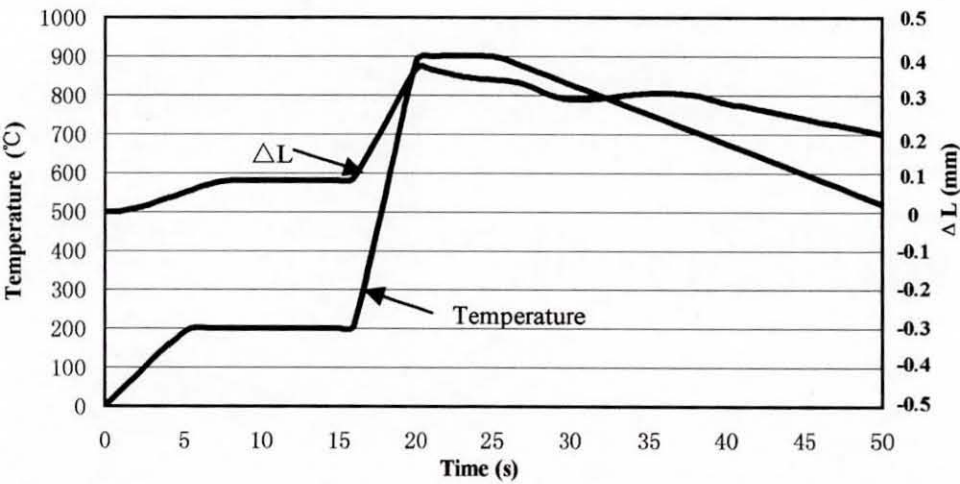
Fig. 5.2. Thermal cycle process (900°C)

After the Gleeble testing, each specimen was cut from the middle (the point of the thermocouple) into two pieces; one half will go through following the PWHT procedure.

5.2.3 PWHT Process

750°C, 2.5hr

After finishing the heat treatment, both slices were sectioned again (Fig. 5.3), then mounted, ground and polished in the usual way for the hardness testing and etched for microstructure observation.
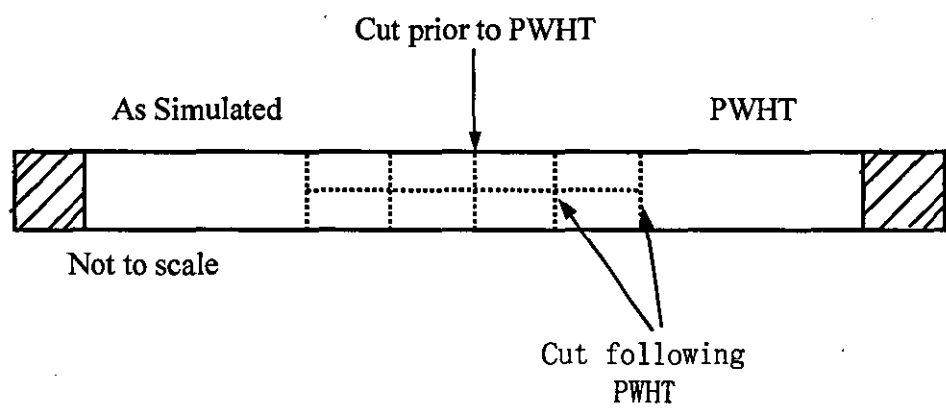
Fig. 5.3. Specimen section map

5.2.4 Hardness Testing

Vickers Hardness testing was conducted along the surface of each specimen both with and without simulated PWHT. Three directional measurements were carried out: firstly the transverse direction along the whole central HAZ plane from the center (the thermocouple position) to the edge of HAZ, i.e. C-E direction; secondly the radial direction of the section of HAZ center (C direction); thirdly the radial direction of cross-section of HAZ edge (E direction). This is shown in Fig.5.4. The hardness was measured transversely at about 1mm intervals, whereas 0.5mm intervals used radially.

E Direction   **C Direction**

2   3

C-E Direction

1

Edge   HAZ   Centre

Hardness Radial 2 3

Section E   Section C

Hardness Traverse 1
Section C-E

Thread End   Middle of Specimen ➝
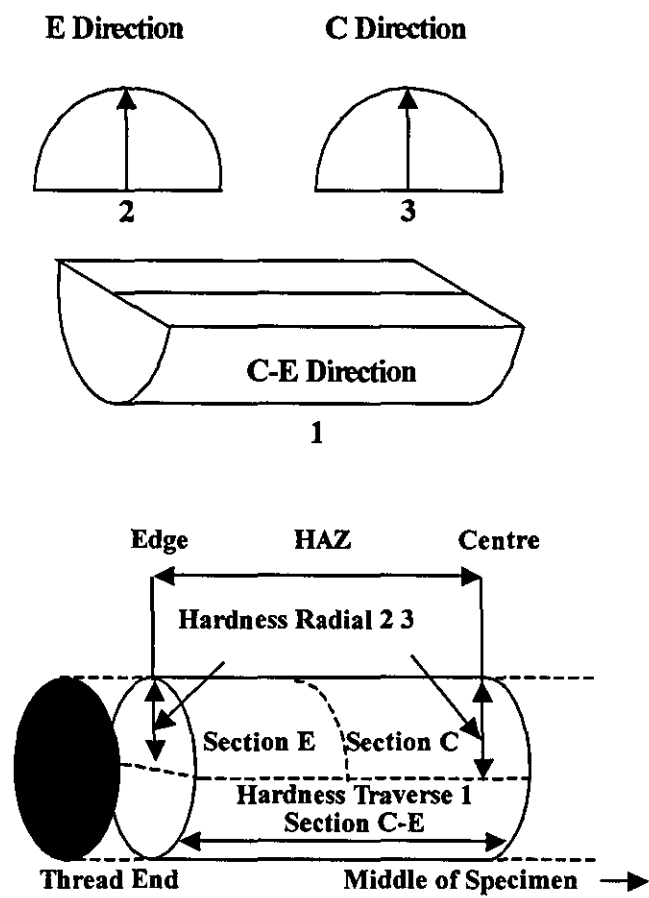
Fig. 5.4. Sections and division of specimen for hardness testing

5.2.5 Microstructure Observation

Specimens were etched with Villela's reagent for 20 seconds (for parent metal) to 1 minute (for reheated metal). Examinations were made using both the optical microscopy and the scanning electron microscope (SEM).

5.3 Results and Discussion

Table 5.2 and 5.3 has given the detailed hardness testing results.

Table 5.2. Vickers hardness testing results

	As Received/Cycled			PWHT		
	Hv*, VPN	ΔHv**(av)VPN	RSD***, %	Hv(av), VPN	ΔHv(av↑),VPN	RSD, %
	C-E⁺ C⁺⁺ E	C-E C E⁺⁺⁺	C-E C E	C-E C E	C-E C E	C-E C E
Parent Metal	233 232 231	— — —	1.01 --- ---	230 226 226	— — —	— — —
850°C	--- 301 225	--- +69 -6	--- 3.25 3.46	207 207 218 (min)	-23 -19 -8 (max)	--- 1.03 2.61
900°C	— 393 232	— +119 +1	— 4.41 1.22	212 221 223 (min)	-18 -5 -3 (max)	--- 4.50 1.22
950°C	— 419 227	--- +187 -4	— 5.92 0.63	208 222 224 (min)	-22 -4 -3 (max)	— 1.33 1.41

*Hv   — Vickers Hardness; Hv_{30};

**ΔHv— Hv value differences between cycled and parent metal.

***RSD—Relative standard deviation; RSD=S/X × 100%, where S is the standard deviation;

↑ --- Average value (X);

+C-E---C-E Direction;

++ C ---C Direction;

+++ E---E Direction.

Table 5.3. Vickers hardness testing data

Sample and Status*	Testing Direction	Hardness Values, VPN
Parent Metal	C-E C E	232,232,234,234,232,234,232,234,232,232,232 232, 234,232,232,232,232 226,232,232,232,232
Parent Metal, PWHT	C-E C E	225,228,229,231,231,231,231,231,231,231,231,229,229 211,226,232,234,232,226,223 226,226,230,225,225,226,226
AXI: 850°C	C-E C E	315,293,255,226,227,224,225,232,232,231,237,231,231,231 277,305,305,308,307,307,299 210,223,227,227,232,232,227
AXII: 850°C, PWHT	C-E C E	207,209,207,210,214,218,217,221,219,221,223,221,225,220 195,209,206,207,206,206 198,218,225,221,223,221
CXI: 900°C	C-E C E	396,393,389,387,385,353,295,232,224,227,227,229 385,406,396,396,393,389,389 223,230,233,232,233,232
CXII: 900°C, PWHT	C-E C E	214,219,219,217,212,216,224,224,224,229,226 218,223,229,216,225,220,219 221,224,223,223,224
EXI: 950°C	C-E C E	411,418,415,411,400,391,373,326,223,224,224 418,409,418,427,418,422 212,226,227,228,227,227,227
EXII: 950°C, PWHT	C-E C E	218,221,220,220,219,216,211,208,220,224,224,223 221,223,223,223,223,221,220 223,226,226,223,223,225

* Sample lablelling:

        A-850°C; B-900°C; C-950°C;

        X-unrestrained;

        I-As cooled condition; II-PWHT (750°C, 2.5hrs)

The results for the three peak temperature cycles, compared with parent materials, show the trend that the hardness increases as peak temperature increases. From Table 5.2, it is also clear that the as-cycled hardness changes along the HAZ zone, there is a lower plateau present, which is the starting point of the soft zone (Fig. 5.5). Then the hardness slightly rises again to the average hardness value of the parent metal. The transformed

zone is considered as the region where the Type IV cracking occurs during creep testing. After PWHT, approximately 10% (-23 ΔHv), 8% (-18 ΔHv) and 9% (–22 ΔHv) maximum hardness drop (softening) were obtained for 850°C, 900°C and 950°C respectively in the soft zone compared with the hardness of the uninfluenced base metal. Meanwhile there are no hardness differences between the centre and the edge of sample, which means the microstructures across both C direction and E directions are quite uniform.
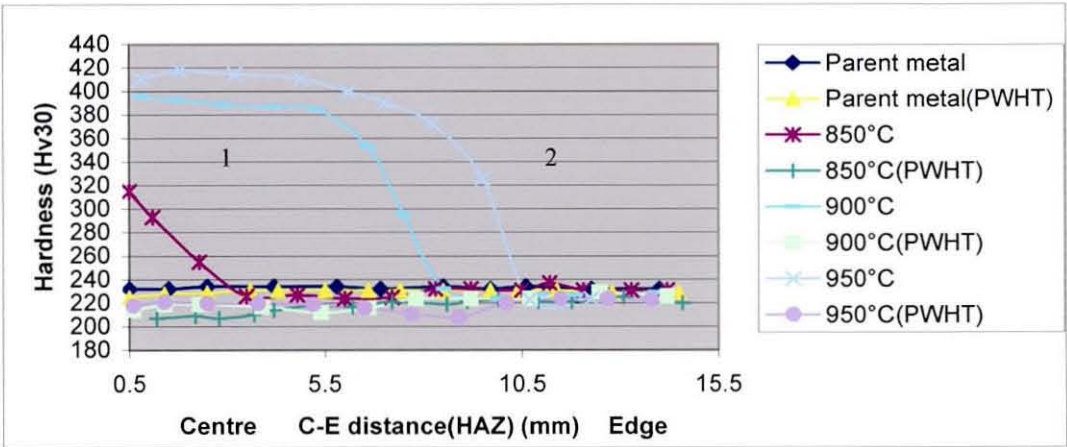
Fig. 5.5. Hardness distribution along HAZ zone
        1-transformed zone, 2-soft zone

Fig.5.6 shows the weld-simulated microstructures of HAZ at three temperatures (transformed zone and soft zone in Fig. 5.5). The microstructures along HAZ zone after tempering at these temperatures are shown in Fig. 5.7. The microstructures of both the retransformed part of HAZ and soft zone are tempered martensitic microstructures. Compared with the typical lath martensite in parent material, fine grain structure and mixed equiaxed grain and short lath martensite are produced in the transformed zone and soft zone respectively.

(a)   (b)

(c)   (d)
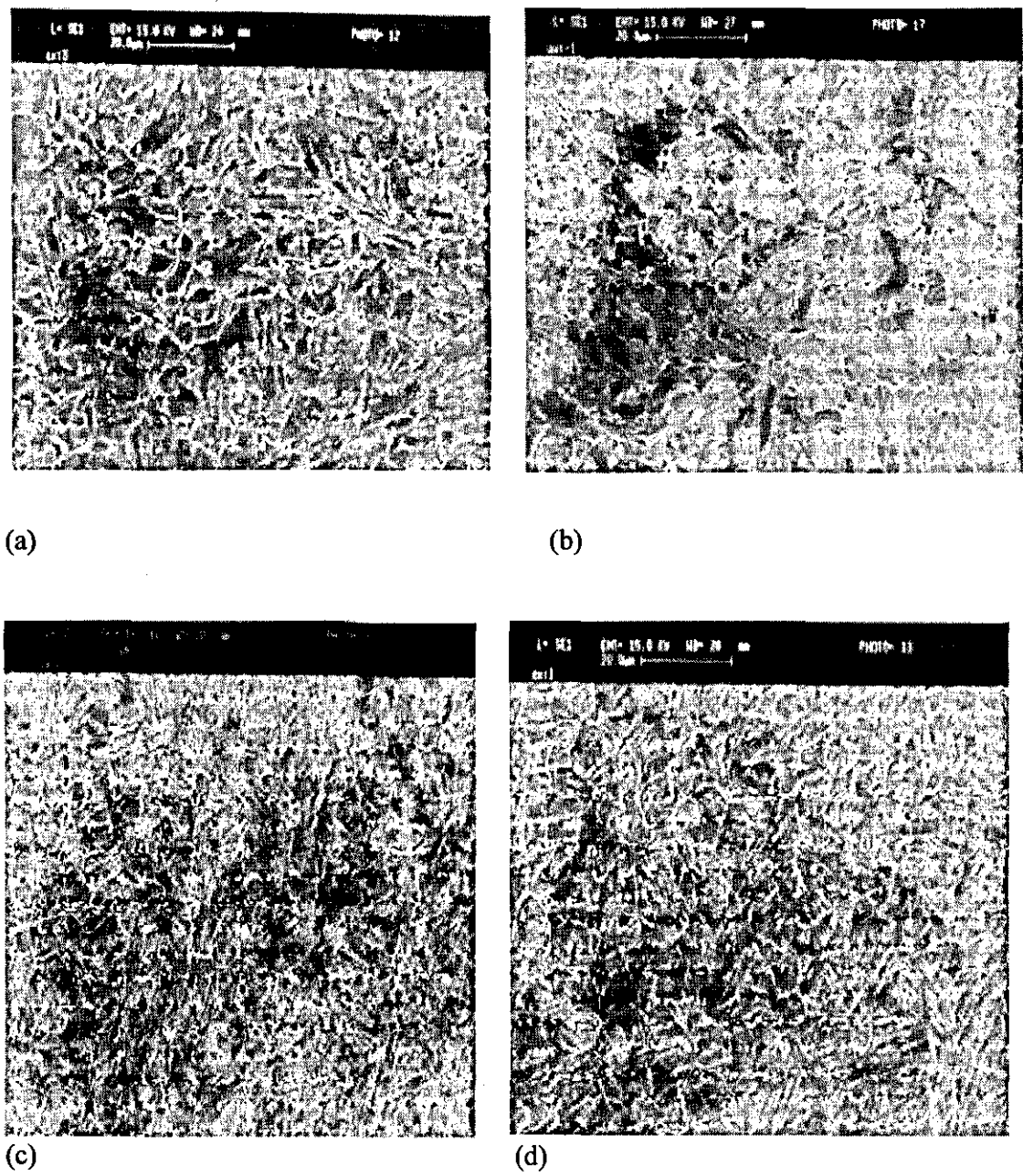
Fig. 5.6. Weld Simulated microstructures in HAZ zone (C direction)

(a) Parent metal, (b) 850°C, (c) 900°C, (d) 950°C,

97

1   2

(a)

1   2

(b)

1   2

(c)
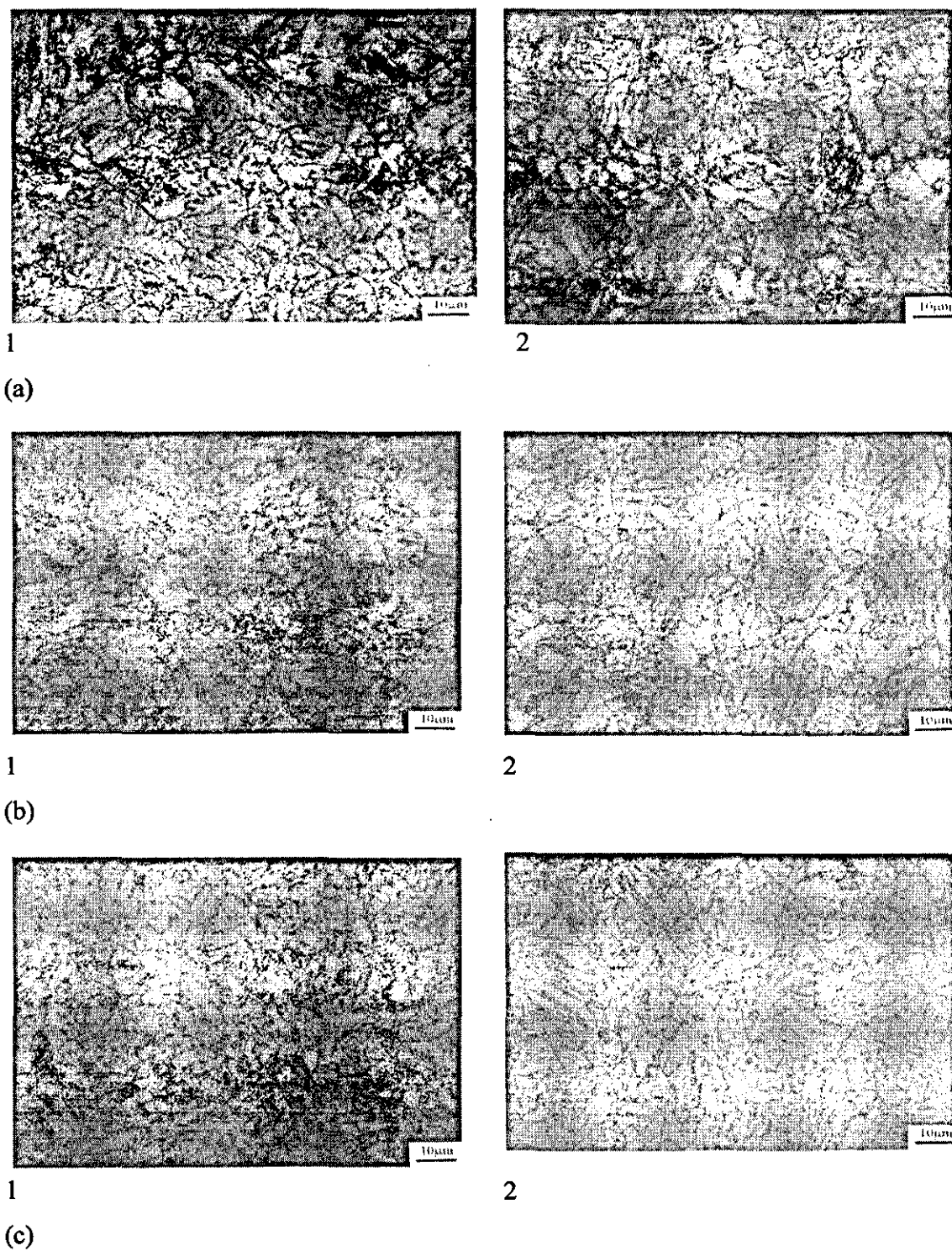
Fig. 5.7. Optical micrograph of HAZ after PWHT

      (a) 850°C + PWHT, (b) 900°C + PWHT, (c) 950°C + PWHT.

      1-transformed zone, 2-soft zone

The softening results from a low peak temperature during weld simulation, which is slightly above the Ac$_3$ or between Ac$_3$ and Ac$_1$ temperature respectively[11, 12]. As large amounts of alloying elements such as Cr, Mo, V in the P91 are present, it will make the austenite quite stable (hardenability). Hence it is difficult for austenite to be transformed during cooling, thus the overcooled austenite will be directly transformed to martensite at a lower temperature when the cooling rate is rather fast.

The M$_s$ temperature of P91 is high (about 380°C), mainly because of low C content. Higher M$_s$ temperature means that more tempering is possible through the cooling. Therefore Fe$_3$C precipitates in the 9%Cr-1%Mo material during cooling could be formed.

It can also be assumed that at a low austenitizing temperature no significant amount of precipitate goes into the solution. This austenite is, therefore, considered to have less carbon than austenite formed at a higher temperature. After transformation a small amount of austenite will still exist, which forms a mixed microstructure of non-transformed base metal and transformed areas. Based on the short time heating and existence of grain-refining elements e.g. Mo, V, Ti, fined equiaxed grains were obtained, which will benefit the HAZ zone by improving the ductility[13].

It was observed that as cycled specimens under similar cooling speed show similar structures, different peak temperature does not seem to affect structures significantly; it is considered that reheating has refined the structures.

In this study, because of the fast cooling rate, block proeutectoid ferrites were not found in the HAZ zone for all specimens. It is different for the HAZ of low Cr ferritic steel described in the reference 14 and 15, where it was explained by the presence of ferrites in an area which was heated to a temperature between Ac$_1$ and Ac$_3$. Therefore, at the maximum temperature, a two-phase microstructure of ferrite and austenite was obtained. Upon cooling, the ferrite remains and the austenite forms into martensite. As the ferrite is a soft constituent, the hardness drop can be related to this two-phase microstructure.

Subsequent PWHT significantly reduces variations in hardness. For the low Cr steel, the softening was found in the as-welded condition and vanished during PWHT. This can be seen as one major difference in the weldability of these two steels. Because no δ-ferrite existed in the HAZ zone in the high Cr steel, it is very possible to form a soft martensite that has caused the soft region.

After reheating, PWHT at 750°C was carried out. As it is around the Ac$_1$, then a series of changes will occur in the HAZ, including martensite decomposition, transformation of residual austenite, carbide precipitation, recovery and recrystallization of lath martensite. Here the carbide precipitation is more important to stabilize and strengthen the structures.

At 850°C, which is the intercritical temperature, little microstructural changes were noticed either in the retransformed zone or in the soft zone. They are more similar to the microstructures in parent materials. At 900°C and 950°C, although it was very difficult to identify, obvious changes could be observed in these two zones before and after tempering. The simulated microstructures in the retransformed zone show fine austenite boundaries and grains. However after tempering the grain boundary became unclear, precipitation increased on the grain boundary; whereas there were no significant differences in microstructures in the soft zone before and after tempering.

The TEM results have confirmed the above observations. Fig. 5.8a depicts the substruture in the fine-grained region of the transformed zone, i.e. Type IV zone in the simulated condition. It shows a tempered martensitic structure with less evidence of carbides and a rather high dislocation density.

a)

b)

c)
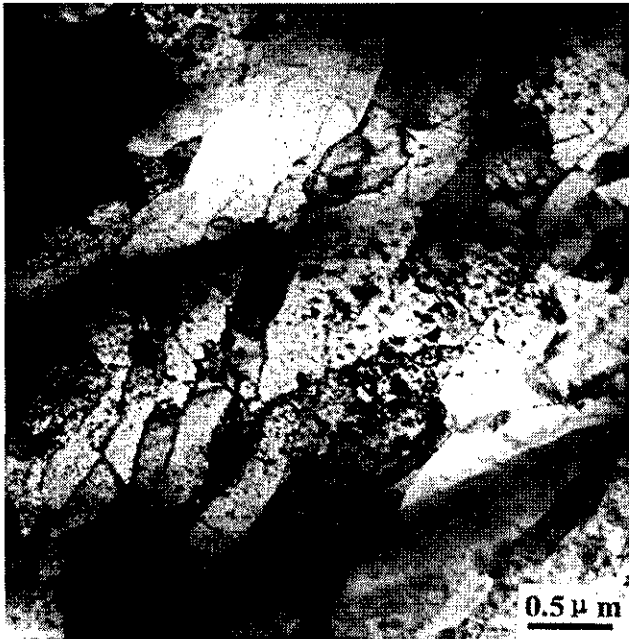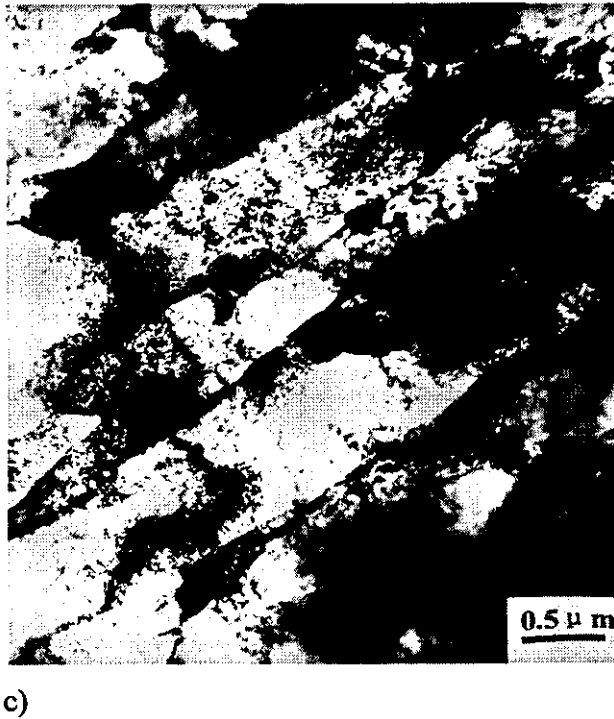
Fig. 5.8. TEM micrograph, simulated condition

    a) Fine grained zone

    b) Soft zone

    c) Parent metal

The substructure at the position, which shows the softening after PWHT, is illustrated in Fig. 5.8b. Although the structure is slightly tempered martensite, it shows, in opposition to the position in the Fig. 5.8a, some carbides. Finally Fig. 5.8c portrays the substructure of the uninfluenced parent metal which is a typical tempered type containing carbides and subgrains.

Fig. 5.9a and b show the different structures which have been found at these positions after PWHT. In the fine-grained zone (Fig. 5.9a), the structure is fully recovered showing subgrains and a large amount of $M_{23}C_6$ carbides. In the soft zone, the structure shows subgrains formation and but not heavy carbide precipitation (Fig. 5.9b). This is because less transformation occurs in this region; therefore the microstructure is more similar to that of the parent metal, which can be expected to be very stable after tempering for 2.5 hours at 750°C, and did not change significantly during PWHT (Fig. 5.9c).
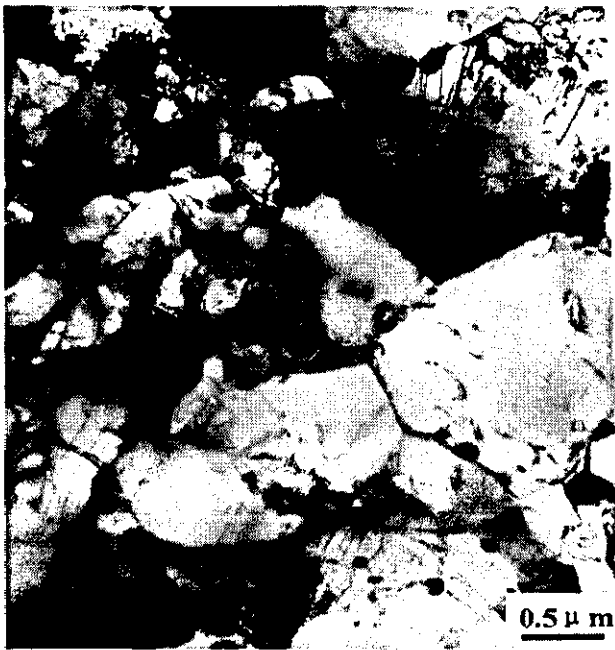
a)
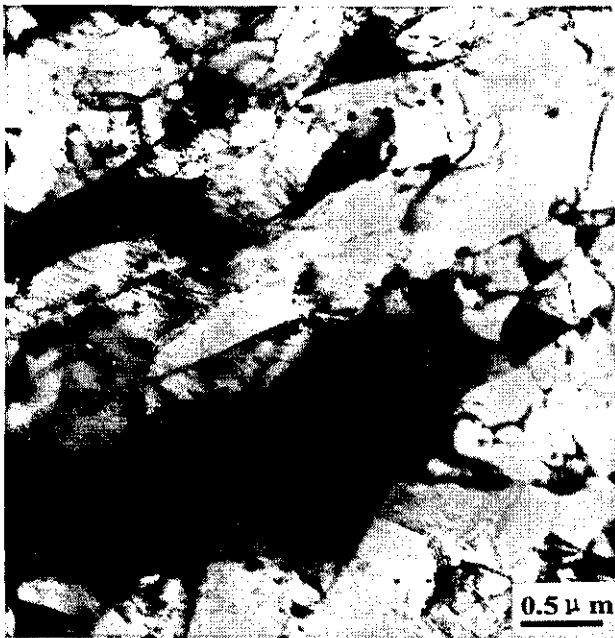
b)
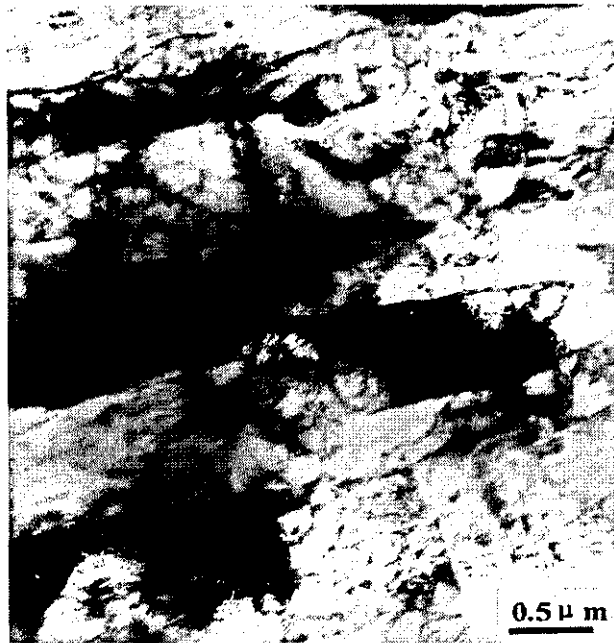
c)

Fig.5.9. TEM micrograph, PWHT condition

    a) Fine grained zone,

    b) Soft zone,

    c) Parent metal

The soft zone was found not very obvious in both the as welded and the simulated condition. Although the lightly tempered martensitic portion of the microstructure increases the hardness, this lightly tempered matensite, transformed from a relatively low austenitizing temperature, contains precipitates (evidenced by Fig. 5.8b) which have not been dissolved during austenitizing. As a consequence, the martensitic matrix contains less carbon since the carbon is trapped in the precipitates. These undissolved precipitates are potential nucleation sites and accelerate the softening during tempering. On the other hand, the lower carbon content could make the body-centred tetragonal martensite less tetragonal, i.e. $c/a \rightarrow 1$, which leads to a softer type martensite.

5.4 Conclusions

1. Maximum 10%, 8% and 9% hardness drop (softening) at 850°C, 900°C and 950°C compared with parent P91 material in PWHT condition were obtained respectively.

2. Fine grain microstructure and mixed equiaxed grain and short lath martensites were produced in the transformed region and the soft zone respectively.

3. No δ-ferrite was found in the HAZ.

References to Chapter 5

1. H. Cerjak, and E. Letofsky, The Effect of Welding on the Properties of Advanced 9-12% Cr-Steels, Science and Technology, 1, 1996, 36-42.

2. R.D. Stout, Weldability of Steels, Welding Research Council, 1987, 238-346.

3. A.J. Murdoch, An Investigation into Weld Type IV Cracking in P91 Steel by Gleeble Simulation, VTT Symposium on Condition and Life Management for Power Plants, Vol.1, ESPOO 2001, 263-273.

4. S.G.R. Brown, J.D. James and J.A. Spittle, Mat. Sci. Eng., 5, 1997, 539-548.

5. H. Cerjak and B. Buchmayr, The Determination of Weldability by Using Simulation Techniques, 7th International Symposium on Physical Simulation of Casting, Hot Rolling and Welding, 21-23,January, 1997.

6. B. Buchmayr, HAZ-CALCULATOR-a software package for metallurgical aspects of weldability, Workshop Computer Aided Welding, 8, 1992. Madrid; IIW-Doc. XII-1304-92.

7. H.S. Ferguson, Recent Developments in Simulation and Testing Using Gleeble Systems, 7th International Symposium on Physical Simulation of Casting, Hot Rolling and Welding, 21-23, January, 1997.

8. W. Bendick, K.H. Mayer, R.U. Husemann, T. Kern and R.B. Scarlin, 3rd Inter. Conf. on Trends in Welding Research, Gatlinburg, TN, USA, 1-5 June, 1992, Conf. Proc., ASM, edited by S. A. David and J. M. Vitek, 587-598.

9. T. Helander, H. Andersson and M.O. Skarsson, Structural Changes in 12-2.25% Cr Weldments-An Experimental and Theoretical Approach, Materials at High Temperatures, 17(3) 389-396.

10. D.J. Allen, Proc. of an Inter. Symposium on Case Histories on Integrity and Failures in Industry, Milan, Italy, 1999, 133-143.

11. D.J. Allen, Proc. EPRI Conf. On Welding and Repair Technology for Fossils Power Plants, Williamshurg, Virginia, March 1994, 128-134.

12. R. Prader, H. Cerjak and G. Nagel, Proc. of the 4th Inter. Conf. On Trends in Welding Research, 5-8 June 1995, Gatlinburg, Tennessee, USA, 1995, 247-251.

13. H. Cerjak, Proc. of the 4th Inter. Conf. On Trends in Welding Research, 5-8 June 1995, Gatlinburg, Tennessee, USA, 563-568.

14. X. Long, Transactions of the China Welding Institution, 2000,21(1), 53-56.

15. J.M. Vitek and S.A. David, Metall. Trans. A, Vol. 21A, 1990, 2021-2035.

CHAPTER 6:

Microstructure Characterization of High Cr Ferritic Steel Weldments

6.1 Introduction

This chapter is concerned a series of microstructures in the real weldments. Additionally it can be used to validate the Gleeble weld simulation results. Four high Cr steel weld materials, P91 (mod. 9Cr-1Mo), P92 (9Cr-0.5Mo-1.8W), E911 (9Cr-1Mo-1W), P122 (12Cr) , from the Nippon pipe and plate, were subjected to weld microstructure investigation. The Type IV zone (and soft zone) of the HAZ is studied in most detail.

6.2 Experimental Procedure

6.2.1 Materials and Welding Conditions

The materials are described in Table 6.1.

Table 6.1. Details of test materials

Experi. Code No.	Material	Status	PTC No	Manuf./ Supplier	MB ID/ Other	Comments
1#	E911	+ weld	KA1274		MR 01/036	Off cut 15-20mm along weld × 19 mm W/T specimen defective Sample size: 150 × 18 × 10mm
2#-1	P92/ NF616	Cast 1 Nippon pipe(parent metal)	KA1277		MET 16	Pipe size: 113 × 40mm thickness
2#-2		+weld +PWHT	KA1276		MR01/036	Macro after welding and PWHT + Gleebles T/P
3#-1	P92/ NF616	Cast 2 SFEL Bar (parent metal)	KA1279	SFEL	MET 20	120 × 120 × 120mm triangle ×160mm length
3#-2		+weld +PWHT	KA1278		MR 01/037	Bar size: 160 × 75 × 14mm
4#	P122/ HCM12A	Casting-weld-forging	KA1280	ABB/ SFEL	MR 01/040	Macro from "as received weld" Plate size: 165 × 60 × 10mm
5#-1	P91	As Received	027A			Plate size:155 × 25 × 10mm
5#-2	P91	Re N + T*	027B			155 × 25 × 10mm
5#-3	P91	Aged	027C			155 × 25 × 10mm

* re N + T: renormalized and tempered

Solution heat treatment and tempering conditions are shown in Table 6.2.

Table 6.2. Heat treatment for the parent materials

material	P91	P92	E911	P122
Manufacturing heat treatment	1040°C/5.5h/AC, 760°C/12h/AC	Nipponpipe:1040°C/3h/OQ,780°C/5h/AC SFEL Bar: 1070°C/ 15h/OQ, 770°C/14h/ AC	1060°C/1h/AC 760°C /2h/AC	1050°C/8h/AC, 670°C/14h/FC, 760°C/14h/AC

The chemical analysis for parent metals is gained in Table 6.3[1,2].

Table 6.3. Chemical analysis of parent metals

elements	P91	P92 Nippon Pipe SFEL bar		E911	P122
C	0.10	0.11	0.09	0.10	0.12
Si	0.22	0.32	0.02	0.21	0.20
Mn	0.47	0.51	0.51	0.30	0.68
P	0.013	0.009	0.010	0.010	0.009
S	0.008	<0.001	0.005	<0.005	0.007
Cr	8.34	9.12	8.98	9.24	11.07
Mo	0.93	0.45	0.51	1.11	0.35
Ni	0.16	0.24	0.09	0.21	0.31
Cu	n.d.	0.05	0.05	0.66	1.01
Nb	0.078	0.06	0.05	0.075	0.054
V	0.19	0.20	0.19	0.22	0.22
W	n.d.	1.80	1.89	0.99	1.94
Al	0.022	<0.005	0.011	n.d.	n.d.
O	n.d.	n.d.	n.d.	n.d.	n.d.
N	0.03	0.044	0.038	n.d.	0.055
Co	n.d.	n.d.	n.d.	n.d.	0.011

After preparation, the pipe or plate sample was preheated to 200°C, then was welded (groove filled or butt weld) using different welding methods (MAW or TIG process), the welding procedures can be seen from Table 6.4. The chemical compositions of the filler metals are given in Table 6.5.

Table 6.4. Welding procedures

Material	P91	P92	E911[5]	P122[6]
Weld proc.	MMA buttering/weld pads; Consumables: Metrode Chromet 9MV,4mm,batch WO15308; Heat input: average 1.95kJ/mm; Preheat: 200°C; Max. interpass: 300°C (in practice <260°C); Weld preparation: 90° sidewall angle; Hold 4h at≥200°C, then cool to 20°C on completion	**Nippon Pipe[3]** MMA buttering weld; Consumables: BWP M2W, 4mm dia. (batch × 546); Heat input: 0.92kj/mm; Preheat:200°C; Max. interpass: 300°C; Weld preparation: 15° sidewall angle; Cool to 100°C on completion. **SFEL Bar[4]:** MMA groove fill weld. Heat input:1.2kJ/mm	TIG/MMA groove fill weld (MMA passes creep tested); Consumables: Bohler Fox C9MVW, 302mm dia.; Heat input: 0.94kj/mm; Preheat: 200°C; Max. interpass: 300°C; Weld preparation: Groove 15° sidewall angle; Cool to 200°C min on completion	MMA horizontal-vertical butt weld; Consumables: Safdry CDV92 (P92 type), 5mm dia. (fill passes); Heat input: 1.8kj/mm; Preheat: 200°C; Max. interpass: 300°C; Weld preparation :10° sidewall angle (cast side, lower), 35-40° sidewall angle (forgeing side, upper); Cool to 150°C on completion

Table 6.5. Chemical analysis of filler metals

elements	P91	P92	E911	P122
C	0.086	0.082	0.12	0.09
Si	0.28	0.36	0.32	0.27
Mn	1.04	0.79	0.77	1.10
P	0.007	0.015	0.011	0.010
S	0.010	0.009	0.007	0.007
Cr	8.50	8.52	8.84	9.10
Mo	1.04	0.53	0.84	0.50
Ni	0.24	0.44	0.70	0.41
Cu	0.05	0.04	0.04	0.02
Nb	0.079	0.07	0.06	0.057
V	0.22	0.23	0.16	0.20
W	0.010	1.71	0.90	1.54
Al	0.009	<0.01	n.d.	0.002
O	n.d.	n.d.	0.066	n.d.
N	0.044	n.d.	0.041	0.043
Co	n.d.	n.d.	n.d.	0.002

After this welding the samples were given a standard post weld heat treatment followed by air cooling (Table 6.6).

Table 6.6. The PWHT details

material	P91	P92	E911	P122
PWHT	**As received**: no further heat treatment; **Re N + T :** 1060°C/2h/AC/ 760°C/1h/AC; **Aged**: 760°C/30h	Soak 765°C+/- 10°C/3h; Above 400°C max heating and cooling rates: 100°C/h	Ramp up 100°C/h; Soak 750°C+/- 10°C/ 50mins/AC	Soak 750°C/8h

The macrostructure and geometry of the welds to be investigated are illustrated in Fig.6.1.
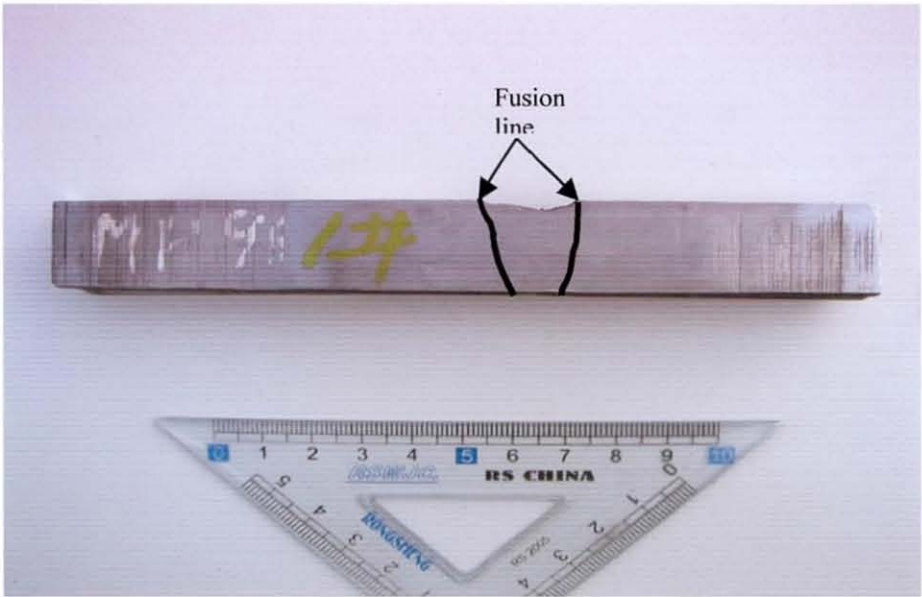
1# (E911)
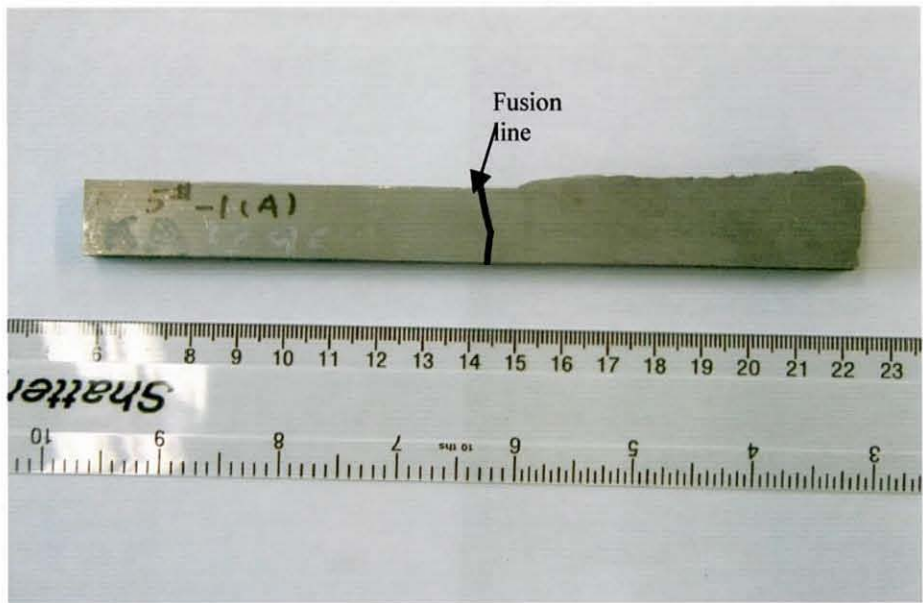
$5^{\#}$-1 (P91)

Fig. 6.1. Materials examined

6.2.2 Hardness Testing

In order to quantify different regions of the weld, microhardness (Hv30) measurements were conducted transversely across the weld.

6.2.3 Microstructure observation

Specimens were mounted and polished down to 1μm, then etched at room temperature using an etchant of 100 ml dist. H_2O, 5 ml of HNO_3 and 1 ml of HF. The etching time was about 20 seconds.

6.3 Results

6.3.1 Hardness and Profile

The resulting hardness values and the profile across the multilayer weld are depicted in Table 6.7 and Fig. 6.2 respectively.

113

Table 6.7. Hardness testing results

Sample No.	Hardness profile, Hv30	Average value and RSD	Comments
1#	240,237,244,239,238,236,*237,226,221,244,* **264,255,253,262,265,265,264,264,***234,224,* *223,233,*237,240,238,242,246,239,237,232, 231,240		The figures in bold and are supposed to be the values in the weld zone and the HAZ zone respectively, they are in line with the macro pictures
2#-1	216,223,223,224,224,224,233,227,223,223, 224,220,223,223,234,224,223,224,224,226, 224	224, 1.7%	
2#-2	**261,261,265,263,263,268,262,262,257,263,** *241,214,197,212,209,*216,219,212,211,215, 213,216,217		
3#-1	210,200,226,207,219,215,226,222,218,212, 215,203,215,205,207,216,219,228,212,219, 221,210,206,216,210,211,214,202,200,216	213, 3.7%	
3#-2	209,195,198,200,191,194,194,194,198,194, 198,202,*192,191,189,189,191,206,222,***248,** **241,242,243,252,245,258,250,266,271,260,** **262,263,255,260,270,252,252,246,247,***234,* *227,189,194,189,191,184,191*		
4#	226,226,226,231,230,228,227,226,227,*221,* *212,223,234,***258,252,236,233,235,224,232,** **229,229,231,236,255,***215,209,214,220,223,* *221,*224,220,226,229,225,224,224		
5#-1	**248,242,248,250,244,245,246,242,240,238,** **237,240,238,***188,184,185,189,195,194,191,* *192,192,192,193,198,194,192,192*		
5#-2	**252,252,248,244,252,261,256,258,254,252,** **252,253,251,***224,216,200,201,207,210,209,* *211,211,208,211,212,212,216,214,214,214,* *217*		
5#-3	**243,240,245,242,246,245,234,236,244,249,** *228,214,185,176,179,181,185,185,188,184,* *188,187,188,187,191,189,189*		
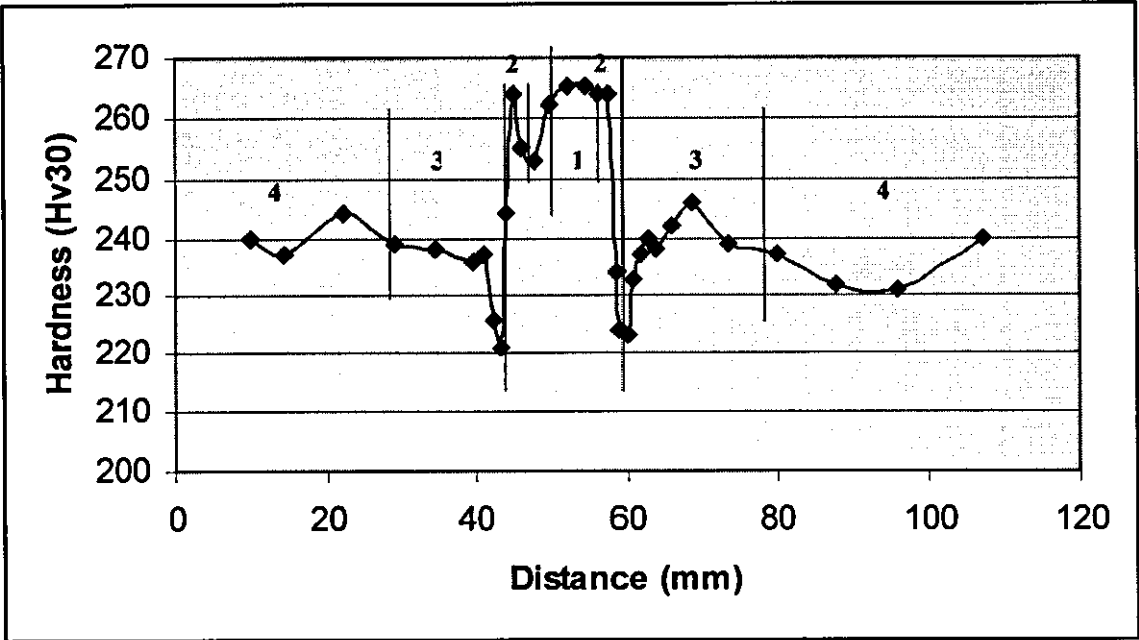
1[#] (E911)
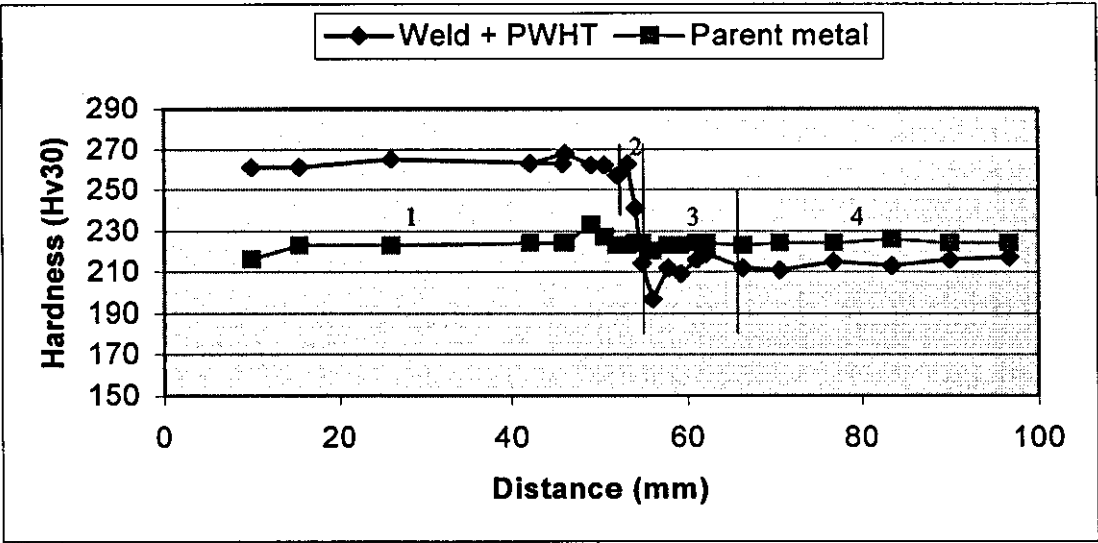
2[#] (2[#]-1 and 2[#]-2) (P92)
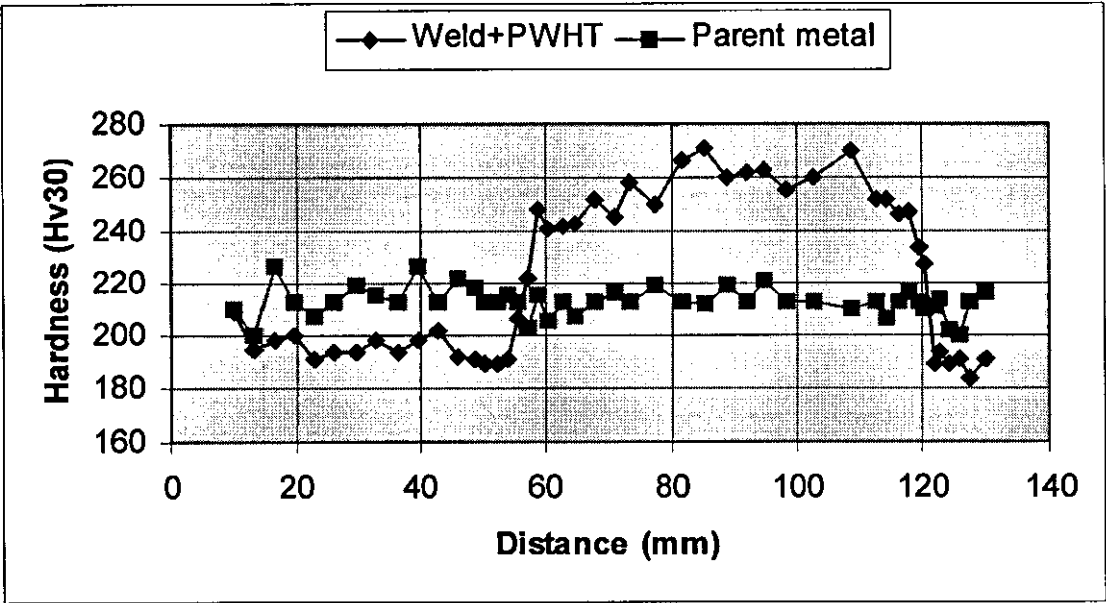
$3^{\#}$ ($3^{\#}$-1 and $3^{\#}$-2) (P92)
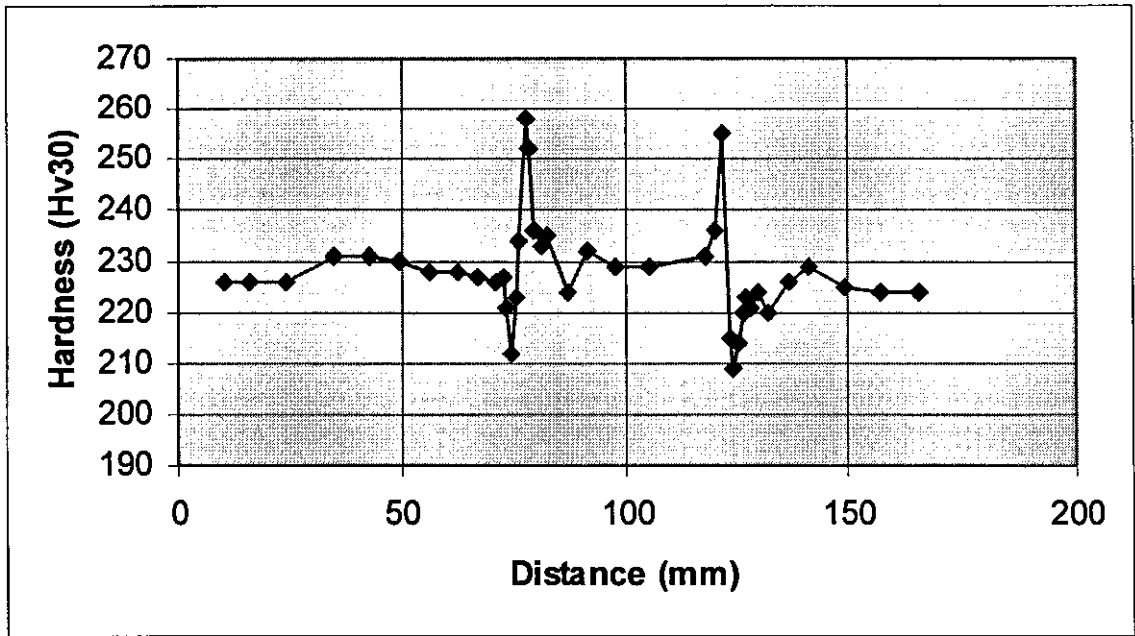
$4^{\#}$(P122)
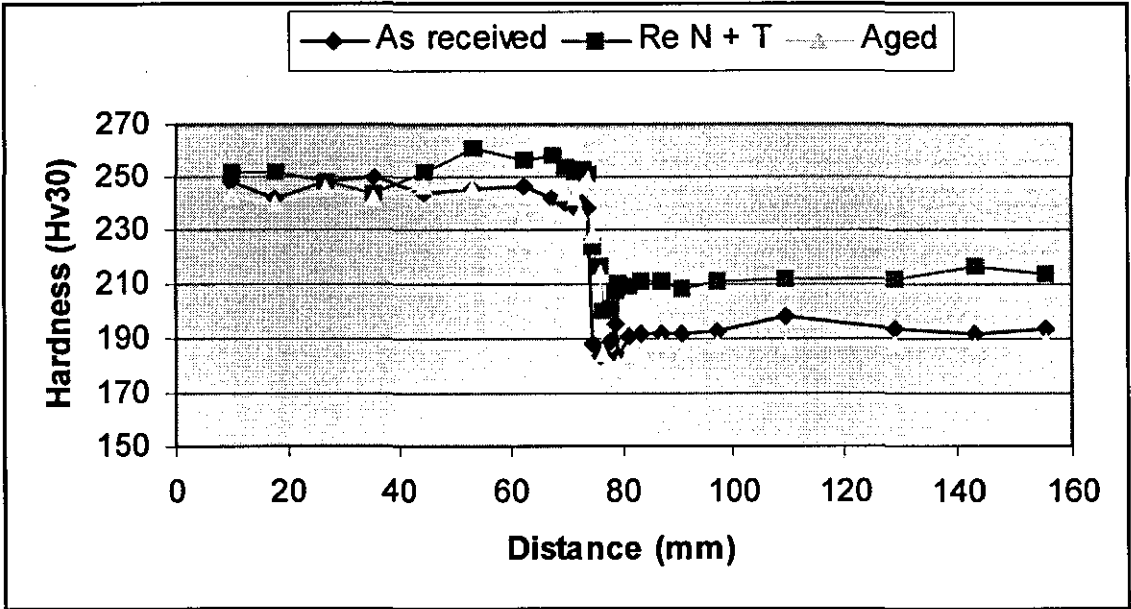
$5^{\#}$ ($5^{\#}1$, $5^{\#}2$ and $5^{\#}3$) (P91)

Fig. 6.2. Hardness profile traverse across weld

1 = weld metal, 2 = retransformed part of HAZ, 3 = soft zone, 4 = parent metal

It can be seen from Fig 6.2 that the hardness is relatively constant across the weld for specimen $1^{\#}$, $2^{\#}$, $3^{\#}$ and $5^{\#}$, but a lower hardness platform appears in the weld for sample $4^{\#}$. Outside the weld the hardness decreases linearly across the HAZ, a hardness minimum in an area adjacent to the unaffected parent metal can be observed. So a weld sample can usually be divided into four different regions as follows[7,8]:

1 = fusion zone (weld metal)

2 = retransformed zone of the HAZ, which include two regions: coarse grained zone
    (CZ) and fine grained zone (FZ)

3 = soft zone

4 = unaffected zone (parent metal)

The hardness surveys of test pieces in the as-welded (AW) and post weld heat treated (PWHT) conditions demonstrated that the weld metal and HAZ zone in high Cr ferritic steels were very resistant to a post weld tempering heat treatment at $750^{\circ}C$, there being hardly any decrease in hardness on moving from the AW to the PWHT condition, the peak figures being measured at around 270Hv in both coarse grained zone (CZ) and weld metal. The failure position in the HAZ is associated with the hardest part of CZ and the softest part of the fine grained zone (FZ) (180Hv). The PM hardness was slightly reduced from 220Hv to 210Hv on moving from AW to heat treated condition. The hardness measurements are in agreement with the values in previous reports[9, 10].

6.3.2 HAZ Width

The HAZ width measurements are taken from the HAZ profile in Fig. 6.2 with a combination of the across HAZ hardness testing. The HAZ width values are given in Table 6.8

Table 6.8. The HAZ width measurements

Materials		HAZ width*, mm	Average, mm
1[#]		2.0,2.2,2.2,2.3,2.3,2.3,2.3,2.2	2.2
2[#]-2		2.1,1.9,2.0,2.1,1.6,2.1,1.7,1.8,2.3	1.9
3[#]-2		1.5,2.4,2.1,2.0,2.0,2.0,2.0	2.0
4[#]	LHS[#]	Measurements were made based on the	2.0
	RHS	microstructure difference under 500×	2.0
5[#]		1.5,1.6,1.9,1.8,1.8,1.7,2.0	1.8

* measurement was taken from one side (left) HAZ zone under x20 macro magnification , another side should be same.

LHS- measurements from left side (casting side); RHS-from right side (forging side).

From the table it can be seen that the width of HAZ is almost constant (about 2mm), and is not affected very much by the welding process or the weld width.

6.3.3 Microstructures

6.3.3.1 Weld metal

The weld microstructures in $1^\#$, $2^\#$, $3^\#$, $4^\#$ and $5^\#$ specimens are shown in Fig. 6.3.

a)

b)

c)

d)
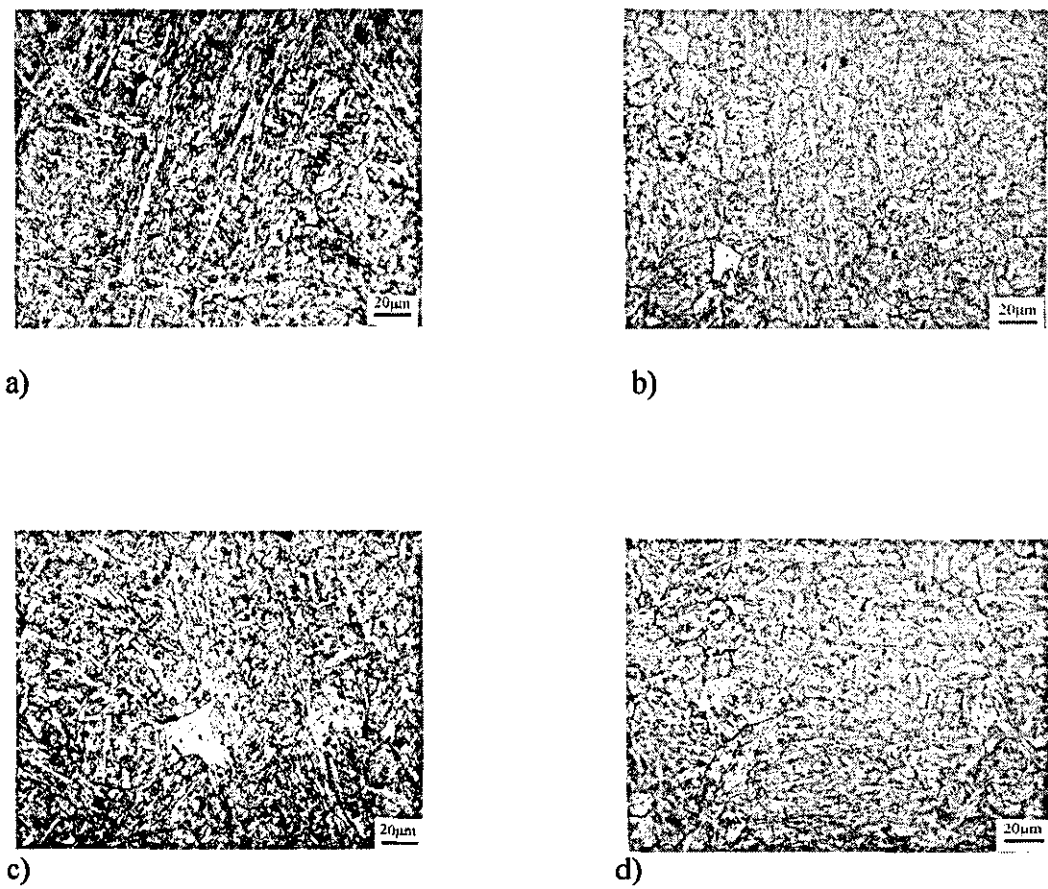
e)

Fig. 6.3. Optical micrographs of five weld metals after PWHT

a)weld 1$^#$, b) weld 2$^#$, c) weld 3$^#$, d) weld 4$^#$, e) weld 5$^#$

In sample 1$^#$ (E911), it is mostly martensite (mixture structures of martensite and austenite) in weld metal, no δ ferrite was found.

In sample 2$^#$ (P92), some lath martensites can be seen; it was found that more lath martensite recrystalized microstructures which are called ferrite (Fig. 6.4).

Fig. 6.4. The blocky ferrite in P92 weld(2$^#$)

In sample 3[#] (P92), the microstructures are similar with sample 2[#] as they are both P92 materials; similarly there are large amounts of δ-ferrite in the weld metal which are dispersed inhomogeneously and are locally seriously agglomerated (Fig. 6.5). Several long grain boundary-like bands exist along the welding bead direction (Fig. 6.6).

In sample 4[#] (P122), which is a casting-weld-forging material, both sides (cast side: C and forged side: F) were studied; the weld microstructures are quite similar, however towards the forged side (F), more clear grain structures can be seen (Fig. 6.7); meanwhile there is a very small amount of δ-ferrite found in the forged side weld metal (Fig. 6.8).
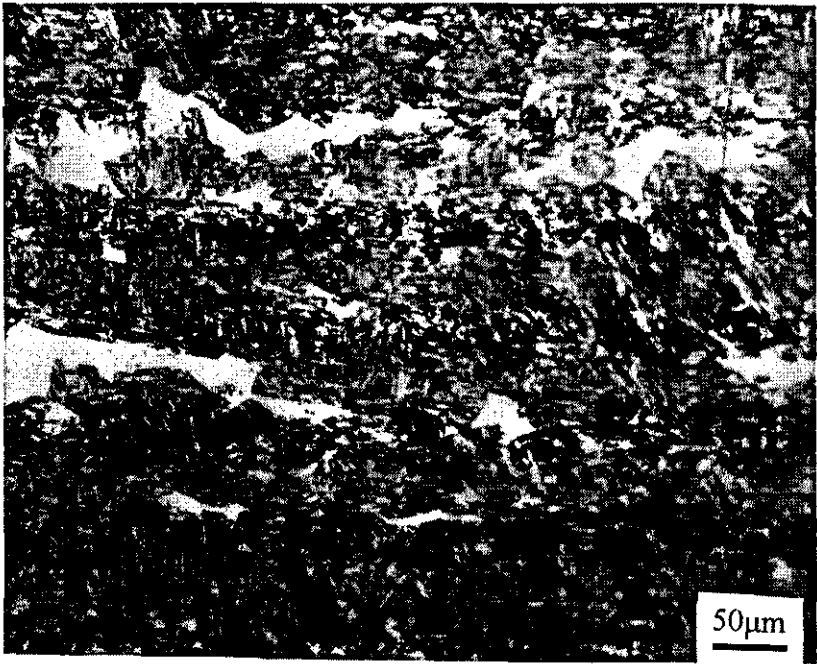
Fig. 6.5. The rich δ-ferrite area in 3[#] (P92)

20μm
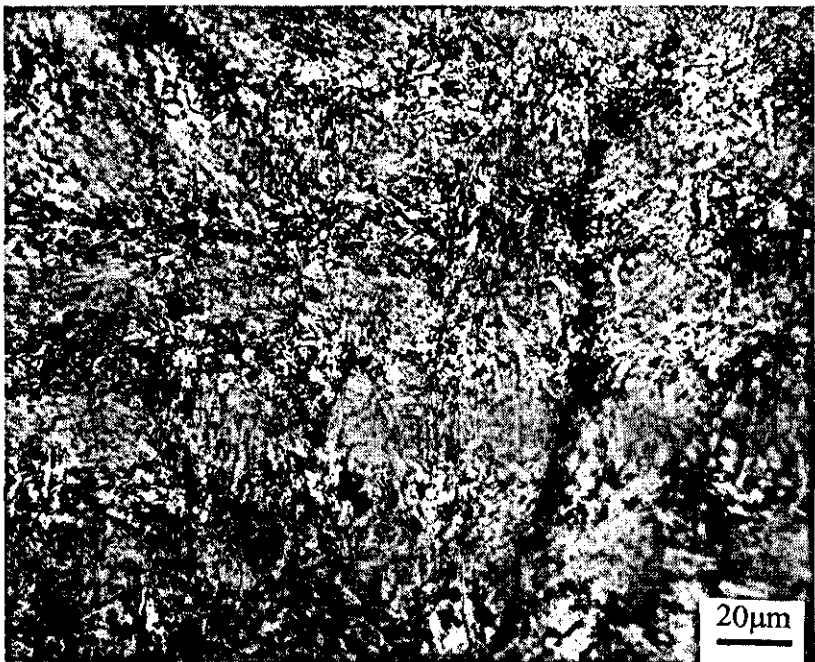
Fig. 6.6. Band in weld of sample 3# (P92)

20μm
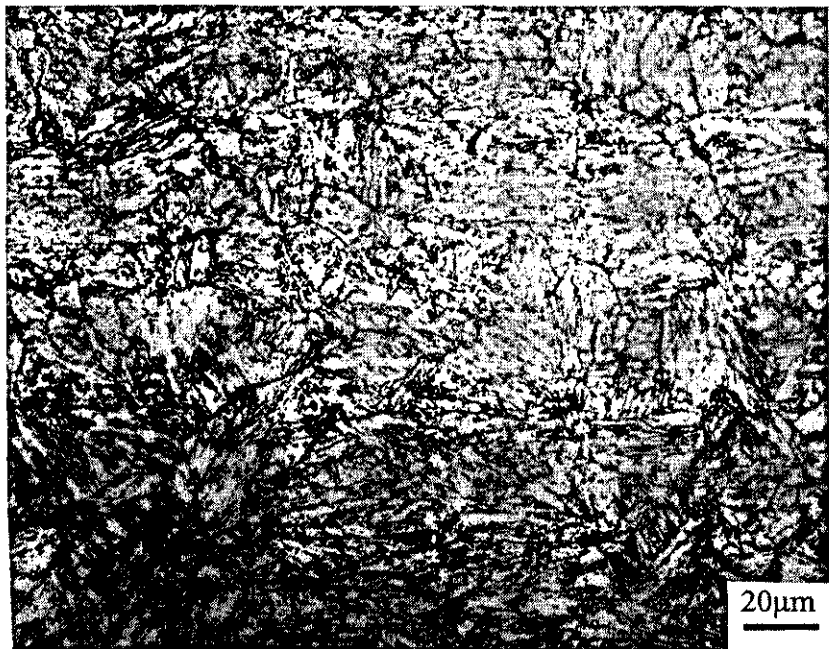
Fig. 6.7. Microstructure of WM in cast side of sample 4#(P122)
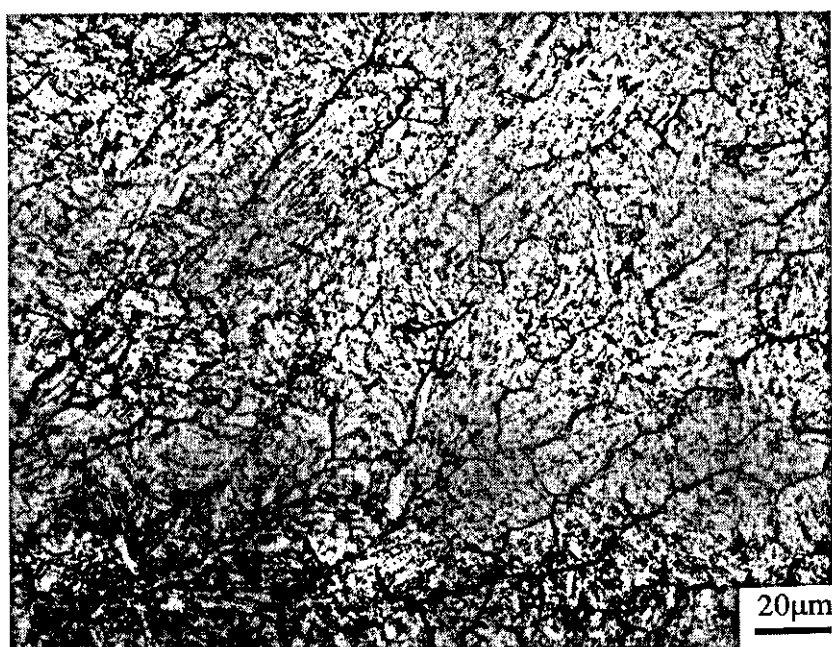
Fig. 6.8. Microstructure of WM in forged side of sample 4$^{\#}$ (P122)

In sample 5$^{\#}$ (P91), three different heat treated materials (as received: 5$^{\#}$-1, re N+T: 5$^{\#}$-2 and aged: 5$^{\#}$-3) were compared. It is clear that the weld microstructures in all three conditions are martensitic. However it can be seen that the structures are not quite homogeneous in sample 5$^{\#}$-1 and 2 (Fig. 6.9); a large number of parallel black lines appeared (Fig. 6.10), and are disconnected and agglomerated in local areas (Fig. 6.11), while there are few black lines in sample 5$^{\#}$-3. The black lines could very possibly be pearlite which needs to be identified further using transmission electron microscopy (TEM). The pearlite consists of many laminated layers of ferrite and cementite. This layer is much thinner than the martensite lath. The flaky pearlite can be sphericized by fracture of cementite and diffusion of carbon below Ac$_1$ temperature.

Fig. 6.9. Inhomogeneous WM microstructures in 5$^{\#}$-1(P91)
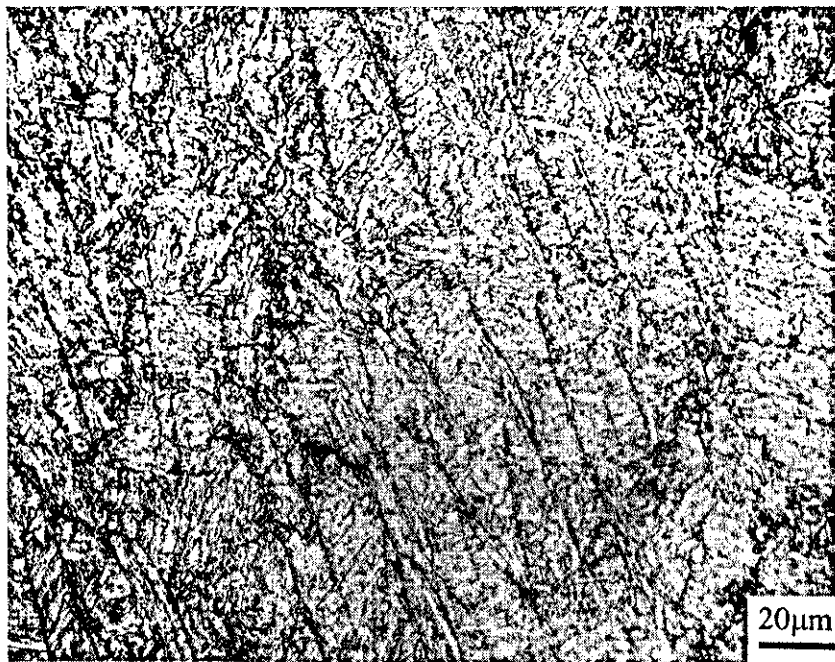
Fig. 6.10. The black bands in sample 5$^{\#}$-2 (P91)
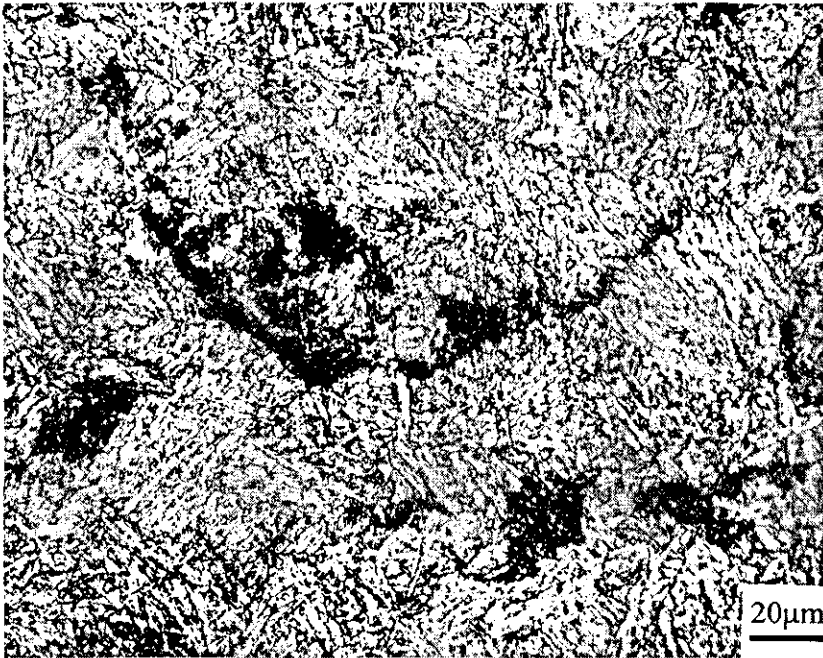
Fig. 6.11.The disconnected and agglomerated lines in WM of P91 (5#-2)

Some coarse carbide precipitates can also be seen on the martensite lath boundary and the prior austenite grain boundaries; these are $M_{23}C_6$. Meanwhile the fine precipitates inside the blocky ferrite could be MX. The unclear lath boundaries are a result of the recrystallization at PWHT temperature.

6.3.3.2 HAZ and Type IV zone

In the HAZ zone, there is clearly a narrow fine equiaxed grain zone which is the retransformed region. Fig.6.12 shows the microstructures of the retransformed zone (region 2 in Fig. 6.2) in all five weld metals.

a)

b)

c)

d)

e)
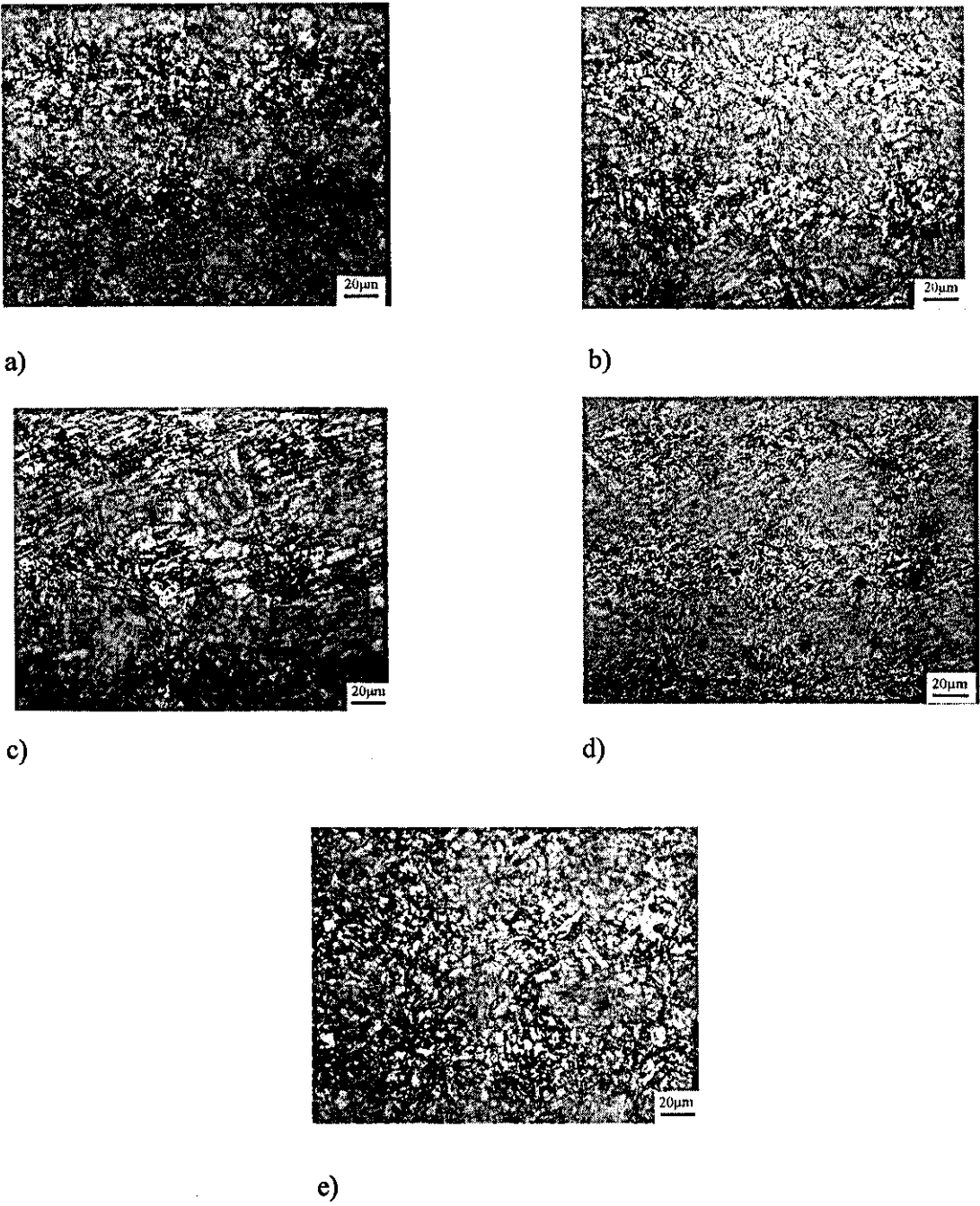
Fig. 6.12. Optical micrographs of HAZ of five weld metals after PWHT
a) weld 1[#], b) weld 2[#], c) weld 3[#], d) weld 4[#], e) weld 5[#]

In sample 1[#], the fine grain structures appear more uniform across the whole HAZ region (Fig. 6.13)

a)   b)
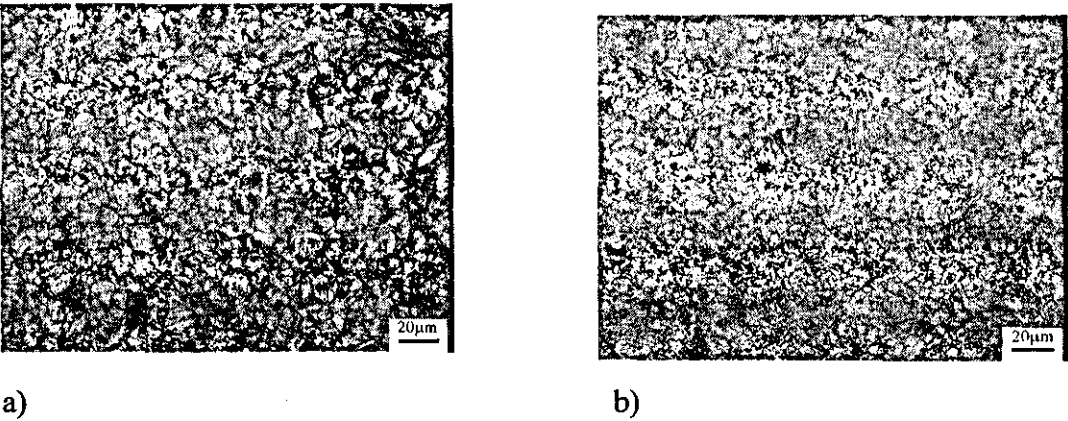
Fig. 6.13. Micrographs of HAZ in sample 1[#] (E911)
    a)close to WM, b)close to PM

In sample 2[#], Fig. 6.14 shows the HAZ microstructure, in which there was no big change across the region.

a)   b)
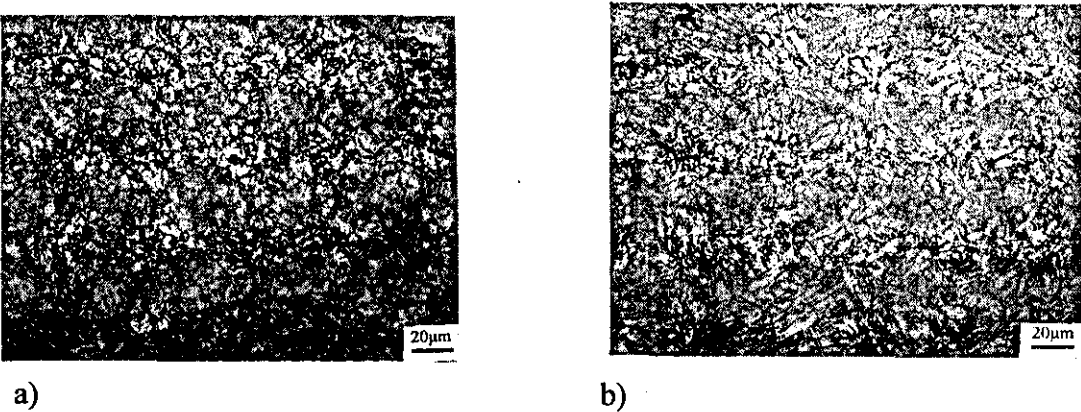
Fig. 6.14. Micrographs of HAZ in sample 2[#] (P92)
    a)close to WM, b)close to PM

In sample 3[#], the grains seem to be more rounded (Fig. 6.15) in the region close to the WM, and continuously networked δ-ferrite which are parallel with the fusion boundary are formed (Fig. 6.16).

a)

b)
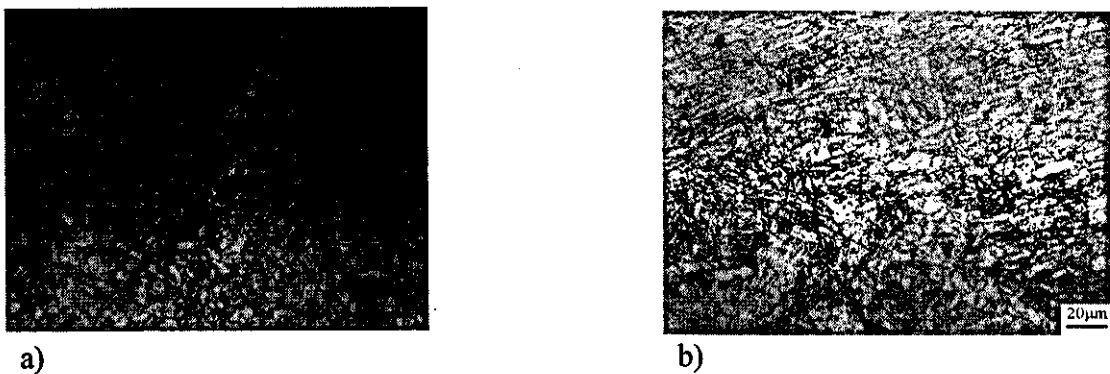
Fig. 6.15. Micrographs of HAZ in sample 3$^{\#}$ (P92)

a)close to WM, b)close to PM
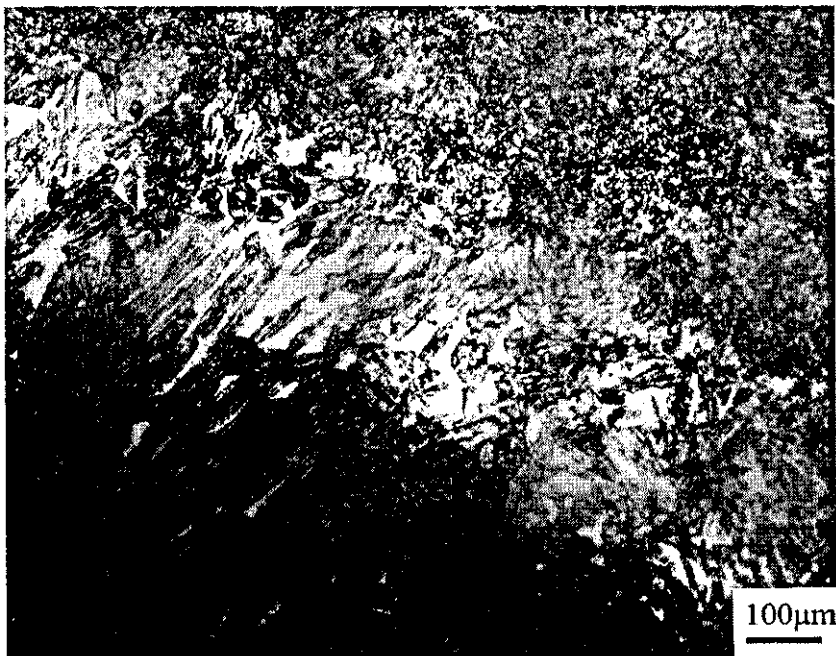
Fig. 6.16. The δ-ferrite band in the HAZ close to WM in sample 3$^{\#}$(P92)

In sample $4^{\#}$, there was no clear HAZ zone (only a WM-HAZ interface, no HAZ-PM interface) for both cast side $4^{\#}$(C) and forged side $4^{\#}$(F). However under high magnification, the structure interface will be distinguished clearly, the HAZ width was measured to 2mm. For the sample $4^{\#}$(C), in the region adjacent to the WM the grains are very fine (Fig. 6.17), with isolated blocky δ-ferrite (Fig. 6.18). And a fine grain structure is seen in the area close to PM (Fig. 6.17b)).

a)   b)
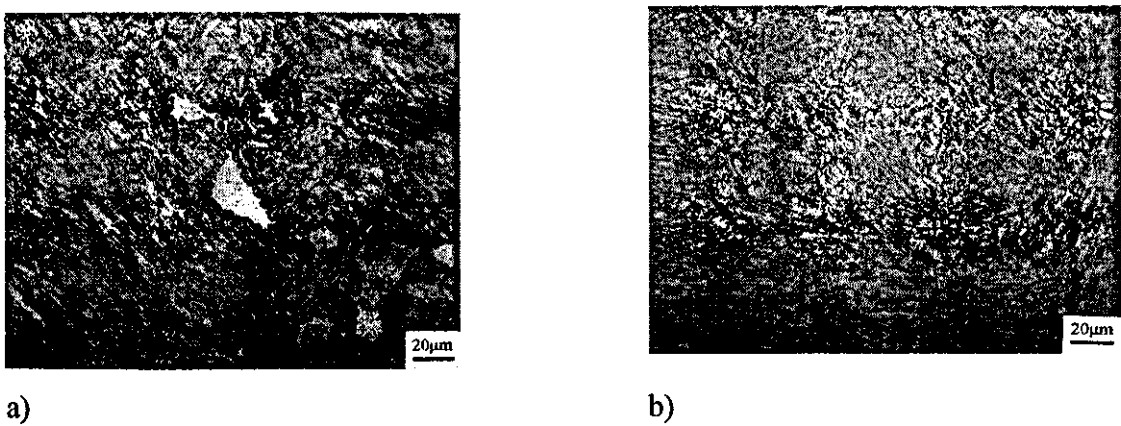
Fig. 6.17. Micrographs of HAZ in sample $4^{\#}$(C) (P122)

a)close to WM, b)close to PM
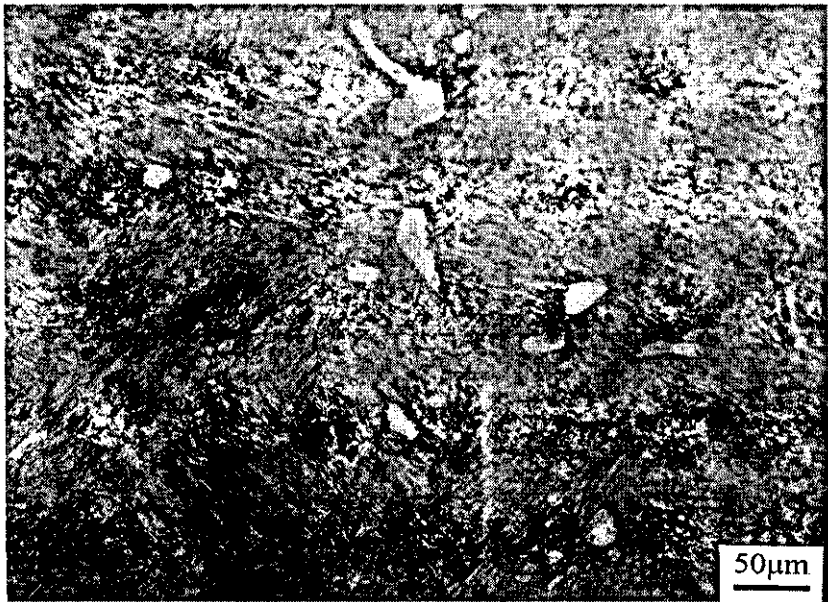
Fig. 6.18. The isolated block δ-ferrite in the HAZ close to WM in sample $4^{\#}$ (C)

For the sample $4^{\#}$(F), the situation is similar; the grains across the HAZ zone are very small. The only difference is that a δ-ferrite band perpendicular to the fusion line was found at the interface of WM and HAZ (Fig. 6.19).
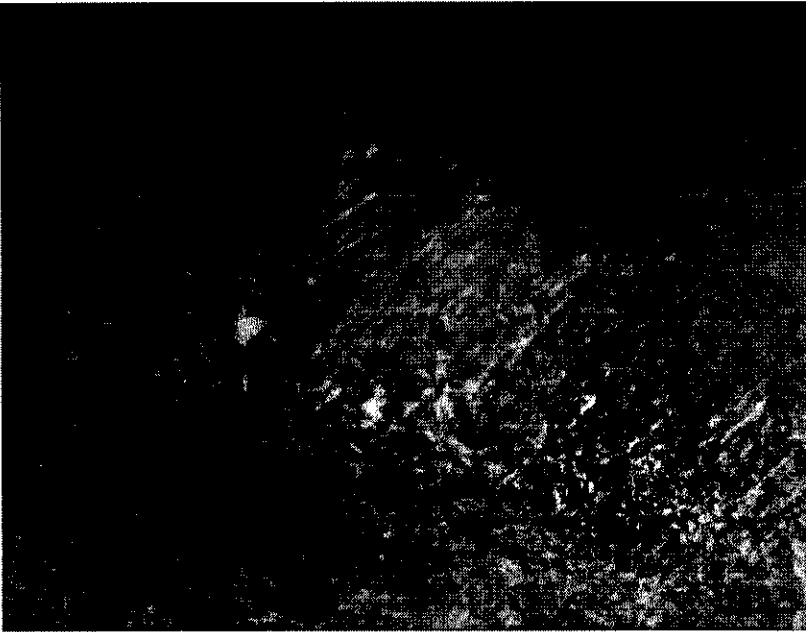
Fig. 6.19. The δ-ferrite band perpendicular to the fusion line was found at the interface
of WM and HAZ (sample $4^{\#}$) (P122)

In sample 5, it is clearly seen that there is fine grain layer in the reheated pass during multipass welding (Fig. 6.20 a)). The HAZ microstructures for P91 material under three conditions are shown in Fig. 6.21.

a)

b)
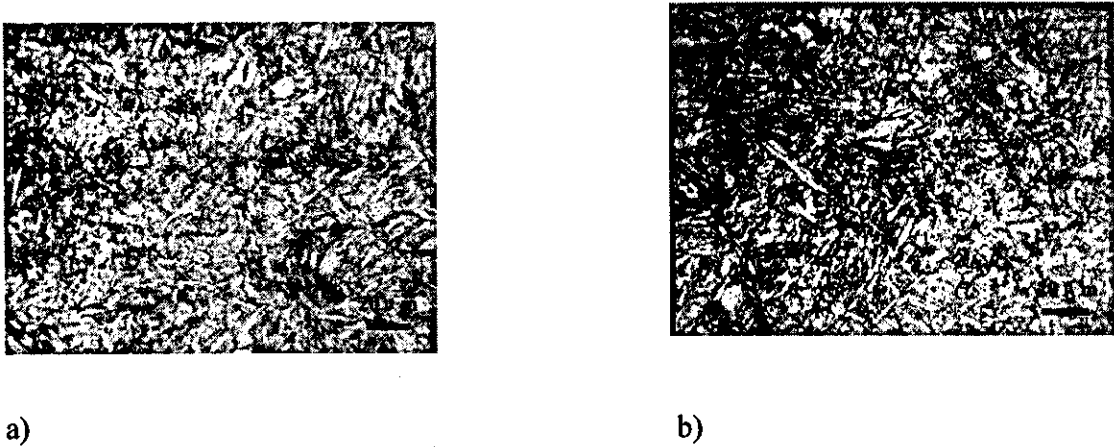
Fig. 6.20. HAZ interfaces in sample 5$^#$ (P91)

a)WM-HAZ (fine grains: left-lower corner/coarse columnar grains: right-upper side), b)HAZ-PM

a)
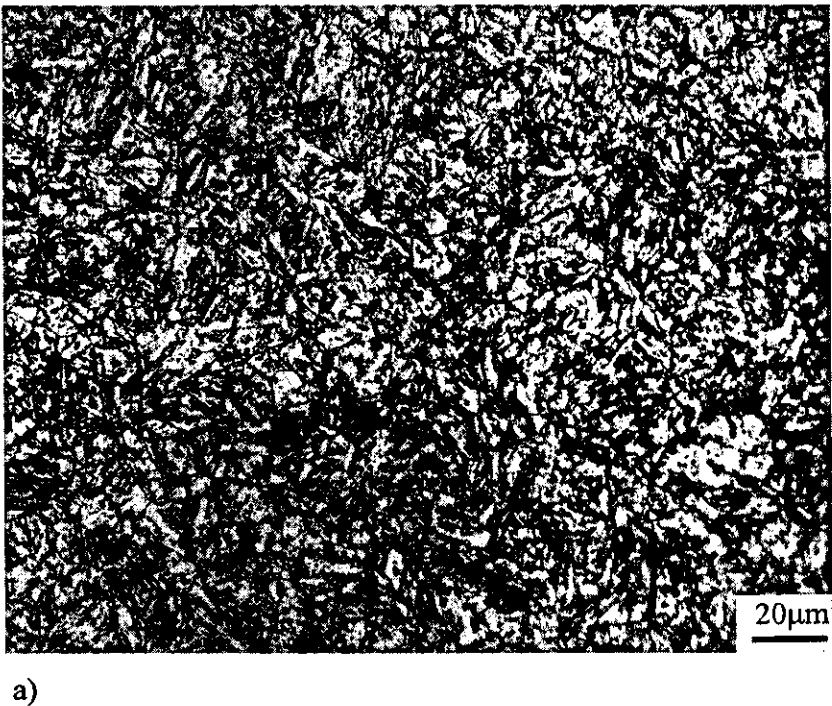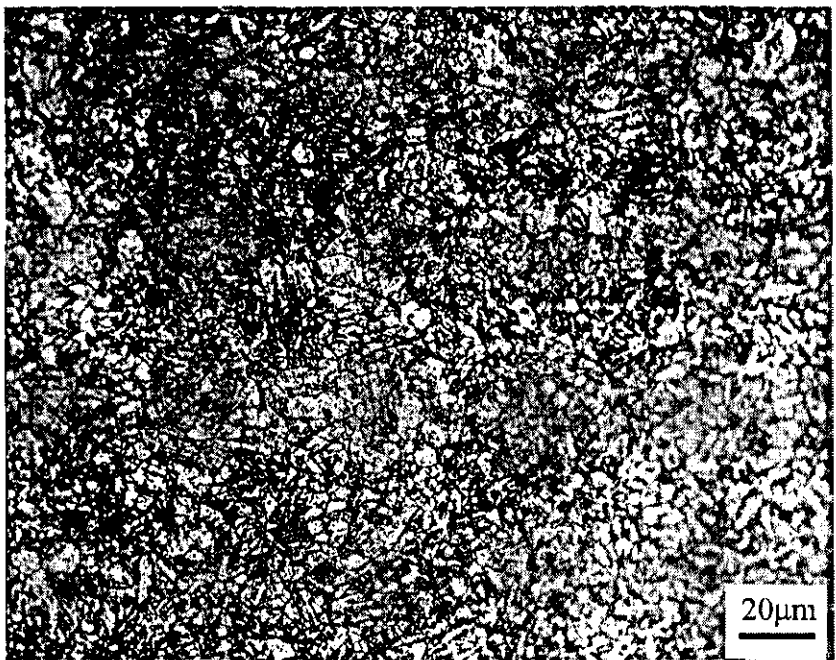
b)
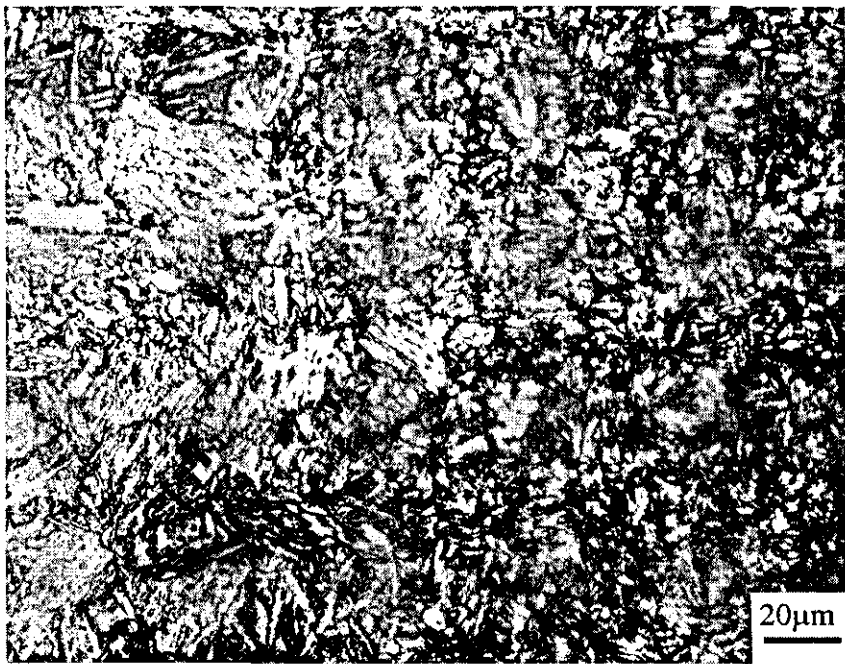
c)

Fig. 6.21. HAZ microstructures of P91 (5$^{\#}$)

a) as received (5$^{\#}$-1), b) re N+T(5$^{\#}$-2), c) aged(5$^{\#}$-3)

6.3.3.3 Soft zone

In sample 1[#], Fig. 6.22 shows tempered structures in the soft zone.
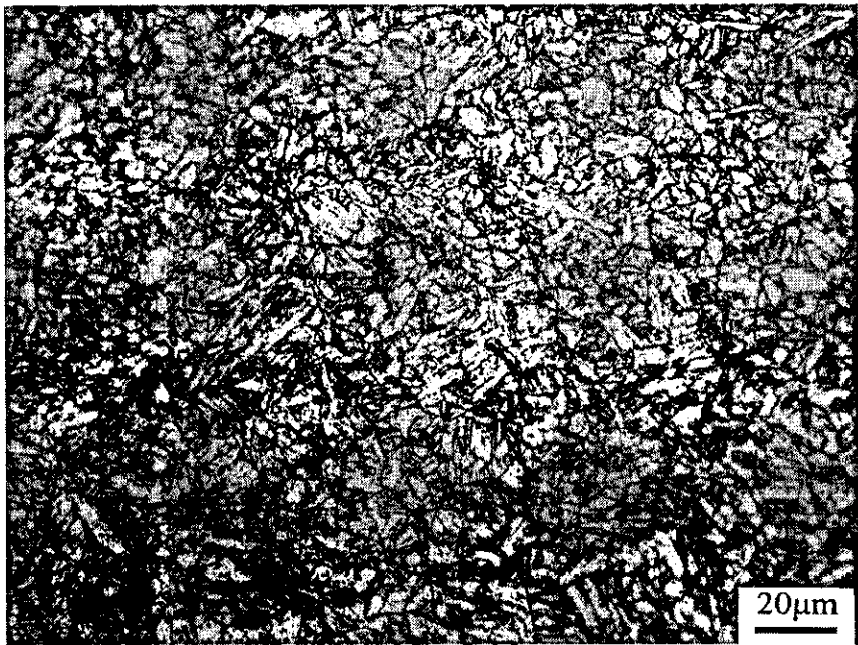
Fig. 6.22. Optical micrograph of soft zone of E911 (1[#])

In sample 2[#], Fig. 6.23 shows almost martensite structures in the soft zone.
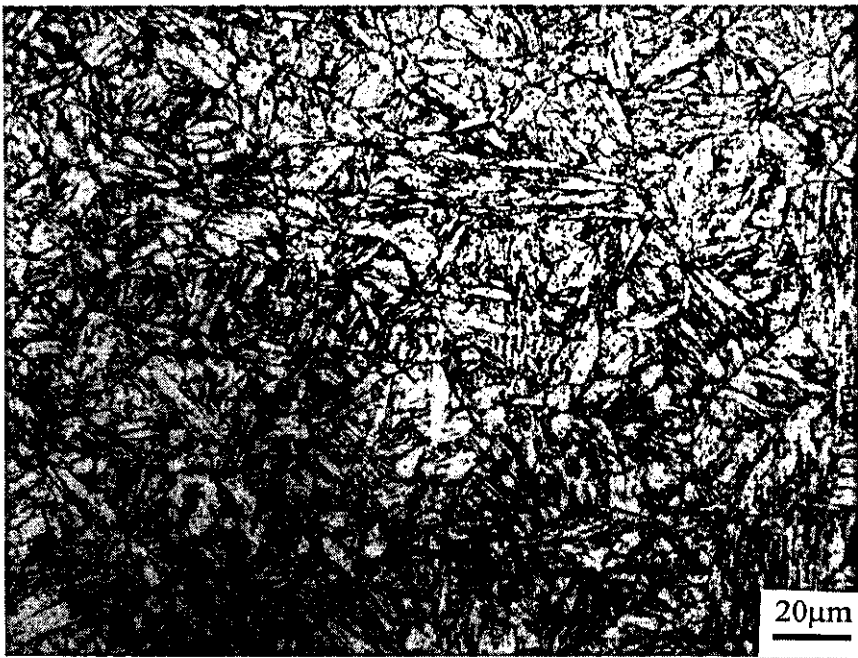
Fig. 6.23. Optical micrograph of soft zone of P92(2#)

In sample 3#, it is clear that martensite is formed in the soft zone (Fig. 6.24).
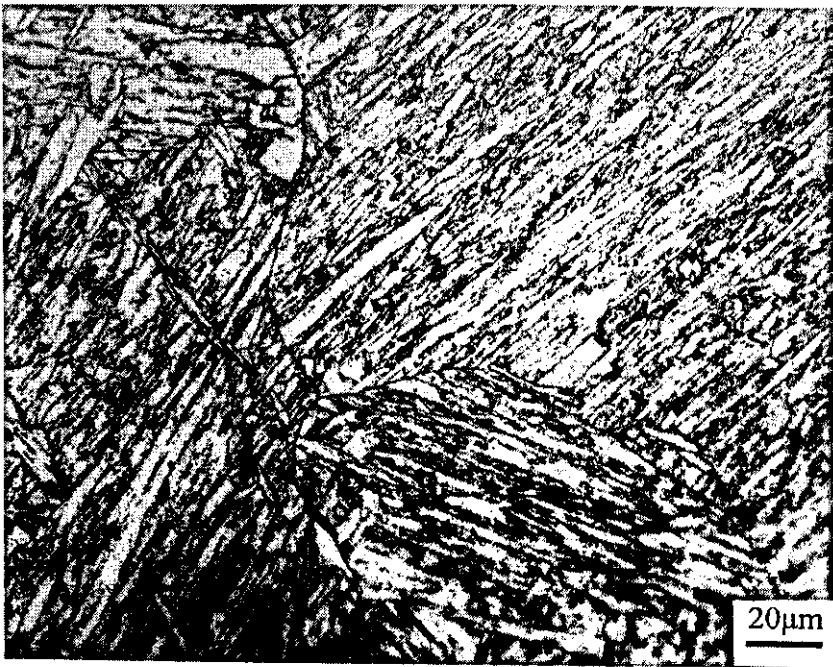
Fig. 6. 24. Optical micrograph of soft zone of P92 (3#)

In sample $4^{\#}$, both casting and forging sides have shown similar soft zone martensite microstructures (Fig. 6.25).

a)   b)
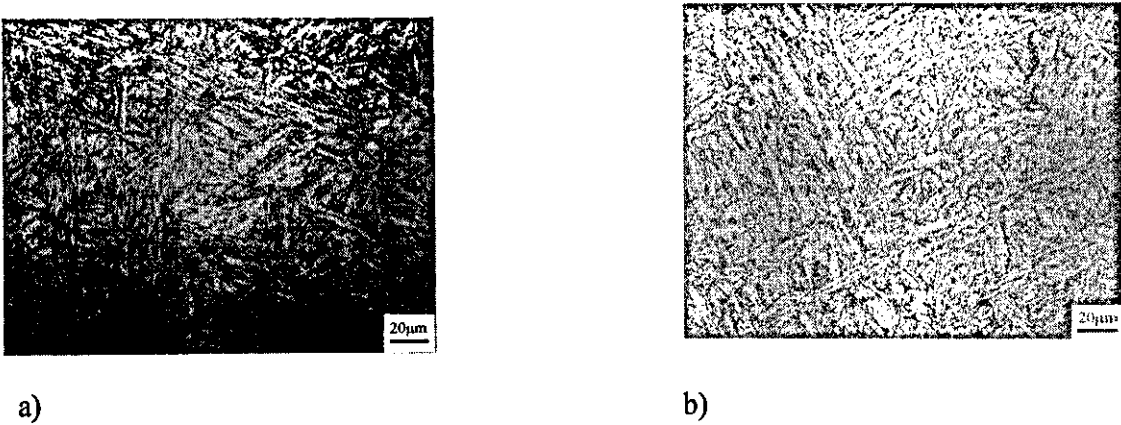
Fig. 6.25. Optical micrograph of soft zone of P122 ($4^{\#}$)

a)cast side, b)forged side

In sample 5, it seems that different microstructures in the soft zone under three heat treatments are produced; Fig. 6.26 indicates the fully lath martensite, and mostly short lath martensite for samples as received ($5^{\#}$-1), renormalization and tempered ($5^{\#}$-2) and aged ($5^{\#}$-3) respectively.

a)   b)   c)
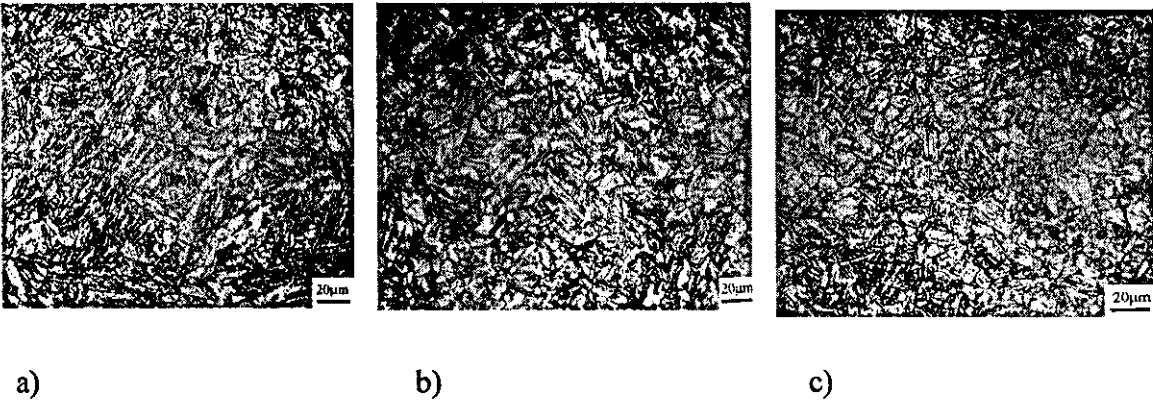
Fig. 6.26. Soft zone microstructures of P91 ($5^{\#}$)

a)as received ($5^{\#}$-1), b)re N+T($5^{\#}$-2), c)aged($5^{\#}$-3)

6.3.3.4 Parent metal

The microstructures in the parent metal have revealed big differences for all these different materials.

In sample 1[#], it is pure ferrite structure which is demonstrated in Fig. 6.27.
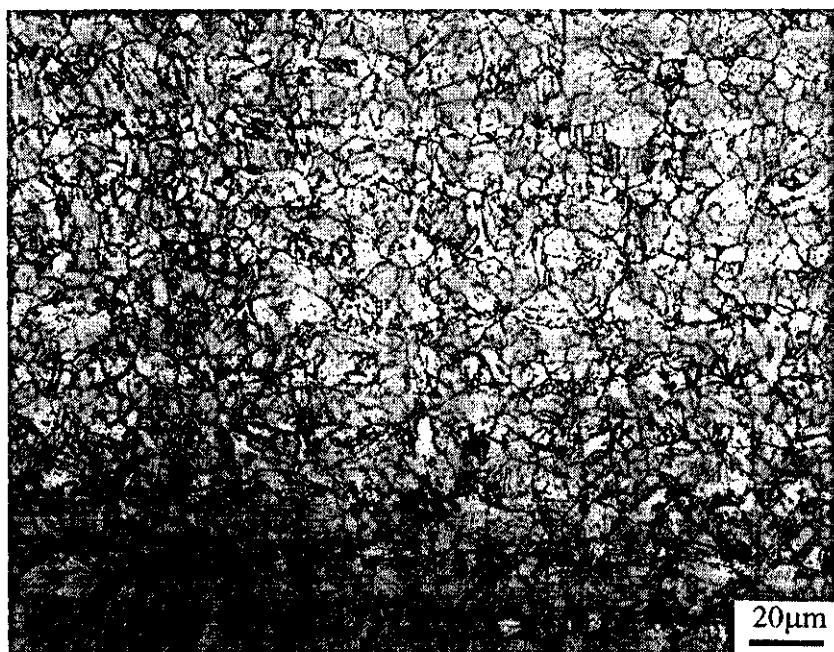
Fig. 6.27. Optical micrograph of parent metal of E911(1[#])

Sample 2[#] is martensitic (Fig. 6.28).
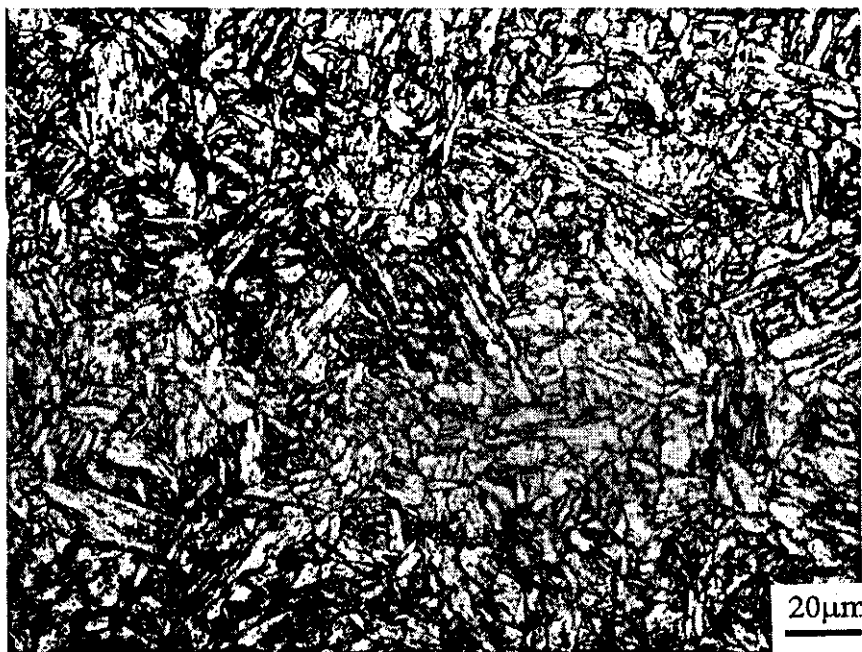
Fig. 6.28. Optical micrograph of parent metal of P92 (2#)

Sample 3# is fully lath martensite structure (Fig. 6.29), with a small amount of oval δ-ferrites (Fig. 6.30).

Fig. 6.29. Optical micrograph of parent metal of P92 (3#)
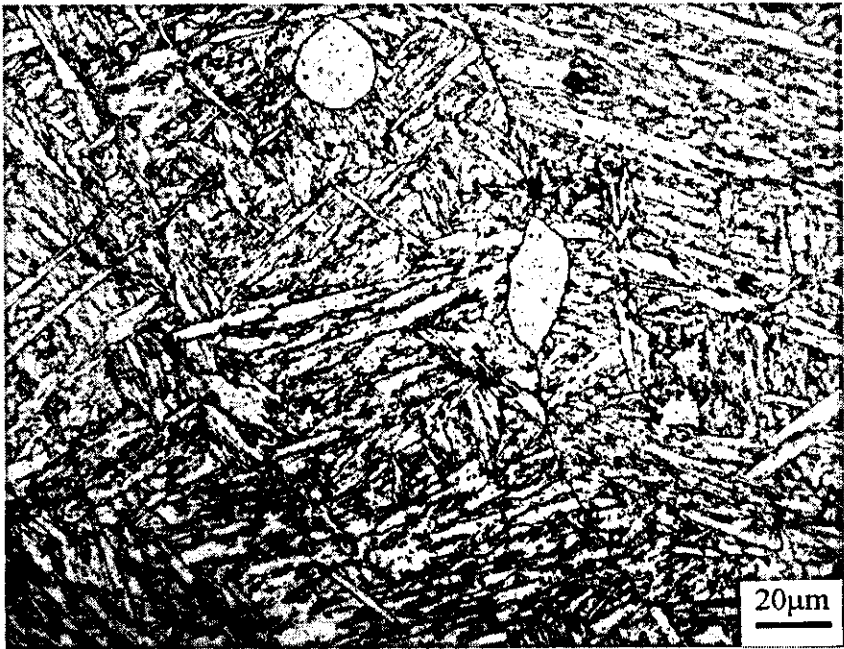
Fig. 6.30. The oval δ-ferrite in PM of P92 (3#)

In sample 4#, the fully lath martensites appeared in both cast and forged sides (Fig. 6.31), the difference is that there were very large amounts of oval δ-ferrites evenly dispersed in the cast side parent metal (Fig. 6.31 a), while no ferrite at all were found in the forged side part (Fig. 6.31 b).
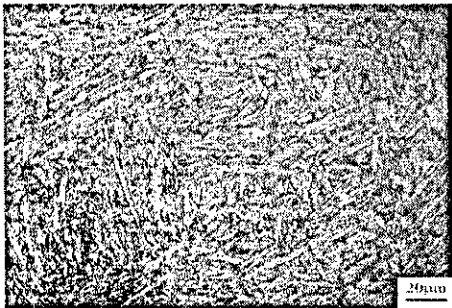
a)   b)

Fig. 6.31. Optical micrograph of parent metal of P122 (4#)

a) cast side, b) forged side

In sample $5^{\#}$, large difference exists under the three conditions (Fig. 6.32). The martensite laths after ageing for sample $5^{\#}$-3 seem shorter. However for the sample $5^{\#}$-1, the

a)   b)   c)
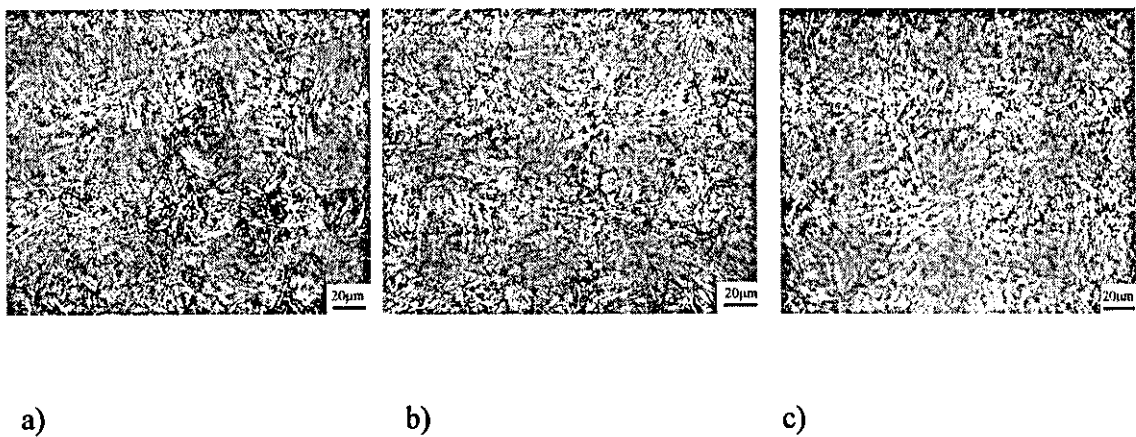
Fig. 6.32. Optical micrograph of parent metal of P91 ($5^{\#}$)

a) as received($5^{\#}$-1), b)re N+T($5^{\#}$-2), c) aged($5^{\#}$-3)

inhomogeneous etched structures can be seen clearly under low magnification (Fig. 6.33). They are divided into light and dark areas, and this is possibly because of the grain mis-orientation, Fig.6.34 shows the microstructures of the two different areas. Furthermore there exist a few continuously black lines in the area (Fig. 6.35). For the sample $5^{\#}$-2, the PM microstructures are more uniform, there are also no black bands found. For the sample $5^{\#}$-3, the microstructures tend to be inhomogeneous, which is again similar to sample $5^{\#}$-1.
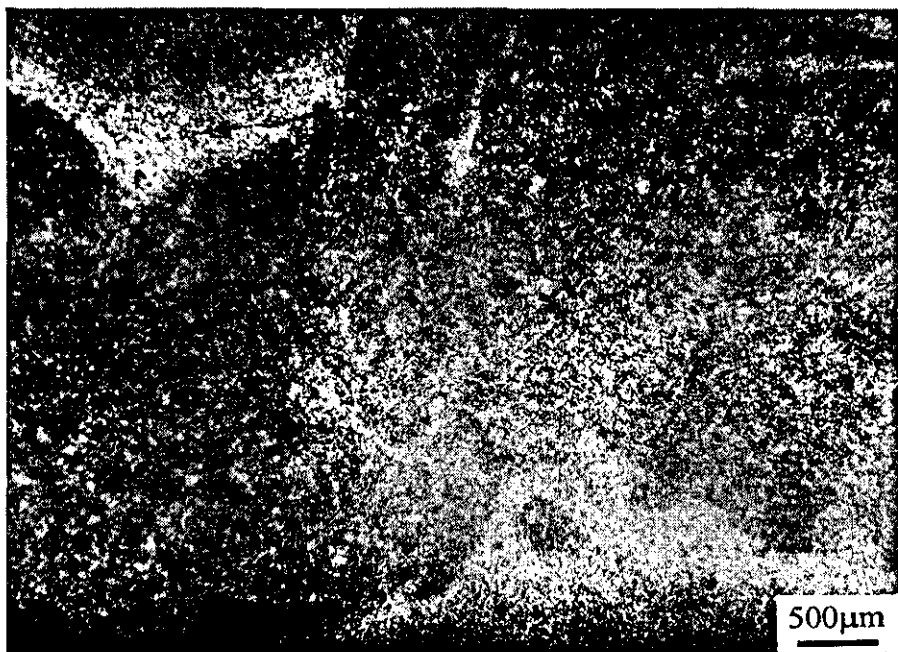
Fig. 6.33. The inhomogeneously etched structures at low magnification in P91(5$^{\#}$)

a)   b)

Fig. 6.34. Microstructures in the light and the dark area in PM of P91 (5$^{\#}$)

a)light area, b)dark area
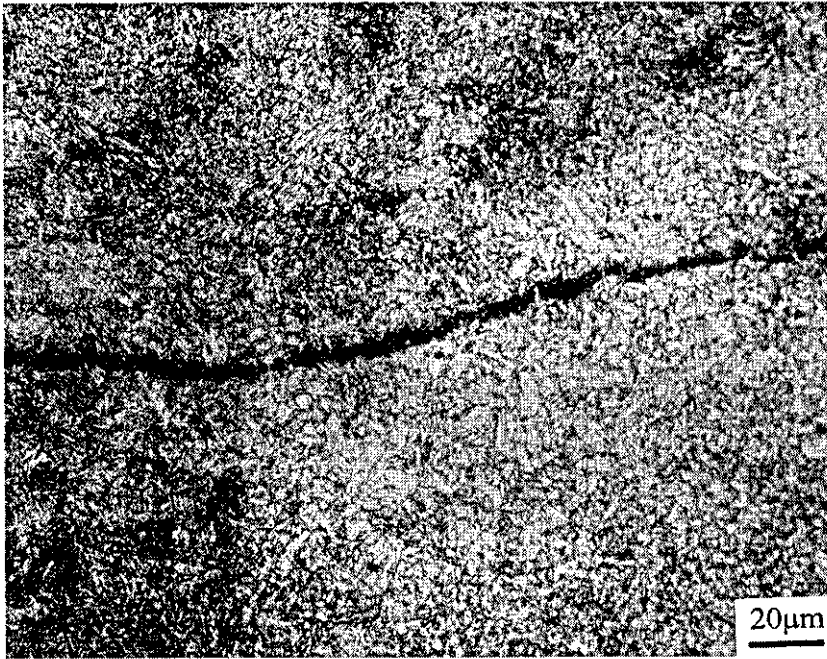
Fig. 6.35. The long lines in the PM of P91 (5$^\#$)

6.4 Discussion

6.4.1 Microstructural Analysis of Weld Metal

During MAW welding, the welding fusion pool temperature can be well above 1700°C. However the cooling time to interlayer temperature is just less than a minute. In this short time, the fusion pool has undertaken a very complicated chemical and metallurgical reaction and microstructural transformation, and has then been formed into weld metal. The very early transformation is the solidification of liquid fusion pool, which is related to the temperature gradient and the constitutional super-cooling, resulting in the formation of large columnar grains. As the temperature decreases further, the microstructure is transformed in the columnar grains; it will mainly result in martensite for modified high Cr steel weld metals. Because of the low carbon content, the martensite is low carbon lath martensite. After the transformation, there will still be a little residual austenite. For the multi-pass welding, the effects among each pass should also be

considered. The late-layer pass reheats the former layer pass, whereas the later layer pass acts as a heat treatment on the fore-layer pass. The heat treatment will make the fore-layer pass weld form a layer of fine equiaxed grains. The mechanism of the fine equiaxed grain formation is similar to that of the HAZ zone. Because the heating temperature is above Ac_3, martensite is transformed to austenite. A large amount of grain refining elements such as Mo, V, and Ti are present in solution. Therefore it is beneficial to provide nuclei for grain nucleation and also restrain the grain growth after nucleation. This leads to the formation of fine equiaxed grains, which are considered to improve the toughness. Hence a post weld heat treatment (PWHT) is good for weld integrity.

After welding, heat treatment is carried out which results in a series of changes in the weld microstructures, including martensite decomposition, transformation of residual austenite, carbide precipitation, and recovery and recrystallisation of lath martensite. Among these changes, the carbide precipitation is probably the most important factor as the microstructure stabilization and strengthening will mainly depend on carbide precipitation.

Much work has been carried out on the carbide precipitation in the high Cr steels during tempering[11-14]. It has shown that tempering at 650-700°C for 1 hour would have no influence on the dislocation structure and the morphology of lath martensite of the 9Cr-1Mo. A small amount of Cr-rich $M_{23}C_6$ is precipitated on the lath or prior austenite boundaries from 650°C to 700°C and the grains have grown from 0.03μm to 0.1μm. There is also very fine Cr_2C precipitation observed. When tempering at 760°C for 1 hour, the dislocation substructures start to rearrange and the lath morphologies of martensite also begin to change. The Cr_2C is precipitated at the beginning, and is then replaced by $M_{23}C_6$. Furthermore VC (V_4C_3) precipitates will grow as the tempering time extends.

The tempering procedure used in the experiment was 760 -780°C for 2.0-14 hours. The TEM micrographs showed that this produces $M_{23}C_6$ as the main precipitate in the weld metal. These coarse particles distribute along the lath martensite boundaries and the prior austenite grain boundaries. $M_{23}C_6$[15-21] is a face-centred cubic structure, and is able to

a)

b)

$$B=[255]$$

c)

d)
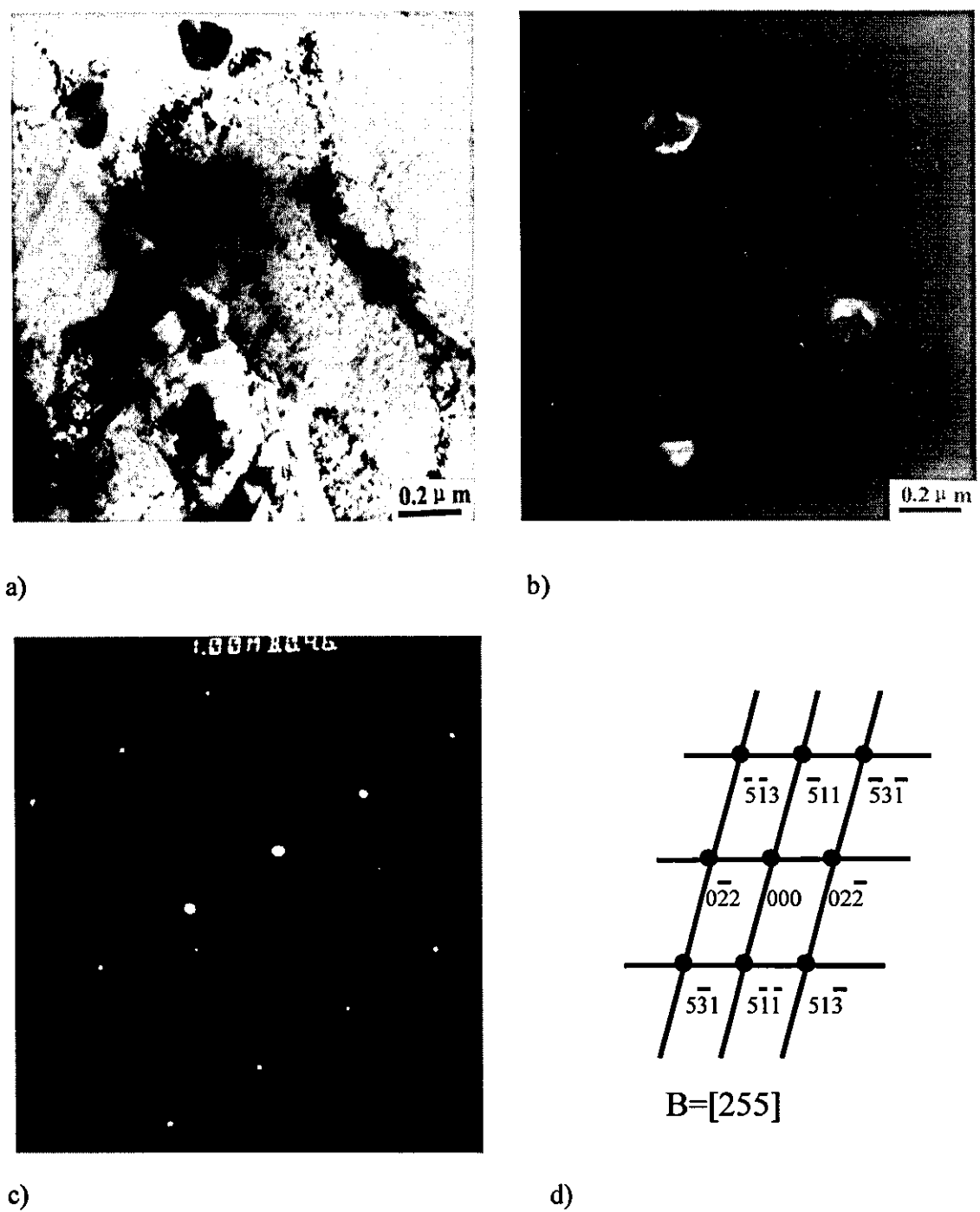
Fig. 6.36. TEM micrograph of weld metal of P91, $M_{23}C_6$ precipitates

a)   light field; b) dark field; c) and d) diffraction pattern.

dissolve Fe and Mo. Sometimes in the high Cr steels Fe/Cr atomic ratio can be over 2, and Mo/Cr can reach 0.6, other alloying elements such as V, Nb can dissolve in $M_{23}C_6$. The changes of $M_{23}C_6$ in the 9Cr-1Mo steel being tempered at 760°C were studied[22], and it was observed that the fine Cr-rich Cr_2C was precipitated first at beginning of tempering (within 16 minutes), then replaced by Cr-rich $(Cr-Fe-Mo)_{23}C_6$ precipitate in 30 minutes. $M_{23}C_6$ is a very stable carbide having a significant influence on the high temperature performances of the high Cr steel. In this research it was found that the $M_{23}C_6$ particle size was about 0.3μm after tempering at 750°C for 4 hours, which is not very different from the 0.25μm (760°C, 1h) mentioned in the reference[23, 24], indicating that the $M_{23}C_6$ has very good stability at high temperature.

During the PWHT, on one hand there exists the residual austenite which will decompose on PWHT; on the other hand because the 750°C chosen in the experiment is higher than the austenisation temperature (about 730°C) of the weld metal, re-austenisation will be taken place. According to the WM-CCT diagram, the austenite will make the proeutectoid transformation to ferrite on cooling along with carbide (mainly $M_{23}C_6$) precipitation. When the temperature is below 360°C, untempered martensite appears. It was observed using TEM that besides the large amount of $M_{23}C_6$, MX precipitates are also found inside the δ-ferrite and in the vicinity of dislocations. The studies showed[25] that the super-cooling was needed for precipitation. Nucleation on dislocations is only 1/2 to 1/3 of that for homogeneous nucleation. The MX phase had often been observed in the residual ferrite of the 12%Cr-1%Mo steel, and this is thought to be VN.

6.4.2 Microstructure Transformation under Continuous Cooling

6.4.2.1 Microstructure transformation characterization

The austenite in the 9%Cr-1%Mo steel welds will be transformed directly into martensite in a high cooling rate range, because large amounts of alloying elements such as Cr, Mo and V in the welds make ferrite very stable. When the cooling rate is lower, the alloying

elements in austenite have enough time to diffuse; and proeutectoid ferrite nucleates and grows at the grain boundary.

There are fewer pearlite and bainite reactions happening in the 9%Cr-1%Mo weld metal, due to the lower carbon and large amount of strong carbide formation elements e.g. V, Cr, Mo and Nb etc. The formation of stable carbide consumes the carbon in austenite and makes the transformation of pearlite and bainite difficult due to the lack of required carbon. The high M_s point also reduces the possibility of occurrence of pearlite and bainite.

6.4.2.2 Martensite transformation

Martenite transformation is a diffusionless transformation in which another through a shear transformation has replaced crystal structure. Based on this feature, martensite will form at high speeds and at low temperatures. It was observed in the experiment that the martensite has the following characteristics:

(1) Lath martensite. The microstructure of ferritic steel while quenching in a wide range

Fig. 6.37. Lath martensite

of cooling rates are martensite which consists of large packets of laths called lath martensite. Within the lath packet the laths are arranged in parallel and separated by low angle grain boundaries (Fig. 6.37).

(2) High dislocation sub-structure. The lath martensite is characterized with high density dislocations inside the laths. This is based on the solid strengthening of the carbon. Fig.6.38 shows large amounts of dislocations in the lath.

Fig. 6.38. Dislocation in the lath

(3) Twin crystal in martensite (Fig.6.39). When the carbon in the steel increases and large amounts of alloying elements which are able to reduce the M_s temperature exist, the twin martensites can be produced after quenching. Fig. 6.39 shows the twin crystal martensite in the weld. However, this type of structure is minor and localized for all the specimens.

Fig. 6.39. Twin crystal martensite

(4) Residual austenite between martensite laths. This resulted from fast cooling. It is generally considered that the residual austenite will be beneficial to improve the fracture toughness of material[26]. However after high temperature PWHT, most residual austenite will decompose.

(5) Fe_3C precipitates. These usually appear when the tempering temperature is over $200^{\circ}C$[27, 28]. As it is a kind of unstable phase, it will be dissolved when tempering temperature increases. Therefore no Fe_3C were observed in the weld after high temperature PWHT.

6.4.2.3 Proeutectoid ferrite transformation

The proeutectoid transformation will happen in slow-cooled austenite in the temperature range of 560-790°C during the continuous cooling of weld metal. Based on the metal transformation theory, the proeutectoid phase (δ-ferrite) will nucleate preferentially on the austenite boundary, and then grow along grain boundary to form a network.

6.4.2.4 Eutectoid transformation (Pearlite)

After forming proeutectoid ferrite transformation, eutectoid transformation will take place to produce pearlite $\alpha+M_{23}C_6$ in further cooling. It can be seen from the equilibrium diagram that the eutectoid temperature is about $800^{\circ}C$. However because the continuous cooling is a non-equilibrium process, the actual eutectoid temperature is lower.

It can be seen from the comparison of the microstructures among the four types of materials that δ-ferrite is only obtained in both weld and parent metal in P122 and P92 materials which contain higher Cr and other alloying elements. This is probably because that higher alloying element increases the nucleation and growth rate of δ-ferrite. It was also observed that there was no δ-ferrite in the soft zone for all the materials. Therefore it can be concluded again that δ-ferrite which is a soft phase is not the reason causing the softening in high Cr steel weldments.

6.5 Conclusions

(1) Hardness testing shows a softening in HAZ of the P91 weldment.

(2) The microstructures in the whole region of the weld are fully lath martensites.

(3) There were no big differences on the microstructures among the three heat treatment conditions. No δ-ferrite found in the HAZ.

References to Chapter 6

1. Power Technology report PT/99/KA1468/R (PIPE project), 1998.

2. Power Technology report PT/99/KA1413/R (PIPE project), 1997.

3. Mitsui Babcock Weld Procedure W785777/01, 2000.

4. Mitsui Babcock Weld Procedure WPS W78075/07, 2001.

5. Mitsui Babcock Weld Procedure W78577/02, 2000.

6. SFEL Weld Procedure Specification WPQ 227, 1998.

7. R. Prader and H. Cerjak, Trends in Weld Research, Proceedings of the 4th Inter. Conf., 5-8 June 1995, Gatlinburg, Tennessee, USA, 247-252.

8. H. Cerjak and R. Prader, Trends in Weld Research, Proceedings of the 4th Inter. Conf., 5-8 June 1995, Gatlinburg, Tennessee, USA, 563-568.

9. R. W. Vanstone, Application of Alloy 122 to Steam Chests for Steam Turbines, ABB Alstom Power, DTI Clean Coal Project 246 Public Report, March 2000.

10. E. Letofsky, H. Cerjak, I. Papst and P. Warbichler The Use of Light and Electron-Microscopic Investigations to Characterise the Creep Behaviour of Welded Joints in Modern Power Station Materials, Met. Sci. Tech., 6, 1995, 124.

11. Loughborough University Report EM/NP/723a for Innogy, Microscopy of Three Samples of 9Cr Steel-Eggbar 257, Eggbar 283 and Shell. Bates, January 2000.

12. Loughborough University Report EM/INN/762 for Innogy, Transmission Electron Microscopy of Aluminium Nitride in 9Cr Steels. Bates, July 2001.

13. H. Cerjak, Microstructural Evaluation of Aged 9-12% Cr Steels Containing W, Proc. Materials Ageing and Component Life Extension, Conf. Milano 10-12 October 1995.

14. H. Cerjak, V. Foldyna, P. Hofer and B. Schaffernak, Microstructure of Advanced High Chromium Boiler Tube Steels, Eds.: Strang A., Gooch D J., The Institute of Materials,1997, 145-158.

15. J. Kameda, J.M. Baik and O. Buck, Long Term Creep Resistance and Microstructural Stability of Ferritic Heat Resistant Steels, 5th Workshop on the Ultra-Steel, 17-18 January, 2001, Japan, 298-311.

16. A. Zielinska-Lipiec, A. Czyrska-Filemonowicz, P.J. Ennis and O. Wachter, The Influence of Heat Treatments on the Microstructure of 9% Chromium Steels Containing Tungsten, Journal of Materials Processing Technology 64, 1997, 397-405.

17. P. Lenk, A. Klenk, A. Kussmaul and K. Maile, Steel Resaerch, 65, 1994, 197.

18. M. Takahashi, K.Ikeuchi, T.Kuroda and J.Liao, Met.Sci.Tech., 6, 1990, 592.

19. F. Abe, T. Horiuchi and M. Igarashi, J. Nucl. Materials, 179-181, 1991, 663.

20. H. Naoi, M. Ohgami, Y. Hasegawa, H. Mimura and T. Fujita, Metall. & Mater.Trans., 28, 1997, 1195.

21. Y.J, Li, J. Wang and B. Zhou, XRD and TEM Analysis of Microstructure in the Welding Zone of 9Cr-1Mo-V-Nb Heat-Resisting Steel, Bull. Mater. Sci., 25(3), June 2002, 213-217.

22. H. Cerjak, P. Hofer and B. Schaffernak, Microstructural Aspects on the Creep Behavior of Advanced Power Plant Steels, Key Engineering Materials Vols. 171-174, 2000, 453-460.

23. P.Hofer, H. Cerjak, B. Schaffernak and P. Warbichler, Steel Resaerch, 69, 1998, 343-348.

24. A. Strang, V. Vodarek, Mater. Sci. Tech., 12, 1996, 552-556.

25. P J. Ennis and A. Czyrska-Filemonowicz, Recent Advances in Creep Resistant Steels for Power Plant Applications, Creep Resistant Steels for Power Plant, OMMI, 1(1) April, 2002, 185-197.

26. F.B. Pickering, and A.D. Vassiliou, Effect of Austenitizing Temperature on Constitution,Transformation,and Tempering of 9Cr-1Mo Steel, Metals Technology, October 1980, 409.

27. S.J. Sanderson, Met. Sci., 11, 1997, 490.

28. C. Shiga, A. Gotoh, T. Kojima, Y. Horii, Y. Fukada, K. Ikeuti and F. Matuda, State of the Art Review on the Effect of PWHT on Properties of Steel Weld Metal, Welding in the World, 37(4), 1996, 163-176.

CHAPTER 7:

Determination of Phosphorous Segregation on the Grain Boundaries

7.1 Introduction

7.1.1 Non-Equilibrium Segregation

As mentioned in previous chapters, Type IV cracking has been observed in the heat affected zone (HAZ) of welds in high Cr ferritic steel. The cracking is inter-granular and occurs in regions where the microstructure is finely grained. Microstructurally the cracking is explained by the possibility that the following effects are responsible[1,2].

- Cavity formation and coalescence enhanced by stress accelerated diffusion
- Fast growth of $M_{23}C_6$ carbides on grain boundaries
- P segregation on grain boundaries

These explanations are reasonable but an alterative proposal is that at the part of the HAZ where crack propagation is observed, the cooling rates and thermal history are such that maximum P non-equilibrium grain boundary segregation could be taking place.

7.1.2 Transmission Electron Microscopy

So far the most widely employed analytical technique in the study of grain boundary segregation is that of electron microscopy, and transmission electron microscopy (TEM) in particular. The characteristic method of data acquisition in TEM is dependent upon the formation and control of the electron beam. Fig.7.1 is a schematic diagram showing the microscopic image.
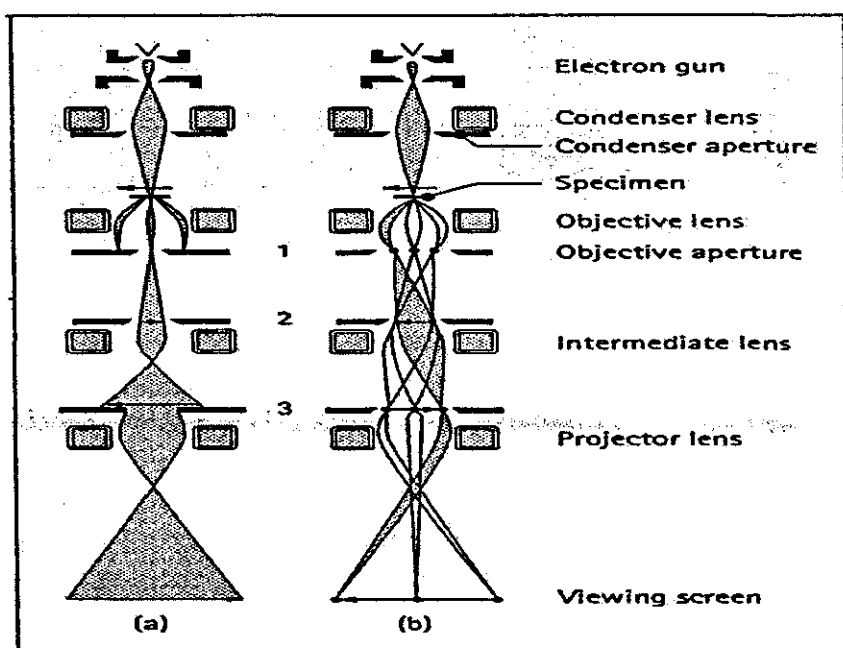
Fig. 7.1. Schematic layout of a TEM[3]

     a) TEM mode, b) Diffraction mode

7.1.2.1 Electron source

There are basically two different types of electron source in electron beam instruments. These are the thermionic electron gun and field emission gun (FEG). In the thermionic electron gun, electrons are emitted from a heated filament (tungsten or lanthanum hexaboride crystal) and then accelerated towards an anode; In the field emission gun, a very strong electric field ($10^9 Vm^{-1}$) is used to extract electrons from a metal filament. Temperatures are lower than that needed for thermionic emission. This gives much higher source brightness and much smaller incident electron beam can be used when compared to both the tungsten filament and LaB_6 crystal.

7.1.2.2 Field emission gun TEM

The most recent field emission gun TEM (FEGTEM) instruments are the Philips Tecnai F20 and Jeol JEM 2010F. The comparison of these two instruments is shown in Table 7.1. Usually FEGTEM was applied with various advanced modes, such as scanning TEM (STEM), parallel electron energy loss spectrometry (PEELS) and

energy filtered imaging (EFI). The STEM covers the scanning attachment to dedicated TEM, which enables the finely focused electron probe to scan across the

Table 7.1. Comparison of Tecnai F20 and JEM 2010F

	Tecnai F20	JEM 2010F
Specifications:		
Imaging modes	TEM/STEM	TEM/STEM
Accel. Voltage	200kV	200 kV
PTP resolusion	0. 24nm	0. 23nm
LTL resolution	0. 14nm	0. 10nm
Source	Field emission	Field emission
Tilt range	±30°	±30°
Ancillary equipments:	CCD camera	Gatan off-axis TC camera
	Gatan imaging filter	Gatan imaging filter
	Oxford Link ISIS 300 EDX system	Oxford 300 EDX
	Gatan digi. PEELS	Gatan PEELS 677
	Environmental cell	Auto-alignment system

sample. Results can be obtained from as many different operating modes as there are detectors fitted, such as detectors for secondary, back-scattered and transmitted electrons and X-rays; The EFI device is attached under the camera chamber and gives the user the capability to carry out electron spectroscopic imaging (ESI) and electron

energy loss spectroscopy (EELS). The EFI incorporates sophisticated electron optics and an energy selecting 'slit', which allows the beam to be filtered to reveal additional information in the form of energy, filtered images, diffraction patterns or spectra. FEGTEM also has a capability for high resolution TEM (HRTEM) imaging.

7.1.2.3 EDXS and EELS

In order to use the FEGTEM technique to measure segregation across an interface such as a grain boundary, it is necessary to determine the chemical composition at various points across the interface. Chemical composition can be determined in one of two ways. Firstly, by analysing X-ray energy spectrum, as in energy dispersive spectroscopy (EDXS), or secondly, by analysing electron energy spectrum, as in EELS or PEELS.

The EDXS technique for X-ray analysis uses a semi-conductor detector to classify X-rays according to energy rather than wavelength. The detector converts the energy of the incident X-ray photons into pulses of current, proportional to the X-ray energy. These pulses are then amplified and fed, typically, into a computer program that manipulates the data into an energy spectrum[3, 4].

The EELS is an alternative technique to EDXS for measuring segregation profiles. However, only a few microscopes have the necessary apparatus to perform this technique. The technique relies on the energy lost by an electron when it produces a characteristic X-ray on passing through the specimen. The spectrum of energies of transmitted electrons contains discontinuities at the ionisation edges, which can be used to derive chemical composition. However, the technique is limited by specimen thickness, and is most useful for determination of light elements, typically sodium and below. EELS also has an advantage over EDXS in that it has a much higher collection efficiency, typically in the range of 50%, compared to around 2% for EDXS. However, the method of collection is much slower than for EDXS, and sometimes requires up to 100 seconds, since the signal to background count ratio is much poorer and the energy levels are detected sequentially. An improvement over this is PEELS, which can measure all energy levels at the same time.

7.2 Experimental Procedure

7.2.1 Material

The materials for the experiment are the same as the materials used in the Chapter 5, i.e. P91. Round samples with the size $\varnothing$ 11 × 110 mm were machined from the origional parent materials for following Gleeble weld simulation program.

7.2.2 Gleeble Testing Programme

The weld simulation was designed by the Gleeble testing to explore phosphorous segregation in the Type IV zone. The testing program is shown in Table 7.2. The Gleeble running program is also the same as that in Chapter 5 in which the cooling rate is constant from the maximum temperature down to 500°C, with subsequent air cooling (Table 7.2 and Fig. 7.2).

Table 7.2. Gleeble testing programmme

Cooing rate, °C/s	Temperature, °C			
	900	950	1100	1300
Fast (typical weld): T_{max} - 500°C: 15°C/s ($t_{8/5}$ = 20s)	×	×	×	×
¼' weld rate: T_{max} - 500°C: 4°C/s ($t_{8/5}$ =80s)	×	×	×	×
Slow rate: T_{max} - 500°C: 0.1°C/s ($t_{8/5}$ = 3000s)	×	×	×	×
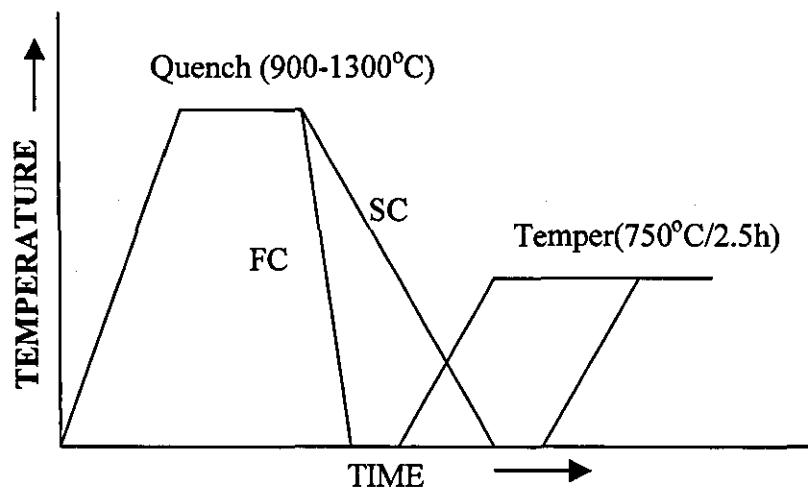
Fig. 7.2. The thermal cycles needed to produce NES

FC-fast cooling, SC-slow cooling

The number of samples was doubled for each testing condition, so totally 24 specimens were obtained. One half underwent the tempering procedure of 750°C for 2.5 hours. The sampling designation for all the specimens is shown in table 7.3.

Table 7.3. Sampling code

Cooing rate, °C/s	Quenching temperature (°C) and heat treat conditions							
	900 (B)		950(C)		1100(D)		1300(E)	
	As-weld	PWHT	As-weld	PWHT	As-weld	PWHT	As-weld	PWHT
	(I)	(II)	(I)	(II)	(I)	(II)	(I)	(II)
Fast (typical weld): (X) T_{max}-500°C: 15°C/s ($t_{8/5}$ = 20s)	BXI	BXII	CXI	CXII	DXI	DXII	EXI	EXII
¼' weld rate: (Y) T_{max}-500°C: 4°C/s ($t_{8/5}$ =80s)	BYI	BYII	CYI	CYII	DYI	DYII	EYI	EYII
Slow rate: (Z) T_{max}-500°C: 0.1°C/s ($t_{8/5}$ = 3000s)	BZI	BZII	CZI	CZII	DZI	DZII	EZI	EZII

7.2.3 Hardness Testing

After the Gleeble testing, each specimen was sectioned along the centreline. One half was used for hardness testing; the other half was for the TEM foil sample preparation to determine the element segregation.

7.2.4 Specimen Preparation

0.3 mm thick slices were sectioned from the thermo-couple point to the interface of HAZ and soft zone by using the cutting machine. Then discs 3 mm in diameter were cut from each slice by the sparking unit and were ground to a thickness of about 70μm. The discs were electropolished to obtain the thin zone using a dual jet electropolisher. A polishing solution of 5% perchloric acid in methanol was used with operating parameters of 28V in voltage, 75mA in current and below –50°C in temperature.

7.2.5 Operation of the Instrument

Both the Tecnai F20 and the JEM 2010F FEGTEM were used to determine the P content at grain boundaries. The operation of the instrument is very important. In order to minimize specimen drift and contamination, the TEM specimen was cleaned in plasma for five minutes and its thin zone was exposed for about 30 minutes to an electron beam at a magnification of 2000× before EDX analysis. The spot size of electron beam is minimized with a full width at half maxium height (FWHM) of about 1nm at an accelerating voltage of 200kV. A straight and narrow boundary was selected for observation. The specimen tilt was carefully adjusted until the image width of the boundary trace was less 5nm. Both TEM and Scanning TEM (STEM) modes of EDX were applied to obtain the most accurate elemental segregation concentration on boundaries. Line and step scanning across the boundary were carried out to compare the analytical results. Magnifications used can be up to a maximum of 910k. A 100nm measurement depth was chosen. Collecting time was optimised to ensure either the effective spectrum counts to be obtained or without beam drifting during the determination. This was monitored periodically. The acquisition status

during determination is also important, so that the deadtime is between 10%-25% to ensure proper accounting. Counting time is set to 50 seconds. Shorter counting time cannot ensure a reasonable accounting number, whereas with longer counting time the beam positioning is difficult to maintain precisely due to the beam drifting. The counting number is optimised to no less than 4000 counts. The positions determined include grain boundaries especially the lath martensite boundaries. Fig. 7.3 portrays these types of boundaries.

a)   b)

c)
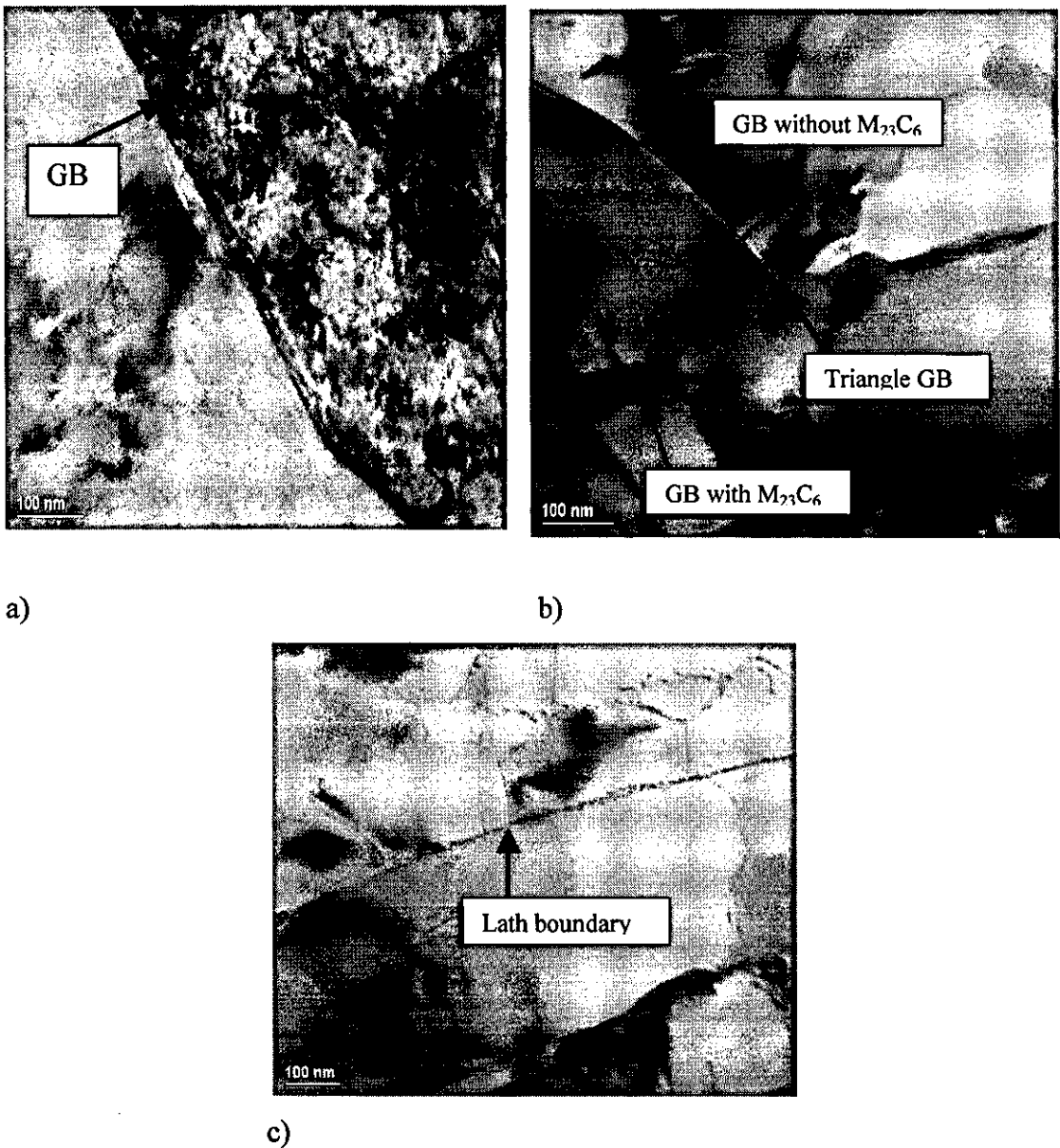
Fig. 7.3. The boundaries studied

      a) grain boundary, b) triangle GB, c) lath boundary

7.3 Results

As a consequence of the broadening of the electron beam as it passes through the foil and there is an increase in the volume from which X-rays are generated, the corrected GB concentration of P is higher than the measured concentration. The measured concentration needs to be convoluted to derive a corrected GB concentration. The corrected GB concentration can be written as [5, 6]

$$C = C_0 + \frac{1}{2}(C_b - C_0) \times \left[erf\left(\frac{x_d + \frac{1}{2}d_0}{\sigma\sqrt{2}}\right) - erf\left(\frac{x_d - \frac{1}{2}d_0}{\sigma\sqrt{2}}\right) \right]$$

where C_b is the concentration in the segregant layer, C_0 is the concentration in the adjacent matrix, σ is the standard deviation of the probe distribution (80%), x_d is nominal beam diameter (3.5nm) and d_0 is a segregation layer width (1nm).

The values of P concentration at grain boundaries for each condition are presented in Table 7.4.

Table 7.4. P concentration at grain boundaries in specimens

Specimen code	BXI	BYI	BZI	DXI	DYI	DZI	EXI	EYI	EZI
P(at.%) (Measured)	0.56*(7**)	0.54(11)	0.55(8)	0.70(4)	1.07(5)	0.85(2)	1.69(3)	--	1.83(1)
P(at.%) (Corrected)	0.59	0.58	0.58	0.77	1.18	0.93	1.85	--	2.03
P(at.%)(Calculated***)	0.34	--	--	0.94	1.05	--	2.65	--	2.78

* Average value.

** Number of the boundaries measured.

*** It is calculated from the Equation (10) in Chapter 3

Besides the status of the instrument, the determination is also affected significantly by many factors related to the specimens, such as quality and quantity of grain boundaries in the thin section, quality of the thin section of the specimen. Therefore it is very difficult to ensure uniform measurement. Generally the scatter of measurements within a same sample is not serious. Table 7.5 shows single measurement for each boundary for all the specimens in Table 7.4.

Table 7.5. Single measurement for all specimens

at%

GB*	1	2	3	4	5	6	7	8	9	10	11	12
Specimen:												
BXI	0.20	0.60	0.14	0.62	0.51	0.49	1.06					
BYI	0.30	0.31	0.50	0.55	0.52	0.50	0.50	0.64	0.63	0.42	0.54	
BZI	0.50	0.45	0.95	0.40	0.51	0.51	0.44	0.50				
DXI	0.68	0.63	0.78	0.72								
DYI	1.22	0.86	0.96	1.40	1.23 (L**)	0.94(L)						
DZI	0.40	0.85										
EXI	1.77	1.60	1.13									
EYI	--	--										
EZI	1.83											

* GB-grain boundary, ** L- lath boundary.

7.4 Discussion

This is based on the grain boundary non-equilibrium segregation (GBS) model which is related to the equations (9) and (10) in Chapter 3.

7.4.1 Maximum GB Concentration

The maximum concentration of P at GB is dominantly controlled by the starting temperature. When the quenching temperature increases, the maximum segregation of P to GB increases significantly (Fig. 7.4).
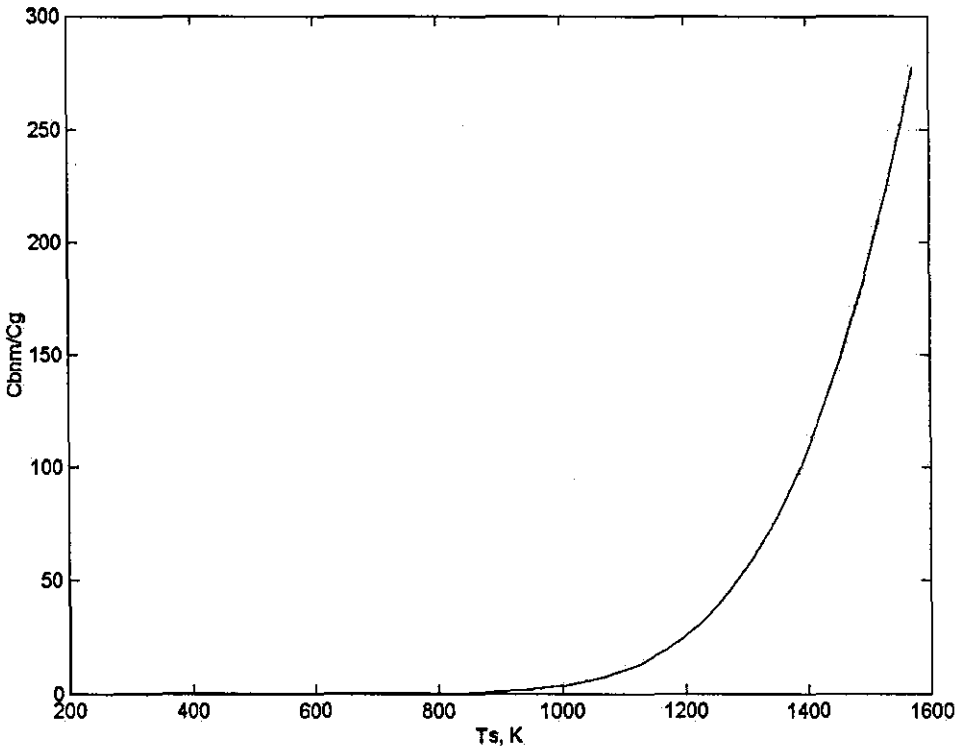
Fig. 7.4. Maximum concentration on grain boundary with temperature

(Quenching rate: 15°C/s)

7.4.2 GB Concentration versus Quenching Time

It can be seen from Fig. 7.5 that the non-segregation of P to grain boundary enhances with increasing the quenching time. However, when the time is longer, the non-equilibrium segregation tends to reach a maximum.
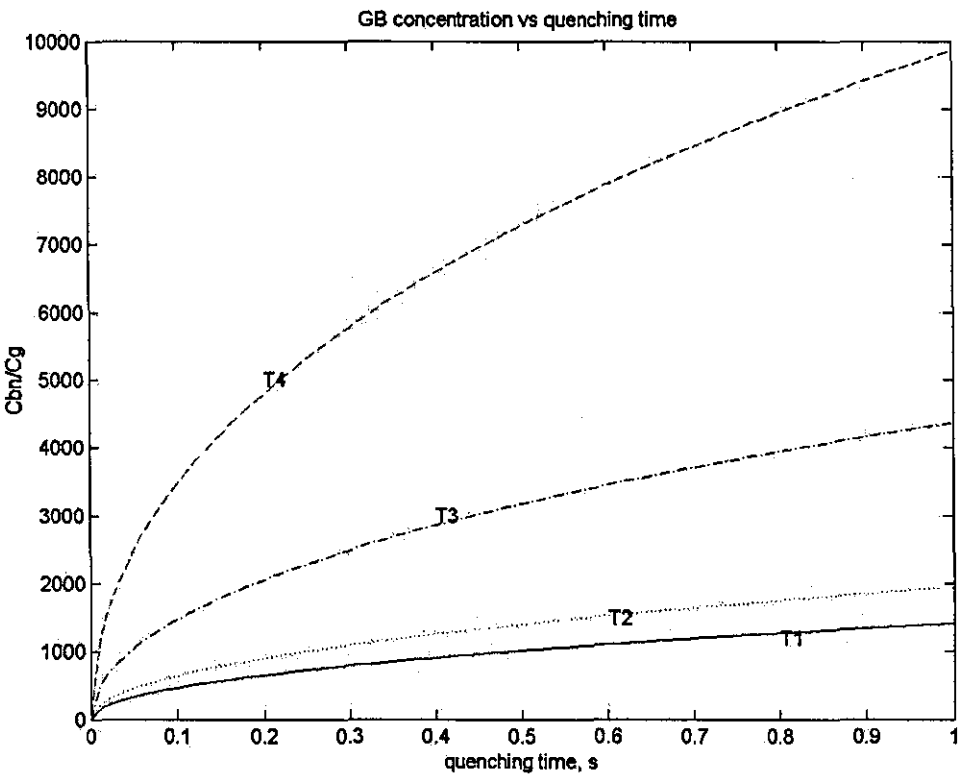
Fig. 7.5. Concentration of P on the grain boundary with time
     $T_1=900°C$, $T_2=950°C$, $T_3=1100°C$, $T_4=1300°C$

7.4.3 The Effects of the Quenching Temperature and Rate on the P Segregation to GB

The simulated P segregation as a function of quenching temperature and rate is shown in Fig. 7.6. It can be seen from the figures that the NES segregation of P to grain boundaries increases almost in a linear manner with the quenching temperature, while the GB concentration decreases as the cooling rate is increased. However the effect of the quenching rate on the NES segregation at the grain boundaries is relatively minor.
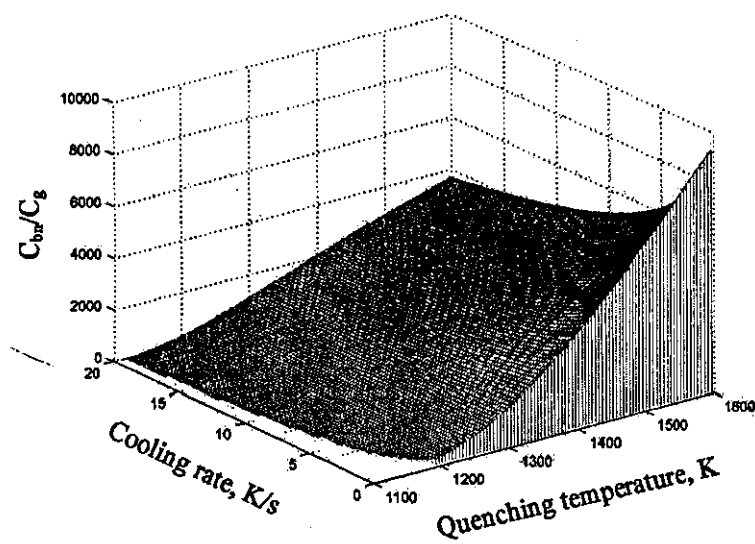
Fig. 7.6. Relationship between GB concentration with the quenching temperature
         and cooling rate

7.4.4 Grain Boundary Segregation (GBS) Model Validation

It is clear that from Fig. 7.7 and 7.8 that the simulated results are in good agreement
with measurements.
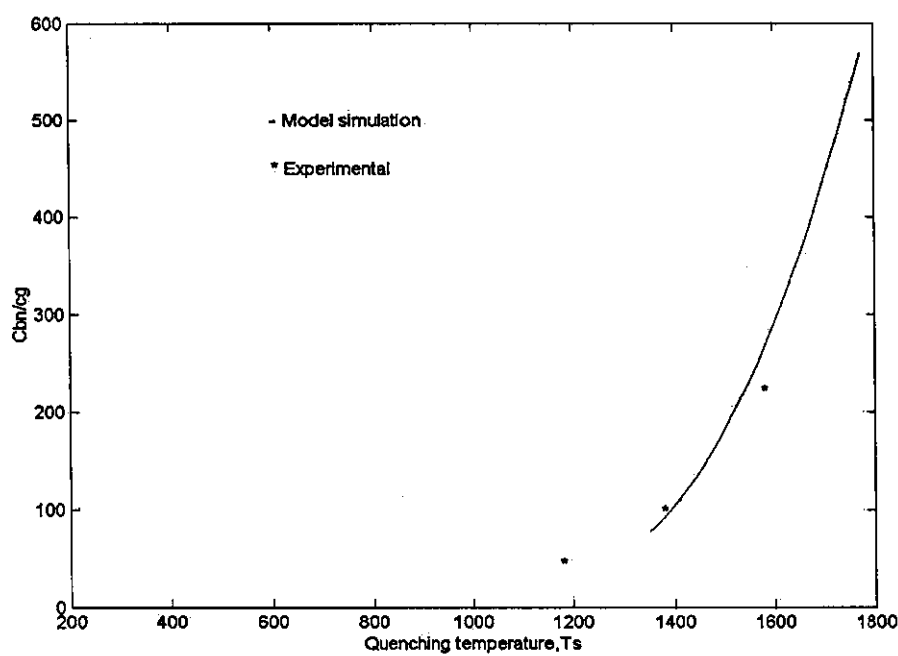
Fig. 7.7. Simulated P segregation kinetics in P91, together with experimental
         Measurements (Quenching rate: $15°C/s$)
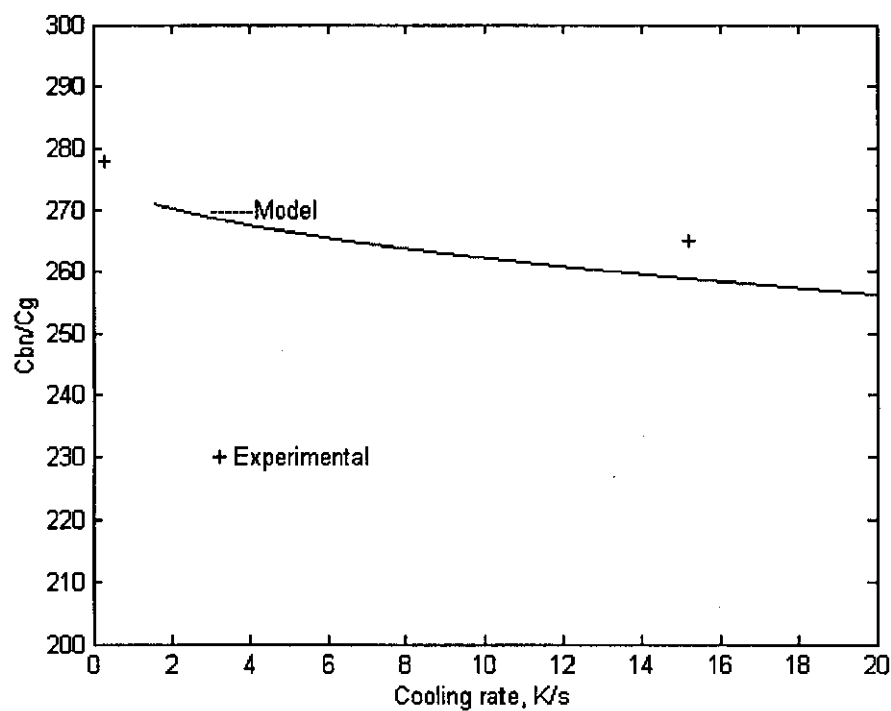
Fig. 7.8. Relationship between GB concentration and the quenching rate

The study reveals a typical phosphorus concentration profile as a function of the distance from the grain boundary, and a significant enrichment of P in boundary
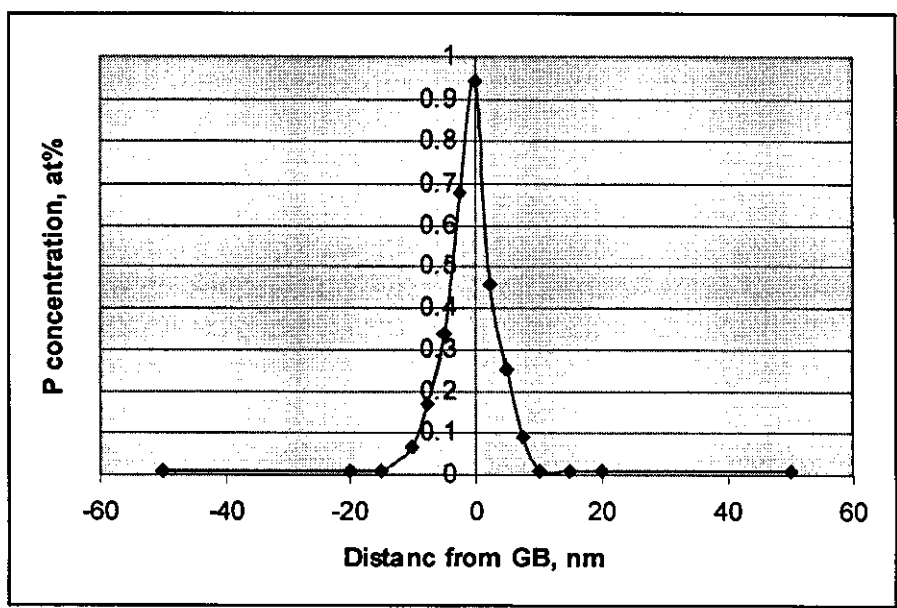
Fig. 7. 9. Phosphorus distribution across the boundary (DYI specimen)

regions $<\sim$7.5nm from the interface (Fig. 7. 9). There is sharp peak of phosphorus concentration in which the NES process is dominant during quenching. This is similar with the result presented by Faulkner and Little[7, 8].

It can be seen from Table 7.5 that phosphorus shows similar segregation behaviour on all types of boundaries. There is big difference between grain boundaries and lath boundaries. The phosphorus appears mainly on the boundaries without $M_{23}C_6$ carbides (Fig. 7.3), this is because that the NES segregation is strongly influenced by site competition. NES segregation can be classified into segregation and desegregation. Desegregation is back diffusion of solute atoms after a critical time. As a result of the effect of the desegregation process, the phosphorus segregation was not determined for all the specimens after post weld heat treatment (PWHT). This agrees with the work of Maier and Morgan[9-11].

The data used in the theoretical calculation are listed in Table 7.6.

Table 7.6. Parameters for the theoretical calculations

Parameters	Phosphorus	Carbon	Molybdenum
B (m)	3×10^{-5}	3×10^{-5}	3×10^{-5}
d (m)	2×10^{-9}	2×10^{-9}	2×10^{-9}
D_{oc}^i (m^2 s^{-1})	1.7×10^{-5} [12]	7×10^{-6} [13]	1.7×10^{-5} [12]
D_{oi} (m^2 s^{-1})	7.12×10^{-3} [14]	3.94×10^{-7} [15]	3.467×10^{-4} [15]
E_A (eV)	1.6 [16]	1.33 [15]	2.56[15]
E_b (eV)	0.36 [16]	0.5 [16]	--
E_f^V (eV)	1.4 [17]	1.4 [17]	1.4 [17]
E_i (eV)	2.68[16]	0.83 [15]	2.51 [15]
E_m^i (eV)	0.87 [16]	1.36 [13]	1.24 [13]
k	1.837×10^{-23}	1.837×10^{-23}	1.837×10^{-23}
Q^i (eV)	0.54 [18]	0.829 [19,20]	0.00104 [18]
R	0.01	0.01	0.01
δ	0.05	0.05	0.05

7.5 Conclusions

1. The non-equilibrium segregation of P to prior austenite grain boundaries and lath boundaries was observed after austenitising and quenching treatment with Gleeble simulation. The maximum segregation to the grain boundary is mainly affected and controlled by the start temperature.

2. The cooling rate has a less significant influence on the non-equilibrium segregation of P to grain boundaries. The P concentration to the grain boundary slightly increases as the cooling rate is reduced (from $15^\circ C$ /s to $0.1^\circ C$/s).

3. The experimental measurements are well in agreement with the GBS model.

References to Chapter 7

1. R.G.Faulkner, S. Song, D. Meade, C.C. Goodwin, Modelling of grain Boundary Segregation in Austenitic Steel Weld Heat-Affected Zones, Inst. of Mechanical Engineers, Nov. 1997, 345-353.

2. Z.X. Yuan, S.H. Song and R.G. Faulkner, J. of Nucl. Materials, 255,1998,189-209.

3. C.C. Goodwin, The Mathematical Modelling of Grain Boundary Segregation in Austenitic Alloys, PhD thesis, 1998, 20-34.

4. D. Meade, Grain Boundary Segregation of Impurity Elements in Reactor Pressure Vessel Steels, PhD thesis, 1999, 35-45.

5. R.G. Faulkner and T.S. Morgan, Analytical Electron Microscopy of Thin Segregated Layers, X-ray Spectrometry, 23, 1994, 195.

6. R. Ding, Effect of Phosphorus Segregation on the Fracture Properties of Two Quenched-and-Tempered Structural Steels, to be published on Mater. Sci. Tech., 2004.

7. R.G. Faulkner, S. Song and P.E.J. Flewitt, Irradiation-Induced Grain and Lath Boundary Segregation in Ferritic--Martensitic Steels, J. of Nuc. Materials. 191-194, 1992, 858-861.

8. E. A. Little, Microchemistry of Neutron Irradiated 12% CrMoVNb Martensitic Steel, Materials Science Forum. 97-99, 1992, 323-328.

9. P. Maier and R.G. Faulkner, Effects of Thermal History and Microstructure on Phosphorus and Manganese Segregation at Grain Boundaries in C-Mn Welds, Materials Characterization, 51, 2003, 49-62.

10. P. Maier, R.G.Faulkner, P.Spellward and J.R. Cowan, Grain boundary segregation of phosphorus, manganese, and carbon in boiler shell weld material. Mater. Sci., 6, 1989, 251-262.

11. T.S. Morgan, Interfacial Segregation in Fast Reactor Irradiated 12% Chromium Martensitic Steel, Effects of Radiation on Materials: 15th International Symposium; Nashville, Tennessee; USA; 19-21 June 1990, ASTM, 1916 Race St, Philadelphia, Pennsylvania 19103, USA.

12. R.G. Faulkner, Met. Mater. Trans., 27A, 1996, 238.

13. E.A. Brandes, G.B. Brook (Eds), Smithell Metals Reference Book, 7th eds., Butterworth-Heinemann, Oxford, 1992, 13-70—13-102.

14. R.G. Faulkner, S.H. Song and P.E.J. Flewitt, Mater. Sci. Technol., 12, 1996. 818-904.

15. S.M. Kim and W.J.L. Buyers, J. Phys., 8, 1978. 103.

16. M. Guttmann, P.h. Dumoulin and M.L. Wayman, Metall. Trans., 13A, 1982, 1693.

17. M. Hashimoto, Y. Ishida, R. Yamamoto, M. Doyama and T. Fujiwara. Acta Metall., 32, 1981, 1.

18. C. Liu, T. Nagoya, K. Abiko and H. Kimura, Metall. Trans., 23A, 1992, 263-269.

CHAPTER 8:

Type IV Cracking Mechanism of High Cr Ferritic Steels

8.1 Introduction

Weld creep testing was used to simulate the service situation for ferritic steel weldments; after that, microstructures mainly in the HAZ were investigated to understand the Type IV crack failure mechanism.

Creep rupture tests were performed at different stresses and temperatures. All materials were tested in the PWHT condition. Thereby, all the creep specimens were taken parallel to the longitudinal direction of the pipe but perpendicular to the welding direction in such a manner that the HAZ was in the middle of the gauge section as shown in Fig. 8.1[1,2].
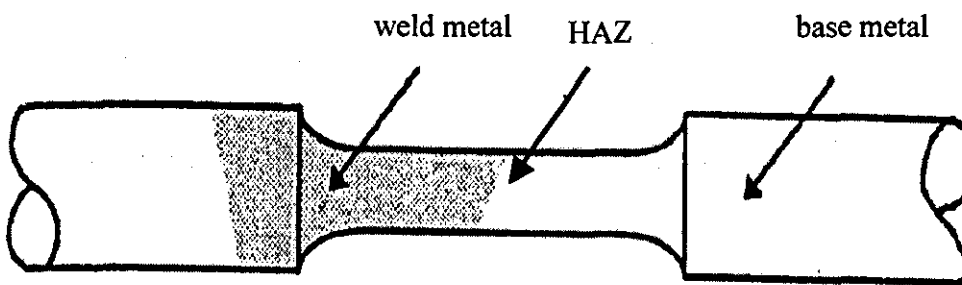
Fig. 8.1. Specimens for creep testing

The gauge section in size $\phi11 \times 90$ mm, therefore, contained base metal, HAZ and weld metal. The test methods used conform to the requirements of ASTM E 139-83.

8.2 Experimental Results

8.2.1 Creep Sample Testing Results

Four types of materials 41 specimens in total were received for examination. The results are shown in Table 8.1.

Table 8.1. Creep specimen testing results

PTC Ref	Test Ref	Temp. °C	Stress MPa	Est. Dur.	Final Dur.	Elong. %	R.of A,%	MBEL comments
P122(HCM12A) Casting Weld (Group ref A)								½ X-weld, from etching a space sample the fusion line appears to be at 80deg to specimen surface, in the centre of the gauge length
KA1281/1	02/005	670	75.0	1000	1240B	5.12	17.75	45deg failure, ¼ of gauge length, failure could be in weld metal
KA1281/2	01/031	625	135.0	1000	1695B	4.38	7.48	Jagged failure, ¼ of gauge length, appears to be in the weld metal
KA1414/1	01/032	625	105.0	3000	(2290T)	3.34	8.50	45deg jagged failure, ¼ gauge length
KA1414/2	02/015	625	75.0	2500	(853T)	5.99	13.35	45deg jagged failure, ¼ gauge length
P122 (HCM12A) Forging/Weld (Group ref B)								½ X-weld, the fusion line appears to be at 45deg to specimen surface, in the centre of the gauge length(from etching a space sample)
KA1414/3	01/034	625	105.0	3000	(1340T)	7.84	13.35	45deg jagged failure, ¼ gauge length
KA1295/1	02/006	670	75.0	1000	1988B	5.16	7.30	45deg jagged failure, ¼ gauge length in weld metal
KA1395/1	02/016	650	75.0	2500	(829T)	3.77	11.85	45deg jagged failure, ¼ gauge length
KA1414/4	03/003	700	60.0	500	599	5.63	12.54	45deg jagged failure, ¼ gauge length
KA1281/3	01/033	625	135.0	1000	1869B	11.24	16.46	some necking at fusion line, but looks like failure in weld metal
P122 (HCM12A) TWI Weld Test Plate W16 (Group ref C)								X-weld with 2 45deg fusion lines, centre of weld is offset from centre of gauge length(from exam. Of failed specimen 01/035)
KA1281/4	02/007	625	75.0	1000	1061B	2.63	12.02	45deg failure at fusion line, at end of gauge length and just beyond
KA1392/1	02/013	625	105.0	3000	5069	2.62	15.51	45deg jagged failure, ½ gauge length
KA1339/1	02/017	650	75.0	2500	2970	3.19	3.87	45deg failure, ½ of gauge length
KA1281/5	01/035	625	135.0	1000	1366B	4.00	7.13	Jagged failure in centre of weld
P92 (NF616) TWI Weld Test Plate W12 (Group ref D)								Unknown construction, suspect X-weld with 2 off 45deg fusion lines
KA1281/6	02/004	670	75.0	1000	1054B	1.69	2.99	45deg failure in centre gauge length
KA1395/2	02/012	625	105.0	3000	6129	1.49	3.16	45deg failure, ½ of GL
KA1392/2	02/014	650	75.0	2500	4421	1.11	0.89	45deg failure, ½ of GL
KA1281/7	01/036	625	135.0	1000	1475B	12.5	39.55	45deg failure in centre of gauge length, severe necking on one side

(continued)

PTC Ref	Test Ref	Temp. °C	Stress MPa	Est. Dur.	Final Dur.	Elong. %	R.of A,%	MBEL comments
E911 Pipe ex-PIPE (rods+H/Ts) (Group ref E)								
	02/001	625	60.0	2000	(1318T)			
KA1281/8	02/002	670	75.0	1000	703B	3.17	19.49	60deg failure in centre of gauge length, could be fusion line
KA1295/2	02/003	650	75.0	2500	2574B	2.46	16.29	60deg failure in centre of gauge length, could be fusion line
P92 (NF616) Nippon Pipe M2W electrodes PWHT 765°C,2hrs (Group ref F)								X-weld with 2 60deg fusion lines (from etched spare specimen)
KA1339/2	02/036	625	135.0	1000	1631	20.77	82.88	cup and cone in parent metal
KA1414/5	02/037	625	105.0	3000	7397	3.06	6.30	15deg failure, ½ GL
KA1339/3	02/038	670	75.0	1000	1567	3.53	11.09	15deg failure
KA1395/3	02/039	650	75.0	2500	5410	2.17	11.55	15 failure, 1/2GL
P92 (NF616) Nippon Pipe M2W electrodes PWHT 765°C,2hrs (Group ref G)								X-weld with 2 60deg fusion lines (from etched spare specimen)
KA1295/3	02/040	625	135.0	1000	506B	24.01	88.31	cup and cone in parent material
KA1414/6	02/041	625	105.0	3000	7454	2.66	5.24	Jagged at 2/3 GL
KA1339/4	02/042	670	75.0	1000	1577	3.44	3.44	Jagged failure, 2/3GL
KA1414/8	02/043	650	75.0	2500	8531	3.35	5.94	Jagged at 2/3 of gauge length
KA1414/7	03/004	700	60.0	500	537	2.40	10.72	45deg jagged at ½ GL
P91 As-Rec'd. MR02/027A Weld with Metrode PWHT 760'c3hrs								½ X-weld, from etching a space sample the fusion line appears to be at 80deg to specimen surface, in the centre of the gauge length
KA1395/4	02/080	600	105	4000	2222	3.97	14.32	90deg failure in the centre of gauge length
KA1339/5	02/047	600	120	1100	934	19.92	78.16	cup and cone in parent material at 2/3 of gauge length
KA1395/5	02/077	635	75	1000	1246	3.06	15.3	90deg failure in the centre of gauge length
KA1392/3	02/067	655	75.0	400	519	3.05	13.68	90deg failure in the centre of gauge length
P91 N&Temper, MR02/027B Weld with Metrode. PWHT 760'cihr								½ X-weld, the fusion line appears to be at 45deg to specimen surface, in the centre of the gauge length(from etching a space sample)
KA1395/6	02/081	600	105.0	4000	2176	3.01	15.47	90deg failure in the centre of gauge length
KA1339/6	02/048	600	120	1100	1366	3.40	7.65	Type IV
KA1392/4	02/096	600	155	100	215	18.34	55.32	at fusion line with necking in parent metal
KA1395/7	02/078	635	75	1000	926	2.57	13.35	90deg failure in the centre of gauge length
KA1392/5	02/068	650	75	400	359	2.31	18.07	90deg failure in the centre of gauge length
P91 Aged, MR02/027C Welded with Metrode.								X-weld with 2 45deg fusion lines, centre of weld is offset from centre of gauge length(from exam. Of failed specimen 01/035)
KA1395/8	02/082	600	105	4000	2054	25.55	82.33	cup and cone in parent metal
KA1339/7	02/049	600	120	1100	677	23.11	82.63	cup and cone in parent metal
KA1395/9	02/079	635	75.0	1000	1111	4.19	16.62	90deg failure, ½ of gauge length
KA1395/10	02/069	650	75.0	400	430	10.46	28.77	90deg failure in the centre of gauge length, some RA of PM

8.2.2 Macroexamination

8.2.2.1 Low mag. photographs of the two specimen halves and the fracture surfaces

The specimen macrographs of the fracture in three regions are shown in Fig. 8.2.
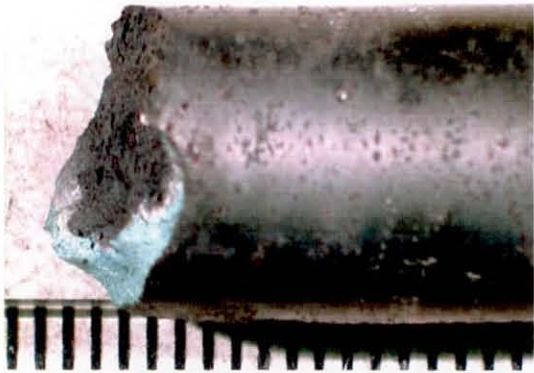
a) (KA1414/1, P122)
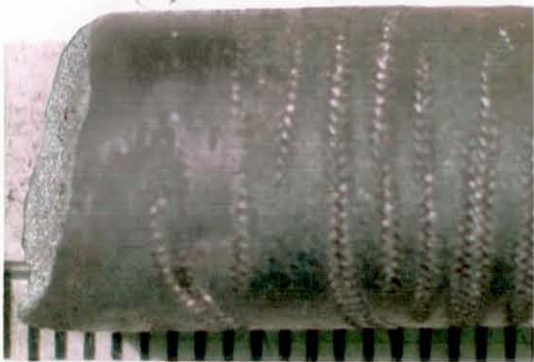
b) (KA1395/5, P91)

c) (KA1395/8, P91)

Fig. 8.2. The macrographs of the fracture

    a) Weld metal failure, b) Type IV crack, c) Parent metal failure

8.2.2.2 Macrographs of sectioned specimens

The macrographs of sectioned specimens are shown in Fig. 8.3.

a) (KA1414/1, P122)
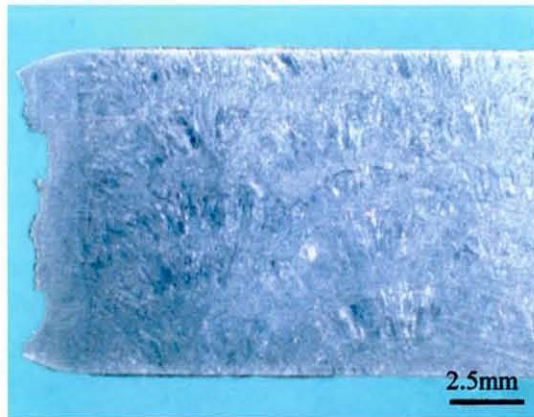
b) (KA1395/5, P91)
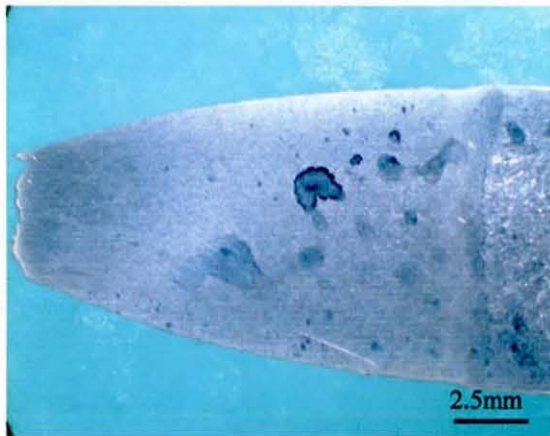
c) (KA1395/8, P91)

Fig. 8.3. Micrographs of the sectioned specimens

    a) WM failure, b) Type IV crack, c) PM failure

8.2.3 Microexamination on the Creep Damage and the Defects

The regions close to the fracture and both sides of the HAZ zones have been examined at higher magnification to observe the creep damage, defects and other phenomena as shown in the following figures:

a)

b)

Fig. 8.4. a) Secondary crack in WM, and b) the fusion line, P122 (KA1281/1)

The HAZ showed no creep damage. The weld metal secondary crack lies in the light-etching zone near the weld inter-run boundary. There is also an undamaged very light-etching zone at the fusion boundary, which may be due to carbon migration.

a)

b)
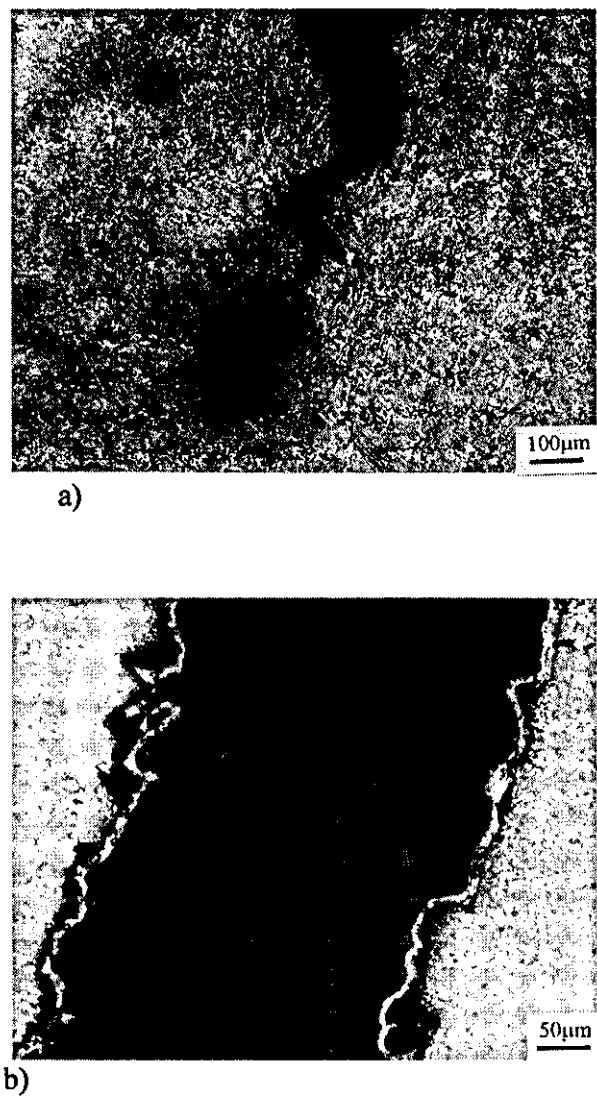
Fig. 8.5. The fusion/slag defect crack, P122 (KA1281/3)

The apparent secondary crack at the fusion boundary in the macrograph is in fact a lack of fusion/slag defect on the weld preparation sidewall.

a)

b)
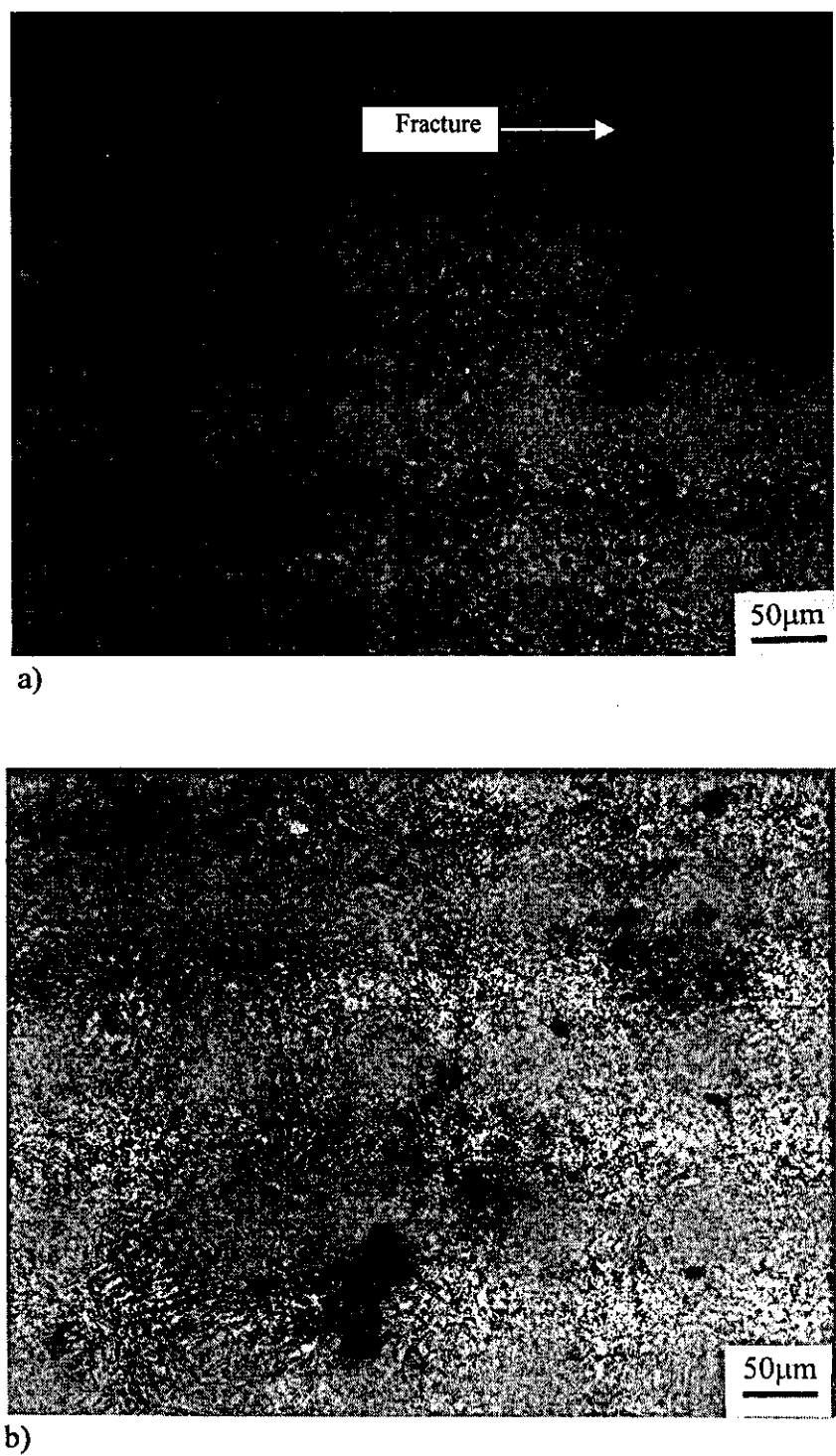
Fig. 8.6. The creep damage in a) HAZ, and b) unfailed HAZ, P122 (KA1281/4) The
          creep damage can be seen in the HAZ adjacent to the failure and also in the
          unfailed HAZ.
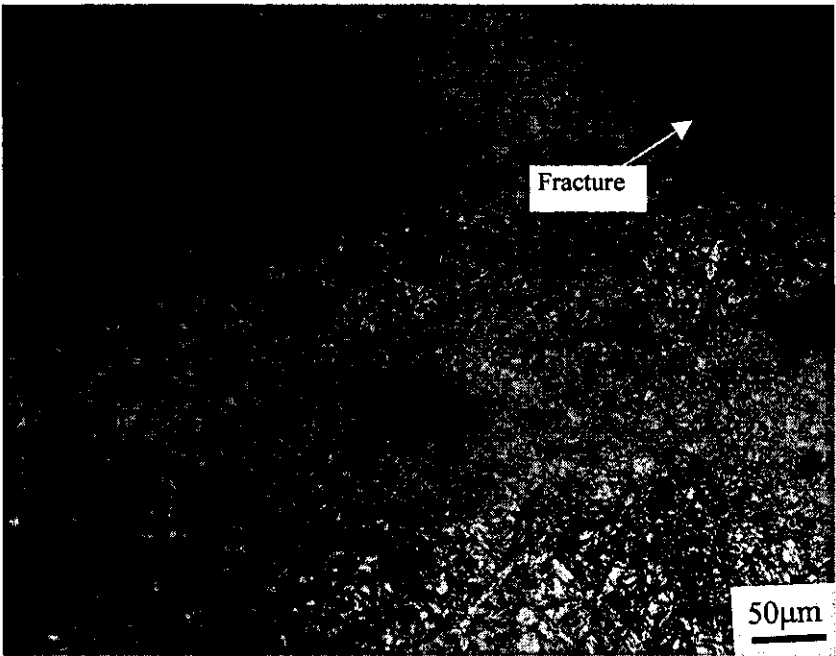
Fig. 8.7. Creep damage in HAZ, P92 (KA1281/6)

Creep damage is observed in HAZ adjacent to crack. No creep damage is observed in the unfailed HAZ.

a)

b)
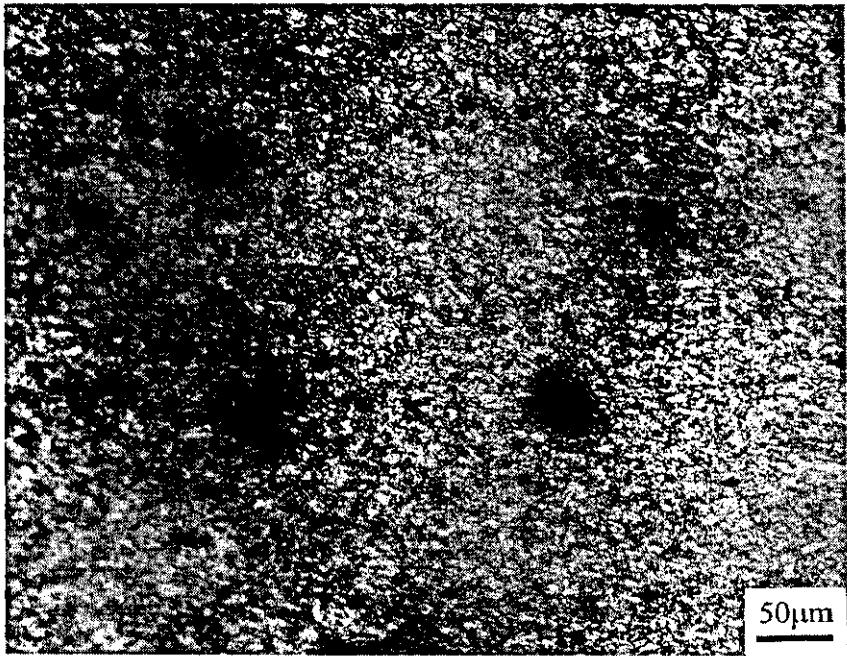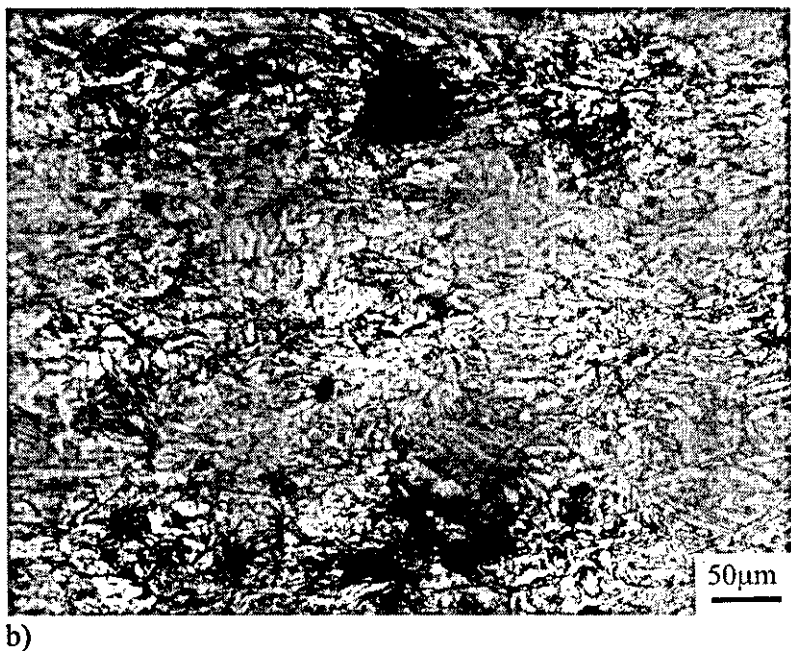
Fig. 8.8. Creep damage in a) HAZ, and b) the necked region, P92 (KA1281/7).

       Large amount of creep damage is present in the unfailed HAZ and in the necked

       region of the parent metal (close to failure) (cavitation and microcracking).
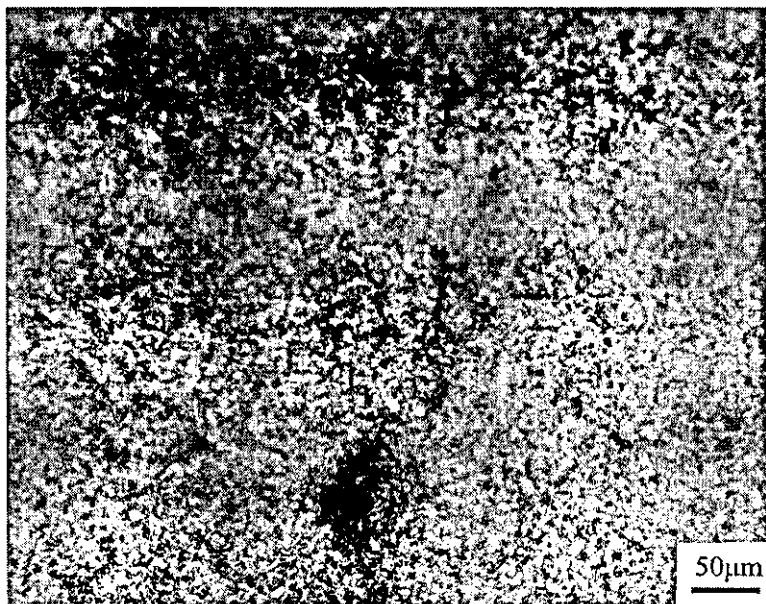
Fig. 8.9. Creep damage and microcrack in HAZ, E911 (KA1281/8)

       Creep damage and microcracking appear in unfailed HAZ.
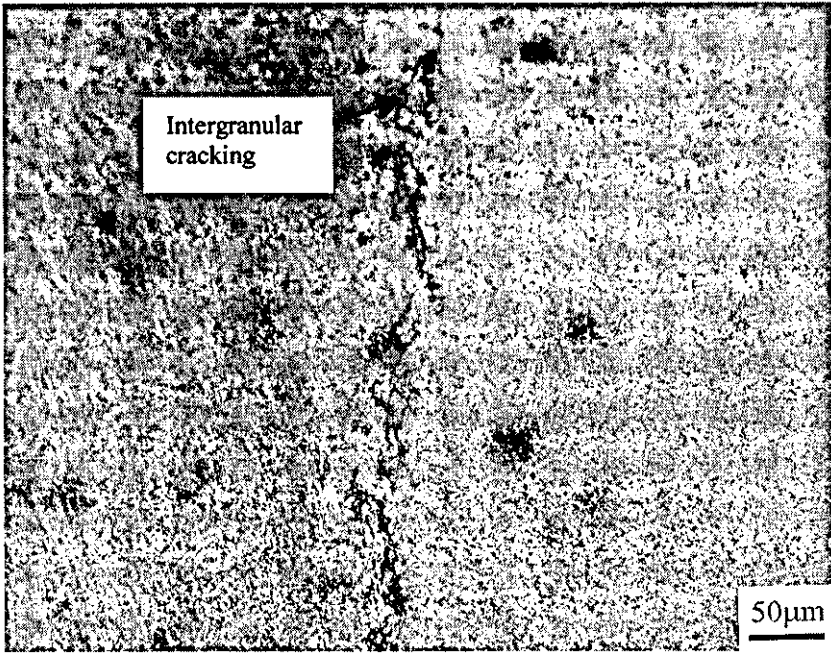
Fig. 8.10. Creep damage and microcrack in HAZ, P122 (KA1295/1)

      HAZ contains microcrack which is intergranular.

8.2.4 Failure Conclusions

The examination results on the fracture for all specimens are given in Table 8.2. Of these 41 specimens, 23 are Type IV cracks, 13 are WM failures and 5 are PM failures.

Table 8.2. Failure examination results

PTC Ref	Test Ref.	Temp. 'C	Stress MPa.	Est. Dur.	Final Dur.	Elong. %	R.of A. %	Failure
P122(HCM12A) Casting Weld (Group ref A)								
KA1281/1	02/005	670	75.0	1000	1240	5.12	17.75	WM
KA1414/2	02/015	650	75.0	2500	7984	5.99	13.35	WM
KA1281/2	01/031	625	135.0	1000	1695	4.38	7.48	WM
KA1414/1	01/032	625	105.0	3000	9162	3.34	8.50	WM
P122(HCM12A) Forging/Weld (Group ref B)								
KA1414/4	03/003	700	60.0	500	599	5.63	12.54	WM
KA1295/1	02/006	670	75.0	1000	1988	5.16	7.30	WM (HAZ microcrack)
KA1395/1	02/016	650	75.0	2500	7050	3.77	11.85	WM (HAZ crack)
KA1281/3	01/033	625	135.0	1000	1869	11.24	16.46	WM (HAZ damage)
KA1414/3	01/034	625	105.0	3000	8819	7.84	13.35	WM
HCM12A (P122) TWI Weld Test Plate W16 (Group ref C)								
KA1281/4	02/007	670	75.0	1000	1061	2.63	12.02	T IV
KA1339/1	02/017	650	75.0	2500	2970	3.19	3.87	T IV (WM crack)
KA1281/5	01/035	625	135.0	1000	1366	4.00	7.13	WM
KA1392/1	02/013	625	105.0	3000	5069	2.62	15.51	T IV
P92 (NF616) TWI Weld Test Plate W12 (Group ref D)								
KA1281/6	02/004	670	75.0	1000	1054	1.69	2.99	T IV
KA1392/2	02/014	650	75.0	2500	4421	1.11	0.89	T IV
KA1281/7	01/036	625	135.0	1000	1475	12.50	39.55	T IV (PM damage,neck)
KA1395/2	02/012	625	105.0	3000	6129	1.49	3.16	T IV (WM microcrack)
E911 Pipe ex-PIPPE(rods+H/Ts) (Group ref E)								
KA1281/8	02/002	670	75.0	1000	703	3.17	19.49	T IV
KA1295/2	02/003	650	75.0	2500	2574	2.46	16.29	T IV
	02/001	625	60.0	20000	10247T			
P92(NF616)Nippon Pipe M2W electrodes PWHT 765'c2hrs (Group ref F)								
KA1339/3	02/038	670	75.0	1000	1567	3.53	11.09	T IV
KA1395/3	02/039	650	75.0	2500	5410	2.17	11.55	T IV
KA1339/2	02/036	625	135.0	1000	1631	20.77	82.88	parent
KA1414/5	02/037	625	105.0	3000	7397	3.06	6.30	TIV (WM microcrack)
P92(NF616)SFEL: bar M2W electrodes PWHT 765°C 2hrs (Group ref G)								
KA1414/7	03/004	700	60.0	500	537	2.40	10.72	T IV (running into WM)
KA1339/4	02/042	670	75.0	1000	1577	3.44	3.34	WM
KA1414/8	02/043	650	75.0	2500	8531	3.35	5.94	WM
KA1295/3	02/040	625	135.0	1000	506	24.01	88.31	parent
KA1414/6	02/041	625	105.0	3000	7454	2.66	5.24	WM

Test Material & History :-			P91 As-Rec'd. MR02/027A Welded withMetrode. PWHT 760'c3hrs					
PTC Ref.	Test Ref.	Temp. 'C	Stress MPa.	Est. Dur.	Final Dur.	Elong. %	R.of A. %	Failure
KA1392/3	02/067	650	75	400	519	3.05	13.68	T IV
KA1395/5	02/077	635	75	1000	1246	3.06	15.3	T IV
								parent (T IV
KA1339/5	02/047	600	120	1100	934	19.92	78.16	microcracks)
KA1395/4	02/080	600	105	4000	2222	3.97	14.32	TIV

Test Material & History :-			P91 N & Tempered. MR02/027B Welded with Metrode. PWHT 760'c1hrs					
PTC Ref.	Test Ref.	Temp. 'C	Stress MPa.	Est. Dur.	Final Dur.	Elong. %	R.of A. %	Failure
KA1392/5	02/068	650	75	400	359	2.31	18.07	T IV
KA1395/7	02/078	635	75	1000	926	2.57	13.35	T IV
								T IV crack (running into
KA1392/4	02/096	600	155	100	215	18.34	55.32	necked parent)
KA1339/6	02/048	600	120	1100	1366	3.4	7.65	T IV
KA1395/6	02/081	600	105	4000	2176	3.01	15.47	T IV

Test Material & History :-			P91 Aged, MR02/027C Welded withMetrode. PWHT 760'c3hrs					
PTC Ref.	Test Ref.	Temp. 'C	Stress MPa.	Est. Dur.	Final Dur.	Elong. %	R.of A. %	
KA1395/10	02/069	650	75	400	430	10.46	28.77	T IV (slight PM neck)
KA1395/9	02/079	635	75	1000	1111	4.19	16.62	T IV
KA1339/7	02/049	600	120	1100	677	23.11	82.63	parent
								parent (minor type IV
KA1395/8	02/082	600	105	4000	2054	25.55	82.33	cavitation)

8.2.5 Microstructures for the Type IV Crack Specimens

The microstructures of the Type IV crack samples were taken at the position shown in Fig. 8.11. The Fig. 8.12 shows the microstructures of P92 weldment.
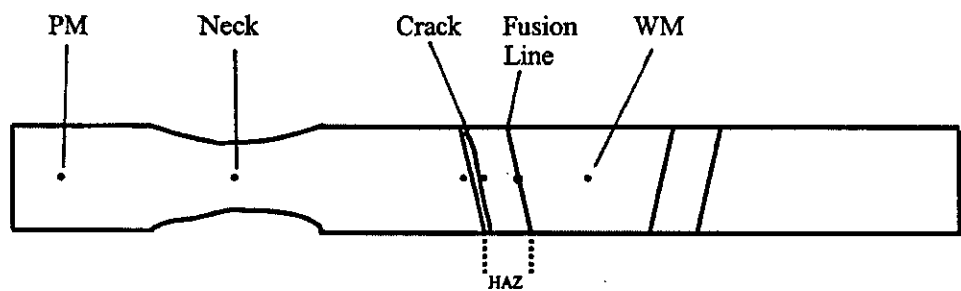
Fig. 8.11. The position where the microstructures were taken
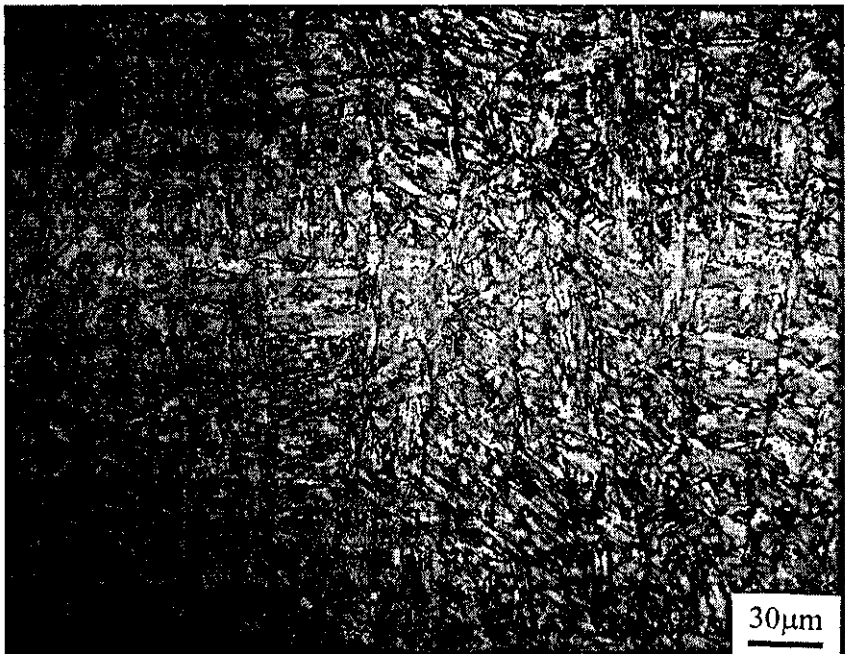
a (WM)
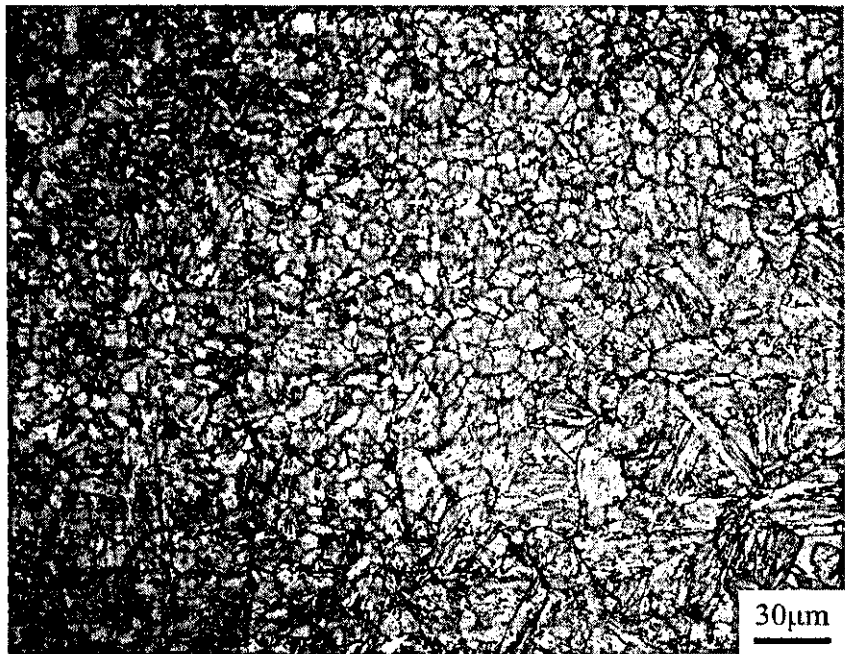
b (interface of WM and HAZ) (fine grain/ coarse columnar grain)
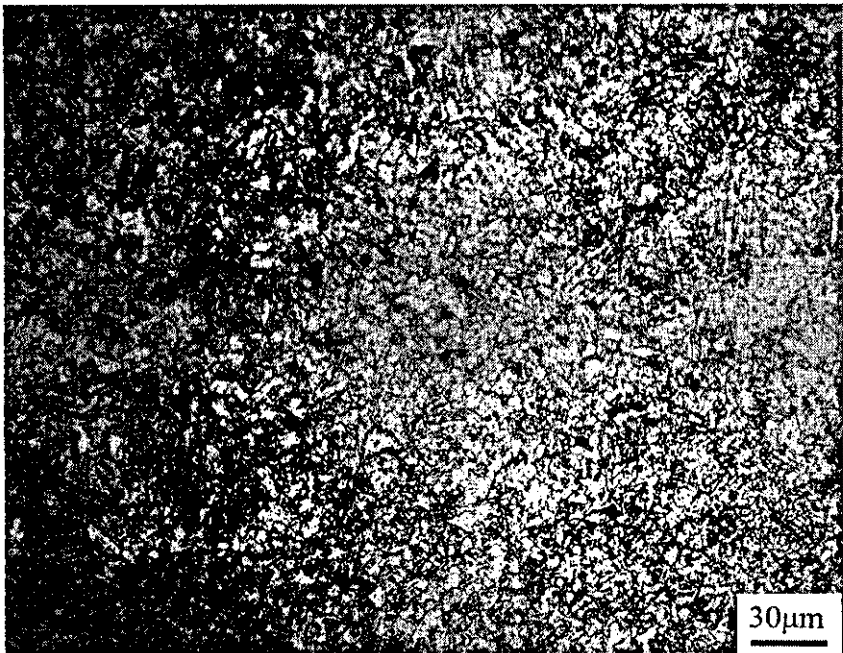
c (retransformed region of HAZ, close to the crack)
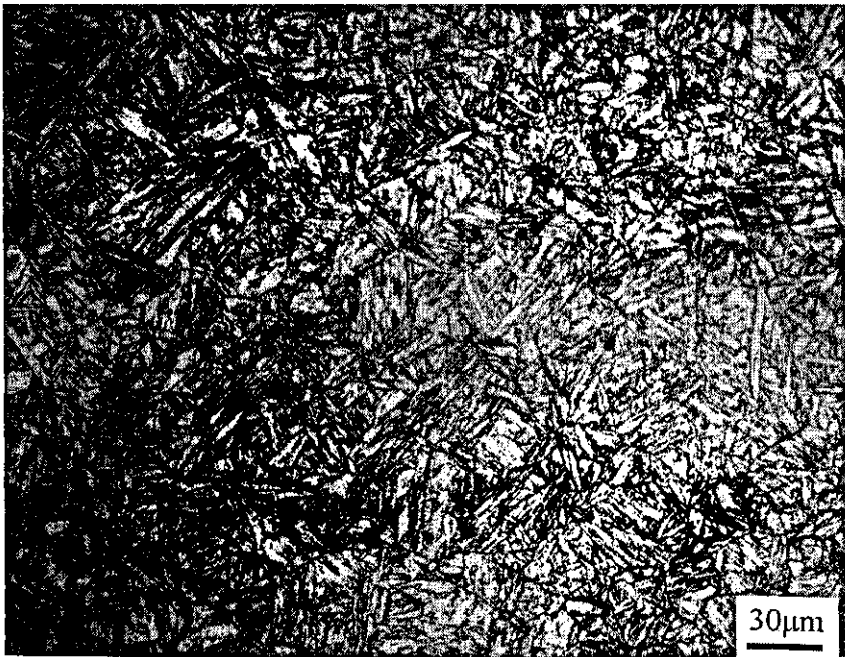
d (soft zone: PM close to the crack)

e (PM)
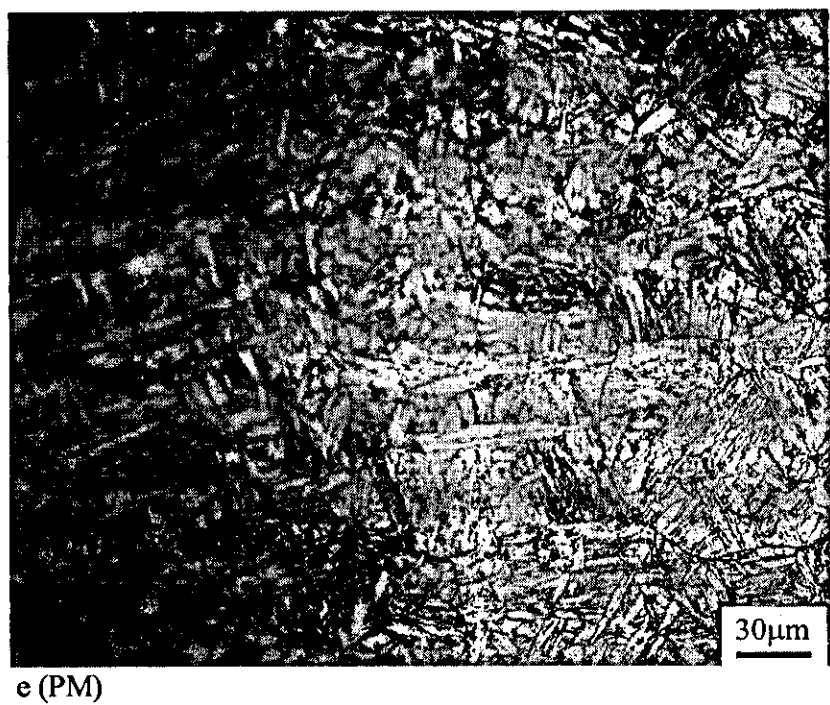
Fig. 8.12. Micrographs of P92 weldment

8.3 Discussion

8.3.1 The Type IV Crack Definition

The heat-affected zone (HAZ) is shown in Fig. 8.13. The Type IV crack is the crack that occurs in the fine-grained zone approximately one quarter of distance from the fine-grained region to the PM. This range is still between intercritical temperatures, Ac_3 and the melting point. For comparison the Type III crack region is also shown. Provided that fusion welding is employed, the Type IV zone will always be present. It is inevitable that there will always be a zone that is above the Ac_3 critical temperature range. The width and the distance of this zone from the fusion boundary may vary; in this case the HAZ zone is about 2.0mm wide while the Type IV zone is in the range of 0.1 to 0.5mm from the edge of the PM.
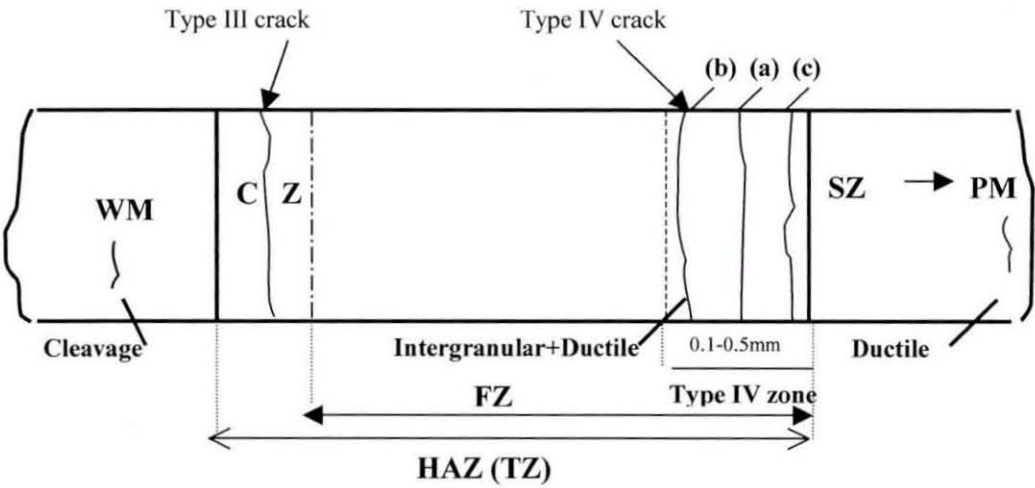
Fig. 8.13. The Type IV crack location

WM-Weld metal, CZ-Coarse grained zone, FZ-Fine grained zone, SZ-Soft zone, TZ-Transformed zone, HAZ-Visible heat affected zone, PM-Parent metal.
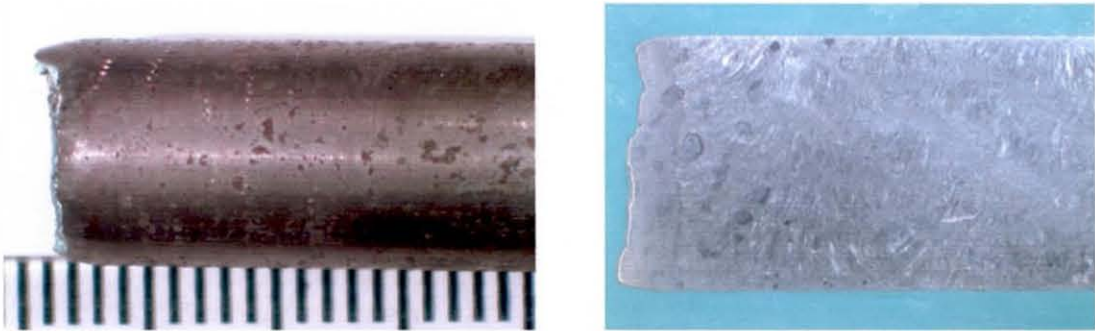
a)   1.7/2.0 (P91) (Elong 3.01%; R of A 15.47%)
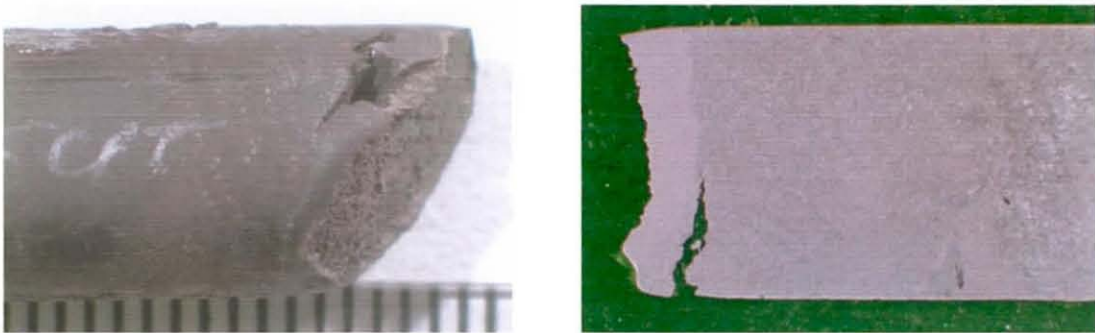
b)   1.5/2.0 (P122) (Elong 3.19%; R of A 3.87%)

c) 1.9/2.0 (P91) (Elong 18.34%; R of A 55.32%)

Fig. 8.14. Type IV cracking varies with the location

The typical Type IV crack (position (a) in Fig. 8.13) is where the crack is about 1.7mm away from the fusion boundary and 0.3mm away from the interface between HAZ and the soft zone. It has shown a flat fracture face (cleavage) and some deformation (ductile)(Fig. 8.14 a)). When the cracking is closer to the weld metal (the position (b) in Fig. 8.13 where the crack is about 1.5mm away from the fusion boundary), the fracture of Type IV crack is more like the cracks in weld metal (e.g. Type I and II cracks) with little deformation (cleavage), and with some secondary cracking in the weld metal (Fig. 8.14 b)). When the cracking moves toward to the interface of HAZ and soft zone (the position (c) in Fig. 8.13) where the distance of the Type IV crack away from the fusion boundary is about 1.9 mm), the Type IV cracking fracture exhibits severe plastic deformation, while the parent metal has almost failed (Fig. 8.14 c)). The welding process will only have an indirect influence through the heat input and the cooling rate and will not change the position of the Type IV cracking. A higher welding temperature will lead to a wider Type IV zone, which will be placed further away from the fusion line [3, 4]. Therefore it can be concluded that the Type IV cracking is strongly related to the parent metal, whereas the Type III crack region is strongly related to the weld metal, on which the heat input would have a significant effect.

8.3.2 Effect of Process Parameters on the Fracture

The testing results of all the creep specimens are summarized in Table 8.2 in order to investigate the effect of the various creep parameters (mainly the stresses and the temperatures).

8.3.2.1 Effect of stress

It can be seen in Fig. 8.15 that all the four types of materials have Type IV cracks and the 9Cr steel (P91, P92 and E911) is more sensitive to Type IV cracking compared with the
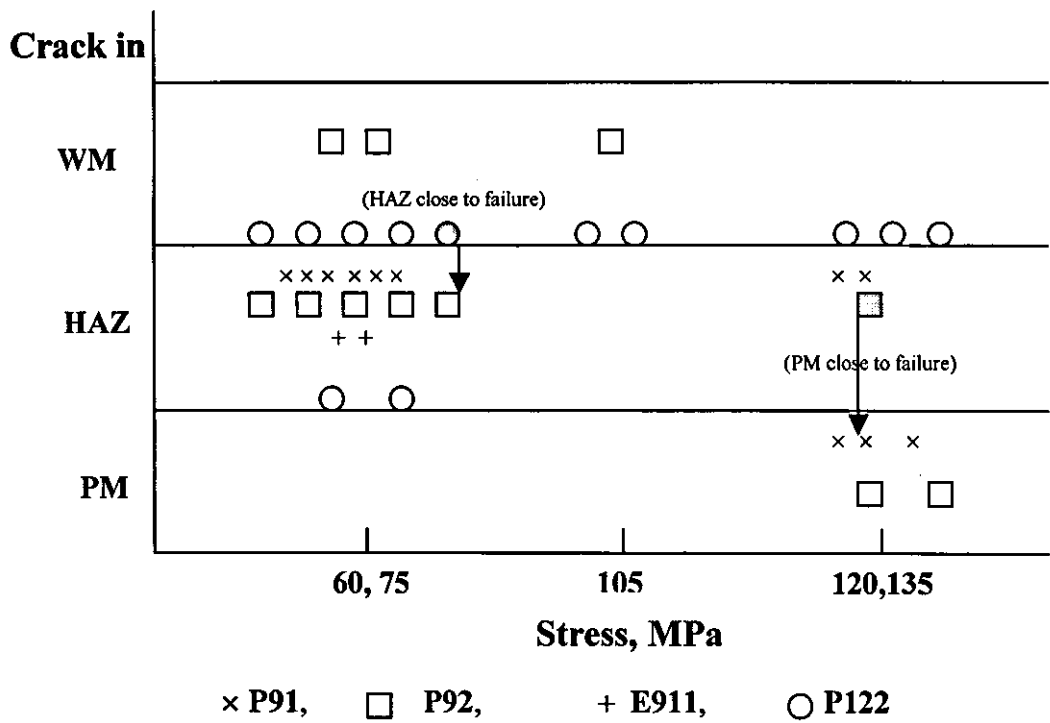
Fig. 8.15. The effect of the stress on the fracture

12Cr steel (P122) which tends to fail in the weld metal. From the Fig. 8.15 it is also clear that at the lower stress level there is more Type IV cracking. As the stress increases, the failure shifts to parent metal, and is more related to parent metal strength.

8.3.2.2 Effect of temperature

Fig. 8.16 shows that the temperature has no significant influence on the Type IV cracking. However, it can be seen that the PM failures always occur at lower temperature.

Crack in

WM

HAZ

PM

Temperature, °C

× P91,   □ P92,   + E911,   ○ P122

600, 625   650   670,700
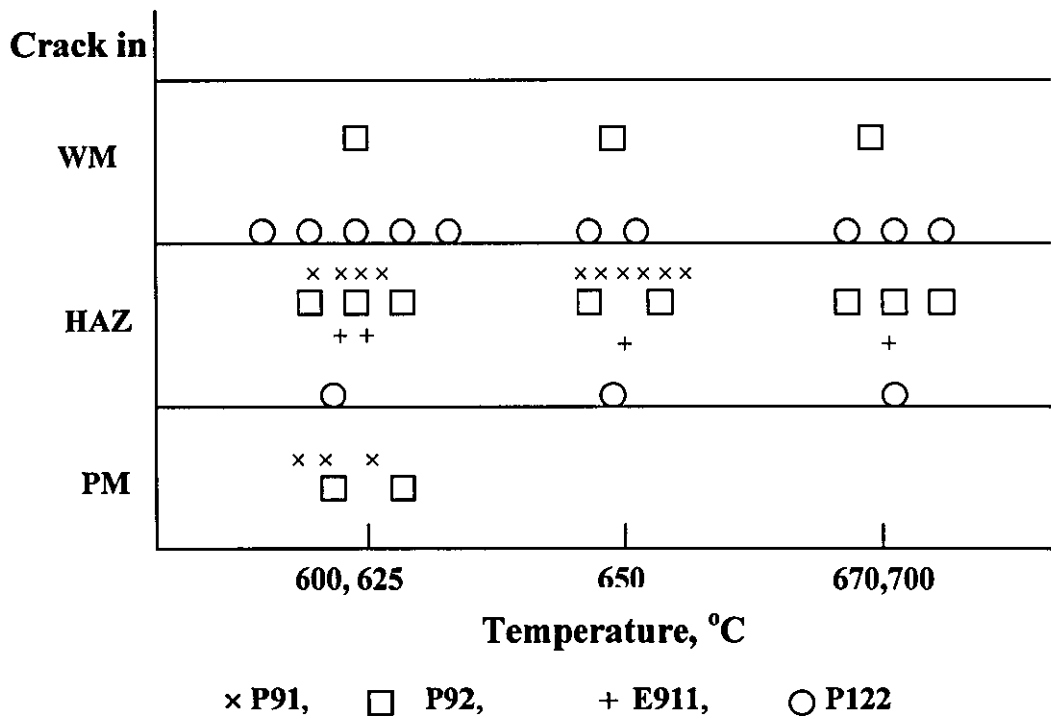
Fig. 8.16. The effect of the temperature on the fracture

8.3.2.3 Cracking sequence

Fig. 8.17 to Fig. 8.18 also shows the individual sequence of cracking at different stresses and temperatures. When the stress decreases at a given temperature, the possibility of the Type IV cracking increases, the amount of the Type IV cracked samples reaches maximum at 75MPa. Meanwhile only one PM failure was obtained at a lower temperature (625°C). When the temperature increases (Fig. 8.18), the cracking situation is almost same, and the amount of the Type IV cracks is unchanged.

625℃, 135MPa

a)
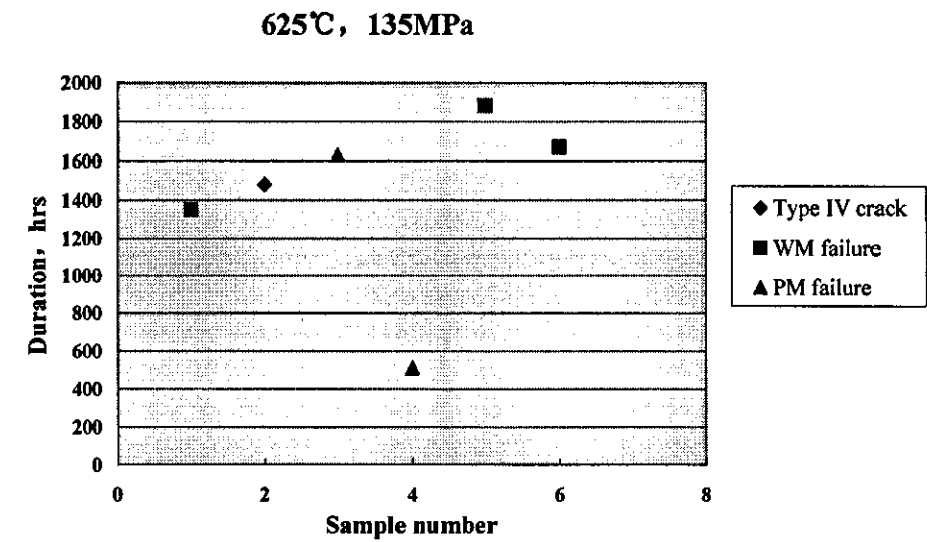
625℃, 105MPa
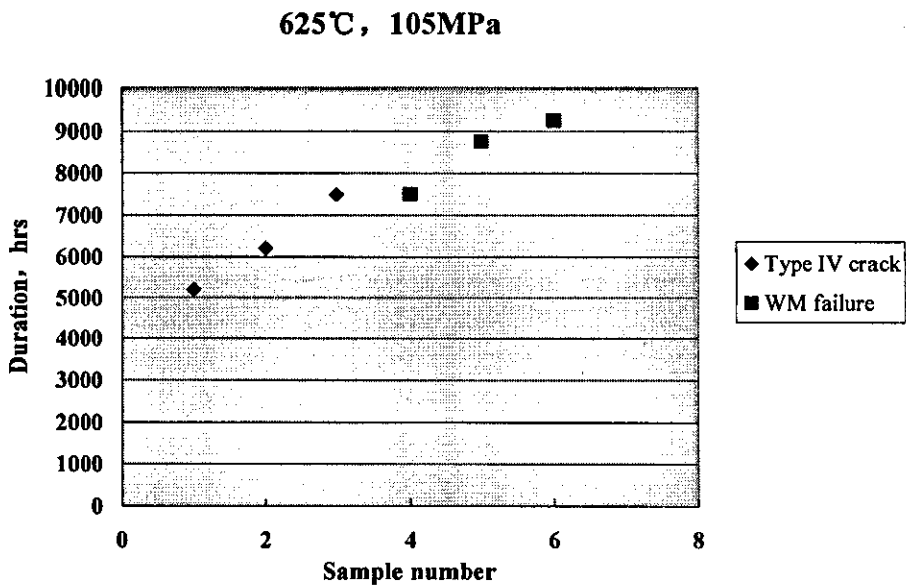
b)

Fig. 8.17. Cracking sequence at different stresses

1-P122 (TWI, 12A), 2-P92 (NF616, TWI), 3-P92 (NF616, W12),

4-P92(NF616SFEL, W12), 5-P122 (HCM12A forged), 6-P122(HCM12A cast)
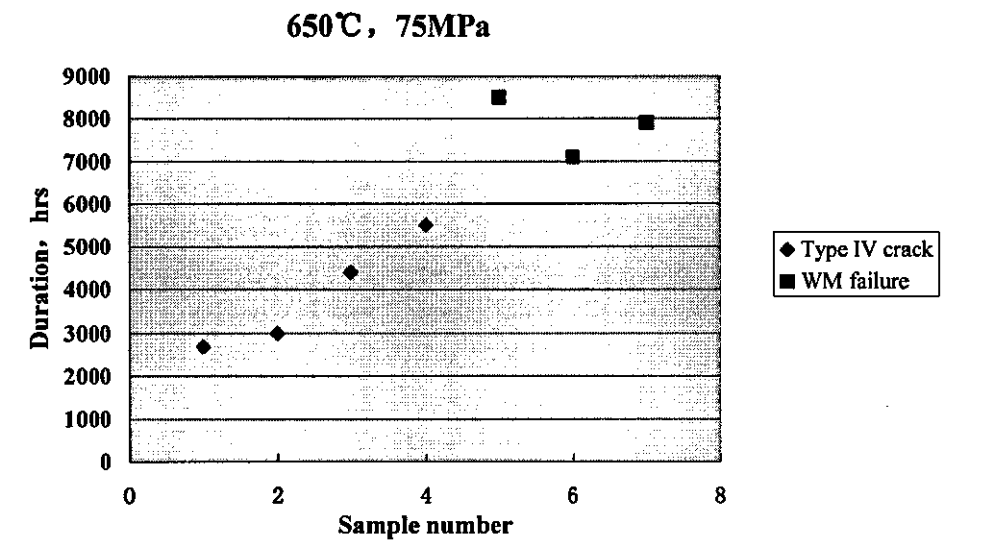
a)
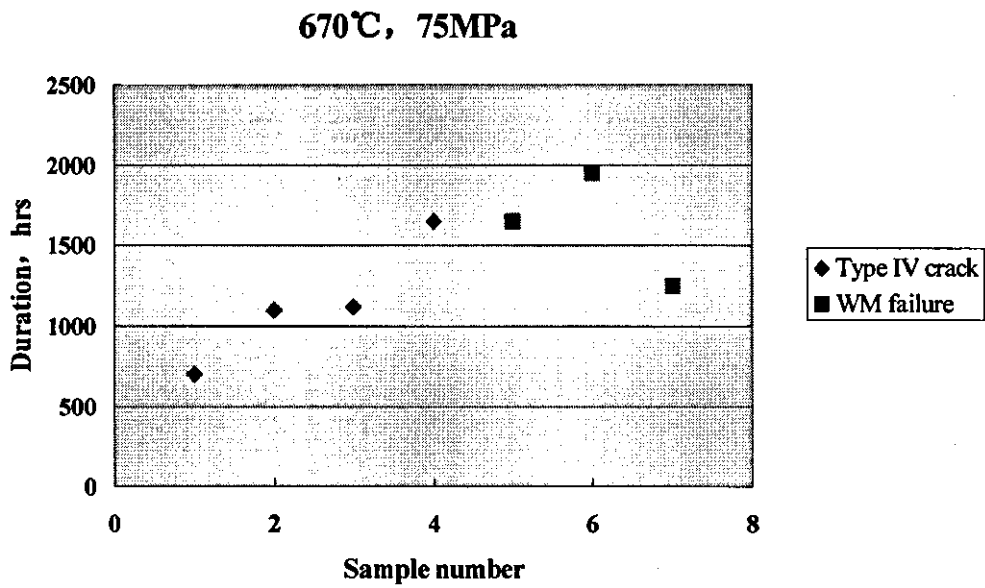
b)

Fig. 8.18. Cracking sequence at different temperatures

1-E911, 2-P122 (TWI 12A), 3-P92 (NF616, TWI), 4-P92 (NF616, W12),

5-P92 (NF616SFEL, W12), 6-P122 (HCM12A forged), 7-P122(HCM12A cast)

8.3.2.4 Effect of time

Fig. 8.19 shows that the type IV crack tends to occur after duration of around 2000 hours, particularly for P91 and P92 materials. The average values for P91 and P92 are 1042 hours and 2500 hours respectively. This is in agreement with other estimations that P91 shows Type IV cracking at a reasonably early stage in life [6,7].
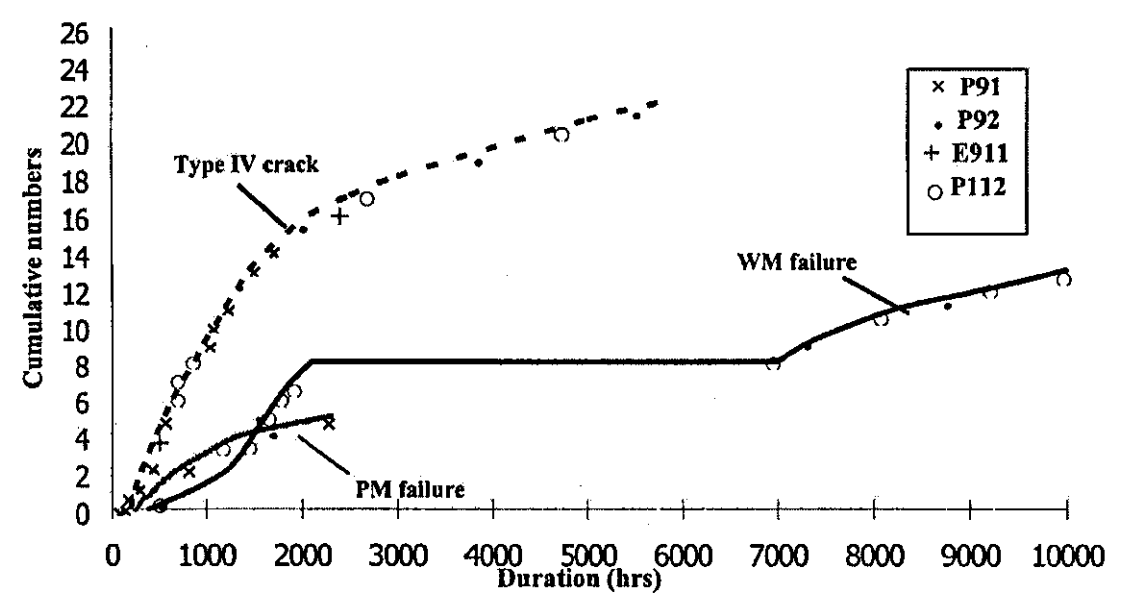
Fig. 8.19. Relative incidence of three cracks

8.4 Analysis on the Micro-Mechanism of the Type IV Cracking

8.4.1 Basic Theory

8.4.1.1 Cleavage fracture

The cleavage is a type of brittle fracture. It occurs by separation across crystallographic planes (crystals of mica split along their weakly bonded basal planes for example) under

the action of normal stress. Normally the cleavage plane is the low index crystalline plane with lower surface energy and theoretical strength. In body centred cubic metal the cleavage mainly happens along {100} plane. Although the cracking rate is rather low, it can still be divided into two stages: crack initiation and unstable propagation.

(1) Energy criterion for cleavage

The crack initiation and unstable propagation of cleavage will meet the Griffith energy criterion, i.e. the crack starts to propagate under the condition that the released elastic energy is larger than the work needed by the newly formed surface. Based on this criterion, the condition of crack propagation in plane stress can be given by[5, 6]:

$$\sigma_c = \left(\frac{\gamma E}{\pi \alpha_a} \right)^{1/2} \tag{1}$$

where σ_c is critical stress, γ is surface energy of the material, α_a is half length of the crack, and E is elastic modulus.

(2) Crack initiation

The crack initiation includes the microcrack initiation and microcrack propagation in the matrix resulting in cleavage. The microcrack will tend to nucleate at the brittle secondary phase particles, blocked slip bands or weak grain boundaries[7]. The propagation does not start immediately after initiation and will possibly stop at some discontinuous boundaries. The crack nuclei will expand in the matrix to induce cleavage only when the local stress reaches a critical value. On the other hand because the cleavage is based on the atomic bond separation occurring along specific crystalline planes, the crack nucleus tip inducing cleavage should have a sharpness equal to the atomic spacing.

(3) Unstable propagation of cleavage crack

This is not a continuous propagation to fracture after initiation: very possibly the propagation contains a series of pause and re-initiation phases. When the crack source induced cleavage crack propagates, it may meet a larger energy barrier e.g. grain boundary or secondary phase particle, and then propagation will not continue. Crack arrest can occur because the preferred orientation of a neighboring grain makes the crack tip passive; after that the newly formed crack nuclei in a high stress region of a crack tip induces the cleavage. The new cleavage crack propagation combines with the original crack and makes the propagation continue.

8.4.1.2 Ductile fracture

This is a common mechanism in materials that undergo easy plastic deformation. These types of fractures are characterized by depressions in the microstructure called dimples, which form from microvoids in places of high local plastic deformation. Voids form when the material is pulled apart internally. Under increased strain these voids (Fig. 8.20) gradually expand and join with other voids (coalescence) to form the fracture surface, which has a dimpled appearance to it. For the most part, these voids form at second-phase particles. In some instances, these particles can be found lying in the dimples on the fracture surface. These dimples are formed by either the particles tearing in half or the particle-matrix interface failing. The size and shape of the dimples is determined by the characteristics of the loading and the material. Also it depends on the stress direction. If the sample fails in tension, the dimples are round and equiaxed. If the sample is torn or sheared apart, the dimples might look like teardrops. Fig. 8.21 shows the parent metal ductile failure of P91.
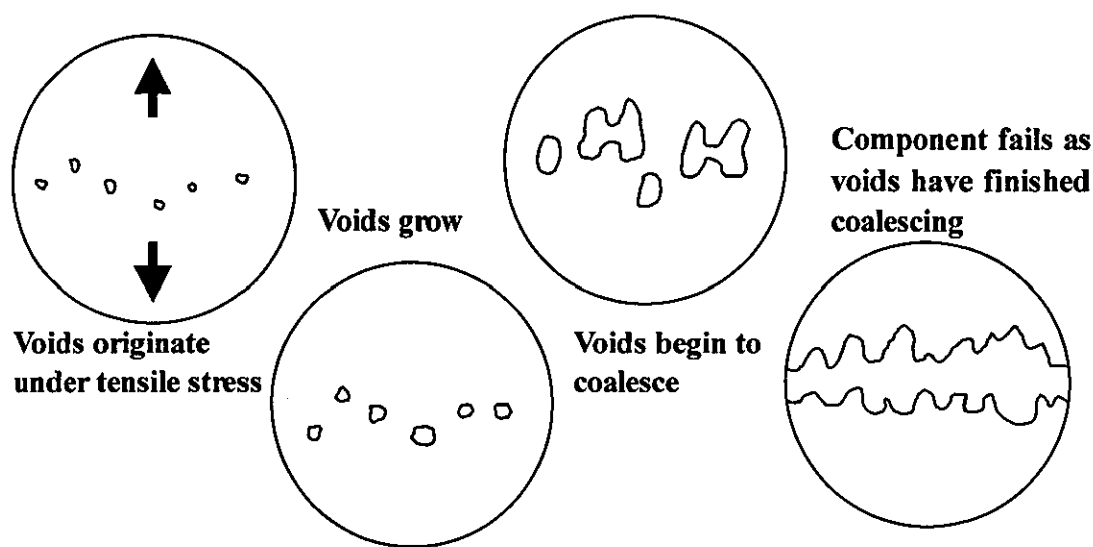
Fig. 8.20. The progression of void coalescence[8]
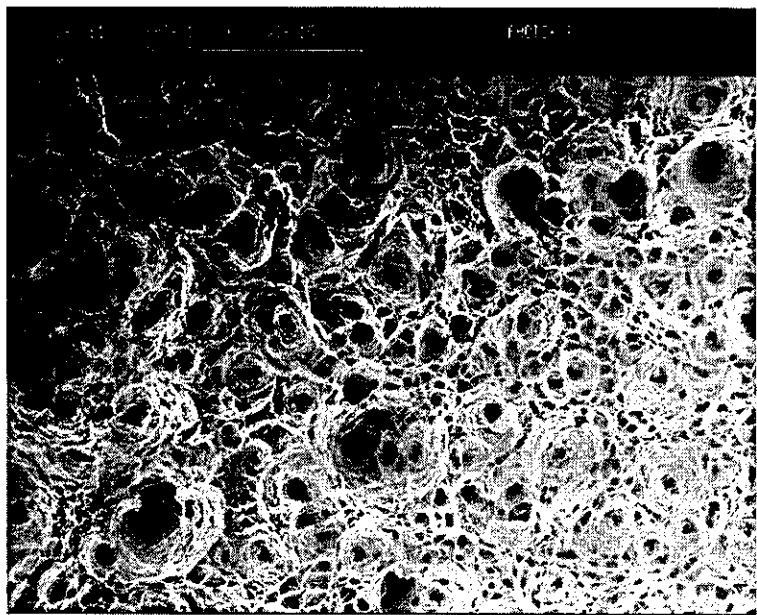
Fig. 8.21. Parent metal fracture, P91 (PM part in Fig. 8.13)

8.4.1.3 Quasi-cleavage

According to Brooks[7]on quasi-cleavage, "a fracture surface forms which consists of regions showing ill-defined or relatively faint signs of cleavage (sometimes called rosettes) separated by regions showing extensive plastic deformation. These latter regions are tear ridges." This is called quasi-cleavage and develops with microcracks and the subsequent tearing of the connecting material. The mechanism of the creep failure is associated with the cavitation at high temperature with the following characteristics:

- Intergranular

- Cavitation initiates at discontinuities in the microstructure, i.e. grain boundary precipitates

- Multiple initiation sites that are very localized at some microstructural features such as grain boundaries, weld fusion lines or weld centerlines

- Very little local deformation at the crack location thus no global deformation.

- Cavities grow slowly by a diffusion-controlled mechanism

- Cavity density and size increase until the cavities link-up and form microcracks

- Microcrack growth at rapid rates is dependent upon the cavity density, local chemistry and local stresses

The properties of creep cavities are as follows:

- They form in grain boundaries

- They are not surface connected or even interconnected until late in life

- They link to form intergranular cracks

- They are localized by weld geometry

This mechanism occurs when the grain boundary is the weakest part (i.e. at high temperature). So the fracture is changed from transgranular to intergranular as the temperature rises. Often other mechanisms can be found, but intergranular separation is the primary mechanism. Cavitation, GB precipitates and impurities in the grain boundaries are prime crack initiation sites. In such a case, small prior austenite grain size and the short martensite laths might not be so important to the fracture, as they both can enhance either the strength and the toughness, which should be good for preventing fracture. Here the prior austenite grain size in the HAZ is in grade 10 (8-10μm) compared with the grain size of grade 5 (40-50μm) in the weld metal (Fig. 8.13).

8.4.1.4 Intergranular fracture

The intergranular fracture is induced mainly by the cavitation (vacancies) and the segregation (impurities). This type of fracture occurs because there is significantly reduced GB energy due to Gibb's thermodynamic absorption of impurities. Generally the segregation of metal or gas-metal impurities changes the GB free energy. The changes of the GB energy result in intergranular cracking.

8.4.1.5 Mixed fracture

The differences of the segregation to GB can also produce a mixed fracture mechanism, in which ductile zones exist simultaneously with intergranular cracks. The brittle intergranular fracture is produced because of the thermal induced segregation to separate the grains along the smooth interface.

Usually the fracture that is caused by simultaneous action of two or more mechanisms is defined as 'mixed fracture'. The fracture induced by the mixed mechanism is dependant upon the following:
- Stress situation
- Load history
- Microstructure

● Environment

The mixed fractures involved in intergranular cracking are mainly as follows:

(1) Cleavage + intergranular. Both the cleavage and the intergranular mechanisms are based on low energy criteria. When the energy required for both mechanisms are equal, it is possible for these two mechanisms to take place simultaneously.

(2) Ductile + intergranular. This is a more common mixed fracture mechanism in the materials such as steels in which the typical intergranular fracture is shown in between ductile tearing regions.

8.4.2 Types of Particles in Ferritic Steels

In general most low carbon lath martensites fail by ductile fracture. However high temperature tempered P91 weld metal will exhibit brittle quasi-cleavage, mainly because of the strengthening effect of large quantities of alloying elements in the material. The strength of the high Cr ferritic steel is improved by large amounts of alloying elements through solid solution hardening and the precipitation mechanisms, which will normally reduce the ductility. The precipitation strengthening is dominant for P91 material. The precipitates and interaction between the precipitation stress fields and dislocations prevent dislocation movement.

The second phase particles in the P91 weld metal can be classified as three types[9, 10]:

● Coarse particles. These particles mainly are non-metallic inclusions (SiO_2 for example) which are not precipitates. They are characterized with larger diameter (e.g. $>1\mu m$), brittleness and low ductility. They will have no effect on the material strength but play a key role in crack formation and initiation

● Medium size particles. These particles are mainly $M_{23}C_6$ precipitates with diameter of about 0.1-$0.5\mu m$. They have a significant effect on the matrix strength and cracking

● Small particles. These types of particles are particularly defined as the fine MX carbides and nitrides formed by precipitation. They possess much smaller particle

diameter (only in order of several 10 microns). They are firmly dispersed, and will strongly influence the strength of the material

Generally when secondary phase strengthening (including precipitation and dispersion strengthening) is considered, the strengthening mechanism is distinguished from the deformation characteristics of the particles. In the tempered martensitic steels, small particles can be intersected by the dislocation, and can be considered as deformable particles. If the particle is larger, it becomes a non-deformable particle, e.g. $M_{23}C_6$ particles. The large inclusions such SiO_2 can be considered as non-deformable particles[11].

8.4.3 Micro-Mechanism of Cracking

8.4.3.1 Micro-mechanism of fracture

The stress in the plane strain condition reaches a maximum when it is at the crack tip (Fig.8.22). The crack propagation or formation will first occur from this position.
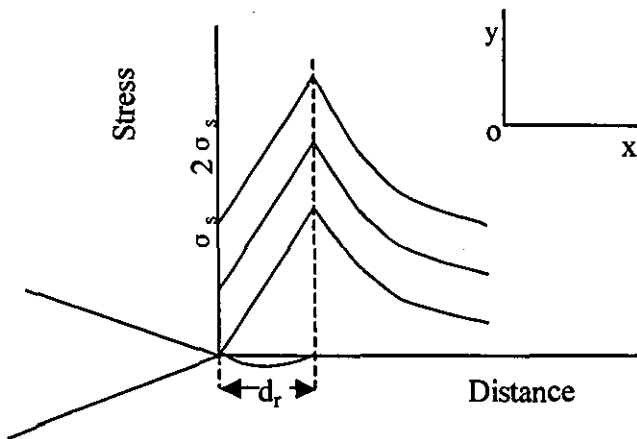
Fig. 8.22. The stress distribution of plasticity zone in plane strain[12]

Because there might be no microcracks at the main crack tip, and the nucleation and growth of the microcracks exists, the connection with the main cracks under the stress results in the propagation of macro-cracks (Fig. 8.23).
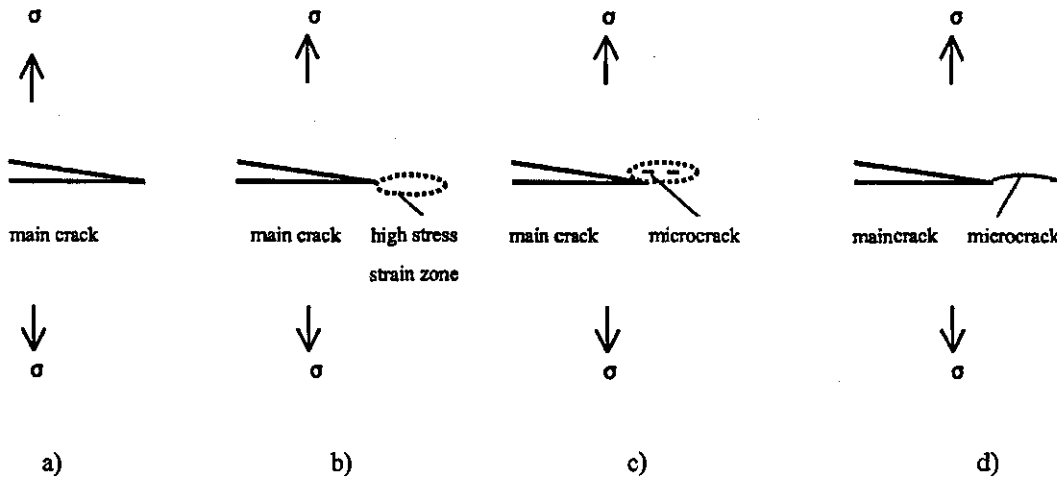
Fig. 8.23. Progress of cleavage induced in the macrocrack tip

   a) Macro-main crack under stress,

   b) A high stress-strain zone on the tip of main crack tip passivated,

   c) Microcrack occurs in the high stress-strain zone,

   d) Microcrack growth, connections with the main crack inducing cleavage

8.4.3.2 Influence of particles on fracture

As mentioned above, there are large quantities of inclusions in the high Cr ferritic steel weld metal. These particles play a significant role in the crack formation and propagation. Although the large particles can promote the nucleation of the microcrack, the volume fraction in the matrix and the HAZ zone is very small and the spacing is too big ($>500\mu m$). Therefore for the crack tip with a displacement of several microns, these inclusions have negative effect on promoting the crack propagation. By contrast, it is those finely dispersed particles and solid solution alloy atoms which play a key role in the propagation, because they prevent the dislocation movement. The matrix is strengthened, the ductile zone and plastic relaxation of the crack tip are reduced by those particles; and

they will enhance the propagation. Hence the fine particles are harmful to the crack growth.

Besides the particles, the grain boundary and sub-boundary can also obstruct the dislocation movement. Fine grain size brings the only method to improve both strength and ductility simultaneously. As the grain size reduces, strength increases. The grain boundaries can be thought as an accumulation of dislocations which produce interaction with the dislocations inside the grains to prevent slip. Multipass welding is used in high Cr ferritic weldments; there is a fine-grained region in the HAZ zone. There is no doubt that this region will benefit the toughness of the material. The sub-grain boundaries (martensite lath) can also have the same action as grain boundaries. Obviously fine martensite lath is better for the strength. However in this work, it was observed that the width of martensite lath in the TZ and SZ regions (Fig. 8.13) of weldments for all the high Cr ferritic steels were almost same. However, the fine grain size in the HAZ has no effect on the Type IV cracking which is an intergranular fracture mechanism, because more grain boundaries will increase the possibility of the intergranular segregation along the grain boundaries.

8.4.3.3 Factors controlling fracture

As known, the microstructure is the key to determining the mechanical properties of materials, hence we always hope to use the microstructure of materials to predict its macro-properties, or determine the microstructures based on the property required, in order to obtain best property/cost ratio materials through metallurgical methods.

It is possible to establish the quantitative relationship between mechanical properties and microstructure in order to provide a precise basis for optimizing the material composition and heat treatment.

Microstructural features, which control the material properties in Fe-Cr steels, include:
- Residual austenite content

- Twin crystal amount
- Carbide size and distribution
- Grain size
- Metallic and non-metallic inclusion and its spacing
- Lath martensite width
- Solute atom strengthening
- Dislocation density

Because the Type IV cracking has been shown to be involved with the ductile and intergranular fracture at high temperature, the carbide precipitation and coarsening at a given temperature on the grain boundary will play a key role in determining this mechanism.

8.4.4 The Grain Boundary Precipitation (GBP) Model Application

This is based on the GBP model in Chapter 4. Fig. 8.24 shows the model prediction and the experimental results, which are in well agreement. There is a very important phenomenon which can be seen in Fig. 8.25 that the $M_{23}C_6$ precipitates grow and coarsen faster in the Type IV zone than in the soft zone. The recovery of excessive dislocations is also faster for the Type IV zone heated up to Ac_3. It is considered that the lower creep strength of fine grained HAZ structures is attributed to the high rate of precipitate growth.
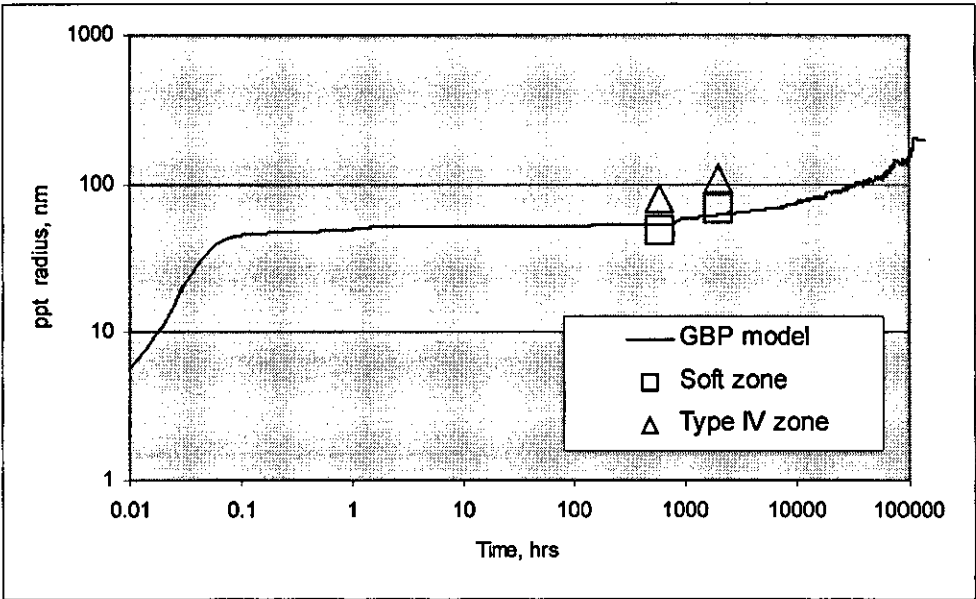
Fig. 8.24. Simulated $M_{23}C_6$ precipitation kinetics in P91, aged at 600°C

a)

b)
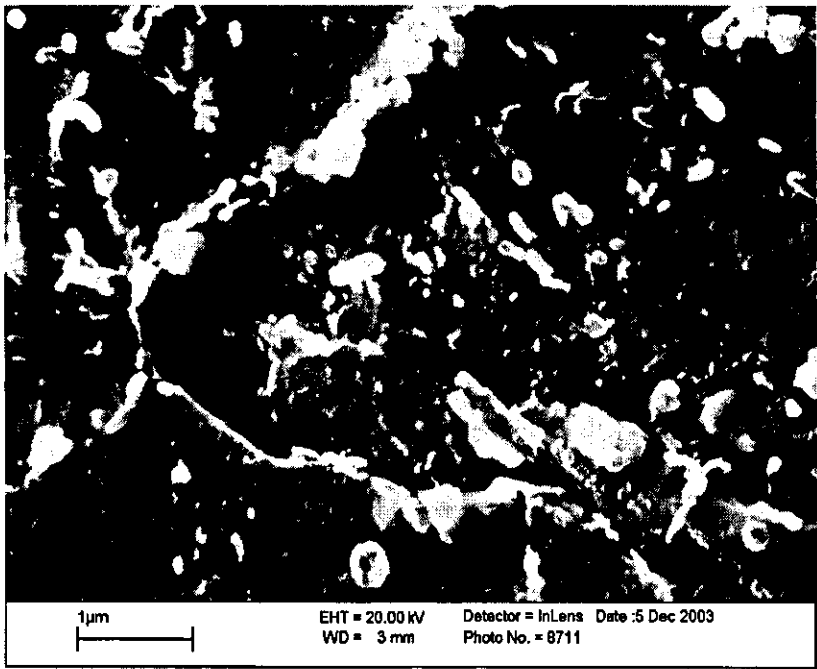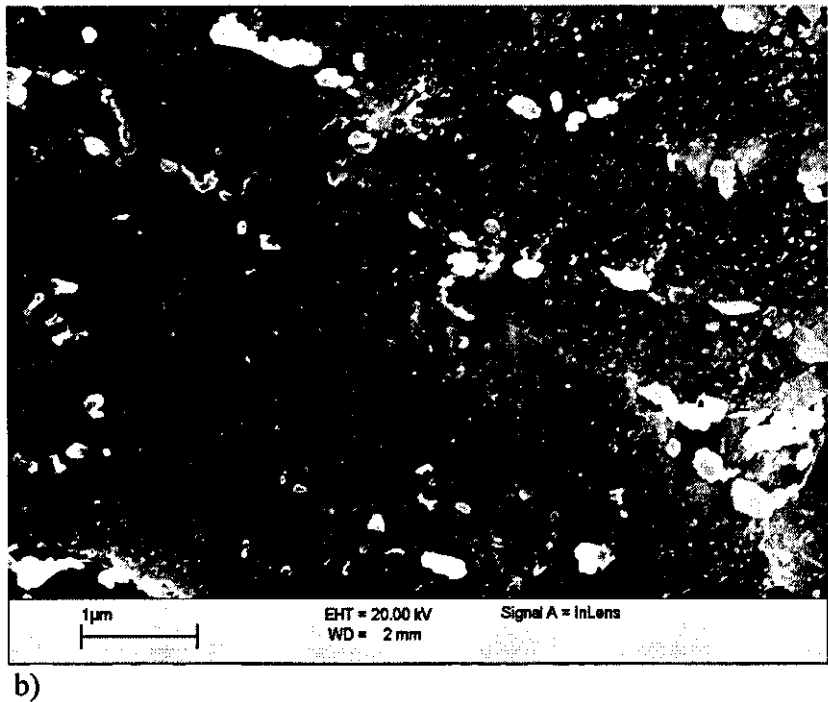
Fig. 8.25. SEM precipitates, 2000h ageing at 600°C

   a) Type IV zone, b) soft zone

In contrast with Type III cracking region where the cracking mechanism has been confirmed to be the carbon depleted zone formed near the fusion line and the large amount of δ-ferrite which will grow significantly with time at service temperature, there is no δ-ferrite in the Type IV region, so the fracture mechanism will be totally different. Although the P122 is a exception (see Fig. 6.8 in Chapter 6), which has a δ-ferrite containing transformed zone, the failure always tends to occur in the weld metal in this material. Hence the soft constituent δ-ferrite does not appear to be a key factor in Type IV cracking.

The data used in the theoretical calculation for the MCS approach in Chapter 4 (Fig. 8.24) are listed in Table 8.3.

Table 8.3. The data used in the theoretical calculation for the MCS approach

	Parameter	Unit	Value	Reference
a	lattice parameter	nm	0.2866	[14]
V_θ	molar volume, precipitate	$m^3 \, mol^{-1}$	1.82×10^{-4}	[14]
V_α	molar volume, matrix	$m^3 \, mol^{-1}$	9.05×10^{-6}	[15]
D_b	grain boundary diffusion pre-exponential term	$m^2 \, s^{-1}$	502	[15]
Q_b	grain boundary diffusion activation energy	$kJ \, mol^{-1}$	283.1	[15]
D_{V0}	volume diffusion pre-exponential term	$m^2 \, s^{-1}$	8.5×10^{-4}	[16]
Q_V	volume diffusion activation energy	$kJ \, mol^{-1}$	240	[16]
ψ	contact angle	degree	57	[13]
ΔH	enthalpy of solution	$kJ \, mol^{-1}$	102.9	
ΔS	entropy of solution	$J \, mol^{-1} \, K^{-1}$	-109.3	

8.4.5 Model for the Type IV Cracking

8.4.5.1 Thermodynamics of impurities and vacancies at grain boundary

Grain boundary adsorption is an important aspect of the thermodynamic and kinetic properties of grain boundaries, such as mobility, energy, diffusivity; and those of polycrystalline systems, such as brittleness. The theory is based on the Gibbs' thermodynamic model and the GB structure.

(1) Impurity absorption at GBs

The Gibbs' thermodynamic method has been applied successfully to GBs. The Gibbs' equation[17]

$$d\sigma = -\sum_i \Gamma_i d\mu_i \tag{2}$$

relates the microscopic parameter: adsorption of ith component, Γ_i; the GB surface tension, σ; and the chemical potentials of the components in the bulk of the grain, μ_i. It is presumed that a grain boundary is as a homogeneous layer of thickness λ and density ρ. Then

$$\Gamma_i = \lambda(N_i^s \rho^s - N_i \rho) \tag{3}$$

where N_i^s and N_i are the atomic fraction of the ith component on the boundary and in the matrix, respectively, ρ^s and ρ are the atomic densities on the boundary and in the matrix, respectively. N_i^s, which represents the Zhuchovitsky adsorption isotherm, is given by[18]

$$N_i^s = \frac{BN_i}{1 - N_i + BN_i} \tag{4}$$

therefore

$$d\sigma = -ZkT\left[\frac{B-1}{1-N_i+BN_i}\right]dN_i \tag{5}$$

i.e. $\sigma - \sigma_1 = -ZkT\ln(1 - N_i + BN_i)$ \hfill (6)

where σ_1 is the equilibrium GB surface tension, Z is the concentration of impurity adsorption sites on the boundary, B is a constant given by

$$B \cong \exp[\frac{0.75E_f}{kT}]$$ (7)

E_f is the formation energy, which is 1.4eV for ferritic steel, k is the Boltzmann constant $(=1.38\times10^{-23}$ JK$^{-1})$.

(2) Adsorption of vacancies at GBs

The description of vacancy adsorption, Γ, by the Gibbs equation is

$$\Gamma = -\frac{N_v}{kT}\frac{d\sigma}{dN_v}$$ (8)

where σ is the grain boundary surface tension, N_v is the vacancy concentration in the bulk. Assuming that the GB consists of bulk matrix atoms and one other component, the vacancy, the GB adsorption isotherm coincides with the Langmuir isotherm for free surfaces.

$$\Gamma = \frac{ZbN_v}{1+ZbN_v}$$ (9)

where b is an absorption constant given by

$$b = b_0 \exp(\frac{0.5H_v}{kT})$$ (10)

H_v is the enthalpy of vacancy formation in the bulk, b_0 is a constant.

Therefore

$$\sigma - \sigma_1 = -ZkT \ln\left(\frac{1+bN_v}{1+bN_v^{eq}}\right) \tag{11}$$

where N_v^{eq} is the equilibrium thermal vacancy concentration for a given temperature. N_v and N_v^{eq} can be expressed by

$$N_v = N_v^0 \exp\left(\frac{-E_f^{\sigma}}{kT}\right) \tag{12}$$

$$N_v^{eq} = N_v^0 \exp\left(\frac{-E_f^0}{kT}\right) \cong \exp\left(\frac{-H_v}{kT}\right) \tag{13}$$

where N_v^0 indicates the number of lattice sites, E_f^{σ} is the formation energy of vacancy when the stress is present, E_f^0 is the formation energy of vacancy when $\sigma = 0$. The volume and number of the vacancies are related to the stress as follows:

$$E_f^{\sigma} = E_f^0 - \sigma_c \Delta V_v \tag{14}$$

where ΔV_v is the volume of a void.

8.4.5.2 Intergranular embrittlement in solids

It is well known that elements like P and S will embrittle materials like steel[19]. The reason for this behavior is believed to be the segregation of impurities to the GBs with a resultant loss of GB energy and thus the resistance to intergranular (IG) fracture. Lim and Watanabe[20] showed that there is a correlation between IG fracture resistance and GB type. GB types are increasingly being characterized in terms of coincidence site relationship terminology. The number of atomic sites on either side of the boundary that coincide as a fraction of total site density is denoted by a Σ value. The Σ value is a measure of the

disordered state of the boundary. High Σ values indicate high levels of disorder whereas low Σ values indicate almost perfect matching, similar to coherent twin boundaries.

Generally the crack initiation and propagation should be in accordance with the Griffith energy criterion (Equation (1)). When the GBs and impurities are considered, a small increment of GB energy caused by changing either the vacancy or impurity concentration on the GB will result in a much larger change in the work of fracture. This is because the work of fracture must be provided by a dislocation pile-up mechanism around the advancing crack tip on the GB. In other words, additional work must be provided to deform the materials at the crack tip in addition to the conventional work needed to overcome the GB energy. The revised formula was given by Orowan

$$\sigma_c = \left[\frac{100 E \gamma_\rho}{\pi d} \right]^{\frac{1}{2}} \tag{15}$$

where γ_ρ is surface energy or elastic deformation work, d is the grain size since it is assumed that cracks of the order of the grain size are present when considering IG fracture.

Therefore, the GB fracture energy in terms of the equilibrium thermodynamics of the impurity-containing GB and the misfit of the impurity with the matrix can be calculated. The only unconsidered feature is that of the GB structure. This is reflected in the value of Z in Equation (5). Z is described as the fraction of GB sites available to be occupied by impurity atoms and related to the Σ value for the GB in the following way

$$Z = \left(1 - \frac{1}{\Sigma} \right) \frac{d_{gb}}{\Omega} \tag{16}$$

where d_{gb} is the GB width (~2nm) and Ω is the atomic volume. This returns us to the discussion of the ideas of Lim and Watanabe[20], who indicate that σ_c will be influenced by GB structure. The above equation supports the contention that as Σ decreases (better fitting, Z reduces and so the reduction in σ_c is less significant. Thus, low Σ boundaries will be stronger than high Σ boundaries.

8.4.5.3 Type IV cracking mechanism

Based on the above basic theory and the experimental results, a new mechanism of the Type IV cracking is established and described in Fig. 8.26. When the weldment is under the tensile stress at a given temperature, the vacancies originate in the matrix and tend to move towards the grain boundary, and then coalesce in the boundary as voids resulting in a stress concentration on the tip leading to the main crack nucleation and formation. Because the stress concentration of the crack tip is at the stage that it is difficult to relax to reach the rupture strength of material, the cracks grow by a mixed cracking mechanism in which the intergranular separation is dominant. At the same time the $M_{23}C_6$ carbides on the grain boundaries grow and coarsen faster at high temperature, and re-initiate microcracks on the tip. The propagation of the main crack is connected with the microcracks. The carbide distribution along the boundaries and faster growth in the fine grained zone of the HAZ allow the crack to propagate easily, which results in weakened grain boundaries and final separation of the grain boundary. Fig.8.27 shows the grain boundary separation caused by the void crack initiation. A clear micro crack around a whole grain boundary can be seen in Fig. 8.28.
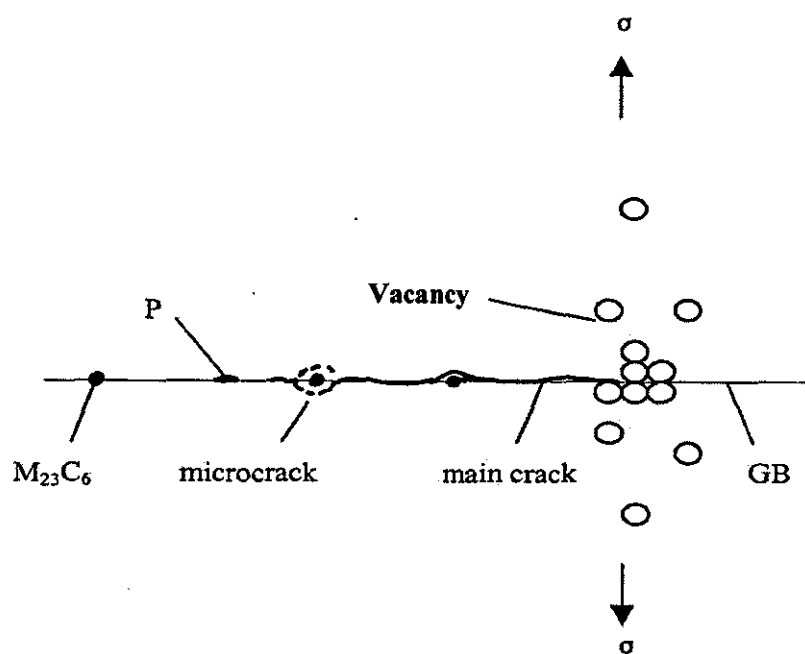
Fig. 8.26. Type IV cracking mechanism
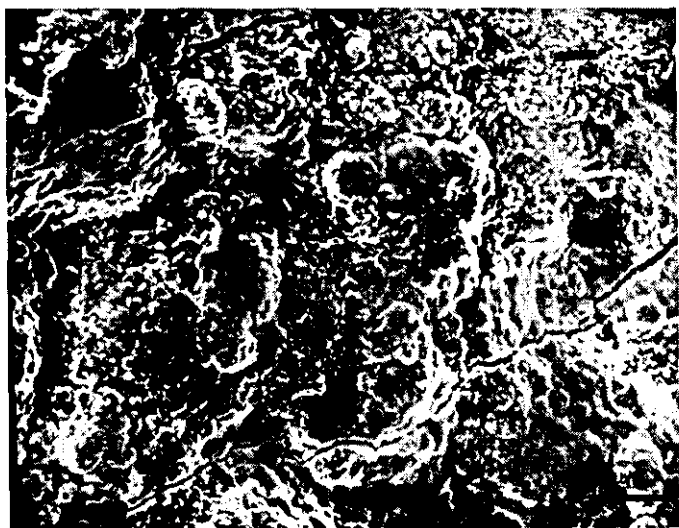
Fig. 8.27. Secondary cracks along the grain boundary
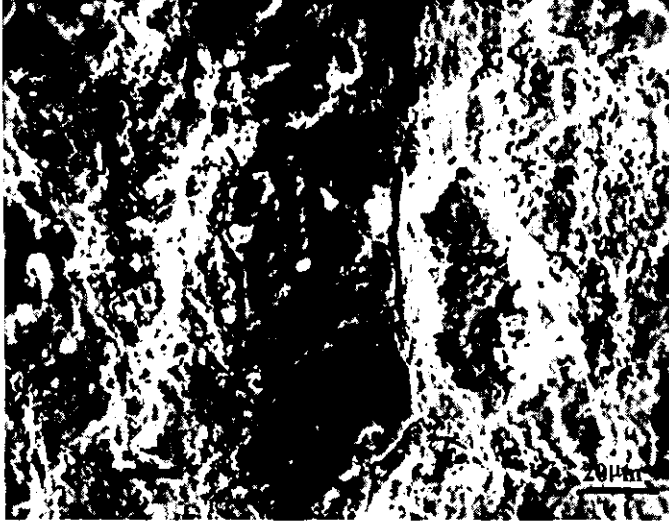
Fig. 8.28. A microcrack around a grain

Based on the Type IV cracking mechanism, the γ_ρ in the equation (15) can be expressed as follows

$$\gamma_\rho = -A\gamma_{\rho S} - B\gamma_{\rho P} - C\gamma_{\rho V}$$ (17)

where $\gamma_{\rho S}$, $\gamma_{\rho P}$ and $\gamma_{\rho V}$ are the elastic deformation work or intergranular work-of-fracture required to overcome the impurities, precipitates and voids, respectively. A, B and C are constant which depends on the degree of segregation, precipitation and void formation.

$\gamma_{\rho S}$ can be obtained from the equation (6)

$$\gamma_{\rho S} = \sigma_1 - ZkT \ln(1 - N_i + BN_i)$$ (18)

where $N_i = C_g^i$, which can be calculated from the equation (7) and (10) in Chapter 3.

$\gamma_{\rho P}$ is related to the precipitate size, spacing, and can be described as

$$\gamma_{\rho P} = \mathrm{f}(\gamma_i, \text{size, spacing}) = \frac{a_2 \sigma_1 L}{d_s} + b_2 \qquad (19)$$

Where γ_i is the interfacial energy, b_2 is the intergranular work-of-fracture related to precipitation. The size (L) and spacing (d_s) of the precipitate can be calculated based on the precipitation model (equation 26 and 34) in Chapter 4 respectively.

$\gamma_{\rho V}$ can be obtained from the equation

$$\gamma_{\rho V} = \sigma_1 - ZkT \ln\left(\frac{1 + bN_v}{1 + bN_v^{eq}}\right) \qquad (20)$$

Therefore the γ_ρ will be a function of the precipitate size, spacing, Z value and the segregation which can be defined as

$$\gamma_\rho = \sigma_1\left(1 - \frac{L}{d_s}\right) - ZkT\left(\ln(1 - N_i + BN_i) + \ln(\frac{1 + bN_v}{1 + bN_v^{eq}})\right) \qquad (21)$$

The relationship between critical stress σ_c and particle size L can be seen from Fig. 8.29 that σ_c decreases significantly as precipitate size increases. When the carbides on the grain boundary grow in the coarsening stage (Fig. 8.24), the fracture stress is minimised. The experiment has shown (Fig. 8.29) that the precipitate size is around 200-250nm when Type IV cracking occurs for both P91 and P92 materials. This is well in agreement with the model simulation.
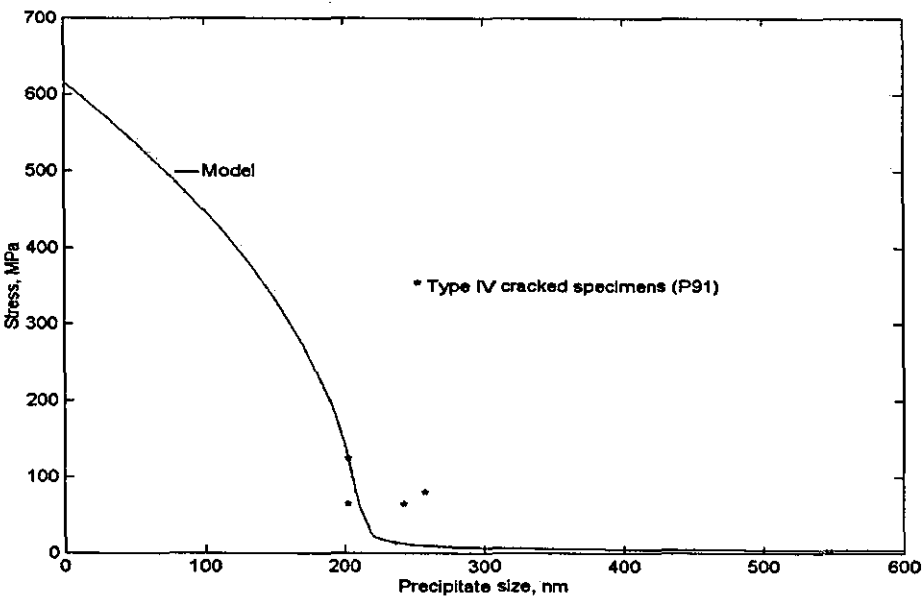
Fig. 8.29. Relationship between fracture stress and precipitate size on the GB

The data used in calculations for equation (21) are shown in Table 8.4.

Table 8.4. Data used in calculations for Equation (21)

Property	Value
σ_1, GB surface energy, Jm^{-2}	2.85
d, grain size, m	5.0×10^{-5}
E_f, formation energy, eV	1.4
Ω, atomic volume, $mm^3\ mol^{-1}$	1.0×10^{-5}
d_{gb}, GB width, m	1.0×10^{-9}
Σ, GB structure parameter	99
E, Young's modulus, MPa	2.1×10^{-5}
H_v, enthalpy of solution, eV	1.0
S_v, entropy of solution, eV	0.02

The data used in calculations for particle size (L) in Equation (26) in Chapter 4 are listed in Table 8.5.

Table 8.5. The data used in calculation for particle size (L)

Parameters	Explanation	Units	Value
T_s	Solute treatment temperature	K	1323
$0.50T_{mp}$	Half of the melting point	K	1023
d	GB width	m	5×10^{-6}
ψ	Angle of GB and precipitate	°	57
a	Lattice parameter	m	3.649×10^{-10}
A_v	Mean collector plate area	m²	6.3×10^{-6}
E_b	Solute-point defect complex binding energy	eV.atom	3.61×10^{-2}
E_f^v	Vacancy formation energy	eV.atom	1.6
ρ_α	Molar density of matrix	mol m⁻³	1.4092×10^5
ρ_θ	Molar density of precipitate	mol m⁻³	5.496×10^3
V_θ	Molar volume of the precipitate phase	mol⁻¹	1.81932×10^{-4}
x_θ	Solute concentration on precipitate phase	mol.fr	0.78
$\sigma_{\alpha\theta}$	Specific interfacial free energy of the interface	J.m⁻²	0.668
δ	Numerical constant		0.05
A	Constant		1
ΔH	Enthalpy of solution of the precipitate	J.k⁻¹	1.2096×10^5
D_I	Volume diffusion coefficient of solute at ageing temperature		1.7×10^{-5}

8.5 Conclusions

1. All Fe-Cr steel weldments exhibit Type IV cracking, which occurs at the outer edge of visible HAZ.

- For P92 welds, the failure at both the higher temperature/lower stress and lower temperature/higher stress seems to be Type IV cracking.
- For E911 material, at the low stress level of 75MPa the crack occurred in the fine grain zone of the HAZ.
- It is more confusing for P122 materials. Type IV cracking occurs in TWI's welds at lower stresses (75MPa) (and higher temperature of 670°C), however for the casting and forging welds, the failures all are in the weld metal, which are not influenced by either stress or temperature.
- Generally at the high stress levels, the crack will occur in the soft zone, whereas at the lower stress levels the crack shifts towards the retransformed region of the HAZ; it can be seen from the testing results that at the higher stress, secondary cracking or necking occurs in parent metal for most creep samples.

2. The microstructures in the HAZ for all the materials are mostly tempered lath martensites. No δ ferrites were observed in any creep specimen.

3. The Type IV crack will be more likely occur at lower stress, whereas at higher stress levels, the crack will shift to the soft zone.

4. There is no strong temperature effect on the Type IV cracking.

5. The cavitation initiation and rapid GB precipitate growth induced inter-granular fracture is the mechanism of the Type IV cracking.

6. The grain boundary segregation precipitation (GBSP) models are contributed to an explanation of Type IV cracking.

7. A new fracture model for the Type IV cracking in high Cr steel weldments is proposed.

8.6 Advices on Practice

From the discussion of Type IV cracking in the preceding paragraph, it might be thought, when the subject is examined from a creep point of view, that the chemical composition of the weld metal is of interest. This is, however, only partly the case. The chemical composition affects the creep strength of the weld metal and, because of the stress distribution mechanisms that are activated in a creep-loaded weld, the creep lifetime of the Type IV zone is also affected. Too strong a weld metal will lead to a concentration of creep strain in the weakest area, i.e. the Type IV zone. Moreover, when deformed, a weld metal that is weaker than the parent metal will attempt to shed its load onto adjacent region and thereby induce a Type IV failure. So the optimum solution is probably to aim at weld metal creep strength in the same range as that of the parent material.

References to Chapter 8

1.   H. Cerjak, R. Prader, R.W. Swindeman and S.A. David, Trends in Welding Research, Proc. of the 4th Inter. Conf., Gatlinburg Tennessee, USA, 5-8 June 1995, 563-568.

2.   H. Cerjak and E. Letofsky, Trends in Welding Research, Proc. of the 5th Inter. Conf., Pine Mountain, Georgia, USA, June 1-5, 1998, 143-148.

3.   E. G. Sanchez, An Initial Study of High Chromium Ferritic Weld Metals, report, Loughborough University, Aug. 2001, 145-149.

4.   Eva-lena Bergquist and A.B. Esab, Consumables and welding modified 9Cr-1Mo steel, Svctsarcn, No. 1-2, 1999, 22-25.

5. S. J. Brett, Type IIIa Cracking in 1/2CrMoV stream Pipework System, Proceedings of IOM/ImechE Conference: Integrity of High-Temperature Welds, P3, Nottingham, November 3-4, 199-208.

6. I. A. Shibli, Creep and fatigue crack growth in P91 weldments, Proceeedings of the 9th Inter. Conf. On Creep & Fracture of Engineering Materials & Structures, Swansea, UK, 1-6 April 2001, 1-12.

7. J. A. Brooks, A.W. Thompson, and A.Williams, Fundamental Study of the Beneficial Effect of Delta Ferrite in Reducing Weld Cracking, Welding Journal, 63(2), 1984, 71-83.

8. D.J. Gooch and S.T. Kimmins, Type IV Cracking in 1/2Cr 1/2Mo1/4V2Cr Mo weldments, Proceedings of the International Conference on Creep and Fracture of Engineering Materials and Structures, Swansea, April, 1987, 88-95.

9. S.J. Brett, Cracking Experience in Steam Pipework Welds in National Power, Proceeding of VGB Conference: Materials and Welding Technology in Power Plants, Essen, March 1994, 15-16.

10. H.J. Schuller, L. Hagn, and A.Woitscheck, Cracking in the Weld Region of Shaped Components in Hot Steam Pipe Lines Materails Investigations, Der Machinenschaden 1974, 47-54.

11. J.D. Parker and A.W.J. Parsons, Int. J. Pres. Ves. and Piping, 57, 1994, 345-356.

12. S.T. Kimmins and D.J. Smith, 5th Int. Conf. on Creep and Fracture of Engineering Materials and Structures, 1993, 67-72.

13. W. B. Pearson, A handbook of Lattice Spacings and structures of metals and alloys, Pergamon Press, London 1958.

14. A. Brandes and G. B. Brook, Smithells Metals Reference Book, Butterworth-Heinemann, Oxford, 1992.

15. Z. Tōkei, K. Hennesen, H. Viefhaus and H. J. Grabke, Materials Science and Technology, 16, 2000, 1129-1138.

16. T. Gladman, Microstructural Stability of Creep Resistant Alloys for High Temp. Plant Applications (ed. A. Strang, et al.), IOM, 1998, 49.

17. V.E. Fradkov and L.S. Shvindlerman, Phys. Metall. Metalloved, 48, 1979, 59.

18. A.A. Zhukovitsky, J. Phys. Chem., 18, 1944, 3.

19. M.P. Seah and E.D. Hondros, Proc. Soc., London A335, 1973, 191.

20. L.C. Lim and T. Watanabe, Acta Metall. Mater., 38, 1990, 2507.

CHAPTER 9:

Overall Discussion, Conclusions and Future Work

9.1 Overall Discussion

In the thesis, an analysis of Type IV cracking in the heat affected zone (HAZ) of high Cr ferritic steel weldments was considered. An investigation of the weld simulation, real welds and the creep specimens was carried out. These three areas have strong inter-dependency. Based on the experimental evidence, a new model for grain boundary segregation and precipitation (GBSP), and cavity coalescence, was validated and used to explain Type IV cracking.

HAZ The hardness of the $850+^oC$ HAZ region is lower than that of the parent metal (Fig. 5.5), although the both specimens have similar lath microstructure (Fig. 5.8 and 5.9). Because 850^oC is much higher that the tempering temperature (750^oC) of the parent metal, the simulated HAZ material from the 850^oC temperature region is over-tempered, which results in a lower hardness than that of the parent metal. The stabilization of laths by the finely dispersed array of $M_{23}C_6$ carbides along lath boundaries present below A_{c1} is considered to cause the longer duration of secondary creep in the parent metal compared to material heated at temperatures above Ac_1.

For these reasons, high Cr ferritic steel is characterized with a softening in certain sectors within the HAZ after welding. The softening occurs throughout the welded joint during creep but the distribution of hardness is similar for specimens before and after creep. The microstructures across the HAZ are similar, in both Gleeble-simulated conditions and real creep samples. No δ-ferrite is observed in the HAZ zone (Fig. 5.7, 6.12 and 8.12) in either simulated HAZs or real creep specimens of the material.

The soft zone was not clearly defined in either the as welded or the simulated weld condition. Although the lightly tempered martensitic portion of the microstructure

increases the hardness, this lightly tempered martensite, transformed from a relatively low austenitizing temperature, contains precipitates (Fig.5.8b) which have not been dissolved during austenitizing. As a consequence, the martensitic matrix contains less carbon since the carbon is trapped in the precipitates. These undissolved precipitates are potent particles for coarsening and accelerate the softening during tempering. Additionally, the lower carbon content matrix makes the body-centred tetragonal martensite less tetragonal, i.e. c/a →1, which leads to a softer type of martensite.

Type IV Cracking One of the major problems that limiting the application of the ferritic steels in power plant applications is Type IV cracking of welds. This is characterized by fracture in the fine-grained HAZ of the weld joints close to the fusion zone and with a rupture life much shorter than that obtained for the parent metal.

Type IV cracking is associated with an enhanced rate of creep void formation in the fine-grained zone. These zones contain coarse carbide particles, leading to a reduction in creep strength; the particles also help nucleate voids. In creep, the weakened Type IV region is sandwiched between the stronger base metal and coarse-grained HAZ. The resulting accumulation of creep damage in the Type IV region causes the premature failure (Fig. 8.7 and 8.10).

Typical ferritic high Cr steels, P91, P92, E911 and P122, are strengthened by solid solution hardening and precipitation hardening as a result of adding a large amount of alloying elements such Cr, W and Mo. However, the high working temperature of ultra-supercritical (USC) plant accelerates the growth and coarsening of precipitates in the steels, which leads to a decrease in hardening. In addition, coarse precipitates may act as sites of initiation of creep voids.

Creep tests of welded joints showed the Type IV cracking occurs predominantly at low stress and high temperature. One of the reasons for Type IV cracking is considered to be the deterioration of creep properties due to coarsened precipitates ($M_{23}C_6$) in the fine-grained HAZ. Because the weld thermal cycle induces different material properties in the weld joint, it can be concluded that there is a relationship

between weld thermal cycle and precipitation behaviour in the HAZ. Grain boundary segregation and precipitation (GBSP) modelling has confirmed this phenomenon.

Phosphorus Segregation The segregation of elements to the boundaries takes place by two mechanisms: equilibrium segregation (ES) and non-equilibrium segregation (NES). Equilibrium segregation is determined by thermodynamics while the non-equilibrium segregation is more of a kinetic process. The ES is caused by the high binding energy for phosphorus at grain boundaries and other defects. This effect decreases with increasing temperature and depends strongly on the grain boundary structure. The NES results from the dissociation of phosphorus-vacancy complexes near the grain boundary which acts as a vacancy sink. In this case, the segregation effect increases as the starting temperature increases (Fig.7.4 and 7.7), and decreases with increasing cooling time (Fig. 7.8). Theoretical studies and experiment indicate that NES is the main cause of substantial grain boundary segregation during the fast cooling stage during welding, and that the situation is altered by post weld heat treatment and service exposure, after which ES-related grain boundary segregation mechanisms take over. The field emission gun TEM (FEGTEM) measures segregation at both prior austenite grain boundaries and lath boundaries with much higher than hitherto analytical spatial resolution.

Phosphorus grain boundary segregation is one of the main influences on cracking susceptibility and embrittlement in steels.

9.2 Overall Conclusions

1. The Gleeble testing is an ideal method for simulating the HAZ of ferritic steel weldments.

2. The modified 9Cr-1Mo weld metal contains a soft zone both before and after tempering.

3. The microstructure of high Cr ferritic steel after PWHT is mainly tempered martensite and $M_{23}C_6$. No δ-ferrite is observed in the HAZ zone for all the high Cr steel (P91, P92, E911, and P122) weldments studied in this work.

4. The Type IV failure tends to occur at the lower stress levels. Temperature has no big influence on Type IV cracking.

5. The carbides ($M_{23}C_6$) are larger in the Type IV zone, probably because the material has been above A_{c1} and therefore there are already large, undissolved carbides present before tempering.

6. The Type IV cracking is characterized with a mixed, quasi-cleavage cracking mechanism, in which the inter-granular grain boundary separation is dominant. Premature failure in the Type IV region is caused by cavity initiation due to vacancy injection on the grain boundaries, segregation of impurity atoms to the grain boundaries, in this case phosphorus, and a more coarse distribution of grain boundary carbides.

7. The grain boundary segregation and precipitation (GBSP) model is in good agreement with the experimental results, and can be properly used to explain the faster grain boundary carbide coarsening at the early stages (~2000 hours) of life at a given temperature.

8. There is significant non-equilibrium segregation of phosphorus to grain boundary observed during weld simulation, in which the effect of quenching temperature is dominant. Equilibrium GB segregation is not dominant after short time heat treatment. This effect is included in the model.

9. The vacancy injection effect is incorporated into the microstructural model for failure by calculating the vacancy supersaturation resulting from high temperature exposure and using this to determine the reduction of grain boundary energy. This is the equivalent of calculating the reduction of grain

boundary strength resulting from cavities forming on the boundaries by high vacancy flux injection.

10. From the practical viewpoint of reducing Type IV cracking, three main options are available: (1) Composition control: use less strong filler metal to join with parent metal; (2) HAZ zone width reduction: either lower the weld torch energy or use advanced welding techniques (e.g. EB or laser beam welding); (3) Stress optimisation: preferably operate in higher stress regime where early Type IV failure is less likely.

9.3 Future Work

1. More fractography on further creep specimens identifying crack initiation sites to better understand the micro-mechanism of Type IV cracking.

2. Refinement of the GBPS model and further validation using the ferritic steel weldments.

3. Continue to validate the P grain boundary segregation models by conducting more thermal cycle simulations and subsequent high resolution analytical electron microscopy.

4. Deeper investigation on the soft region of the HAZ to explore the softening mechanism in the high Cr ferritic steel weldments in more detail.

APPENDIX A: Publication Lists

1. B. Sun, R. Faulkner, D. Allen, Characterization on the Type IV Crack in High Cr Steel Weldments, to be submitted.

2. B. Sun, R. Faulkner, D. Allen, Weld Simulation of P91 Materials on Gleeble Testing Machine, to be submitted.

3. B. Sun, R. Faulkner, D. Allen, Microstructures of the P91 Ferritic Steel Weldments, The 10th Annual Congress of the Chinese Materials Association in UK (CMA-UK2004), 14-15th August, 2004, Birmingham, UK.

4. B. Sun, R. Faulkner, D. Allen, Fracture morphology of Type IV crack in High Cr Steel Weldments, to be submitted to Metall.Trans.

5. B. Sun, R. Faulkner, Y. Yin, D. Allen, Characterization and Modelling of the Type IV Cracking High Cr Steel Weldments, to be submitted to Acta Metall..

APPENDIX B-1: Results of Phosphorus Determination by FEGTEM on As-Weld Specimens (Part of the Results)

TEMQuant results. Listed at 15:56:51 on 13/07/04
Operator: ben
Spectrum label: **BXI-GB4**
Calibration data: Energy Resn. Area
 Strobe: -7.6 138.43 756623
 Calib. element: 4504.8 180.09 139875
 Gain factor = 50.039
 Livetime   = 50.0 seconds
Sample data: Energy Resn. Area
 Strobe: -7.4 61.04 41258
 Total spectrum counts = 15972
 Livetime   = 43.6 seconds
System resolution = 72 eV
Geometry (degrees):
 Tilt   = 18.00
 Elevation = 20.00
 Azimuth   = 0.00
 Entry angle = 0.00

Accelerating voltage = 200.00 kV

Quantitative method: Cliff-Lorimer Ratio Thin Section.(4 iterations).
Ratio standard element and line: Silicon, K Series
 Analysed all elements
Density = 5.120 g/cm³
Thickness = 100.00 nm

 1 peak possibly omitted: 0.00 keV

Standards :
None

Elmt	Peak Area	Stat. Sigma	Obser. %	k Factor	Abs. Corrn.	Element %	Sigma %	Atomic %	
Al K	2*	16	0.01*	1.030	1.047	0.02*	0.15	0.03*	
Si K	33*	17	0.26*	1.000	1.000	0.28*	0.15	0.56*	
P K	42*	24	0.32*	1.000	0.971	0.34*	0.20	0.62*	
V K	15*	19	0.13*	1.121	0.914	0.13*	0.17	0.15*	
Cr K	938	58	8.25	1.129	0.912	8.24	0.49	8.81	
Mn K	-9*	-38	-0.09*	1.184	0.000	-0.09*	-0.35	-0.09*	
Fe K	9543	165	89.26	1.202	0.912	89.14	1.00	88.74	
Ni K	14*	16	0.14*	1.279	0.922	0.14*	0.16	0.14*	
Nb L	37*	45	0.49*	1.707	0.960	0.52*	0.62	0.31*	
Mo L	91	40	1.22	1.725	0.952	1.27	0.55	0.74	
Total			100.00		100.00		100.00		

Beam broadening estimate = 8.40 nm
Density estimate   = 7.81 g/cm³
* = <2 sigma

TEMQuant results. Listed at 15:11:38 on 12/08/04
Operator: ben
Client: none
Job: 101
Spectrum label: **BYI-GB5**

Calibration data: Energy Resn.   Area
Strobe: -7.6 138.43 756623
Calib. element: 4504.8 180.09 139875
Gain factor = 50.039
Livetime   = 50.0 seconds

Sample data: Energy Resn.   Area
Strobe: -7.5 61.20   40159
Total spectrum counts = 21655
Livetime   = 42.8 seconds

System resolution = 72 eV

Geometry (degrees):
Tilt   = 18.00
Elevation = 20.00
Azimuth   = 0.00
Entry angle = 0.00

Accelerating voltage = 200.00 kV

Quantitative method: Cliff-Lorimer Ratio Thin Section.(4 iterations).
Ratio standard element and line: Silicon, K Series
 Analysed all elements
Density = 5.120 g/cm³
Thickness = 100.00 nm

 1 peak possibly omitted: 0.00 keV

Standards :
None

Elmt	Peak Area	Stat. Sigma	Obser. %	k Factor	Abs. Corrn.	Element %	Sigma %	Atomic %
Al K	12*	18	0.07*	1.030	1.047	0.08*	0.13	0.17*
Si K	159	25	0.95	1.000	1.000	1.04	0.16	2.04
P K	**46***	**27**	**0.27***	**1.000**	**0.972**	**0.29***	**0.17**	**0.52***
V K	16*	27	0.11*	1.121	0.914	0.11*	0.18	0.11*
Cr K	1205	68	8.10	1.129	0.913	8.08	0.44	8.56
Mn K	-2*	-54	-0.02*	1.184	0.913	-0.02*	-0.38	-0.02*
Fe K	12486	189	89.27	1.202	0.912	89.10	0.91	87.87
Ni K	-7*	-20	-0.05*	1.279	0.922	-0.05*	-0.15	-0.05*
Nb L	41*	51	0.42*	1.707	0.961	0.44*	0.55	0.26*
Mo L	87*	46	0.89*	1.725	0.953	0.93*	0.49	0.53*
Total			100.00			100.00		100.00

Beam broadening estimate = 8.42 nm
Density estimate   = 7.76 g/cm³

* = <2 sigma

TEMQuant results. Listed at 13:48:23 on 20/07/04
Operator: ben
Spectrum label: **BZI-GB1**

Calibration data: Energy Resn. Area
Strobe: -7.6 138.43 756623
Calib. element: 4504.8 180.09 139875
Gain factor = 50.039
Livetime   = 50.0 seconds

Sample data: Energy Resn. Area
Strobe: -7.5 61.09 33977
Total spectrum counts = 7109
Livetime   = 35.5 seconds

System resolution = 72 eV

Geometry (degrees):
Tilt   = 18.00
Elevation = 20.00
Azimuth   = 0.00
Entry angle = 0.00

Accelerating voltage = 200.00 kV

Quantitative method: Cliff-Lorimer Ratio Thin Section.(4 iterations).
Ratio standard element and line: Silicon, K Series
 Analysed all elements
Density = 5.120 g/cm³
Thickness = 100.00 nm

 1 peak possibly omitted: 0.00 keV

Standards :
 None

Elmt	Peak Area	Stat. Sigma	Obser. %	k Factor	Abs. Corrn.	Element %	Sigma %	Atomic %	
Al K	-7*	-12	-0.13*	1.030	1.047	-0.15*	-0.26	-0.31*	
Si K	6*	12	0.10*	1.000	1.000	0.11*	0.25	0.23*	
P K	14*	15	0.26*	1.000	0.971	0.28*	0.30	0.50*	
V K	4*	15	0.09*	1.121	0.915	0.09*	0.30	0.10*	
Cr K	391	37	8.13	1.129	0.913	8.12	0.74	8.79	
Mn K	3*	26	0.06*	1.184	0.912	0.06*	0.56	0.07*	
Fe K	3974	106	87.97	1.202	0.913	87.81	1.64	88.47	
Ni K	-4*	-9	-0.08*	1.279	0.921	-0.09*	-0.22	-0.08*	
Nb L	54*	32	1.69*	1.707	0.960	1.78*	1.03	1.08*	
Mo L	60*	30	1.90*	1.725	0.953	1.98*	0.98	1.16*	
Total			100.00		100.00		100.00		

Beam broadening estimate = 8.51 nm
Density estimate   = 7.86 g/cm³

* = <2 sigma

TEMQuant results. Listed at 13:55:51 on 20/07/04
Operator: ben
Spectrum label: **BZI-GB2**

Calibration data: Energy Resn. Area
Strobe: -7.6 138.43 756623
Calib. element: 4504.8 180.09 139875
Gain factor = 50.039
Livetime   = 50.0 seconds

Sample data: Energy Resn. Area
Strobe: -7.3 61.39 42899
Total spectrum counts = 7089
Livetime   = 44.8 seconds

System resolution = 72 eV

Geometry (degrees):
Tilt   = 18.00
Elevation = 20.00
Azimuth   = 0.00
Entry angle = 0.00

Accelerating voltage = 200.00 kV

Quantitative method: Cliff-Lorimer Ratio Thin Section.(4 iterations).
Ratio standard element and line: Silicon, K Series
 Analysed all elements
Density = 5.120 g/cm³
Thickness = 100.00 nm

 1 peak possibly omitted: 0.00 keV

Standards :
 None

Elmt	Peak Area	Stat. Sigma	Obser. %	k Factor	Abs. Corrn.	Element %	Sigma %	Atomic %	
Al K	-5*	-12	-0.09*	1.030	1.047	-0.11*	-0.27	-0.22*	
Si K	12*	13	0.25*	1.000	1.000	0.27*	0.27	0.53*	
P K	12*	15	0.24*	1.000	0.971	0.25*	0.32	0.45*	
V K	6*	13	0.14*	1.121	0.913	0.14*	0.29	0.15*	
Cr K	422·	39	9.40	1.129	0.912	9.40	0.83	10.04	
Mn K	-30*	-25	-0.70*	1.184	0.910	-0.70*	-0.59	-0.71*	
Fe K	3786	105	89.77	1.202	0.912	89.70	1.71	89.19	
Ni K	-5*	-10	-0.12*	1.279	0.921	-0.13*	-0.26	-0.12*	
Nb L	12*	30	0.41*	1.707	0.960	0.44*	1.05	0.26*	
Mo L	21*	27	0.71*	1.725	0.952	0.74*	0.96	0.43*	
Total			100.00			100.00		100.00	

Beam broadening estimate = 8.44 nm
Density estimate   = 7.80 g/cm³

* = <2 sigma

TEMQuant results. Listed at 13:58:52 on 20/07/04
Operator: ben
Spectrum label: **BZI-GB3**

Calibration data: Energy Resn.   Area
Strobe: -7.6 138.43 756623
Calib. element: 4504.8 180.09 139875
Gain factor = 50.039
Livetime   = 50.0 seconds

Sample data: Energy Resn.   Area
Strobe: -7.5 61.14   42997
Total spectrum counts = 6324
Livetime   = 45.0 seconds

System resolution = 72 eV

Geometry (degrees):
Tilt   = 18.00
Elevation = 20.00
Azimuth   = 0.00
Entry angle = 0.00

Accelerating voltage = 200.00 kV

Quantitative method: Cliff-Lorimer Ratio Thin Section.(4 iterations).
Ratio standard element and line: Silicon, K Series
 Analysed all elements
Density = 5.120 g/cm³
Thickness = 100.00 nm

 1 peak possibly omitted: 0.00 keV

Standards :
 None

Elmt	Peak Area	Stat. Sigma	Obser. %	k Factor	Abs. Corrn.	Element %	Sigma %	Atomic %	
Al K	-10*	-10	-0.21*	1.030	1.046	-0.24*	-0.26	-0.50*	
Si K	27	11	0.57	1.000	1.000	0.62	0.26	1.22	
P K	24*	17	0.50*	1.000	0.972	0.53*	0.38	0.95*	
V K	-8*	-14	-0.20*	1.121	0.913	-0.20*	-0.34	-0.22*	
Cr K	512	40	12.16	1.129	0.914	12.13	0.92	12.98	
Mn K	-35*	-25	-0.88*	1.184	0.916	-0.88*	-0.61	-0.89*	
Fe K	3379	97	85.35	1.202	0.914	85.19	1.86	84.83	
Ni K	-4*	-9	-0.11*	1.279	0.921	-0.11*	-0.24	-0.11*	
Nb L	25*	33	0.91*	1.707	0.961	0.96*	1.24	0.57*	
Mo L	53*	30	1.93*	1.725	0.954	2.00*	1.11	1.16*	
Total			100.00		100.00		100.00		

Beam broadening estimate = 8.43 nm
Density estimate   = 7.79 g/cm³

* = <2 sigma

TEMQuant results. Listed at 14:07:34 on 20/07/04
Operator: ben
Spectrum label: **BZI-GB4**

Calibration data: Energy Resn.   Area
Strobe: -7.6 138.43 756623
Calib. element: 4504.8 180.09 139875
Gain factor = 50.039
Livetime   = 50.0 seconds

Sample data: Energy Resn.   Area
Strobe: -7.6 61.08   42108
Total spectrum counts = 10154
Livetime   = 44.3 seconds

System resolution = 72 eV

Geometry (degrees):
Tilt   = 18.00
Elevation = 20.00
Azimuth   = 0.00
Entry angle = 0.00

Accelerating voltage = 200.00 kV

Quantitative method: Cliff-Lorimer Ratio Thin Section.(4 iterations).
Ratio standard element and line: Silicon, K Series
 Analysed all elements
Density = 5.120 g/cm³
Thickness = 100.00 nm

 1 peak possibly omitted: 0.00 keV

Standards :

Elmt	Peak Area	Stat. Sigma	Obser. %	k Factor	Abs. Corrn.	Element %	Sigma %	Atomic %	
Al K	-3*	-13	-0.04*	1.030	1.046	-0.04*	-0.20	-0.09*	
Si K	16*	14	0.20*	1.000	1.000	0.22*	0.20	0.44*	
P K	16*	20	0.21*	1.000	0.971	0.22*	0.27	0.40*	
V K	-7*	-16	-0.10*	1.121	0.914	-0.10*	-0.24	-0.11*	
Cr K	566	45	8.33	1.129	0.913	8.32	0.64	8.95	
Mn K	-41*	-32	-0.63*	1.184	0.912	-0.63*	-0.50	-0.64*	
Fe K	5715	131	89.59	1.202	0.912	89.46	1.37	89.53	
Ni K	4*	13	0.07*	1.279	0.922	0.07*	0.22	0.07*	
Nb L	26*	37	0.58*	1.707	0.960	0.61*	0.85	0.37*	
Mo L	79	33	1.78	1.725	0.952	1.86	0.76	1.08	
Total			100.00			100.00		100.00	

Beam broadening estimate = 8.45 nm
Density estimate   = 7.84 g/cm³

* = <2 sigma

TEMQuant results. Listed at 14:09:33 on 20/07/04
Operator: ben
Spectrum label: **BZI-GB5**

Calibration data: Energy Resn.   Area
Strobe: -7.6 138.43 756623
Calib. element: 4504.8 180.09 139875
Gain factor = 50.039
Livetime   = 50.0 seconds

Sample data: Energy Resn.   Area
Strobe: -7.5 60.63   41905
Total spectrum counts = 10562
Livetime   = 44.2 seconds

System resolution = 72 eV

Geometry (degrees):
Tilt   = 18.00
Elevation = 20.00
Azimuth   = 0.00
Entry angle = 0.00

Accelerating voltage = 200.00 kV

Quantitative method: Cliff-Lorimer Ratio Thin Section.(4 iterations).
Ratio standard element and line: Silicon, K Series
 Analysed all elements
Density = 5.120 g/cm³
Thickness = 100.00 nm

1 peak possibly omitted: 0.00 keV

Standards :
 None

Elmt	Peak Area	Stat. Sigma	Obser. %	k Factor	Abs. Corrn.	Element %	Sigma %	Atomic %	
Al K	-10*	-13	-0.13*	1.030	1.046	-0.15*	-0.20	-0.32*	
Si K	35	14	0.45	1.000	1.000	0.49	0.20	0.97	
P K	21*	19	0.27*	1.000	0.971	0.28*	0.26	0.51*	
V K	2*	17	0.03*	1.121	0.914	0.03*	0.25	0.03*	
Cr K	540	45	7.91	1.129	0.912	7.90	0.64	8.44	
Mn K	-2*	-32	-0.03*	1.184	0.912	-0.03*	-0.49	-0.03*	
Fe K	5796	133	90.31	1.202	0.912	90.21	1.38	89.75	
Ni K	-17*	-12	-0.27*	1.279	0.922	-0.28*	-0.20	-0.26*	
Nb L	25*	37	0.55*	1.707	0.960	0.57*	0.86	0.34*	
Mo L	42*	34	0.93*	1.725	0.953	0.97*	0.78	0.56*	
Total		100.00			100.00		100.00		

Beam broadening estimate = 8.39 nm
Density estimate   = 7.80 g/cm³
* = <2 sigma

TEMQuant results. Listed at 15:29:55 on 20/07/04
Operator: ben
Spectrum label: **BZI-GB6**

Calibration data: Energy Resn.   Area
Strobe: -7.6 138.43 756623
Calib. element: 4504.8 180.09 139875
Gain factor = 50.039
Livetime   = 50.0 seconds

Sample data: Energy Resn.   Area
Strobe: -7.6 61.10   34924
Total spectrum counts = 9874
Livetime   = 36.8 seconds

System resolution = 72 eV

Geometry (degrees):
Tilt   = 18.00
Elevation = 20.00
Azimuth   = 0.00
Entry angle = 0.00

Accelerating voltage = 200.00 kV

Quantitative method: Cliff-Lorimer Ratio Thin Section.(4 iterations).
Ratio standard element and line: Silicon, K Series
 Analysed all elements
Density =   5.120 g/cm³
Thickness = 100.00 nm

 1 peak possibly omitted: 0.00 keV

Standards :
 None

Elmt	Peak Area	Stat. Sigma	Obser. %	k Factor	Abs. Corrn.	Element %	Sigma %	Atomic %	
Al K	-7*	-14	-0.10*	1.030	1.044	-0.12*	-0.22	-0.24*	
Si K	31*	17	0.43*	1.000	1.000	0.47*	0.26	0.93*	
P K	19*	19	0.27*	1.000	0.971	0.28*	0.28	0.51*	
V K	12*	18	0.18*	1.121	0.914	0.18*	0.27	0.20*	
Cr K	631	46	9.83	1.129	0.913	9.82	0.69	10.48	
Mn K	-35*	-32	-0.57*	1.184	0.913	-0.57*	-0.53	-0.57*	
Fe K	5335	127	88.52	1.202	0.913	88.41	1.34	87.83	
Ni K	-3*	-11	-0.06*	1.279	0.922	-0.06*	-0.19	-0.05*	
Nb L	19*	32	0.45*	1.707	0.960	0.48*	0.80	0.28*	
Mo L	44*	29	1.04*	1.725	0.953	1.09*	0.70	0.63*	
Total			100.00			100.00		100.00	

Beam broadening estimate = 8.45 nm
Density estimate   = 7.79 g/cm³
* = <2 sigma

TEMQuant results. Listed at 15:30:46 on 20/07/04
Operator: ben
Spectrum label: **BZI-GB7**

Calibration data: Energy Resn. Area
Strobe: -7.6 138.43 756623
Calib. element: 4504.8 180.09 139875
Gain factor = 50.039
Livetime = 50.0 seconds

Sample data: Energy Resn. Area
Strobe: -7.6 61.35 41931
Total spectrum counts = 11865
Livetime = 44.1 seconds

System resolution = 72 eV

Geometry (degrees):
Tilt = 18.00
Elevation = 20.00
Azimuth = 0.00
Entry angle = 0.00

Accelerating voltage = 200.00 kV

Quantitative method: Cliff-Lorimer Ratio Thin Section.(4 iterations).
Ratio standard element and line: Silicon, K Series
 Analysed all elements
Density = 5.120 g/cm³
Thickness = 100.00 nm

 1 peak possibly omitted: 0.00 keV

Standards :
None

Elmt	Peak Area	Stat. Sigma	Obser. %	k Factor	Abs. Corrn.	Element %	Sigma %	Atomic %	
Al K	-10*	-15	-0.12*	1.030	1.044	-0.14*	-0.20	-0.29*	
Si K	43	19	0.50	1.000	1.000	0.54	0.24	1.07	
P K	20*	20	0.23*	1.000	0.971	0.24*	0.25	0.44*	
V K	1*	19	0.02*	1.121	0.914	0.02*	0.24	0.02*	
Cr K	762	50	10.02	1.129	0.913	10.01	0.64	10.67	
Mn K	-39*	-35	-0.54*	1.184	0.913	-0.54*	-0.49	-0.54*	
Fe K	6349	140	88.87	1.202	0.912	88.78	1.24	88.07	
Ni K	-12*	-12	-0.17*	1.279	0.922	-0.17*	-0.18	-0.16*	
Nb L	14*	35	0.28*	1.707	0.960	0.29*	0.73	0.18*	
Mo L	46*	31	0.92*	1.725	0.953	0.96*	0.64	0.55*	
Total			100.00			100.00		100.00	

Beam broadening estimate = 8.43 nm
Density estimate = 7.79 g/cm³
* = <2 sigma

TEMQuant results. Listed at 15:39:07 on 20/07/04
Operator: ben
Spectrum label: **BZI-GB8**

Calibration data: Energy Resn. Area
Strobe: -7.6 138.43 756623
Calib. element: 4504.8 180.09 139875
Gain factor = 50.039
Livetime   = 50.0 seconds

Sample data: Energy Resn. Area
Strobe: -7.5 61.25 43165
Total spectrum counts = 5438
Livetime   = 45.0 seconds

System resolution = 72 eV

Geometry (degrees):
Tilt   = 18.00 .
Elevation = 20.00
Azimuth   = 0.00
Entry angle = 0.00

Accelerating voltage = 200.00 kV

Quantitative method: Cliff-Lorimer Ratio Thin Section.(4 iterations).
Ratio standard element and line: Silicon, K Series
 Analysed all elements
Density = 5.120 g/cm³
Thickness = 100.00 nm

 1 peak possibly omitted: 0.00 keV

Standards :
 None

Elmt	Peak Area	Stat. Sigma	Obser. %	k Factor	Abs. Corrn.	Element %	Sigma %	Atomic %	
Al K	-10*	-8	-0.25*	1.030	1.047	-0.28*	-0.23	-0.59*	
Si K	14*	10	0.32*	1.000	1.000	0.35*	0.26	0.70*	
P K	11*	14	0.26*	1.000	0.971	0.28*	0.34	0.50*	
V K	1*	13	0.04*	1.121	0.914	0.04*	0.34	0.04*	
Cr K	299	32	7.99	1.129	0.913	7.98	0.82	8.61	
Mn K	-40*	-24	-1.13*	1.184	0.915	-1.13*	-0.69	-1.15*	
Fe K	3156	94	89.74	1.202	0.913	89.59	1.85	90.04	
Ni K	-3*	-10	-0.10*	1.279	0.921	-0.10*	-0.29	-0.10*	
Nb L	33*	28	1.34*	1.707	0.960	1.41*	1.17	0.85*	
Mo L	44*	25	1.80*	1.725	0.953	1.88*	1.05	1.10*	
Total			100.00		100.00		100.00		

Beam broadening estimate = 8.49 nm
Density estimate   = 7.85 g/cm³
* = <2 sigma

TEMQuant results. Listed at 13:43:37 on 20/07/04
Operator: ben
Client: none
Job: 101
Spectrum label:

Calibration data: Energy Resn. Area
Strobe: -7.6 138.43 756623
Calib. element: 4504.8 180.09 139875
Gain factor = 50.039
Livetime   = 50.0 seconds

Sample data: Energy Resn. Area
Strobe: -7.6 61.25 42786
Total spectrum counts = 6966
Livetime   = 44.7 seconds

System resolution = 72 eV

Geometry (degrees):
Tilt   = 18.00
Elevation = 20.00
Azimuth = 0.00
Entry angle = 0.00

Accelerating voltage = 200.00 kV

Quantitative method: Cliff-Lorimer Ratio Thin Section.(4 iterations).
Ratio standard element and line: Silicon, K Series
 Analysed all elements
Density = 5.120 g/cm³
Thickness = 100.00 nm

 1 peak possibly omitted: 0.00 keV

Standards :
None

Elmt	Peak Area	Stat. Sigma	Obser. %	k Factor	Abs. Corrn.	Element %	Sigma %	Atomic %
Al K	-12*	-12	-0.25*	1.030	0.000	-0.28*	-0.28	-0.58*
Si K	25*	13	0.50*	1.000	1.000	0.55*	0.30	1.09*
P K	-8*	-15	-0.17*	1.000	0.000	-0.18*	-0.33	-0.32*
V K	-5*	-14	-0.11*	1.121	0.000	-0.11*	-0.31	-0.12*
Cr K	373	36	8.60	1.129	0.911	8.61	0.81	9.19
Mn K	-42*	-25	-1.01*	1.184	0.910	-1.01*	-0.62	-1.02*
Fe K	3746	105	91.87	1.202	0.911	91.86	1.74	91.36
Ni K	9*	12	0.24*	1.279	0.921	0.24*	0.31	0.23*
Nb L	-24*	-29	-0.82*	1.707	0.000	-0.87*	-1.06	-0.52*
Mo L	32*	26	1.13*	1.725	0.952	1.18*	0.95	0.69*
Total			100.00			100.00		100.00

Beam broadening estimate = 8.42 nm
Density estimate   = 7.84 g/cm³

* = <2 sigma

TEMQuant results. Listed at 14:14:19 on 13/07/04
Operator: ben
Spectrum label: **DXI-GB3**

Calibration data: Energy Resn.   Area
Strobe: -7.6 138.43 756623
Calib. element: 4504.8 180.09 139875
Gain factor = 50.039
Livetime   = 50.0 seconds

Sample data: Energy Resn.   Area
Strobe: -7.5 60.77 40790
Total spectrum counts = 16181
Livetime   = 43.1 seconds

System resolution = 72 eV

Geometry (degrees):
Tilt   = 18.00
Elevation   = 20.00
Azimuth   = 0.00
Entry angle = 0.00

Accelerating voltage = 200.00 kV

Quantitative method: Cliff-Lorimer Ratio Thin Section.(4 iterations).
Ratio standard element and line: Silicon, K Series
 Analysed all elements
Density = 5.120 g/cm³
Thickness = 100.00 nm

 1 peak possibly omitted: 0.00 keV

Standards :
 None

Elmt	Peak Area	Stat. Sigma	Obser. %	k Factor	Abs. Corrn.	Element %	Sigma %	Atomic %	
Al K	-13*	-13	-0.10*	1.030	1.048	-0.12*	-0.12	-0.24*	
Si K	34	17	0.27	1.000	1.000	0.29	0.14	0.58	
P K	52	25	0.41	1.000	0.971	0.43	0.20	0.78	
V K	36*	22	0.32*	1.121	0.915	0.32*	0.19	0.35*	
Cr K	1093	62	9.65	1.129	0.913	9.64	0.53	10.34	
Mn K	99	42	0.92	1.184	0.913	0.92	0.39	0.93	
Fe K	9163	165	86.14	1.202	0.913	86.01	1.06	85.84	
Ni K	-16*	-16	-0.16*	1.279	0.920	-0.16*	-0.16	-0.15*	
Nb L	102	50	1.37	1.707	0.960	1.43	0.69	0.86	
Mo L	88	44	1.18	1.725	0.953	1.23	0.61	0.72	
Total			100.00			100.00		100.00	

Beam broadening estimate = 8.43 nm
Density estimate   = 7.80 g/cm³
* = <2 sigma

TEMQuant results. Listed at 11:56:40 on 08/07/04
Operator: ben
Spectrum label: **DYI-GB1**
Calibration data: Energy Resn.   Area
 Strobe: -7.6 138.43 756623
 Calib. element: 4504.8 180.09 139875
 Gain factor = 50.039
 Livetime   = 50.0 seconds

Sample data: Energy Resn.   Area
 Strobe: -7.4 61.03   43163
 Total spectrum counts = 4159
 Livetime   = 45.0 seconds

System resolution = 72 eV

Geometry (degrees):
 Tilt   = 18.00
 Elevation = 20.00
 Azimuth   = 0.00
 Entry angle = 0.00

Accelerating voltage = 200.00 kV

Quantitative method: Cliff-Lorimer Ratio Thin Section.(4 iterations).
Ratio standard element and line: Silicon, K Series
 Analysed all elements
Density = 5.120 g/cm³
Thickness = 100.00 nm

 1 peak possibly omitted: 0.00 keV

Standards :
 None

Elmt	Peak Area	Stat. Sigma	Obser. %	k Factor	Abs. Corrn.	Element %	Sigma %	Atomic %	
Al K	-5*	-8	-0.16*	1.030	1.045	-0.19*	-0.32	-0.38*	
Si K	4*	8	0.13*	1.000	1.000	0.15*	0.30	0.29*	
P K	19*	12	0.64*	1.000	0.971	0.68*	0.43	1.22*	
V K	-7*	-16	-0.27*	1.121	0.919	-0.27*	-0.61	-0.30*	
Cr K	228	30	8.53	1.129	0.913	8.52	1.09	9.14	
Mn K	-7*	-24	-0.26*	1.184	0.916	-0.26*	-0.94	-0.27*	
Fe K	2244	78	89.19	1.202	0.913	89.06	2.35	88.98	
Ni K	-4*	-7	-0.15*	1.279	0.925	-0.15*	-0.31	-0.14*	
Nb L	24*	24	1.35*	1.707	0.960	1.42*	1.42	0.85*	
Mo L	18*	22	1.00*	1.725	0.953	1.05*	1.30	0.61*	
Total		100.00		100.00		100.00			

Beam broadening estimate = 8.44 nm
Density estimate   = 7.81 g/cm³

* = <2 sigma

TEMQuant results. Listed at 13:05:19 on 08/07/04
Operator: ben
Spectrum label: **DYI-GB2**

Calibration data: Energy Resn.   Area
Strobe: -7.6 138.43 756623
Calib. element: 4504.8 180.09 139875
Gain factor = 50.039
Livetime   = 50.0 seconds

Sample data: Energy Resn.   Area
Strobe: -7.5 61.38   43041
Total spectrum counts = 4201
Livetime   = 44.9 seconds

System resolution = 72 eV

Geometry (degrees):
 Tilt   = 18.00
 Elevation = 20.00
 Azimuth   = 0.00
 Entry angle = 0.00

Accelerating voltage = 200.00 kV

Quantitative method: Cliff-Lorimer Ratio Thin Section.(4 iterations).
Ratio standard element and line: Silicon, K Series
 Analysed all elements
Density = 5.120 g/cm³
Thickness = 100.00 nm

 1 peak possibly omitted: 0.00 keV

Standards :
 None

Elmt	Peak Area	Stat. Sigma	Obser. %	k Factor	Abs. Corrn.	Element %	Sigma %	Atomic %	
Al K	8*	8	0.30*	1.030	1.047	0.34*	0.31	0.70*	
Si K	0*	9	0.00*	1.000	1.000	0.00*	0.34	0.01*	
P K	13*	14	0.45*	1.000	0.970	0.48*	0.52	0.86*	
V K	-7*	-16	-0.27*	1.121	0.915	-0.27*	-0.61	-0.29*	
Cr K	247	32	9.75	1.129	0.912	9.74	1.21	10.35	
Mn K	-30*	-25	-1.24*	1.184	0.911	-1.24*	-1.06	-1.24*	
Fe K	2143	77	90.10	1.202	0.912	89.99	2.60	89.09	
Ni K	-2*	-7	-0.07*	1.279	0.923	-0.07*	-0.33	-0.07*	
Nb L	3*	26	0.19*	1.707	0.960	0.20*	1.60	0.12*	
Mo L	13*	22	0.79*	1.725	0.952	0.82*	1.39	0.47*	
Total			100.00			100.00		100.00	

Beam broadening estimate = 8.42 nm
Density estimate   = 7.79 g/cm³
* = <2 sigma

TEMQuant results. Listed at 13:12:04 on 08/07/04
Operator: ben
Spectrum label: **DYI-GB3**

Calibration data: Energy Resn.   Area
Strobe: -7.6 138.43 756623
Calib. element: 4504.8 180.09 139875
Gain factor = 50.039
Livetime   = 50.0 seconds

Sample data: Energy Resn.   Area
Strobe: -7.5 61.27 42969
Total spectrum counts = 4341
Livetime   = 44.9 seconds

System resolution = 72 eV

Geometry (degrees):
Tilt   = 18.00
Elevation = 20.00
Azimuth   = 0.00
Entry angle = 0.00

Accelerating voltage = 200.00 kV

Quantitative method: Cliff-Lorimer Ratio Thin Section.(4 iterations).
Ratio standard element and line: Silicon, K Series
 Analysed all elements
Density = 5.120 g/cm³
Thickness = 100.00 nm

 1 peak possibly omitted: 0.00 keV

Standards :
 None

Elmt	Peak Area	Stat. Sigma	Obser. %	k Factor	Abs. Corrn.	Element %	Sigma %	Atomic %	
Al K	-1*	-6	-0.05*	1.030	1.048	-0.06*	-0.27	-0.13*	
Si K	1*	8	0.05*	1.000	1.000	0.05*	0.31	0.10*	
P K	14*	14	0.51*	1.000	0.970	0.54*	0.52	0.96*	
V K	16*	16	0.62*	1.121	0.913	0.62*	0.63	0.68*	
Cr K	223	33	8.91	1.129	0.912	8.90	1.27	9.49	
Mn K	-15*	-25	-0.63*	1.184	0.911	-0.63*	-1.04	-0.64*	
Fe K	2107	78	89.61	1.202	0.912	89.55	2.56	88.87	
Ni K	4*	10	0.19*	1.279	0.921	0.19*	0.44	0.18*	
Nb L	1*	24	0.06*	1.707	0.960	0.06*	1.51	0.03*	
Mo L	12*	21	0.75*	1.725	0.952	0.78*	1.35	0.45*	
Total			100.00		100.00		100.00		

Beam broadening estimate = 8.42 nm
Density estimate   = 7.79 g/cm³
* = <2 sigma

TEMQuant results. Listed at 14:40:45 on 08/07/04
Operator: ben
Spectrum label: **DYI-GB4**

Calibration data: Energy Resn. Area
Strobe: -7.6 138.43 756623
Calib. element: 4504.8 180.09 139875
Gain factor = 50.039
Livetime   = 50.0 seconds

Sample data: Energy Resn. Area
Strobe: -7.5 61.19 42988
Total spectrum counts = 4272
Livetime   = 44.9 seconds

System resolution = 72 eV

Geometry (degrees):
Tilt   = 18.00
Elevation = 20.00
Azimuth   = 0.00
Entry angle = 0.00

Accelerating voltage = 200.00 kV

Quantitative method: Cliff-Lorimer Ratio Thin Section.(4 iterations).
Ratio standard element and line: Silicon, K Series
 Analysed all elements
Density = 5.120 g/cm³
Thickness = 100.00 nm

 1 peak possibly omitted: 0.00 keV

Standards :
 None

Elmt	Peak Area	Stat. Sigma	Obser. %	k Factor	Abs. Corrn.	Element %	Sigma %	Atomic %	
Al K	3*	9	0.09*	1.030	1.046	0.11*	0.37	0.22*	
Si K	15*	10	0.51*	1.000	1.000	0.55*	0.39	1.10*	
P K	21*	13	0.74*	1.000	0.971	0.78*	0.46	1.40*	
V K	-3*	-14	-0.10*	1.121	0.915	-0.10*	-0.54	-0.11*	
Cr K	225	31	8.75	1.129	0.914	8.73	1.16	9.34	
Mn K	-2*	-28	-0.07*	1.184	0.911	-0.07*	-1.12	-0.07*	
Fe K	2094	77	86.64	1.202	0.914	86.39	2.31	86.07	
Ni K	-5*	-8	-0.20*	1.279	0.921	-0.21*	-0.35	-0.19*	
Nb L	22*	22	1.27*	1.707	0.961	1.34*	1.35	0.80*	
Mo L	40	19	2.37	1.725	0.954	2.47	1.14	1.43	
Total			100.00			100.00		100.00	

Beam broadening estimate = 8.47 nm
Density estimate   = 7.79 g/cm³
* = <2 sigma

TEMQuant results. Listed at 13:25:05 on 08/07/04
Operator: ben
Spectrum label: **DYI-Lath1**

Calibration data: Energy Resn. Area
Strobe: -7.6 138.43 756623
Calib. element: 4504.8 180.09 139875
Gain factor = 50.039
Livetime   = 50.0 seconds

Sample data: Energy Resn. Area
Strobe: -7.4 60.97 43185
Total spectrum counts = 3999
Livetime   = 44.9 seconds

System resolution = 72 eV

Geometry (degrees):
 Tilt   = 18.00
 Elevation = 20.00
 Azimuth   = 0.00
 Entry angle = 0.00

Accelerating voltage = 200.00 kV

Quantitative method: Cliff-Lorimer Ratio Thin Section.(4 iterations).
Ratio standard element and line: Silicon, K Series
 Analysed all elements
Density = 5.120 g/cm³
Thickness = 100.00 nm

 1 peak possibly omitted: 0.00 keV

Standards :
 None

Elmt	Peak Area	Stat. Sigma	Obser. %	k Factor	Abs. Corrn.	Element %	Sigma %	Atomic %	
Al K	-1*	-9	-0.04*	1.030	1.046	-0.05*	-0.36	-0.10*	
Si K	14*	10	0.52*	1.000	1.000	0.57*	0.38	1.12*	
P K	18*	13	0.65*	1.000	0.971	0.69*	0.50	1.23*	
V K	0*	16	0.01*	1.121	0.915	0.01*	0.64	0.01*	
Cr K	227	31	9.29	1.129	0.914	9.27	1.23	9.92	
Mn K	12*	25	0.52*	1.184	0.913	0.52*	1.06	0.52*	
Fe K	1972	75	85.89	1.202	0.914	85.69	2.49	85.35	
Ni K	1*	7	0.03*	1.279	0.923	0.03*	0.35	0.03*	
Nb L	19*	24	1.20*	1.707	0.961	1.26*	1.56	0.75*	
Mo L	31*	21	1.94*	1.725	0.954	2.02*	1.33	1.17*	
Total			100.00			100.00		100.00	

Beam broadening estimate = 8.45 nm
Density estimate   = 7.79 g/cm³
* = <2 sigma

TEMQuant results. Listed at 13:56:25 on 08/07/04
Operator: ben
Spectrum label: **DYI-Lath2**

Calibration data: Energy Resn.   Area
Strobe: -7.6 138.43 756623
Calib. element: 4504.8 180.09 139875
Gain factor = 50.039
Livetime   = 50.0 seconds

Sample data: Energy Resn.   Area
Strobe: -7.4 60.90   43054
Total spectrum counts = 4297
Livetime   = 44.9 seconds

System resolution = 72 eV

Geometry (degrees):
 Tilt   = 18.00
 Elevation = 20.00
 Azimuth   =   0.00
 Entry angle =   0.00

Accelerating voltage = 200.00 kV

Quantitative method: Cliff-Lorimer Ratio Thin Section.(4 iterations).
Ratio standard element and line: Silicon, K Series
 Analysed all elements
Density = 5.120 g/cm³
Thickness = 100.00 nm

 1 peak possibly omitted: 0.00 keV

Standards :
 None

Elmt	Peak Area	Stat. Sigma	Obser. %	k Factor	Abs. Corrn.	Element %	Sigma %	Atomic %	
Al K	2*	9	0.08*	1.030	1.046	0.10*	0.39	0.20*	
Si K	24	10	0.85	1.000	1.000	0.92	0.40	1.82	
P K	14*	13	0.50*	1.000	0.972	0.53*	0.49	0.94*	
V K	-8*	-16	-0.33*	1.121	0.913	-0.32*	-0.64	-0.35*	
Cr K	244	33	9.74	1.129	0.913	9.72	1.26	10.31	
Mn K	-5*	-24	-0.22*	1.184	0.912	-0.22*	-1.02	-0.22*	
Fe K	2052	78	87.16	1.202	0.913	86.96	2.46	85.95	
Ni K	0*	7	0.01*	1.279	0.922	0.01*	0.33	0.01*	
Nb L	13*	23	0.76*	1.707	0.961	0.80*	1.48	0.47*	
Mo L	24*	20	1.45*	1.725	0.954	1.51*	1.28	0.87*	
Total			100.00		100.00	100.00			

Beam broadening estimate = 8.46 nm
Density estimate   = 7.76 g/cm³
* = <2 sigma

TEMQuant results. Listed at 15:59:24 on 29/06/04
Operator: ben
Spectrum label: **DZI-GB1**

Calibration data: Energy Resn.   Area
Strobe: -7.6 138.43 756623
Calib. element: 4504.8 180.09 139875
Gain factor = 50.039
Livetime   = 50.0 seconds

Sample data: Energy Resn.   Area
Strobe: -7.5 60.51   17223
Total spectrum counts = 4450
Livetime   = 13.0 seconds

System resolution = 72 eV

Geometry (degrees):
Tilt   = 18.00
Elevation = 20.00
Azimuth   = 0.00
Entry angle = 0.00

Accelerating voltage = 200.00 kV

Quantitative method: Cliff-Lorimer Ratio Thin Section.(4 iterations).
Ratio standard element and line: Silicon, K Series
Analysed all elements
Density = 5.120 g/cm³
Thickness = 100.00 nm

1 peak possibly omitted: 0.00 keV

Standards :
None

Elmt	Peak Area	Stat. Sigma	Obser. %	k Factor	Abs. Corrn.	Element %	Sigma %	Atomic %	
Al K	-3*	-7	-0.09*	1.030	1.046	-0.11*	-0.24	-0.22*	
Si K	9*	8	0.49*	1.000	1.000	0.40*	0.47	0.79*	
P K	16*	10	0.85*	1.000	0.971	0.47*	0.53	0.85*	
V K	8*	10	0.46*	1.121	0.915	0.41*	0.59	0.45*	
Cr K	148	23	8.69	1.129	0.914	8.87	1.31	9.48	
Mn K	-3*	-19	-0.21*	1.184	0.000	-0.15*	-1.18	-0.15*	
Fe K	1403	64	87.57	1.202	0.913	87.97	2.67	87.48	
Ni K	-6*	-6	-0.38*	1.279	0.000	0.23*	-0.40	0.21*	
Nb L	8*	17	0.75*	1.707	0.961	0.73*	1.53	0.43*	
Mo L	17*	15	1.50*	1.725	0.954	1.18*	1.41	0.68*	
Total			100.00			100.00		100.00	

Beam broadening estimate = 8.45 nm
Density estimate   = 7.74 g/cm³

* = <2 sigma

TEMQuant results. Listed at 11:39:00 on 29/06/04
Operator: ben
Spectrum label: **EXI-GB1**

Calibration data: Energy Resn.   Area
Strobe: -7.6 138.43 756623
Calib. element: 4504.8 180.09 139875
Gain factor = 50.039
Livetime   = 50.0 seconds

Sample data: Energy Resn.   Area
Strobe: -7.5 60.51   17223
Total spectrum counts = 2804
Livetime   = 18.0 seconds

System resolution = 72 eV

Geometry (degrees):
Tilt   = 18.00
Elevation = 20.00
Azimuth   = 0.00
Entry angle = 0.00

Accelerating voltage = 200.00 kV

Quantitative method: Cliff-Lorimer Ratio Thin Section.(4 iterations).
Ratio standard element and line: Silicon, K Series
 Analysed all elements
Density = 5.120 g/cm³
Thickness = 100.00 nm

 1 peak possibly omitted: 0.00 keV

Standards :
 None

Elmt	Peak Area	Stat. Sigma	Obser. %	k Factor	Abs. Corrn.	Element %	Sigma %	Atomic %	
Al K	5*	9	0.29*	1.030	1.046	0.33*	0.52	0.68*	
Si K	9*	8	0.49*	1.000	1.000	0.54*	0.47	1.05*	
P K	16*	10	0.85*	1.000	0.971	0.90*	0.53	1.60*	
V K	8*	10	0.46*	1.121	0.915	0.46*	0.59	0.49*	
Cr K	148	23	8.69	1.129	0.914	8.67	1.31	9.19	
Mn K	-3*	-19	-0.21*	1.184	0.000	-0.21*	-1.18	-0.21*	
Fe K	1403	64	87.57	1.202	0.913	87.35	2.67	86.19	
Ni K	-6*	-6	-0.38*	1.279	0.000	-0.39*	-0.40	-0.36*	
Nb L	8*	17	0.75*	1.707	0.961	0.78*	1.53	0.46*	
Mo L	17*	15	1.50*	1.725	0.954	1.57*	1.41	0.90*	
Total			100.00			100.00		100.00	

Beam broadening estimate = 8.45 nm
Density estimate   = 7.74 g/cm³

* = <2 sigma

TEMQuant results. Listed at 10:40:49 on 12/08/04
Operator: ben
Client: none
Job: 101
Spectrum label: **EZI-GB9**

Calibration data: Energy Resn. Area
Strobe: -7.6 138.43 756623
Calib. element: 4504.8 180.09 139875
Gain factor = 50.039
Livetime   = 50.0 seconds

Sample data: Energy Resn. Area
Strobe: -7.4 61.33 18665
Total spectrum counts = 2857
Livetime   = 19.6 seconds

System resolution = 72 eV

Geometry (degrees):
Tilt   = 18.00
Elevation = 20.00
Azimuth   = 0.00
Entry angle = 0.00

Accelerating voltage = 200.00 kV

Quantitative method: Cliff-Lorimer Ratio Thin Section.(5 iterations).
Ratio standard element and line: Silicon, K Series
 Analysed all elements
Density = 5.120 g/cm³
Thickness = 100.00 nm

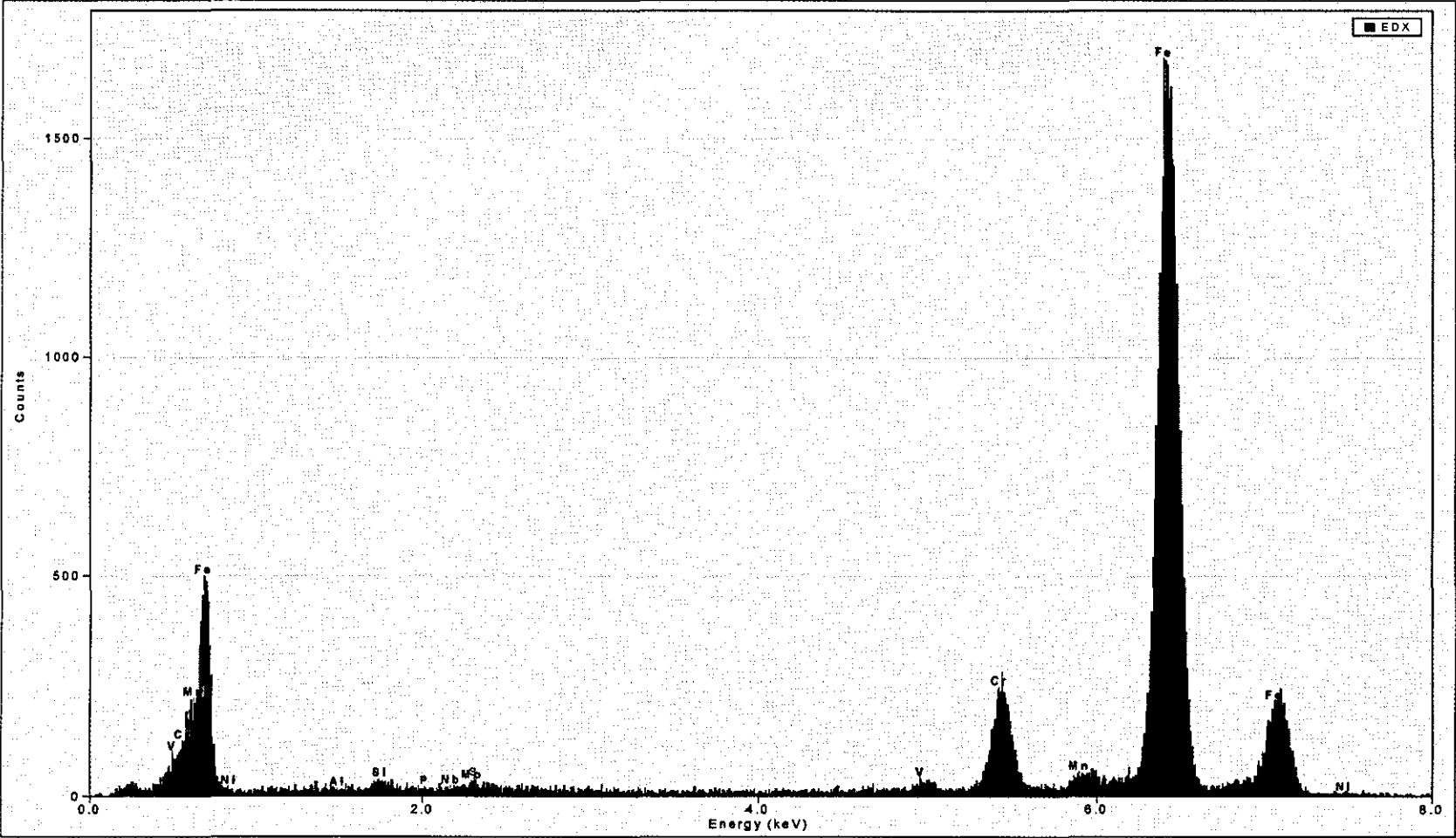1 peak possibly omitted: 0.00 keV

Standards :
None

| Elmt	Peak Area	Stat. Sigma	Obser. %	k Factor	Abs. Corrn.	Element %	Sigma %	Atomic %
Al K	-11*	-9	-0.63*	1.030	1.043	-0.71*	-0.58	-1.36*
Si K	140	17	7.47	1.000	1.000	8.05	1.00	14.94
P K	19*	11	1.03*	1.000	0.981	1.09*	0.62	1.83*
V K	8*	12	0.46*	1.121	0.922	0.46*	0.74	0.47*
Cr K	146	25	8.82	1.129	0.921	8.75	1.45	8.77
Mn K	-7*	-18	-0.42*	1.184	0.919	-0.42*	-1.16	-0.40*
Fe K	1242	59	79.81	1.202	0.921	79.16	2.96	73.89
Ni K	-6*	-7	-0.42*	1.279	0.924	-0.42*	-0.46	-0.37*
Nb L	23*	20	2.10*	1.707	0.971	2.19*	1.89	1.23*
Mo L	19*	19	1.79*	1.725	0.963	1.85*	1.76	1.01*
Total			100.00		100.00		100.00	

Beam broadening estimate = 8.27 nm
Density estimate   = 7.38 g/cm³

* = <2 sigma

APPENDIX B-2: Results of Phosphorus Determination by FEGTEM on PWHT Specimens(Part of the Results)

II
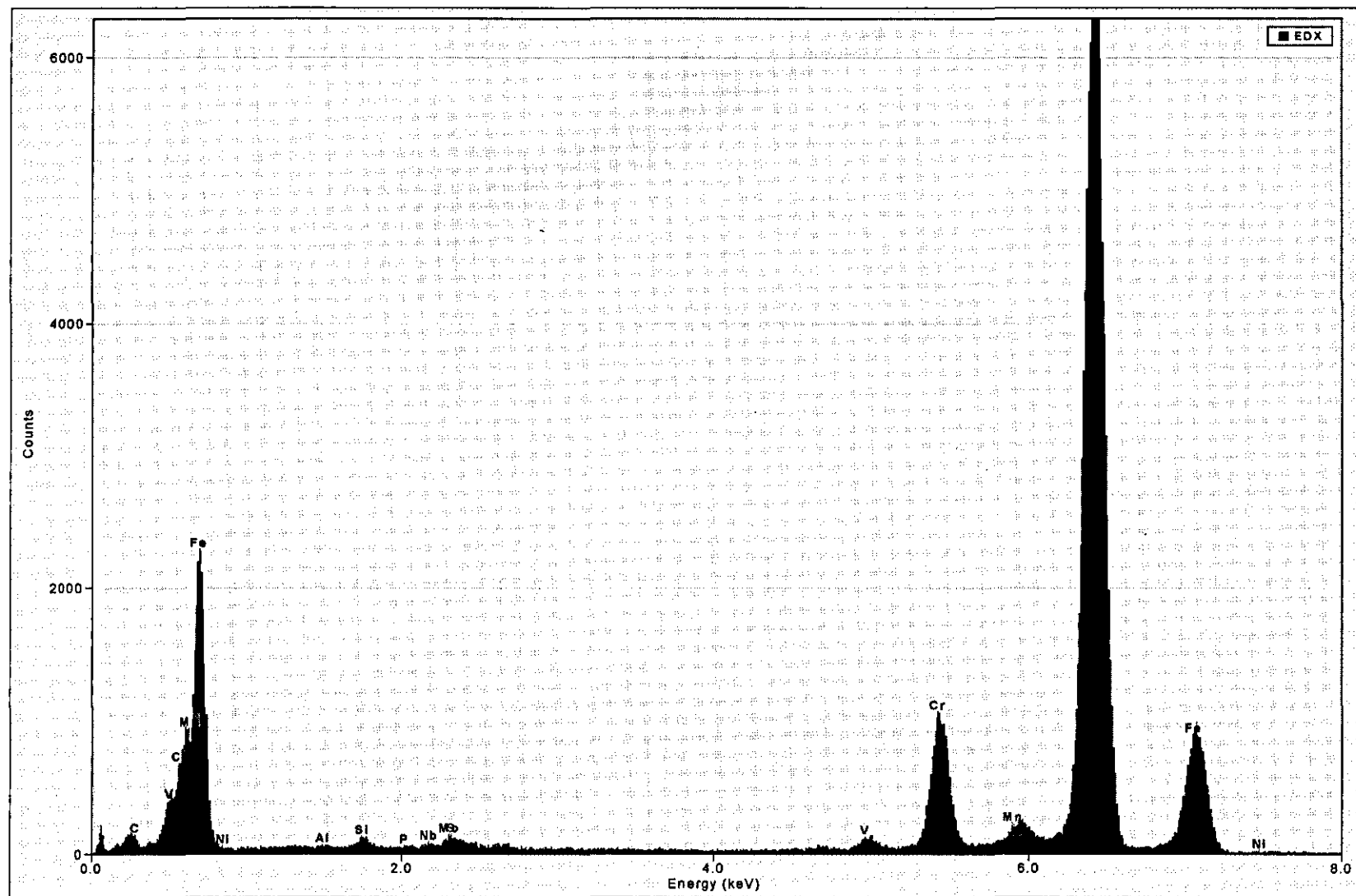
Spectrum processing :
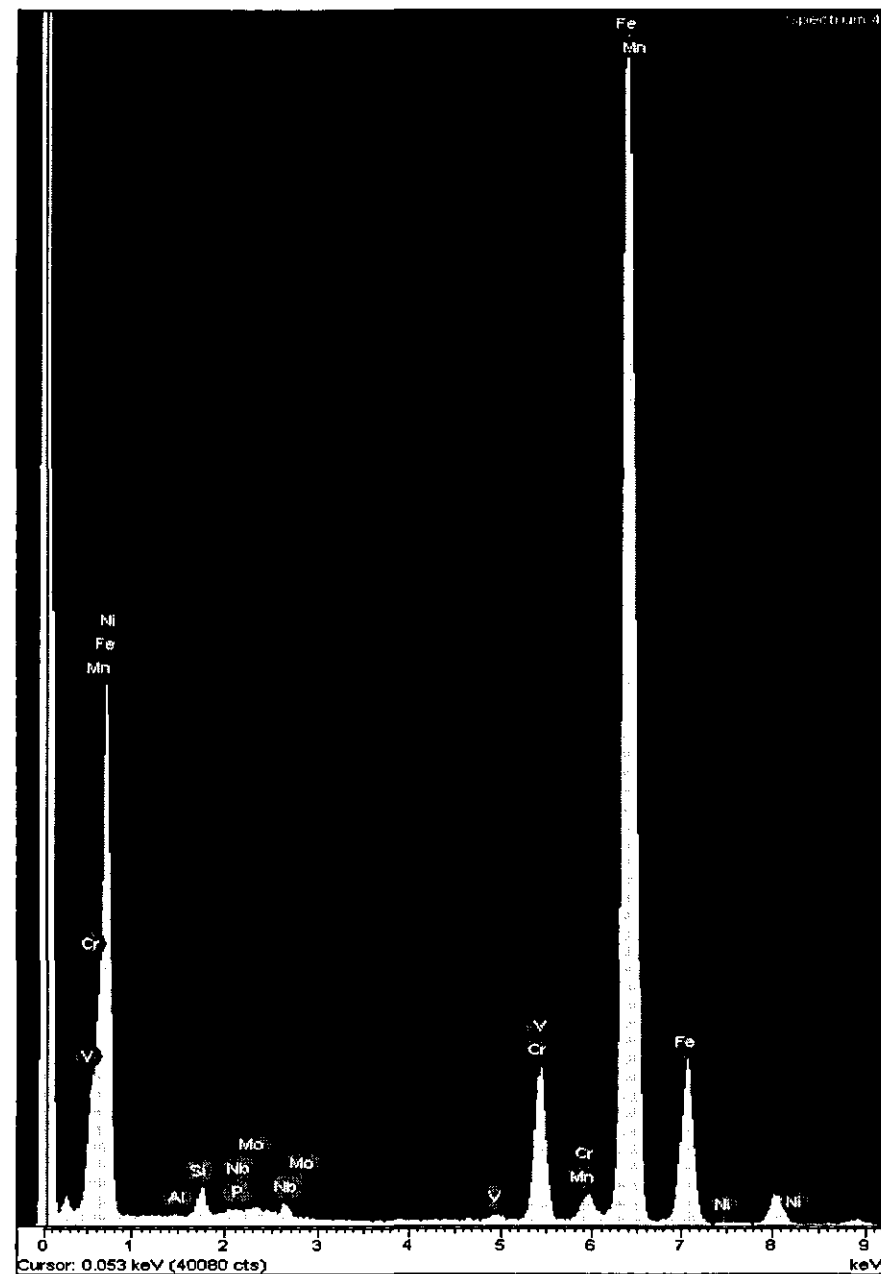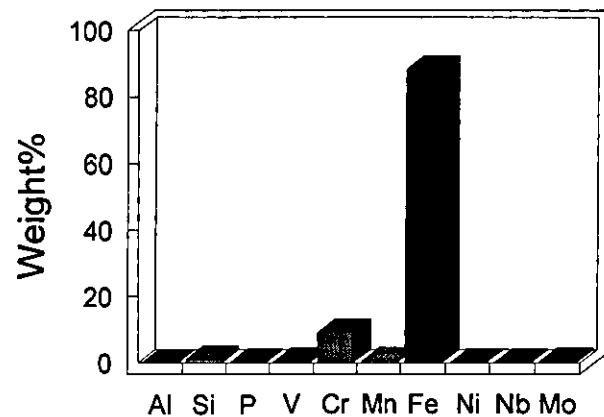Peaks possibly omitted : 8.891, 17.480 keV

Quantitation method : Cliff Lorimer thin ratio section.
Processing option : All elements analysed (Normalised)

Number of iterations = 1

Standardless

Element	Peak Area	Area Sigma	k factor	Abs Corrn.	Weight %	Weight % Sigma	Atomic %
Al K	3	50	1.044	1.000	0.00	0.04	0.01
Si K	1282	71	1.000	1.000	1.07	0.06	2.10
P K	124	90	0.992	1.000	0.10	0.07	0.18
V K	417	67	1.093	1.000	0.38	0.06	0.41
Cr K	9982	175	1.100	1.000	9.20	0.16	9.72
Mn K	524	103	1.153	1.000	0.51	0.10	0.51
Fe K	89984	490	1.170	1.000	88.19	0.34	86.74
Ni K	66	53	1.245	1.000	0.07	0.06	0.06
Nb L	36	163	1.687	1.000	0.05	0.23	0.03
Mo L	295	140	1.701	1.000	0.42	0.20	0.24
Totals					100.00		

Quantitative results

III

Spectrum processing :
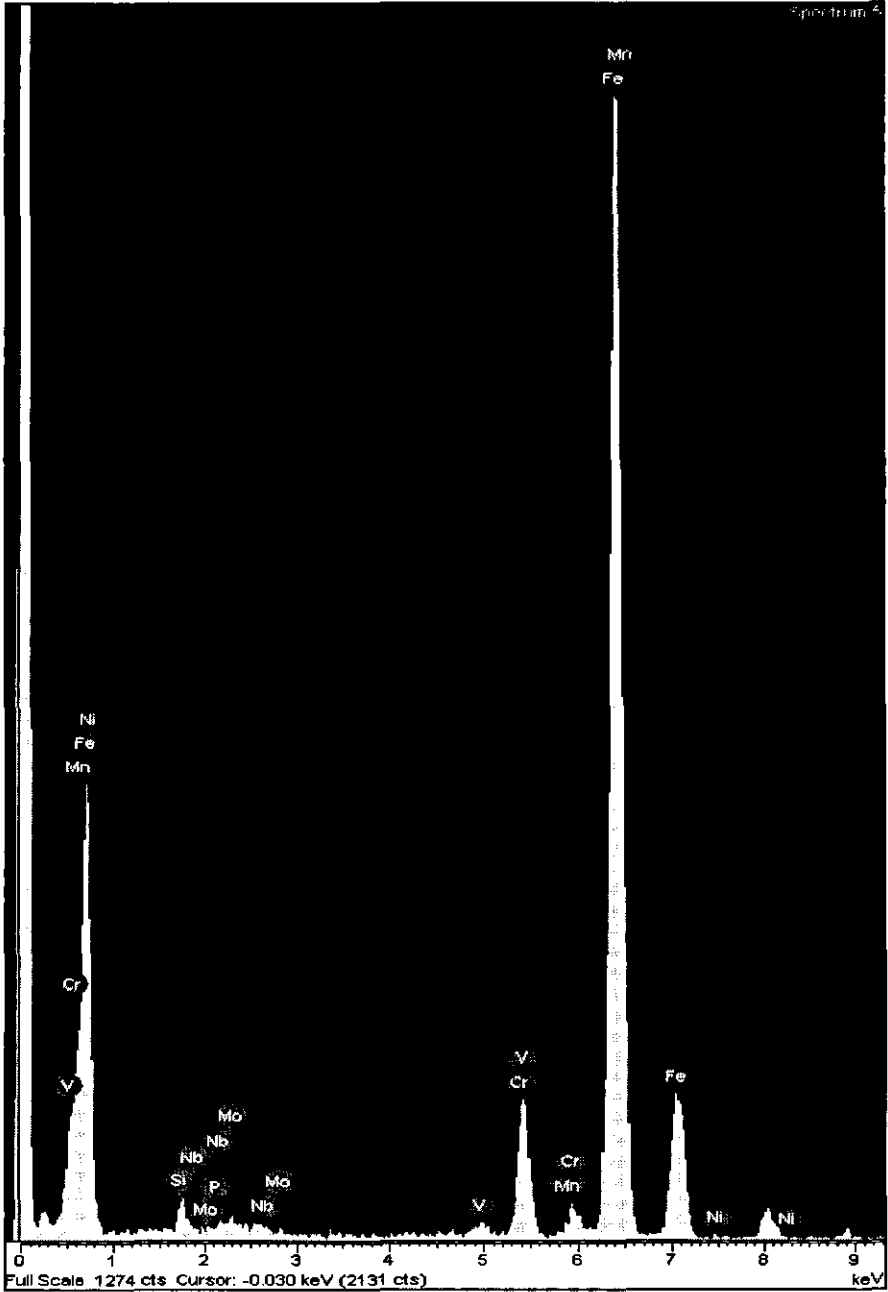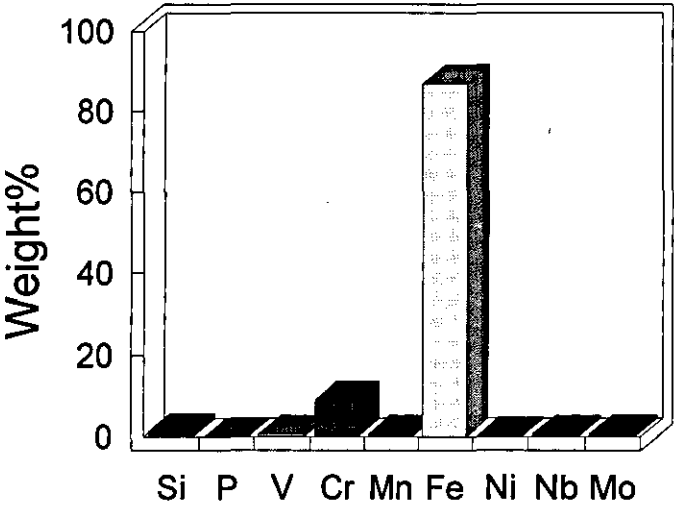Peak possibly omitted : 8.860 keV

Quantitation method : Cliff Lorimer thin ratio section.
Processing option : All elements analysed (Normalised)

Number of iterations = 1

Standardless

Element	Peak Area	Area Sigma	k factor	Abs Corrn.	Weight %	Weight % Sigma	Atomic %
Si K	174	24	1.000	1.000	1.27	0.18	2.49
P K	1	29	0.992	1.000	0.01	0.21	0.02
V K	84	25	1.093	1.000	0.67	0.20	0.72
Cr K	1116	59	1.100	1.000	8.94	0.46	9.47
Mn K	83	35	1.153	1.000	0.70	0.29	0.70
Fe K	10197	163	1.170	1.000	86.93	1.01	85.71
Ni K	11	19	1.245	1.000	0.10	0.17	0.10
Nb L	54	57	1.687	1.000	0.66	0.69	0.39
Mo L	58	49	1.701	1.000	0.72	0.60	0.41
Totals					100.00		

Quantitative results

IV

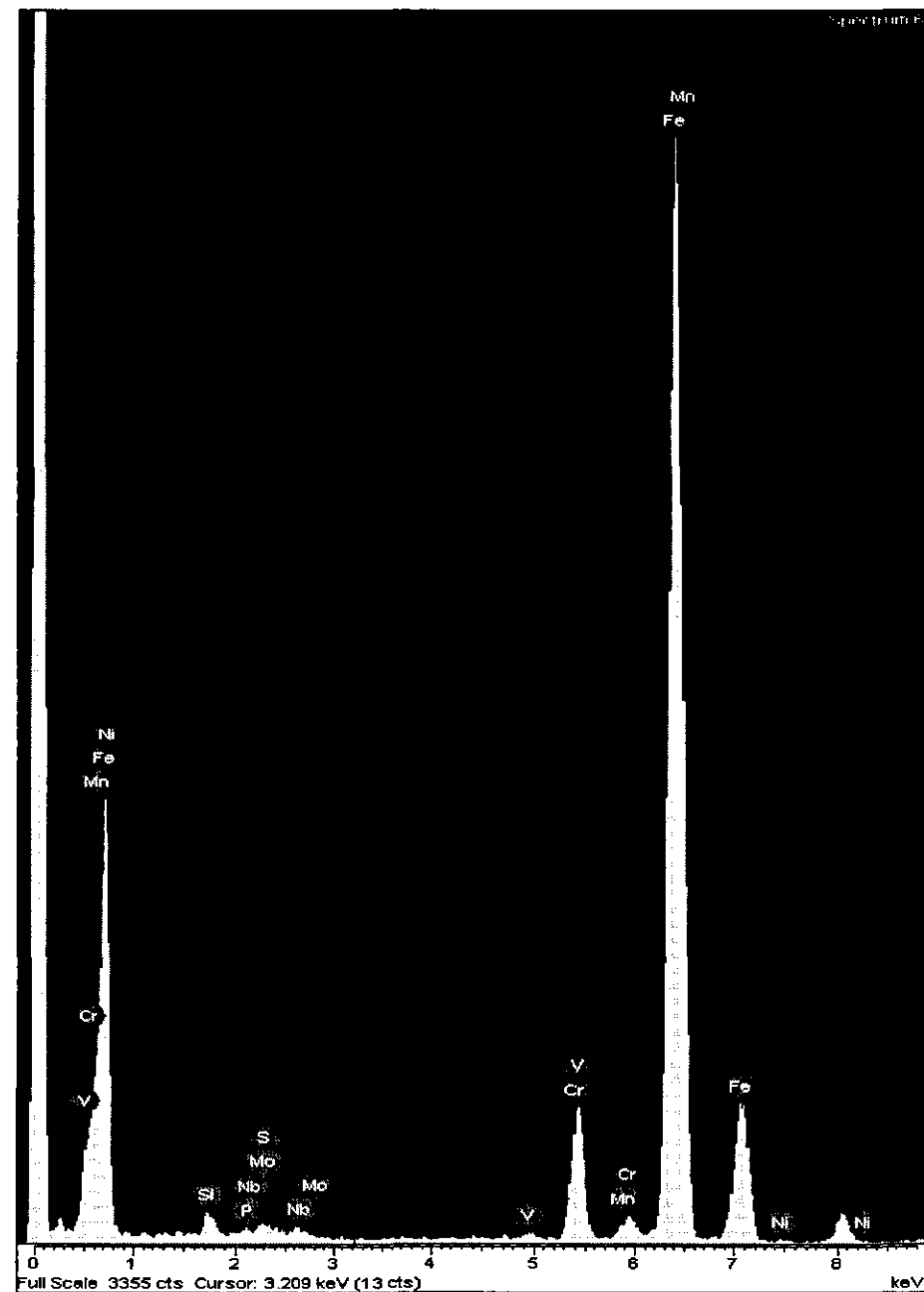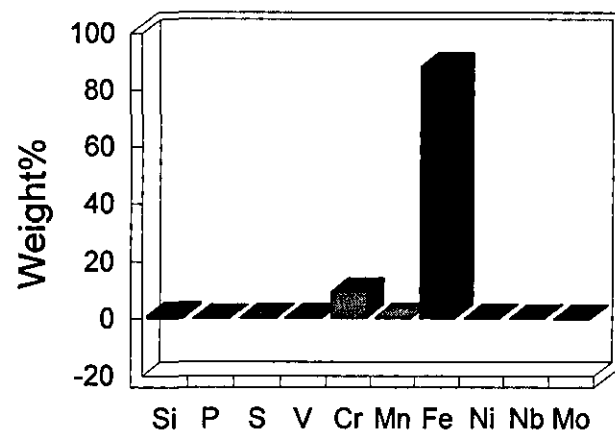Spectrum processing :
No peaks omitted

Quantitation method : Cliff Lorimer thin ratio section.
Processing option : All elements analysed (Normalised)

Number of iterations = 1

Standardless

Element	Peak	Area	k	Abs	Weight %	Weight %	Atomic %
	Area	Sigma	factor	Corrn.		Sigma	
Si K	351	37	1.000	1.000	1.03	0.11	2.00
P K	1	47	0.992	1.000	0.00	0.14	0.00
S K	152	130	0.940	1.000	0.42	0.36	0.71
V K	116	36	1.093	1.000	0.37	0.11	0.40
Cr K	2906	95	1.100	1.000	9.33	0.31	9.82
Mn K	178	56	1.153	1.000	0.60	0.19	0.60
Fe K	25818	263	1.170	1.000	88.19	1.17	86.37
Ni K	52	27	1.245	1.000	0.19	0.10	0.18
Nb L	23	88	1.687	1.000	0.12	0.43	0.07
Mo L	-48	225	1.701	1.000	-0.24	1.12	-0.14
Totals					100.00		

Quantitative results

Full Scale 3355 cts Cursor: 3.209 keV (13 cts)

V

Spectrum processing :
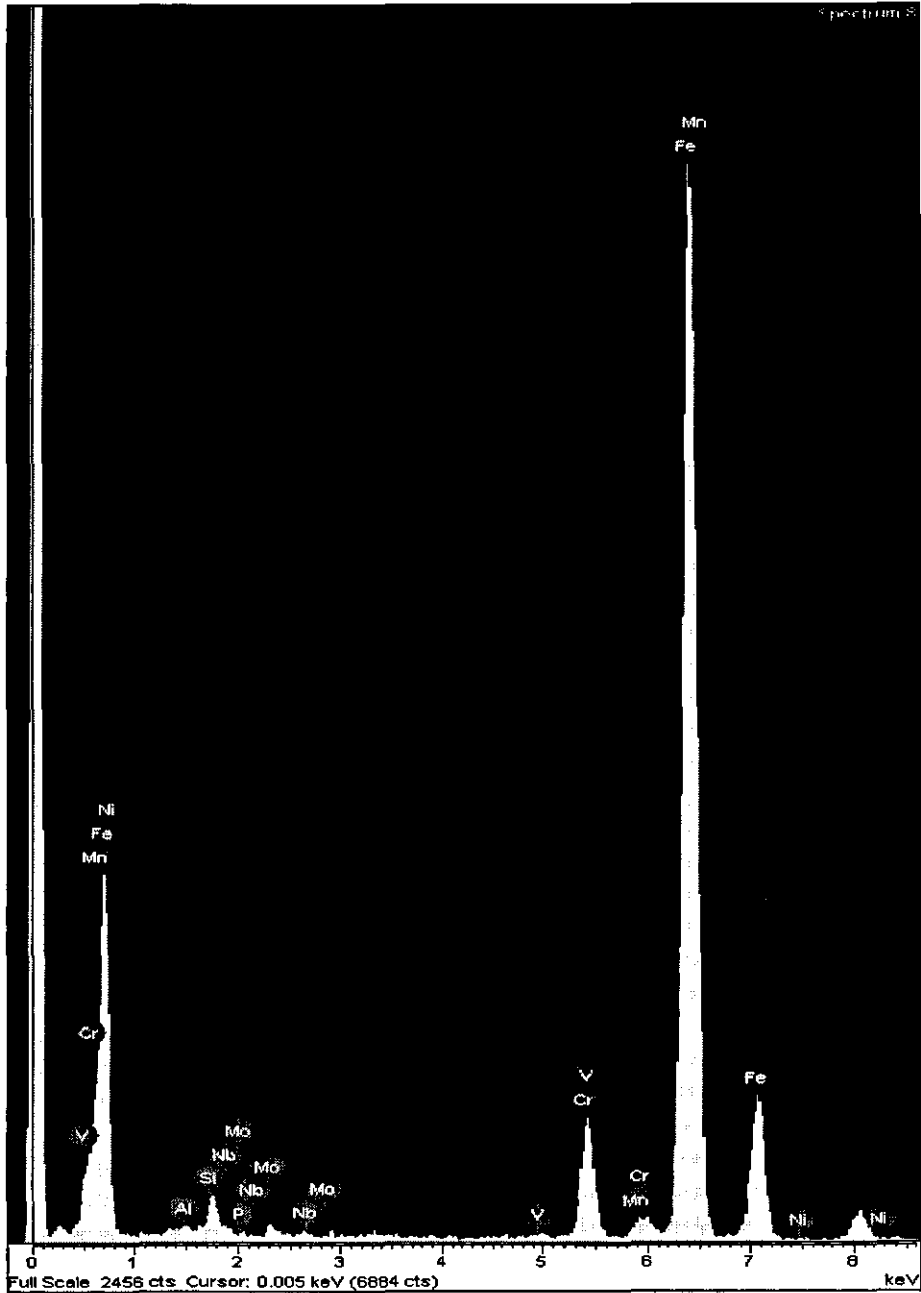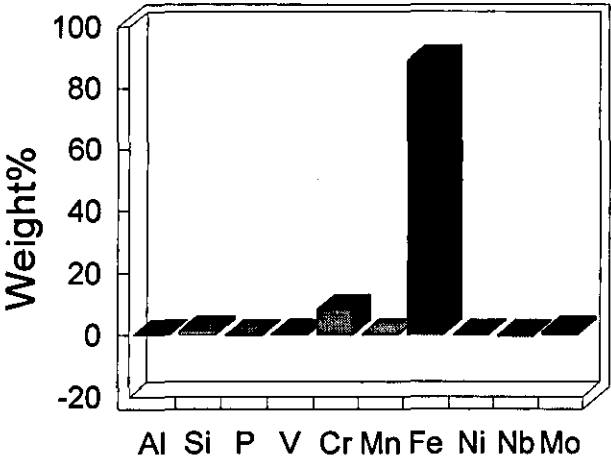Peak possibly omitted : 8.920 keV

Quantitation method : Cliff Lorimer thin ratio section.
Processing option : All elements analysed (Normalised)

Number of iterations = 1

Standardless

Element	Peak Area	Area Sigma	k factor	Abs Corn.	Weight %	Weight % Sigma	Atomic %
Al K	14	27	1.044	1.000	0.06	0.12	0.13
Si K	332	37	1.000	1.000	1.38	0.15	2.69
P K	-52	36	0.992	1.000	-0.21	0.15	-0.38
V K	57	29	1.093	1.000	0.26	0.13	0.28
Cr K	1836	77	1.100	1.000	8.36	0.34	8.84
Mn K	73	46	1.153	1.000	0.35	0.22	0.35
Fe K	18399	222	1.170	1.000	89.13	0.69	87.69
Ni K	14	20	1.245	1.000	0.07	0.10	0.07
Nb L	-68	61	1.687	1.000	-0.48	0.43	-0.28
Mo L	153	53	1.701	1.000	1.08	0.37	0.62
Totals					100.00		

Quantitative results

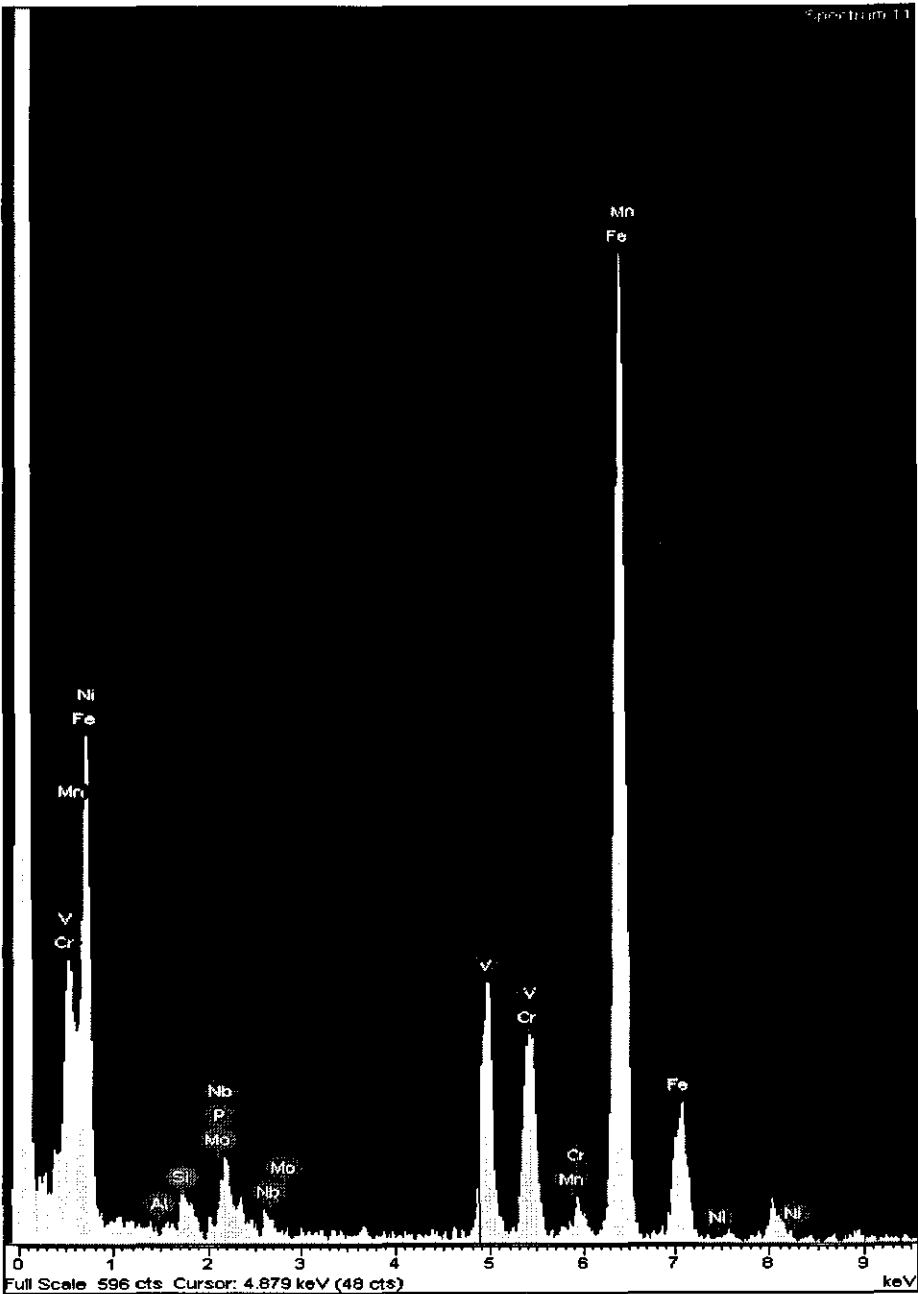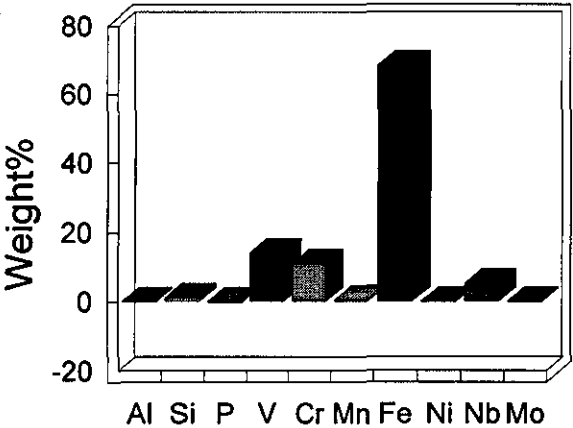VI

Spectrum processing :
No peaks omitted

Quantitation method : Cliff Lorimer thin ratio section.
Processing option : All elements analysed (Normalised)

Number of iterations = 1

Standardless

| Element	Peak Area	Area Sigma	k factor	Abs Corrn.	Weight %	Weight % Sigma	Atomic %
Al K	-10	14	1.044	1.000	-0.14	0.21	-0.29
Si K	81	20	1.000	1.000	1.13	0.28	2.23
P K	-14	28	0.992	1.000	-0.19	0.39	-0.34
V K	929	51	1.093	1.000	14.19	0.78	15.40
Cr K	715	53	1.100	1.000	10.98	0.78	11.69
Mn K	36	29	1.153	1.000	0.58	0.47	0.59
Fe K	4185	105	1.170	1.000	68.41	1.65	67.75
Ni K	-5	19	1.245	1.000	-0.08	0.33	-0.07
Nb L	219	59	1.687	1.000	5.17	1.33	3.08
Mo L	-2	49	1.701	1.000	-0.06	1.18	-0.03
Totals					100.00		

Quantitative results

VII

Spectrum processing :
Peak possibly omitted : 8.920 keV

Quantitation method : Cliff Lorimer thin ratio section.
Processing option : All elements analysed (Normalised)

Number of iterations = 1

Standardless

Element	Peak Area	Area Sigma	k factor	Abs Corrn.	Weight %	Weight % Sigma	Atomic %
Al K	57	36	1.044	1.000	0.08	0.05	0.17
Si K	240	47	1.000	1.000	0.32	0.06	0.64
P K	-82	63	0.992	1.000	-0.11	0.08	-0.20
V K	251	57	1.093	1.000	0.37	0.08	0.40
Cr K	6191	140	1.100	1.000	9.21	0.20	9.83
Mn K	271	83	1.153	1.000	0.42	0.13	0.43
Fe K	56032	390	1.170	1.000	88.69	0.40	88.12
Ni K	36	42	1.245	1.000	0.06	0.07	0.06
Nb L	-71	111	1.687	1.000	-0.16	0.25	-0.10
Mo L	481	96	1.701	1.000	1.11	0.22	0.64
Totals					100.00		

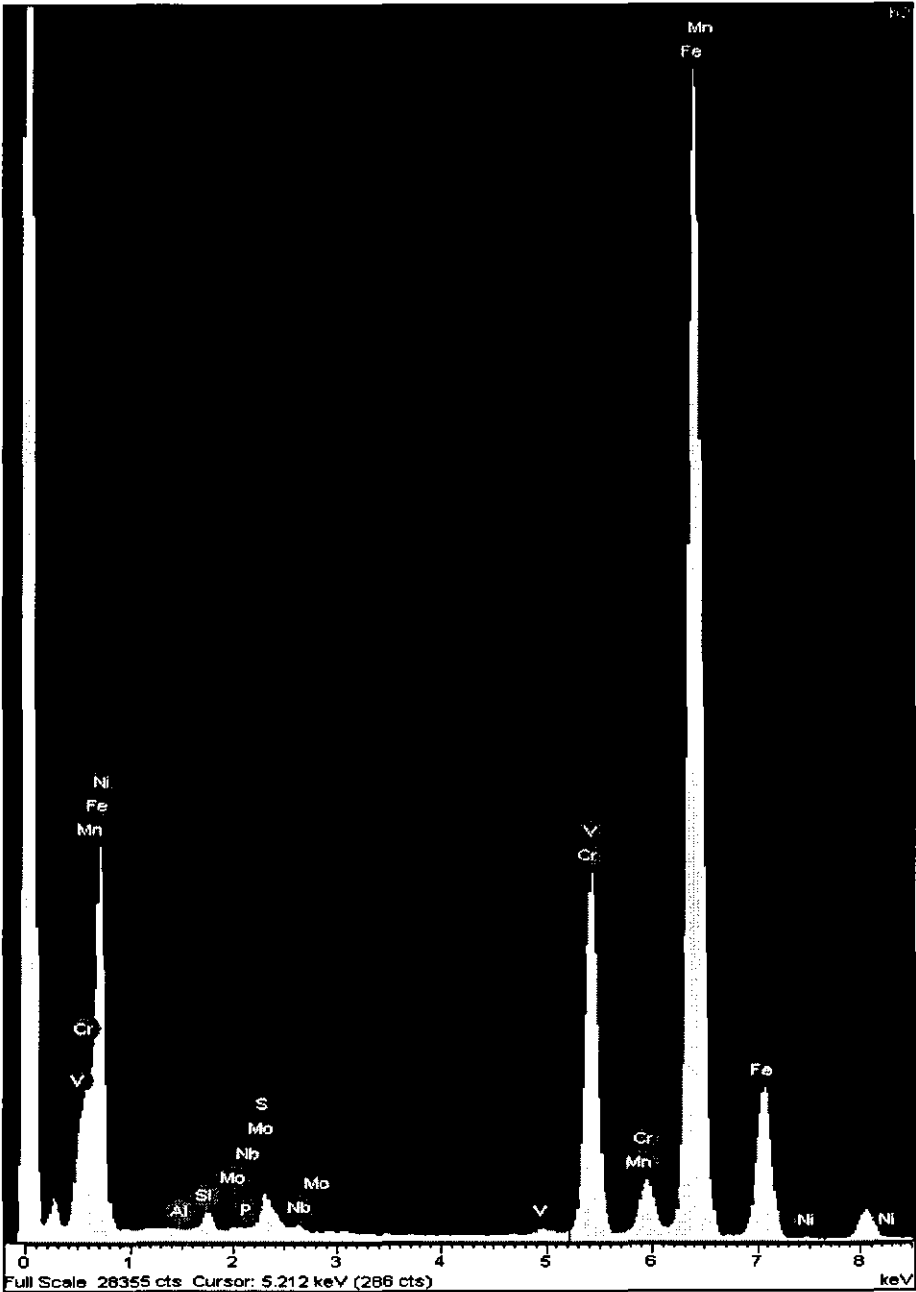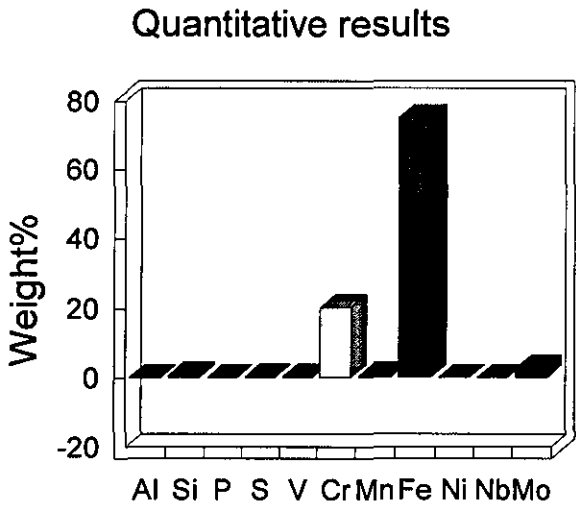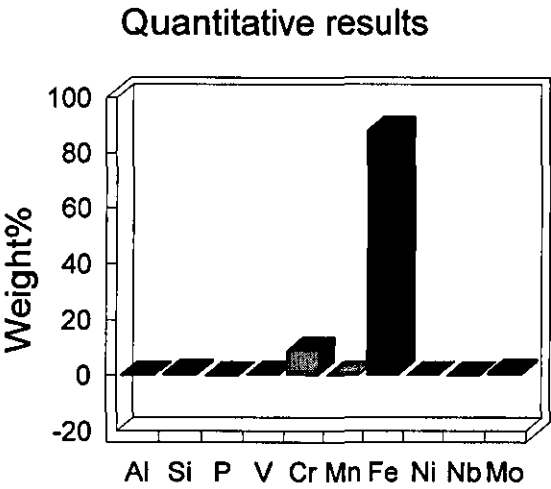## Quantitative results

VIII
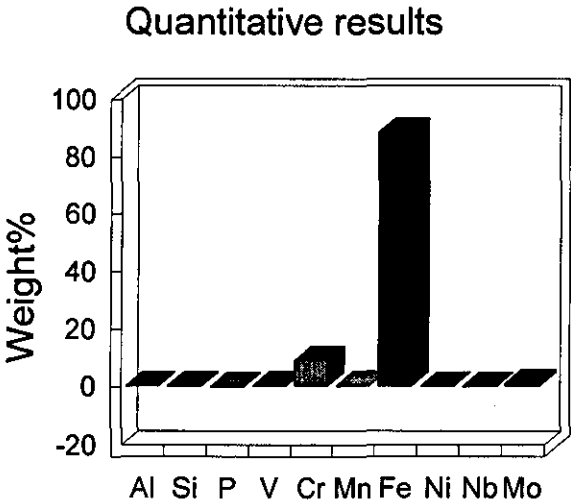
Spectrum processing :
Peaks possibly omitted : 8.889, 17.427 keV

Quantitation method : Cliff Lorimer thin ratio section.
Processing option : All elements analysed (Normalised)

Number of iterations = 1

Standardless

Element	Peak Area	Area Sigma	k factor	Abs Corm.	Weight %	Weight % Sigma	Atomic %
Al K	-220	90	1.044	1.000	-0.06	0.03	-0.13
Si K	2345	113	1.000	1.000	0.64	0.03	1.27
P K	178	152	0.992	1.000	0.05	0.04	0.09
S K	724	489	0.940	1.000	0.19	0.13	0.32
V K	861	122	1.093	1.000	0.26	0.04	0.28
Cr K	67011	434	1.100	1.000	20.27	0.15	21.54
Mn K	2032	222	1.153	1.000	0.64	0.07	0.65
Fe K	233311	793	1.170	1.000	75.06	0.35	74.25
Ni K	265	88	1.245	1.000	0.09	0.03	0.09
Nb L	187	313	1.687	1.000	0.09	0.15	0.05
Mo L	5930	826	1.701	1.000	2.77	0.38	1.60
Totals					100.00		

Quantitative results

IX

Spectrum processing :
Peaks possibly omitted : 8.892, 17.441 keV

Quantitation method : Cliff Lorimer thin ratio section.
Processing option : All elements analysed (Normalised)

Number of iterations = 1

Standardless

| Element	Peak Area	Area Sigma	k factor	Abs Corrn.	Weight %	Weight % Sigma	Atomic %
Al K	-86	35	1.044	1.000	-0.21	0.08	-0.42
Si K	382	43	1.000	1.000	0.88	0.10	1.73
P K	-28	52	0.992	1.000	-0.06	0.12	-0.11
V K	183	45	1.093	1.000	0.46	0.11	0.50
Cr K	3587	106	1.100	1.000	9.09	0.26	9.68
Mn K	109	62	1.153	1.000	0.29	0.16	0.29
Fe K	32788	296	1.170	1.000	88.41	0.56	87.66
Ni K	11	33	1.245	1.000	0.03	0.09	0.03
Nb L	-36	95	1.687	1.000	-0.14	0.37	-0.08
Mo L	316	82	1.701	1.000	1.24	0.32	0.72
Totals					100.00		

Quantitative results

X

Spectrum processing :
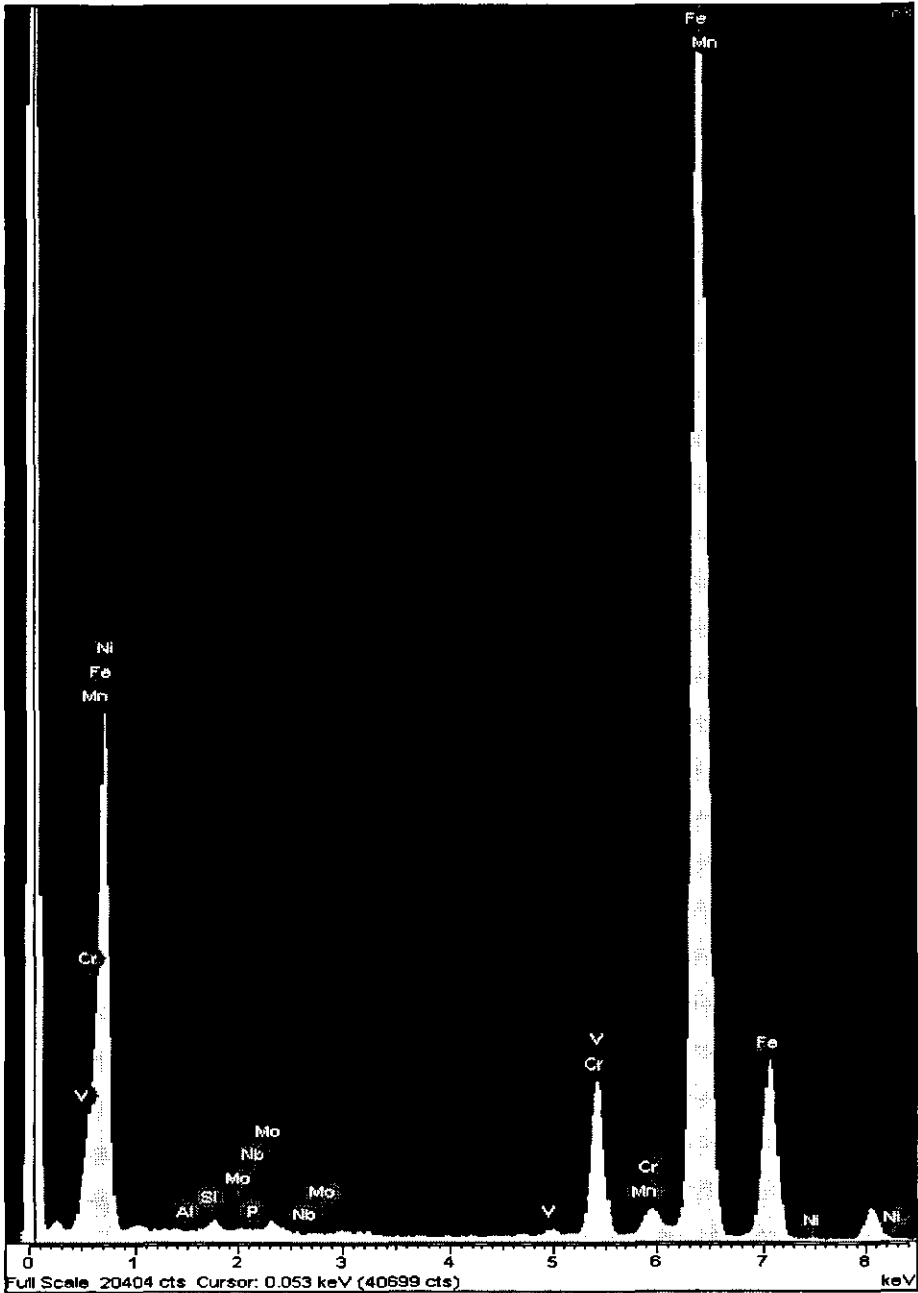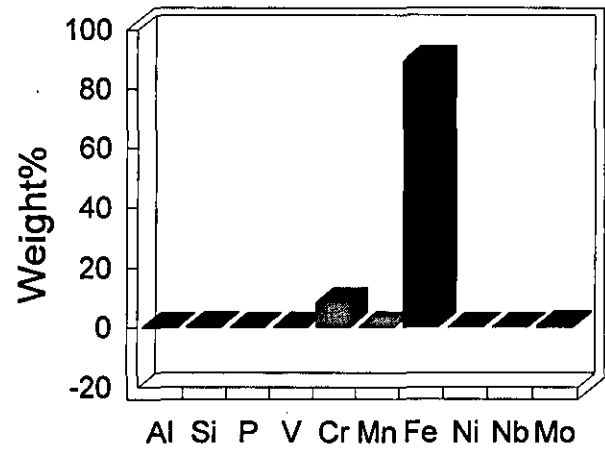Peak possibly omitted : 8.918 keV

Quantitation method : Cliff Lorimer thin ratio section.
Processing option : All elements analysed (Normalised)

Number of iterations = 1

Standardless

Element	Peak Area	Area Sigma	k factor	Abs Corrn.	Weight %	Weight % Sigma	Atomic %
Al K	22	30	1.044	1.000	0.10	0.14	0.20
Si K	107	30	1.000	1.000	0.46	0.13	0.92
P K	38	36	0.992	1.000	0.16	0.15	0.29
V K	9	30	1.093	1.000	0.04	0.14	0.05
Cr K	1834	78	1.100	1.000	8.68	0.36	9.28
Mn K	90	48	1.153	1.000	0.44	0.24	0.45
Fe K	17417	219	1.170	1.000	87.63	0.76	87.27
Ni K	49	27	1.245	1.000	0.26	0.15	0.25
Nb L	98	68	1.687	1.000	0.71	0.49	0.43
Mo L	206	60	1.701	1.000	1.51	0.43	0.87
Totals					100.00		

Quantitative results

XI
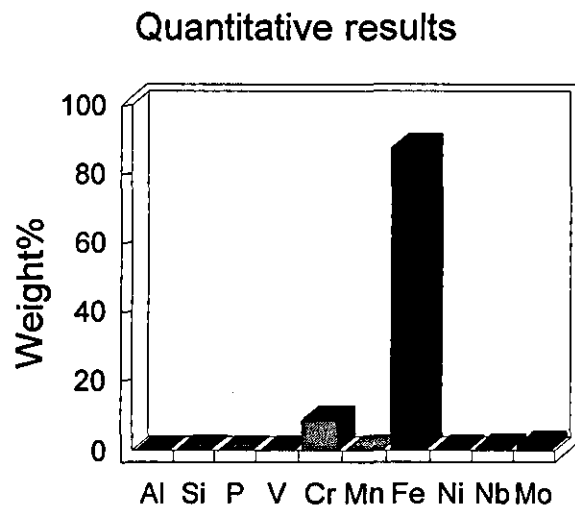
Spectrum processing :
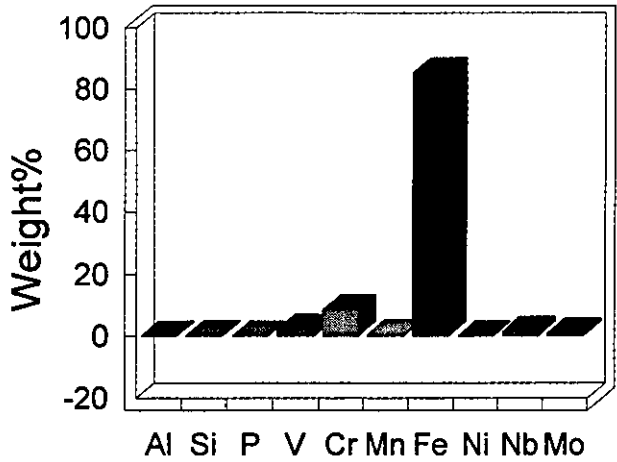Peaks possibly omitted : 8.901, 17.431 keV

Quantitation method : Cliff Lorimer thin ratio section.
Processing option : All elements analysed (Normalised)

Number of iterations = 1

Standardless

Element	Peak Area	Area Sigma	k factor	Abs Corrn.	Weight %	Weight % Sigma	Atomic %
Al K	-139	75	1.044	1.000	-0.06	0.03	-0.12
Si K	978	89	1.000	1.000	0.38	0.03	0.75
P K	114	118	0.992	1.000	0.04	0.05	0.08
V K	699	101	1.093	1.000	0.30	0.04	0.32
Cr K	20027	255	1.100	1.000	8.52	0.10	9.09
Mn K	1066	156	1.153	1.000	0.48	0.07	0.48
Fe K	197651	726	1.170	1.000	89.40	0.22	88.82
Ni K	179	77	1.245	1.000	0.09	0.04	0.08
Nb L	86	216	1.687	1.000	0.06	0.14	0.03
Mo L	1220	186	1.701	1.000	0.80	0.12	0.46
Totals					100.00		

Quantitative results

XII

Spectrum processing :
Peaks possibly omitted : 8.899, 16.572 keV
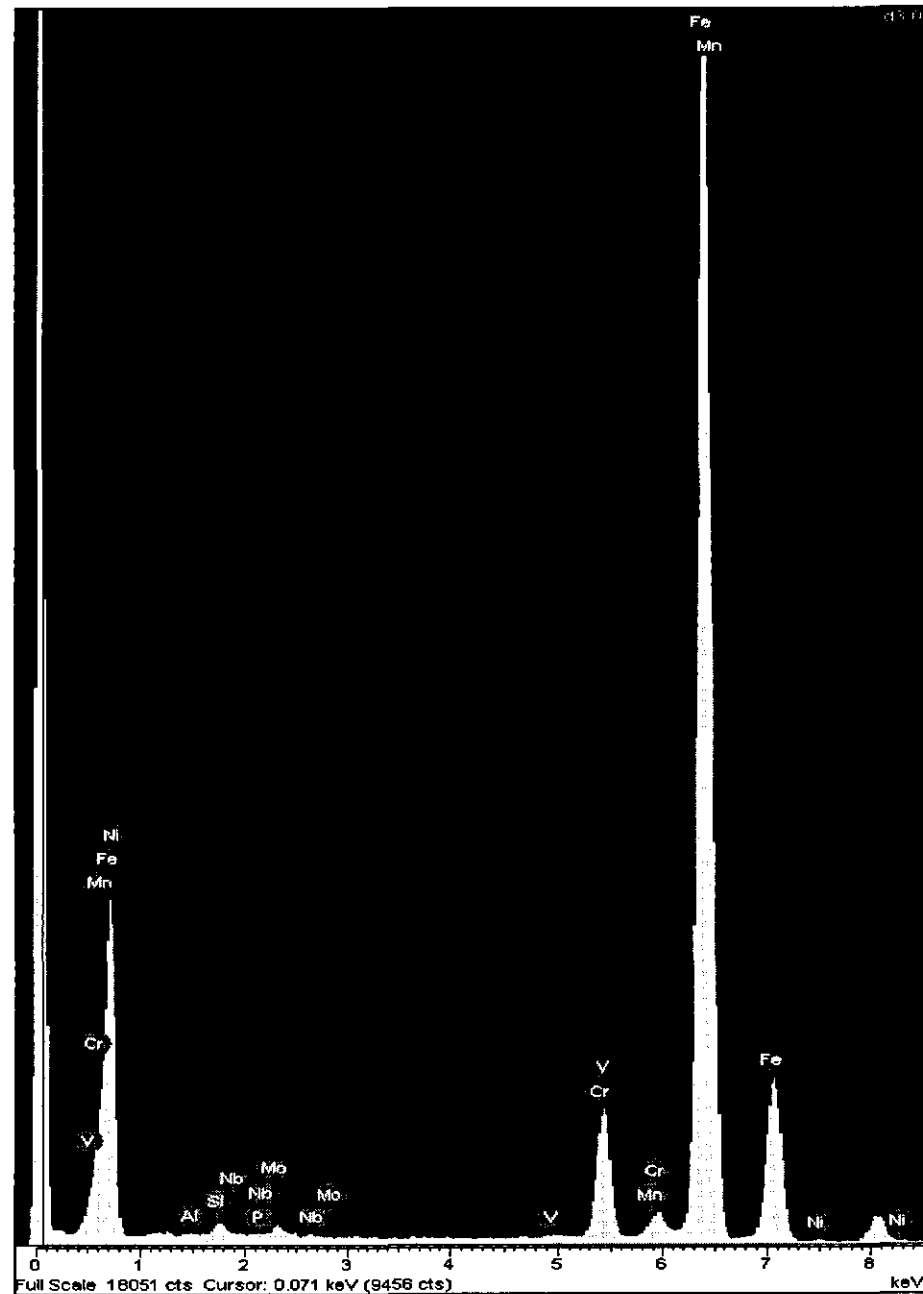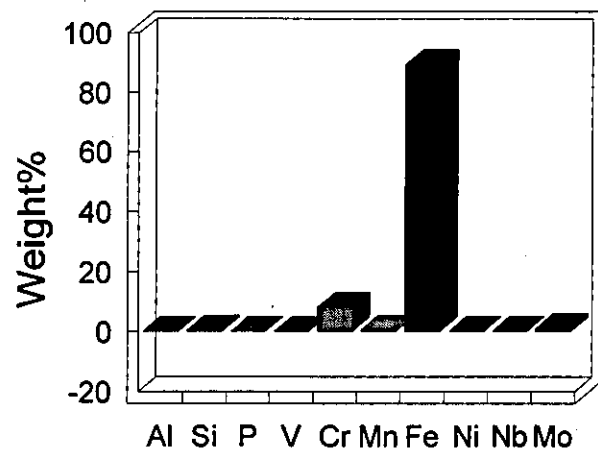
Quantitation method : Cliff Lorimer thin ratio section.
Processing option : All elements analysed (Normalised)

Number of iterations = 1

Standardless

Element	Peak Area	Area Sigma	k factor	Abs Corrn.	Weight %	Weight % Sigma	Atomic %
Al K	-20	39	1.044	1.000	-0.02	0.04	-0.05
Si K	274	52	1.000	1.000	0.29	0.05	0.58
P K	30	75	0.992	1.000	0.03	0.08	0.06
V K	1998	95	1.093	1.000	2.32	0.11	2.54
Cr K	7442	160	1.100	1.000	8.69	0.18	9.32
Mn K	441	96	1.153	1.000	0.54	0.12	0.55
Fe K	68810	432	1.170	1.000	85.44	0.39	85.35
Ni K	93	47	1.245	1.000	0.12	0.06	0.12
Nb L	895	151	1.687	1.000	1.60	0.27	0.96
Mo L	548	130	1.701	1.000	0.99	0.23	0.58
Totals					100.00		

Quantitative results

XIII

Spectrum processing :
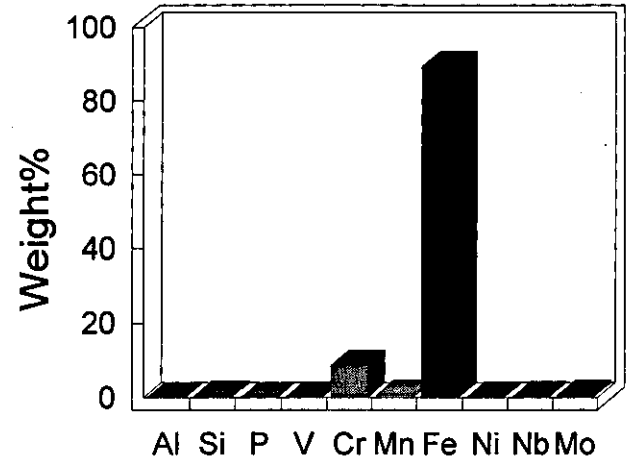Peaks possibly omitted : 1.210, 8.894, 17.432 keV

Quantitation method : Cliff Lorimer thin ratio section.
Processing option : All elements analysed (Normalised)

Number of iterations = 1

Standardless

Element	Peak Area	Area Sigma	k factor	Abs Corrn.	Weight %	Weight % Sigma	Atomic %
Al K	83	66	1.044	1.000	0.04	0.03	0.09
Si K	859	82	1.000	1.000	0.42	0.04	0.83
P K	-25	105	0.992	1.000	-0.01	0.05	-0.02
V K	264	90	1.093	1.000	0.14	0.05	0.15
Cr K	15276	227	1.100	1.000	8.19	0.12	8.74
Mn K	1008	142	1.153	1.000	0.57	0.08	0.57
Fe K	156823	651	1.170	1.000	89.42	0.25	88.88
Ni K	169	73	1.245	1.000	0.10	0.04	0.10
Nb L	192	192	1.687	1.000	0.16	0.16	0.09
Mo L	1180	166	1.701	1.000	0.98	0.14	0.57
Totals					100.00		

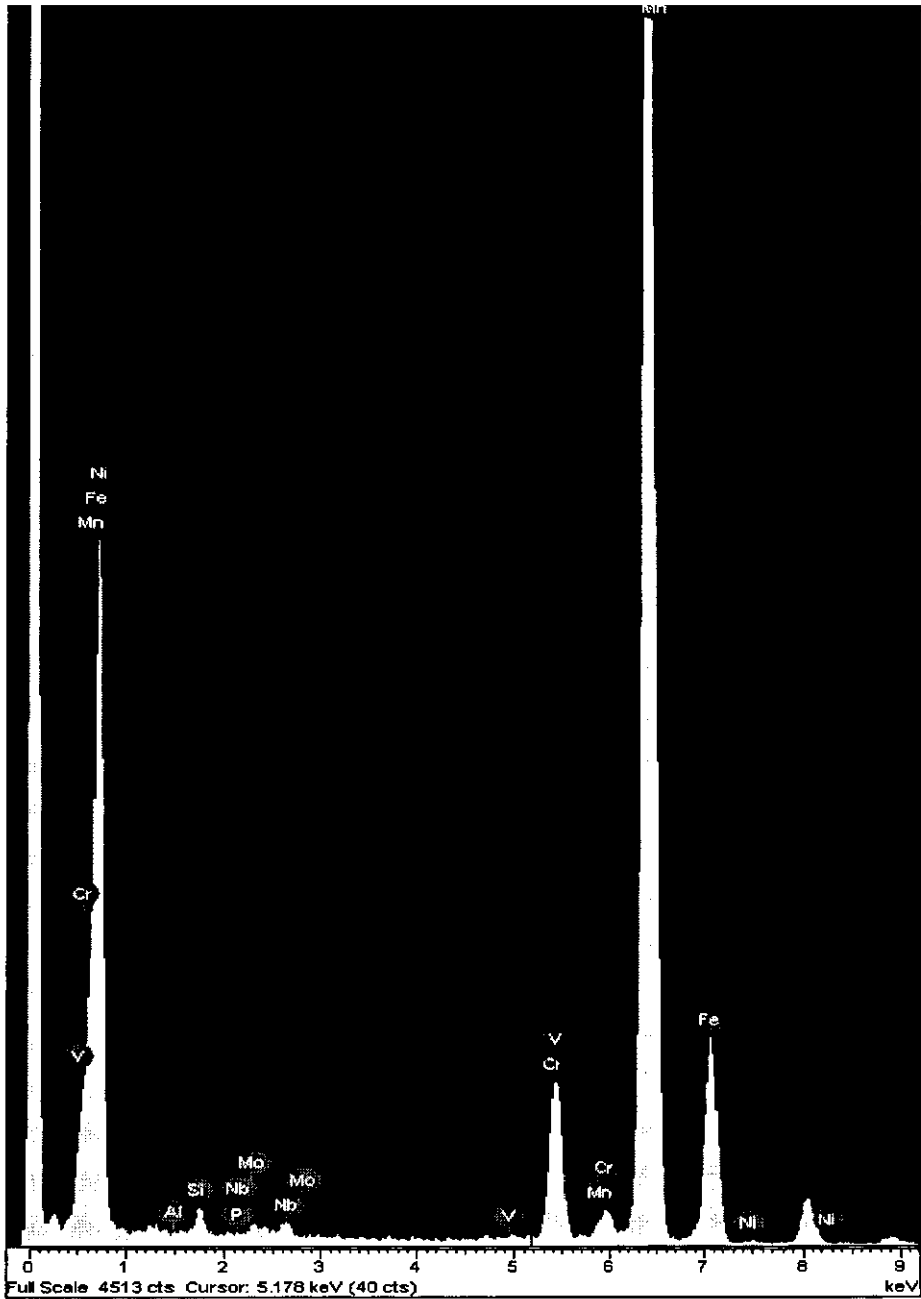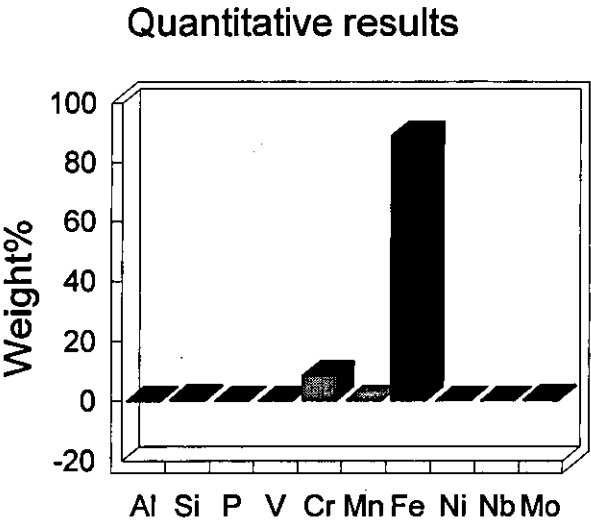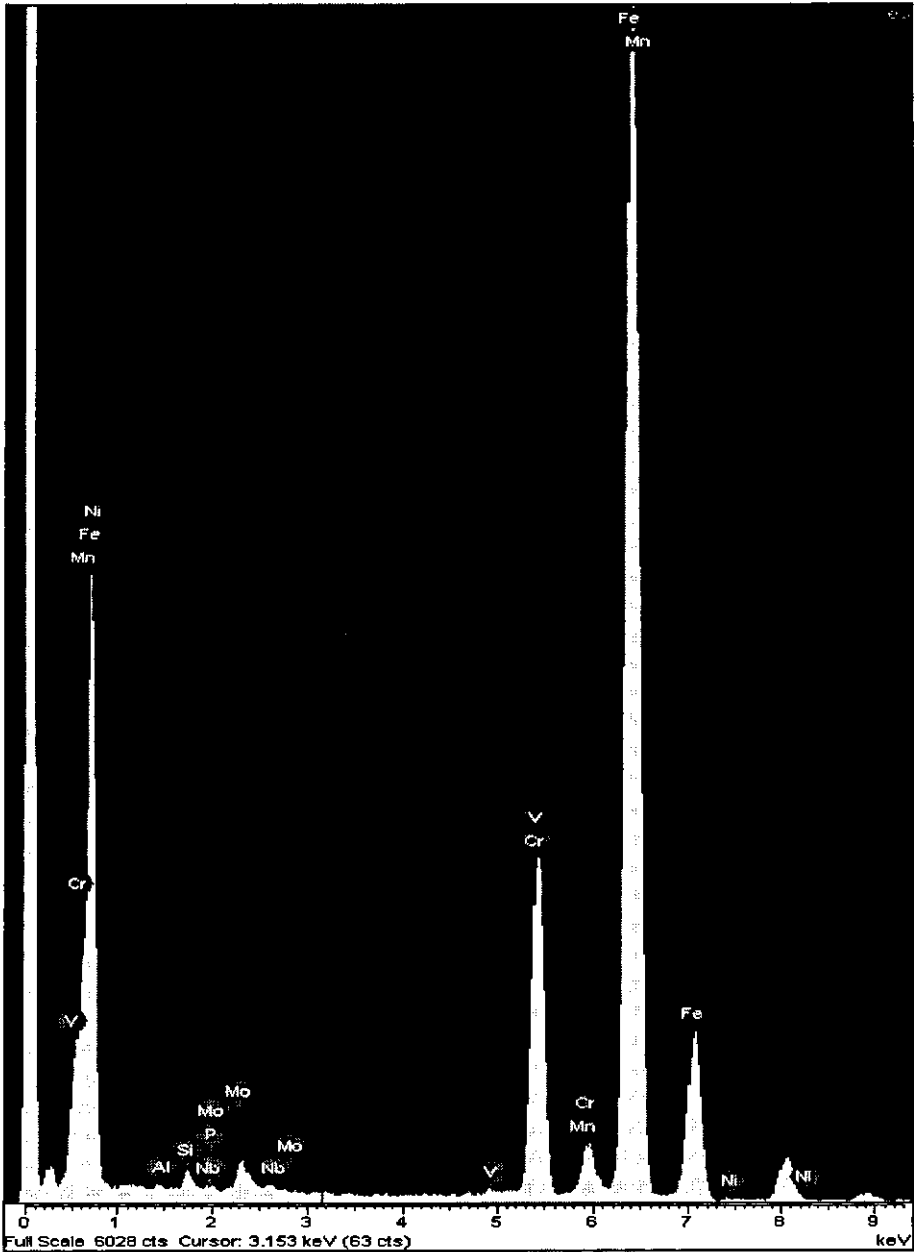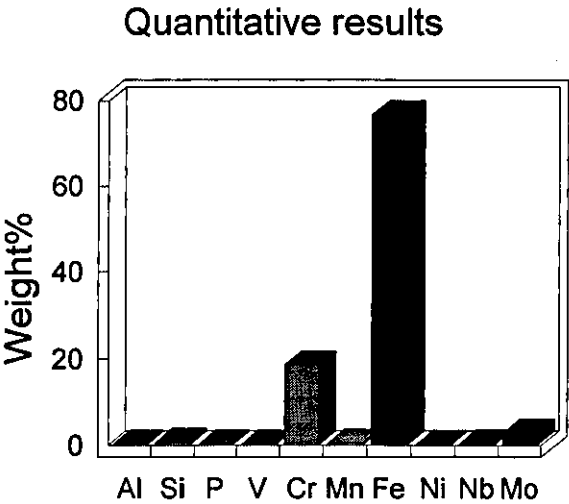## Quantitative results

XIV

Spectrum processing :
Peak possibly omitted : 8.900 keV

Quantitation method : Cliff Lorimer thin ratio section.
Processing option : All elements analysed (Normalised)

Number of iterations = 1

Standardless

Element	Peak Area	Area Sigma	k factor	Abs Corrn.	Weight %	Weight % Sigma	Atomic %
Al K	29	52	1.044	1.000	0.02	0.04	0.05
Si K	531	63	1.000	1.000	0.43	0.05	0.86
P K	21	85	0.992	1.000	0.02	0.07	0.03
V K	107	70	1.093	1.000	0.10	0.06	0.10
Cr K	9529	175	1.100	1.000	8.58	0.15	9.15
Mn K	537	109	1.153	1.000	0.51	0.10	0.51
Fe K	93301	501	1.170	1.000	89.37	0.32	88.71
Ni K	68	54	1.245	1.000	0.07	0.05	0.06
Nb L	214	153	1.687	1.000	0.30	0.21	0.18
Mo L	431	128	1.701	1.000	0.60	0.18	0.35
Totals					100.00		

Quantitative results


XV

Peak possibly omitted : 8.889 keV

Quantitation method : Cliff Lorimer thin ratio section.
Processing option : All elements analysed (Normalised)

Number of iterations = 1

Standardless

Element	Peak Area	Area Sigma	k factor	Abs Corrn.	Weight %	Weight % Sigma	Atomic %
Al K	-41	39	1.044	1.000	-0.07	0.07	-0.14
Si K	469	48	1.000	1.000	0.78	0.08	1.53
P K	35	57	0.992	1.000	0.06	0.09	0.10
V K	77	47	1.093	1.000	0.14	0.09	0.15
Cr K	4708	125	1.100	1.000	8.59	0.22	9.13
Mn K	207	75	1.153	1.000	0.40	0.14	0.40
Fe K	45895	351	1.170	1.000	89.06	0.46	88.17
Ni K	68	38	1.245	1.000	0.14	0.08	0.13
Nb L	29	104	1.687	1.000	0.08	0.29	0.05
Mo L	294	92	1.701	1.000	0.83	0.26	0.48
Totals					100.00		

Quantitative results

XVI

Spectrum processing :
Peaks possibly omitted : 8.895, 17.425 keV

Quantitation method : Cliff Lorimer thin ratio section.
Processing option : All elements analysed (Normalised)

Number of iterations = 1

Standardless

Element	Peak Area	Area Sigma	k factor	Abs Corrn.	Weight %	Weight % Sigma	Atomic %
Al K	79	47	1.044	1.000	0.10	0.06	0.20
Si K	497	57	1.000	1.000	0.59	0.07	1.16
P K	73	74	0.992	1.000	0.09	0.09	0.15
V K	91	61	1.093	1.000	0.12	0.08	0.13
Cr K	14265	202	1.100	1.000	8.62	0.25	9.84
Mn K	306	104	1.153	1.000	0.42	0.14	0.42
Fe K	55319	389	1.170	1.000	86.81	0.42	86.17
Ni K	92	46	1.245	1.000	0.14	0.07	0.13
Nb L	168	145	1.687	1.000	0.34	0.29	0.20
Mo L	1377	133	1.701	1.000	2.78	0.26	1.61
Totals					100.00		

Quantitative results

XVII

Spectrum processing :
Peak possibly omitted : 8.905 keV

Quantitation method : Cliff Lorimer thin ratio section.
Processing option : All elements analysed (Normalised)

Number of iterations = 1

Standardless

Element	Peak Area	Area Sigma	k factor	Abs Corm.	Weight %	Weight % Sigma	Atomic %
Al K	-6	58	1.044	1.000	0.00	0.04	-0.01
Si K	759	69	1.000	1.000	0.54	0.05	1.07
P K	34	92	0.992	1.000	0.02	0.06	0.04
V K	524	82	1.093	1.000	0.41	0.06	0.45
Cr K	10801	188	1.100	1.000	8.48	0.14	9.07
Mn K	471	114	1.153	1.000	0.39	0.09	0.39
Fe K	105849	532	1.170	1.000	88.42	0.32	87.98
Ni K	-25	56	1.245	1.000	-0.02	0.05	-0.02
Nb L	666	177	1.687	1.000	0.80	0.21	0.48
Mo L	790	152	1.701	1.000	0.96	0.18	0.56
Totals					100.00		

Quantitative results

XVIII
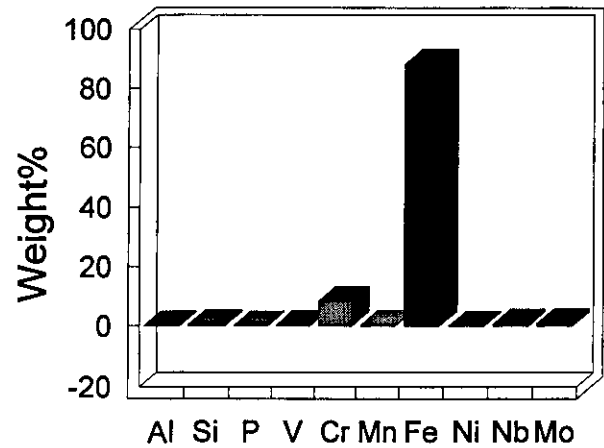
C:\MTHIN\USR\Sun Ben Shuang\A-1.spc

Acquisition Time:23:49:42   Date:13-Apr-2004

kV:200.00   Azimuth:45.00   Elevation:0.00   AmpT:12.8

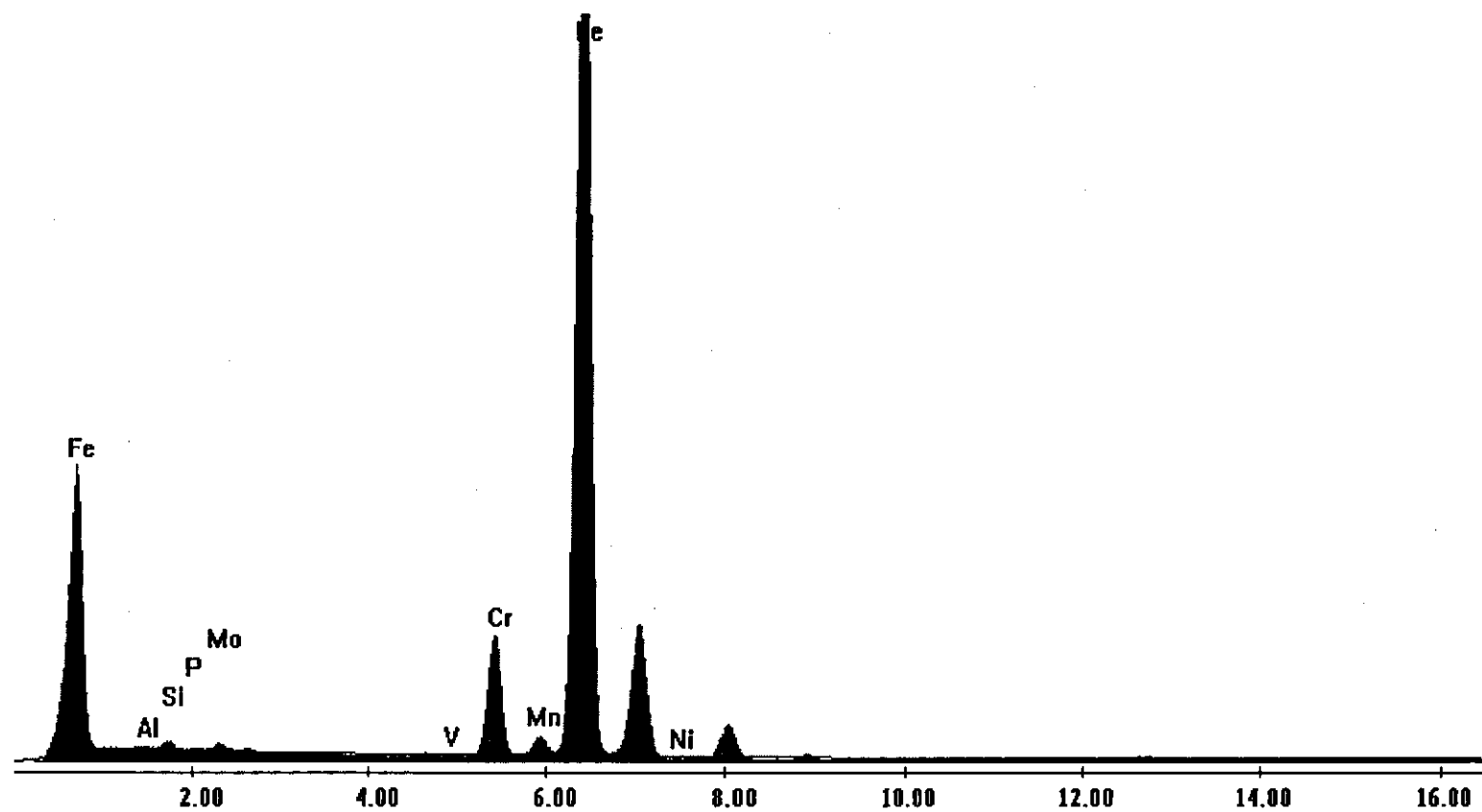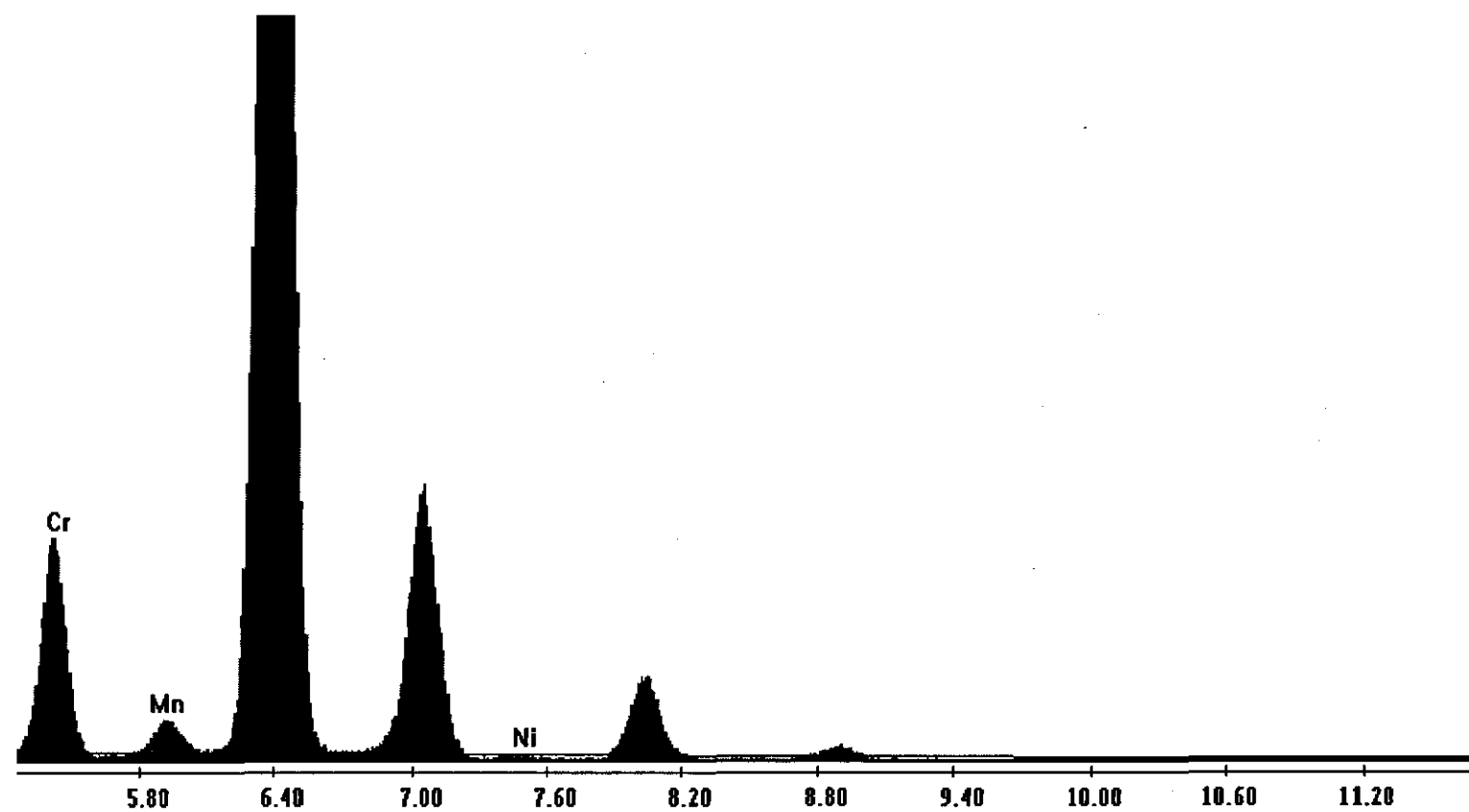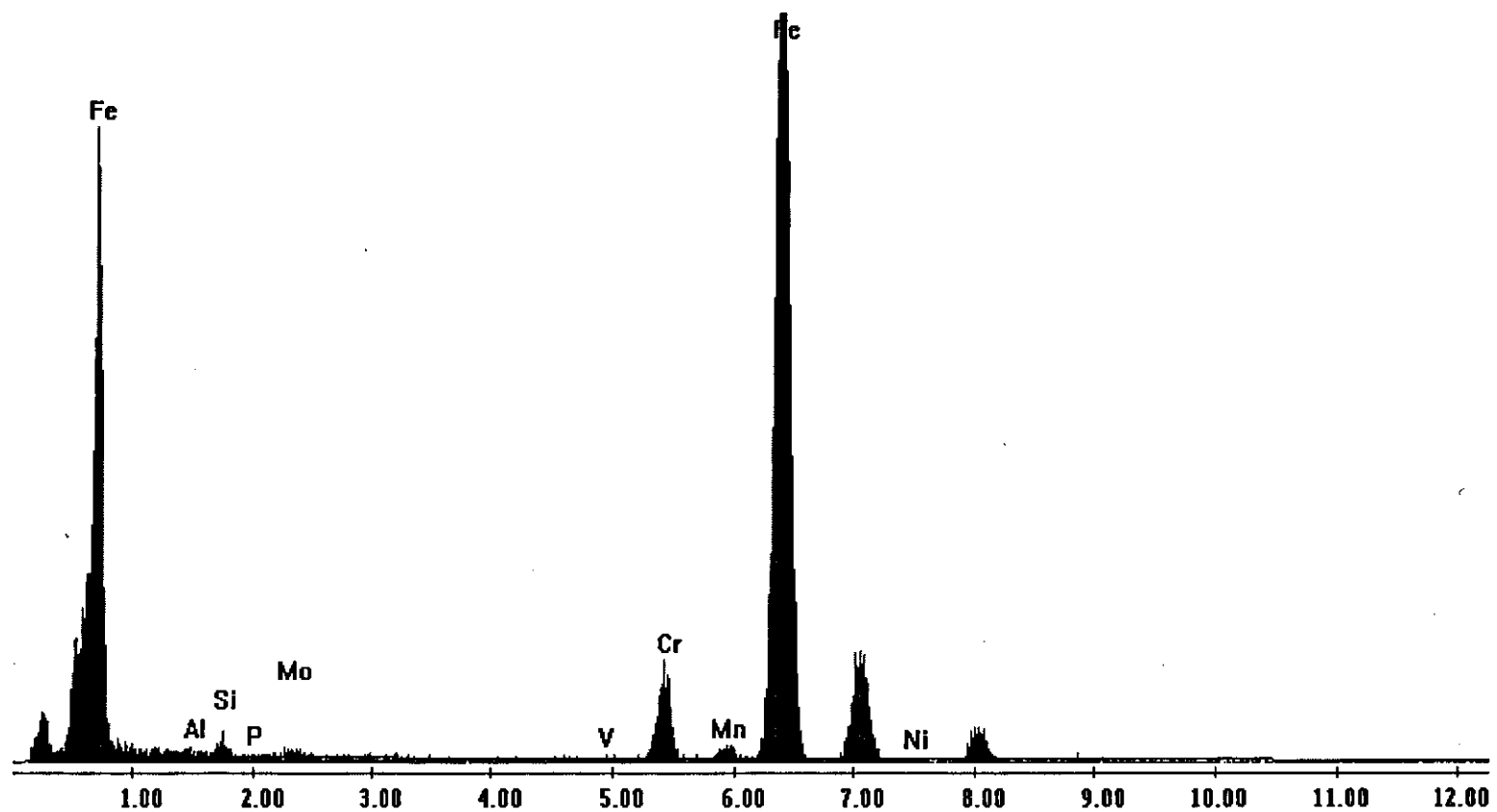Detector Type :SUTW-Sapphire   Resolution :151.61   Lsec :47

Thin Apx

KAB Set : User   Elements

Elem	Weight %	Atomic %
C K	0.8	3.5
NaK	2.4	5.5
MgK	0.8	1.8
SiK	0.5	1
P K	0	0.1
S K	0.9	1.4
LaL	0.7	0.3
V K	1.3	1.3
NdL	1.5	0.6
CrK	13.4	13.5
MnK	0.4	0.4
FeK	71.9	67.1
CuK	2.8	2.3
PbL	0	0
NbK	0.7	0.4
MoK	1.7	0.9
Total	100	100

Label A:
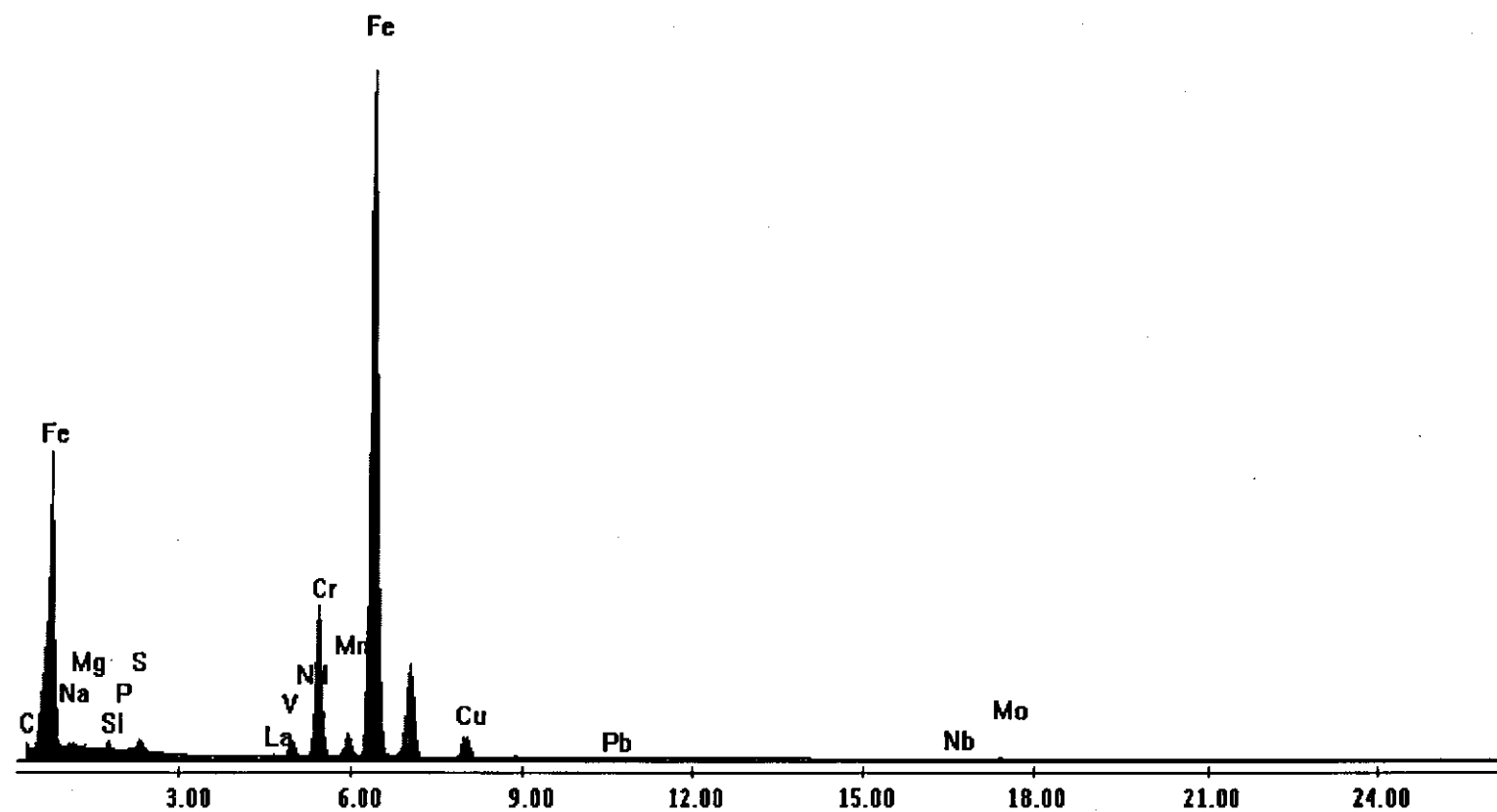
C:\MTHIN\USR\Sun Ben Shuang\A2.spc

Acquisition Time:01:45:05   Date:14-Apr-2004

kV:200.00   Azimuth:45.00   Elevation:0.00   AmpT:6.4
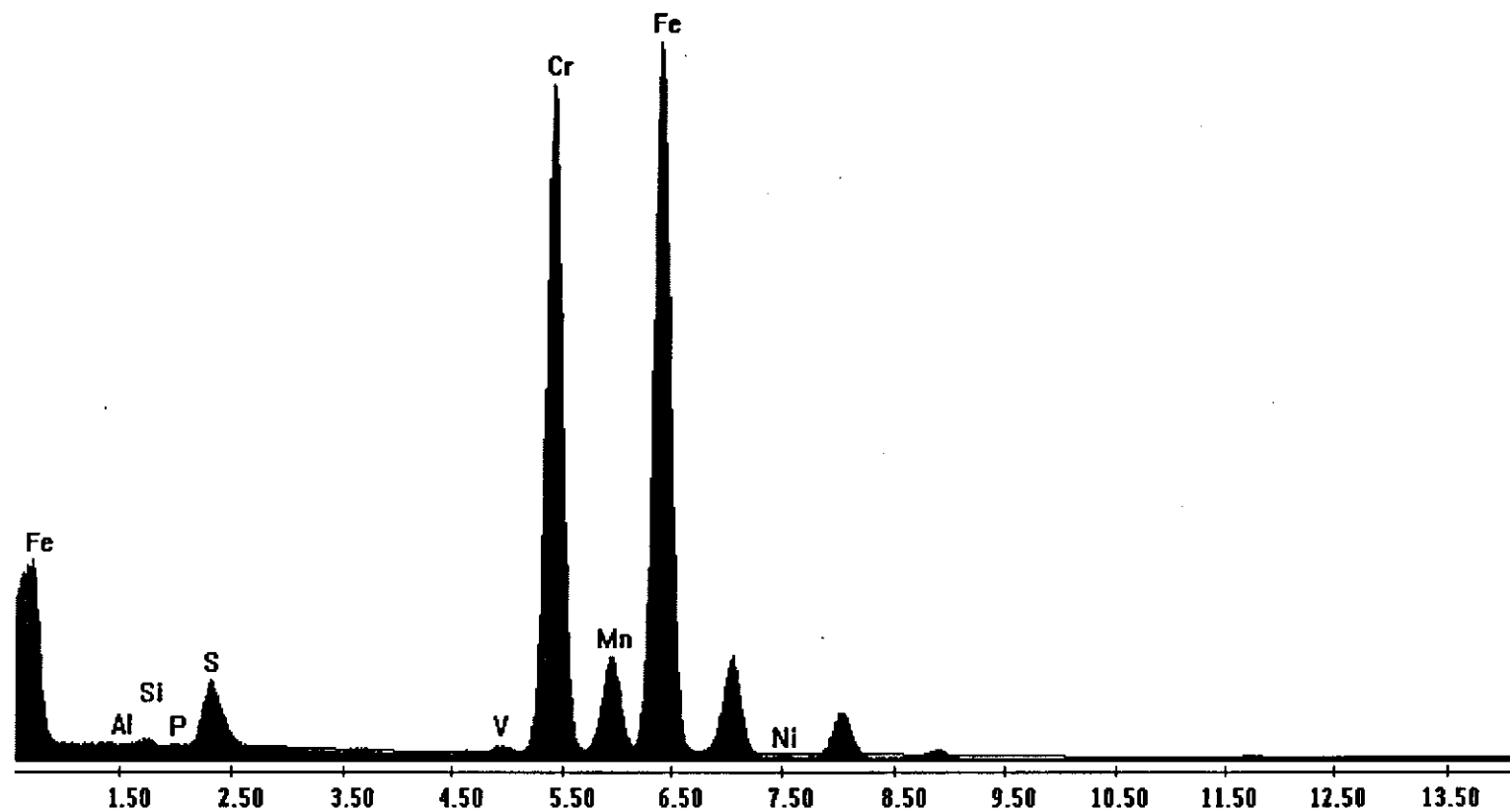Detector Type :SUTW-Sapphire   Resolution :176.58   Lsec :63

Thin Apx
KAB Set : User   Elements

Elem	Weight %	Atomic %
AlK	0.7	1.4
SiK	0.6	1.2
P K	0.1	0.2
V K	0.1	0.1
CrK	9.7	10.2
MnK	0.4	0.4
FeK	87.3	85.8
NiK	0	0
NbK	0.1	0
MoK	1	0.6
Total	100	100

Label A:

C:\MTHIN\USR\Sun Ben Shuang\C1.spc

Acquisition Time:04:42:32   Date:14-Apr-2004

kV:200.00   Azimuth:45.00   Elevation:0.00   AmpT:51.2
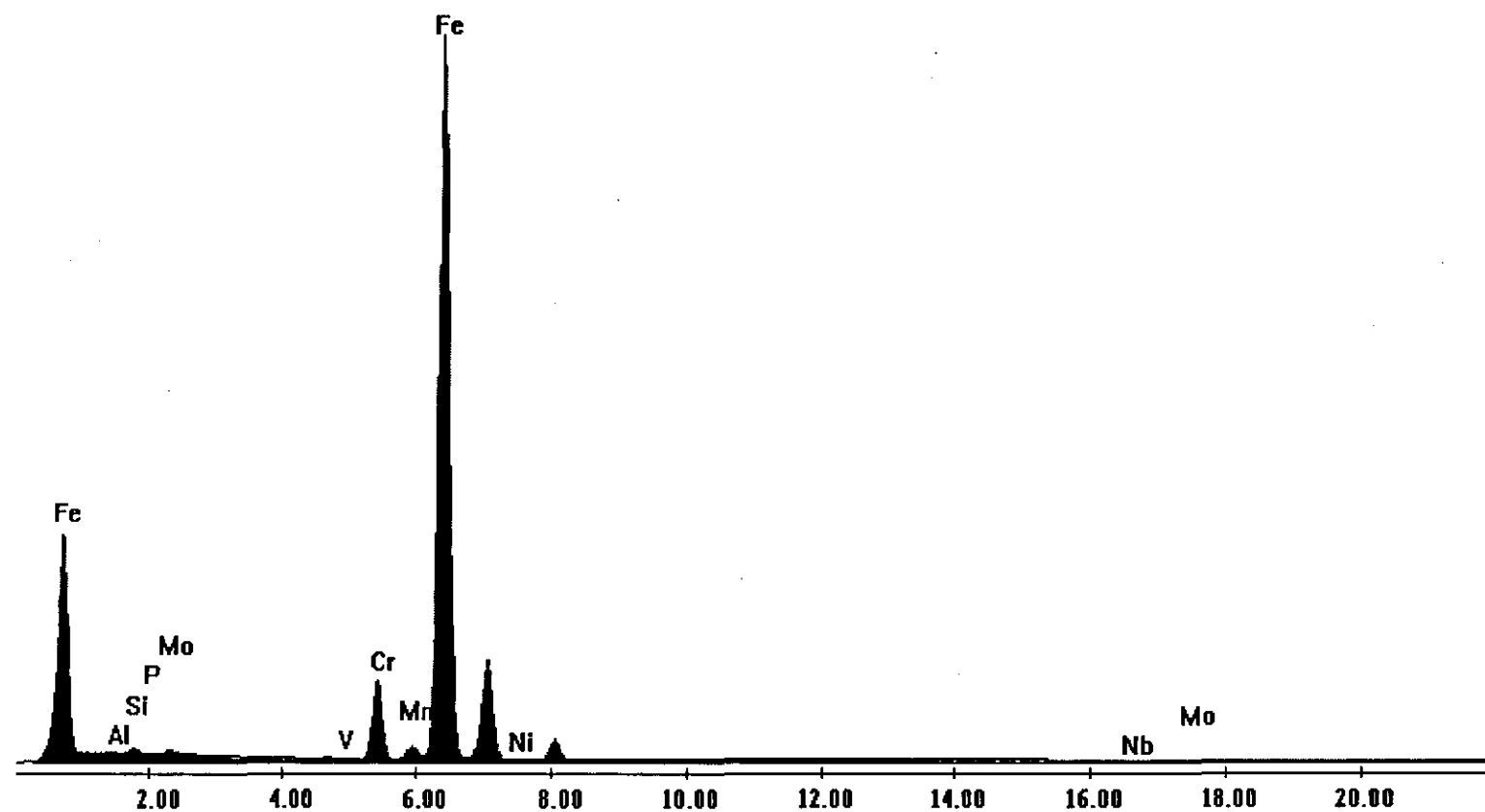Detector Type :SUTW-Sapphire   Resolution :134.75   Lsec :177

Thin Apx
KAB Set : User   Elements

Elem	Weight %	Atomic %
AlK	0.6	1.3
SiK	0.8	1.6
P K	0	0.1
V K	0.1	0.1
CrK	8.2	8.7
MnK	0.4	0.4
FeK	89	87.4
NiK	0	0
MoK	0.8	0.5
Total	100	100

C:\MTHIN\USR\Sun Ben Shuang\C1.spc

Label A:

XXIV

C:\MTHIN\USR\Sun Ben Shuang\C2.spc

Acquisition Time:04:52:56   Date:14-Apr-2004

kV:200.00   Azimuth:45.00   Elevation:0.00   AmpT:51.2
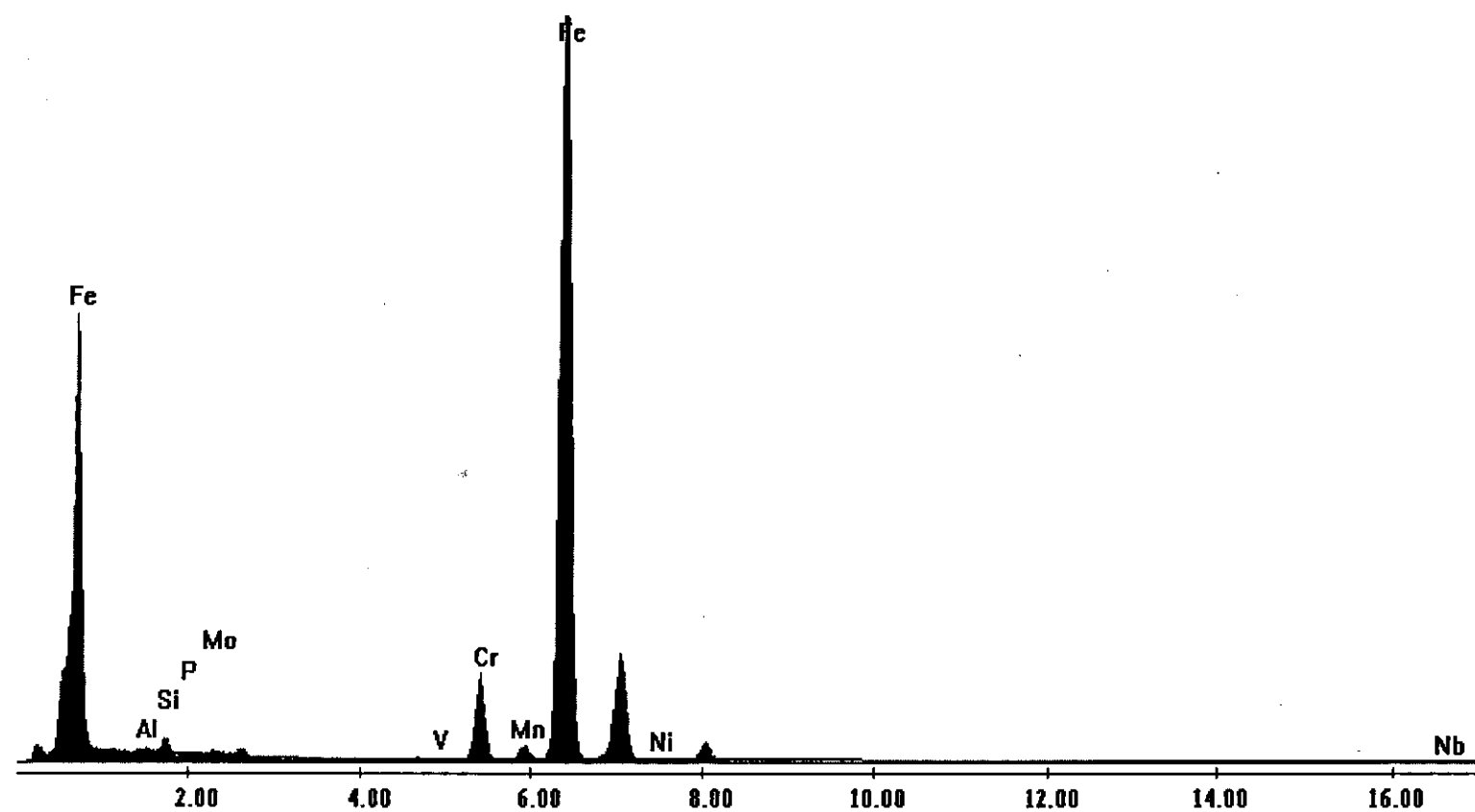Detector Type :SUTW-Sapphire   Resolution :134.75   Lsec :37

Thin Apx
KAB Set : User   Elements

Elem	Weight %	Atomic %
AlK	0.6	1.2
SiK	0.8	1.6
P K	0.1	0.2
V K	0.2	0.2
CrK	7.7	8.2
MnK	0.5	0.5
FeK	89	87.6
NiK	0.1	0
NbK	0.2	0.1
MoK	0.9	0.5
Total	100	100

C:\MTHIN\USR\Sun Ben Shuang\C2.spc

Label A:

C:\MTHIN\USR\Sun Ben Shuang\Cr1.spc

Acquisition Time:01:36:15   Date:14-Apr-2004

kV:200.00   Azimuth:45.00   Elevation:0.00   AmpT:6.4
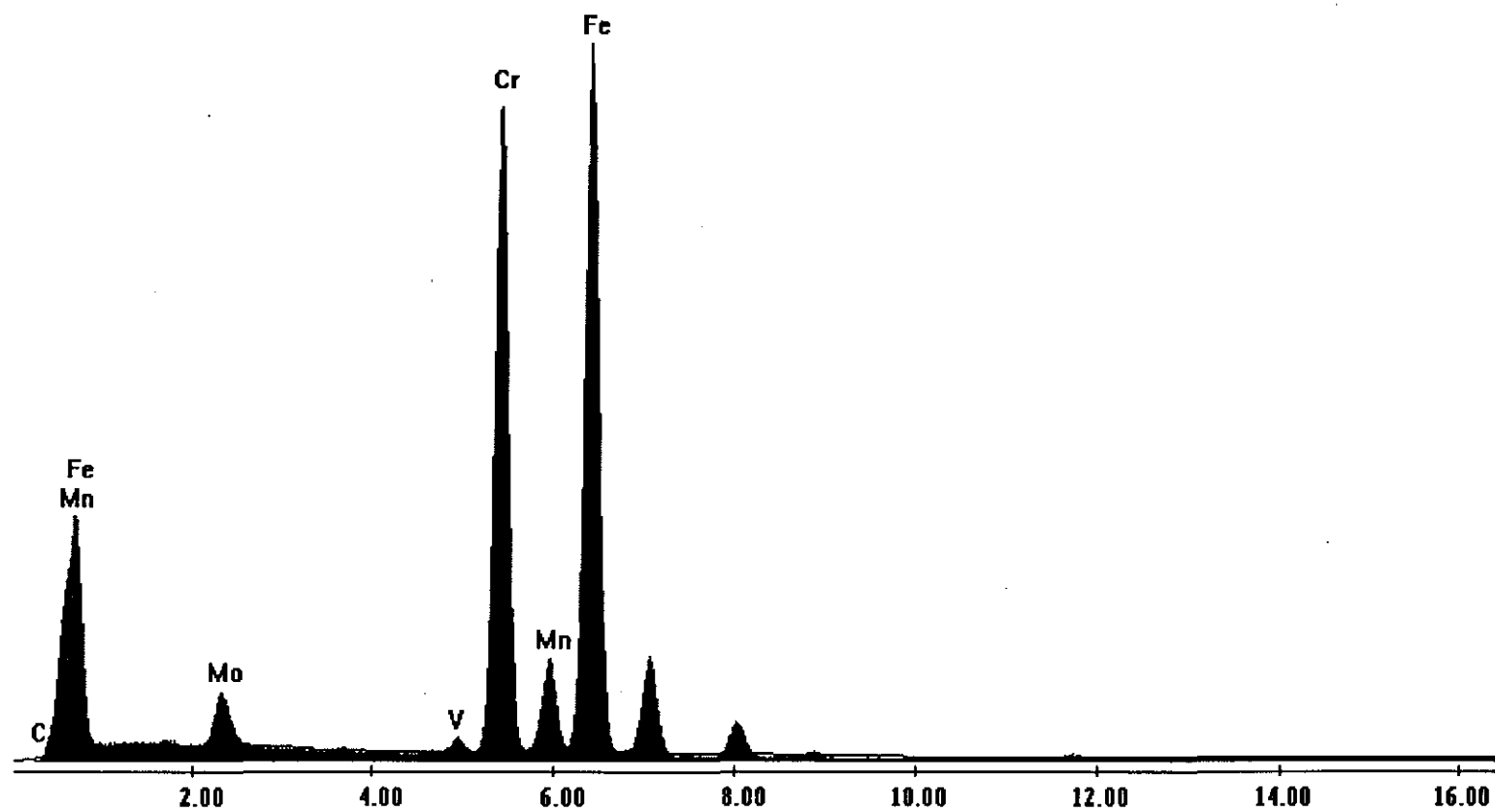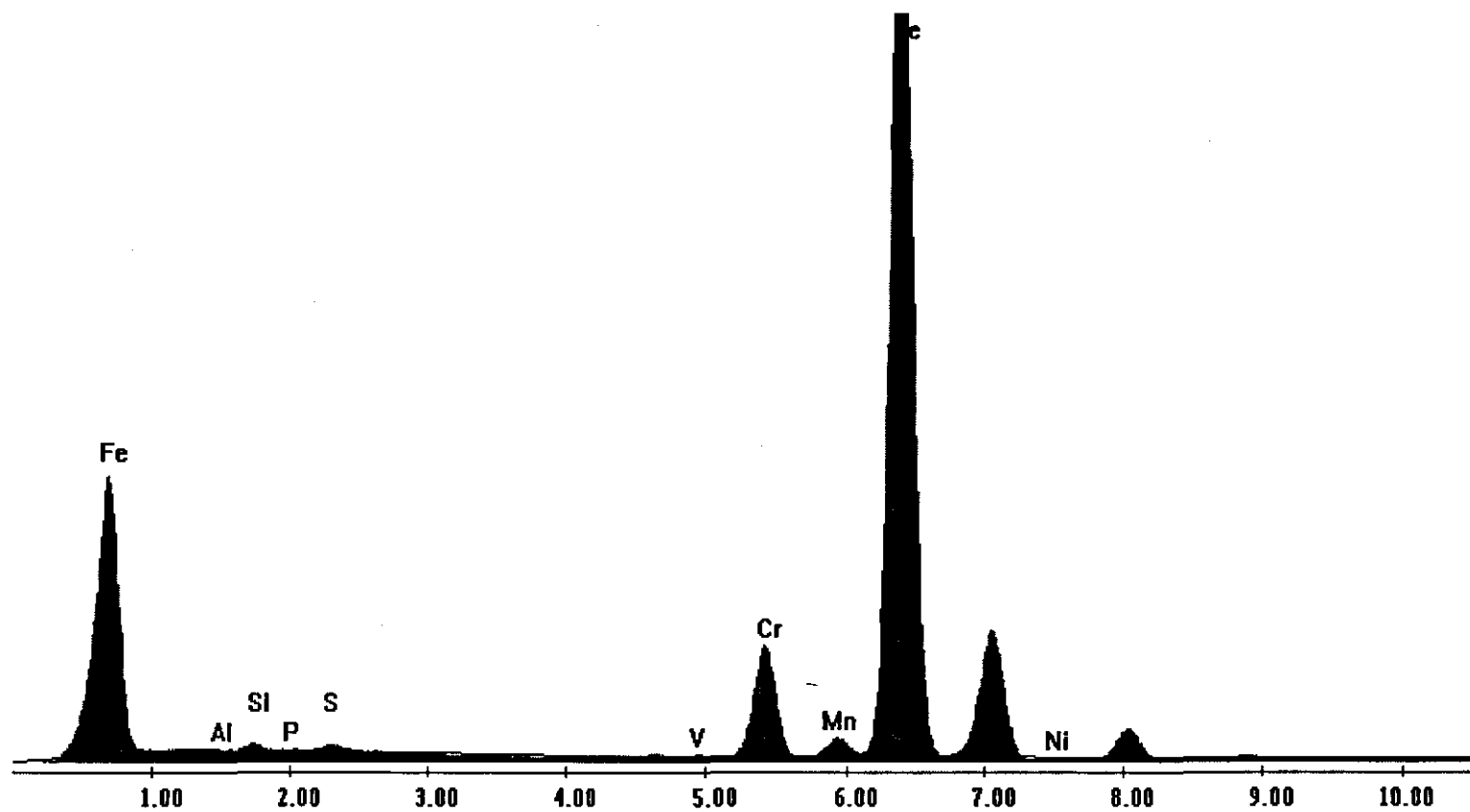Detector Type :SUTW-Sapphire   Resolution :176.58   Lsec :68

Thin Apx
KAB Set : User   Elements

Elem	Weight %	Atomic %
AlK	0.4	0.9
SiK	0.4	0.7
P K	0	0
V K	0.5	0.5
CrK	42	44.4
MnK	1	1
FeK	49.9	49.1
NiK	0	0
MoK	5.8	3.3
Total	100	100

C:\MTHIN\USR\Sun Ben Shuang\Cr1.spc

Label A:

XXVIII

C:\MTHIN\USR\Sun Ben Shuang\D2.spc

Acquisition Time:21:49:30   Date:14-Apr-2004

kV:200.00   Azimuth:45.00   Elevation:0.00   AmpT:6.4
Detector Type :SUTW-Sapphire   Resolution :176.58   Lsec :134

Thin Apx
KAB Set : User   Elements

Elem	Weight %	Atomic %
AlK	0.5	1
SiK	0.6	1.2
P K	0.1	0.2
V K	0.1	0.1
CrK	8.6	9.1
MnK	0.5	0.5
FeK	88.8	87.5
NiK	0	0
NbK	0	0
MoK	0.8	0.5
Total	100	100

Label A:

XXX

C:\MTHIN\USR\Sun Ben Shuang\D3.spc

Acquisition Time:23:13:23   Date:14-Apr-2004

kV:200.00   Azimuth:45.00   Elevation:0.00   AmpT:25.6
Detector Type :SUTW-Sapphire   Resolution :138.88   Lsec :70

Thin Apx
KAB Set : User   Elements

Elem	Weight %	Atomic %		
AlK	0.7	1.5		
SiK	1.2	2.3		
P K	0.1	0.1		
V K	0	0		
CrK	8.2	8.6		
MnK	0.4	0.4		
FeK	88.7	86.6		
NiK	0	0		
NbK	0	0		
MoK	0.7	0.4		
Total	100	100		
MoK	5.83	5.25	8.27	1.11

C:\MTHIN\USR\Sun Ben Shuang\D3.spc

Label A:

XXXII

C:\MTHIN\USR\Sun Ben Shuang\D-Cr.spc

Acquisition Time:21:35:16   Date:14-Apr-2004

kV:200.00   Azimuth:45.00   Elevation:0.00   AmpT:6.4
Detector Type :SUTW-Sapphire   Resolution :176.58   Lsec :47

Thin Apx
KAB Set : User   Elements

Elem	Weight %	Atomic %
C K	0	0.1
V K	0.8	0.9
CrK	41.9	44.5
MnK	0.9	1
FeK	51.1	50.6
MoK	5.3	3
Total	100	100

Label A:

C:\MTHIN\USR\Sun Ben Shuang\substrate

Acquisition Time:01:06:45   Date:14-Apr-2004

kV:200.00   Azimuth:45.00   Elevation:0.00   AmpT:6.4
Detector Type :SUTW-Sapphire Resolution :176.58   Lsec :118

Thin Apx
KAB Set : User   Elements

Elem	Weight %	Atomic %
AlK	0.4	0.8
SiK	0.6	1.1
P K	0.1	0.2
S K	0.5	0.9
V K	0.2	0.2
CrK	9.4	9.9
MnK	0.4	0.4
FeK	87.5	86
NiK	0	0
MoK	0.9	0.5
Total	100	100

Label A:

APPENDIX C: Reports on the Type IV Crack Failure Examination
(Part of the results)

FOURCRACK creep specimen failure examination (KA1392/1)

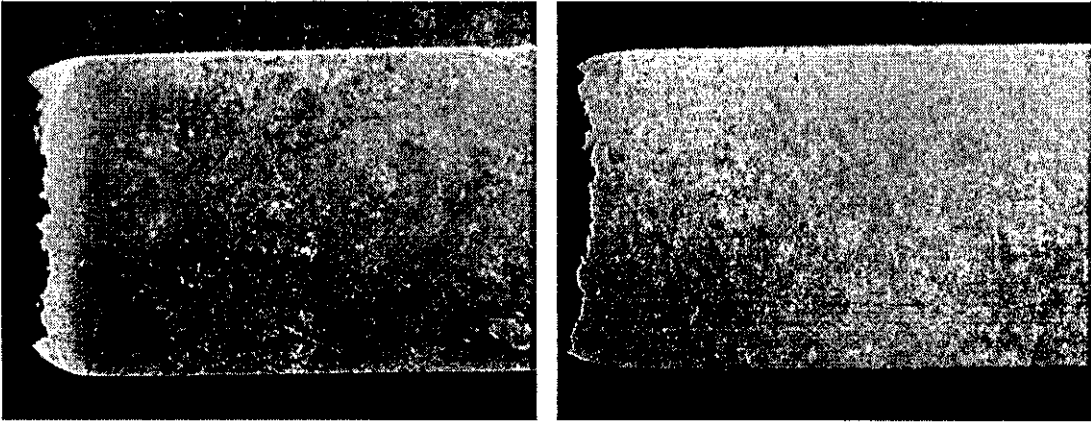| Micro Number	PTC Ref.	Test Ref.	Temp. °C	Stress MPa	Est. Dur.	Final Dur.	Elong. %	R. of A. %	Failure
03/110 03/111	KA1392/1 (1#,2#)	02/013	625	105.0	3000	5069	2.62	15.51	Type IV

HCM 12A (P122) TWI Weld Plate W16

Macroexamination

Length of specimen halves (longer half + shorter half)(mm): 55 + 50
Distance from the fracture to other surface defect/s (mm):   none

Low mag. photograph (optical stereomicrograph) of the two specimen halves and the
fracture surface/s, alongside a ruler.
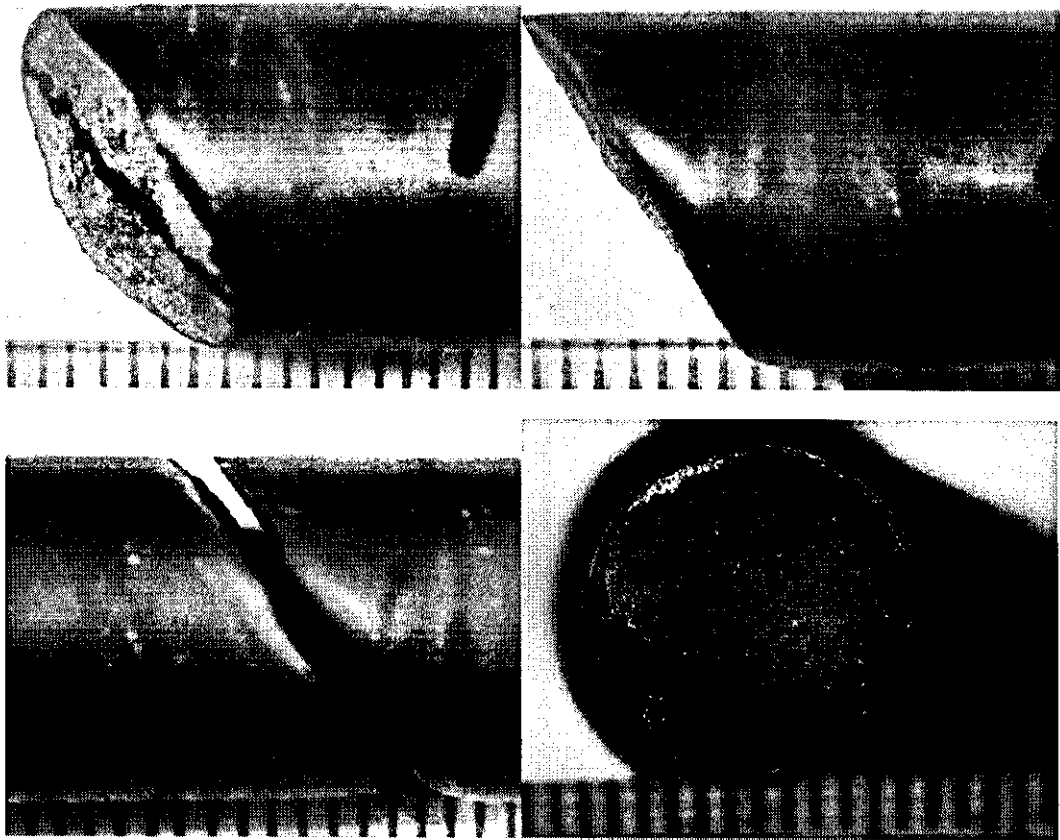
Comments: 45 deg failure at end of gauge length and just beyond.

Sectioning and Microexamination
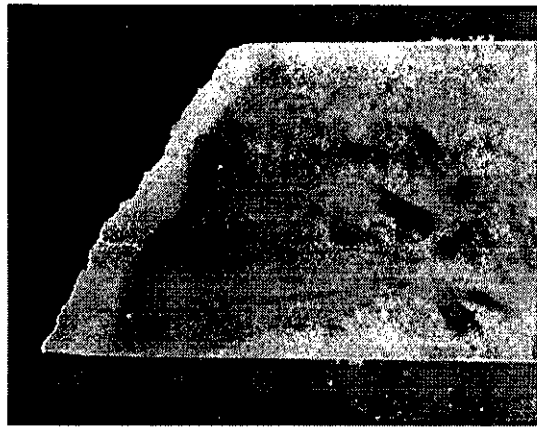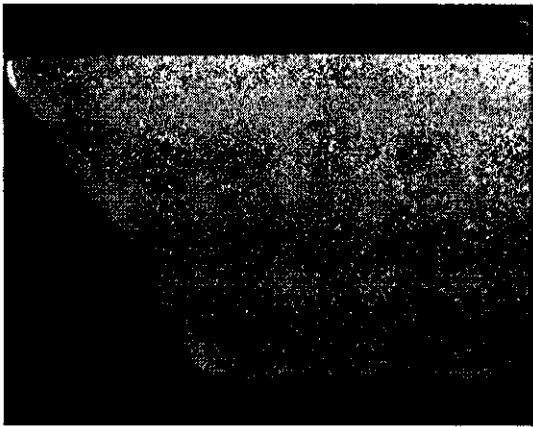
(Creep specimen width in this view = 10.9mm)

Comments: Failure in HAZ. No obvious creep damage in HAZ.

Conclusions

Type IV failure

Drafted by: Ben Sun

Verified by: D. Allen

FOURCRACK creep specimen failure examination (KA1392/2)

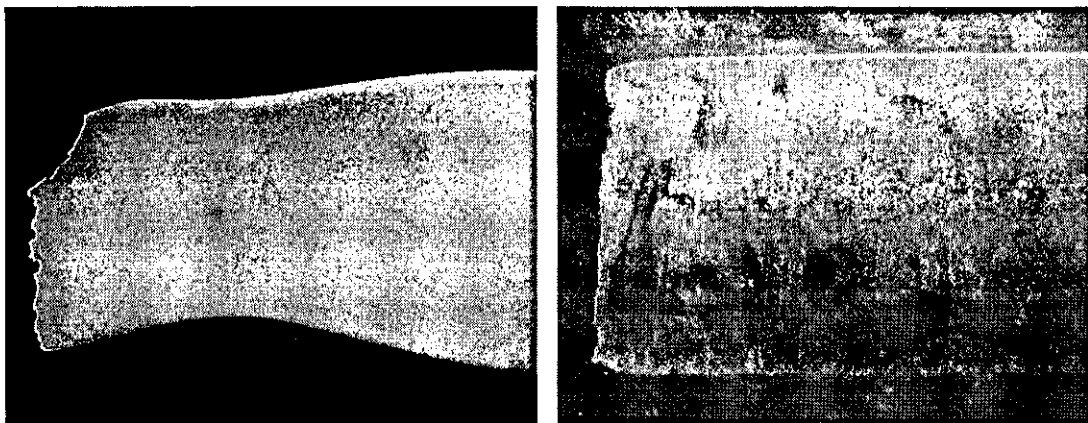| Micro Number	PTC Ref.	Test Ref.	Temp. °C	Stress MPa	Est. Dur.	Final Dur.	Elong. %	R. of A. %	Failure
03/112 03/113	KA1392/2 (1#,2#)	02/014	650	75.0	2500	4421	1.11	0.89	Type IV

P92 (NF616) TWI Weld Plate W12

Macroexamination

Length of specimen halves (longer half + shorter half)(mm): 55 + 50
Distance from the fracture to other surface defect/s (mm):   none

Low mag. photograph (optical stereomicrograph) of the two specimen halves and the fracture surface/s, alongside a ruler.
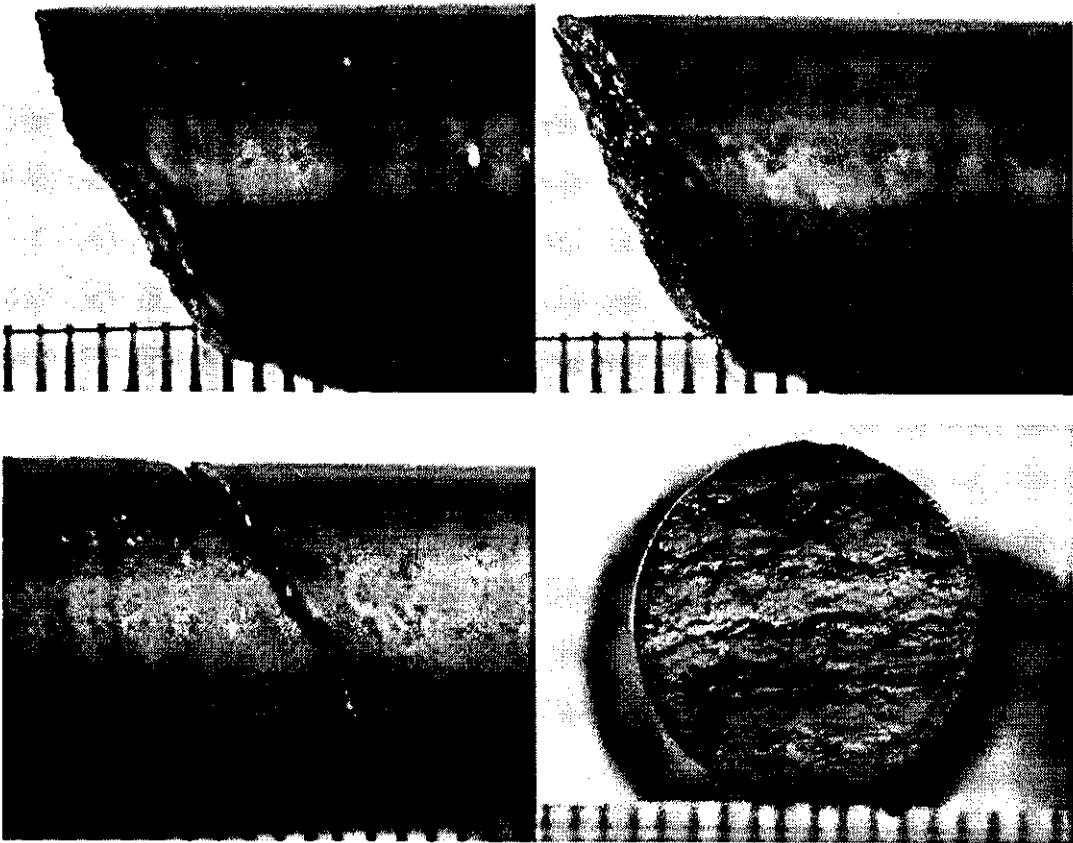

Comments: 45 deg failure in centre of gauge length.

Sectioning and Microexamination
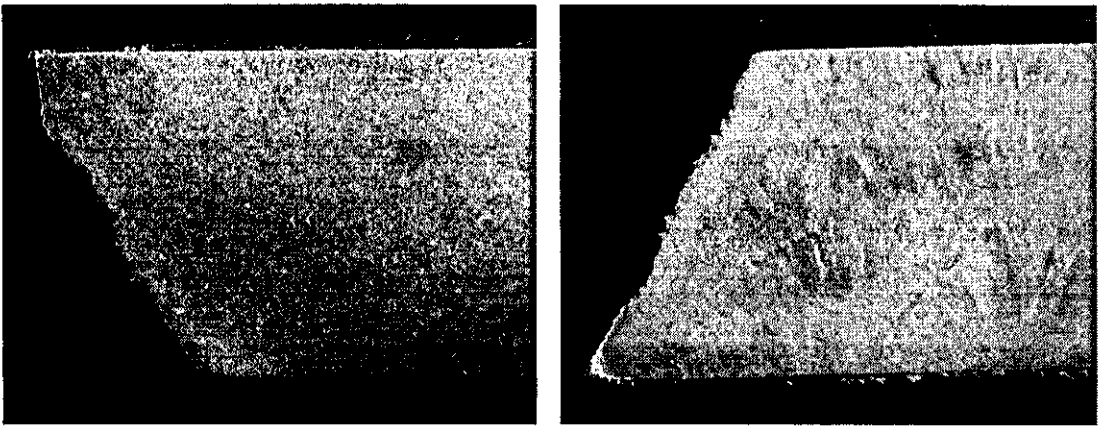
(Creep specimen width in this view = 10.9mm)

Comments: Failure in HAZ. Significant creep damages in HAZ.

× 200

Conclusions

Type IV failure

d

FOURCRACK creep specimen failure examination (KA1392/3)

Micro Number	PTC Ref.	Test Ref.	Temp. °C	Stress MPa	Est. Dur.	Final Dur.	Elong. %	R. of A. %	Failure
03/114 03/115	KA1392/3 (1#,2#)	02/067	650	75.0	400	519	3.05	13.68	Type IV

P91 As-Rec'd. MR02/027A Welded with Metrode
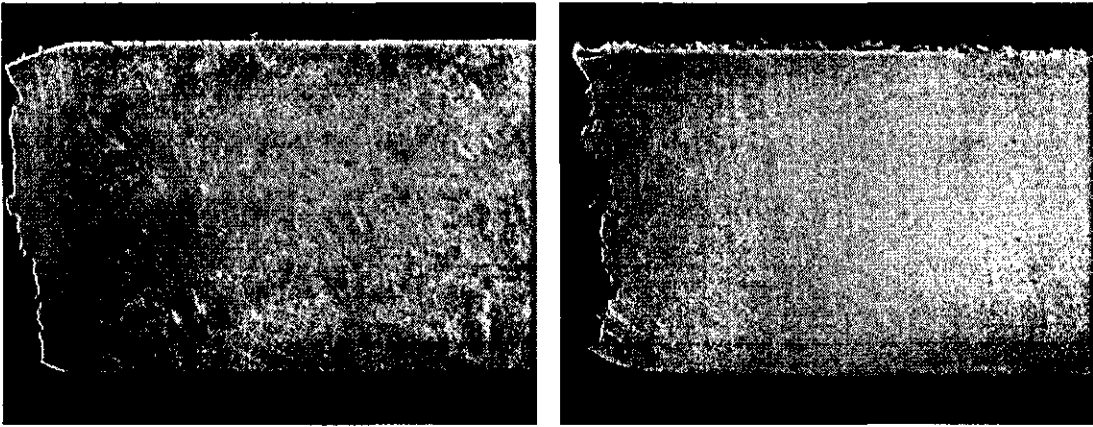
Macroexamination

Length of specimen halves (longer half + shorter half)(mm): 53 + 52
Distance from the fracture to other surface defect/s (mm):   none

Low mag. photograph (optical stereomicrograph) of the two specimen halves and the fracture surface/s, alongside a ruler.
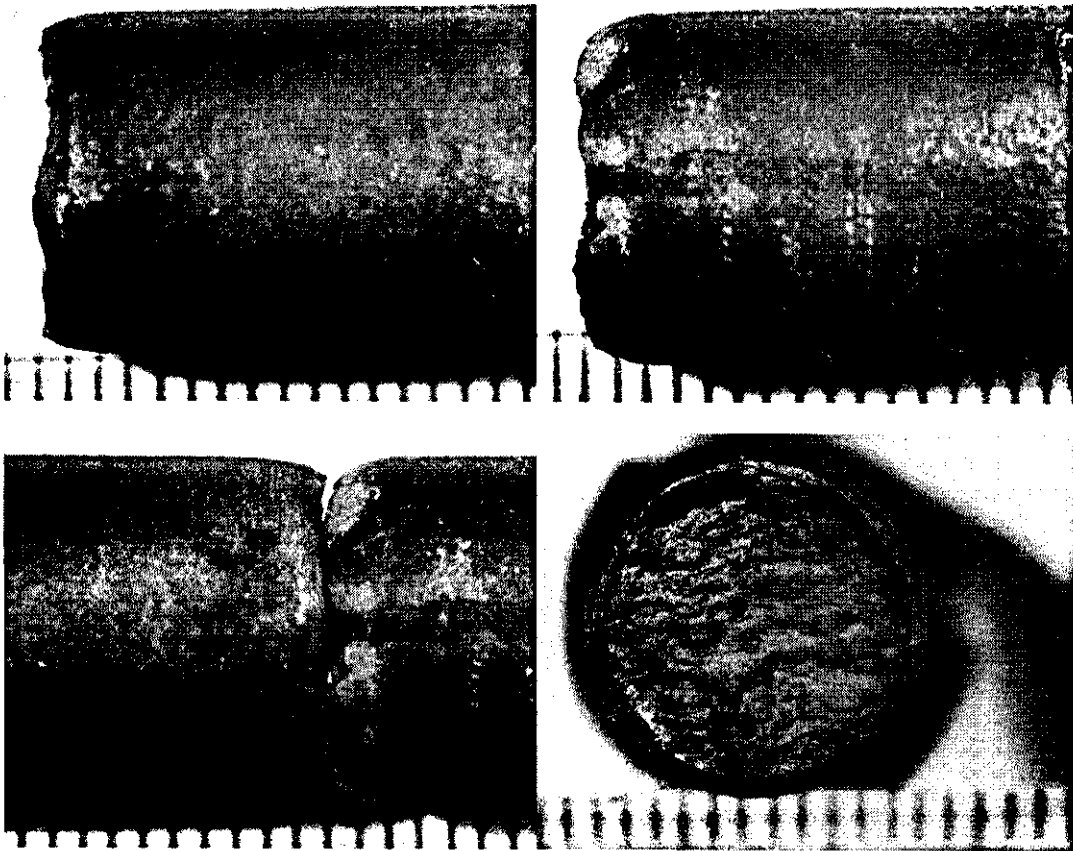
Comments: 90 deg failure in centre of gauge length.

Sectioning and Microexamination

(Creep specimen width in this view = 10.9mm)

Comments: Failure in HAZ . Some creep damages in HAZ.

Conclusions

Type IV failure

FOURCRACK creep specimen failure examination (KA1392/4)

Micro Number	PTC Ref.	Test Ref.	Temp. °C	Stress MPa	Est. Dur.	Final Dur.	Elong. %	R. of A. %	Failure
03/116 03/117	KA1392/4 (1#,2#)	02/0696	600	155	100	215	18.34	55.32	Type IV

P91 N & Temper, . MR02/027B Welded with Metrode

Macroexamination

Length of specimen halves (longer half + shorter half)(mm): 60 + 55
Distance from the fracture to other surface defect/s (mm):   neck 7mm

Low mag. photograph (optical stereomicrograph) of the two specimen halves and the fracture surface/s, alongside a ruler.

Comments: near fusion line with necking in parent metal.

Sectioning and Microexamination

(Creep specimen width in this view = 10.9mm)

Comments: Failure in HAZ. No obvious creep damage in HAZ. Some creep damages in the neck region.
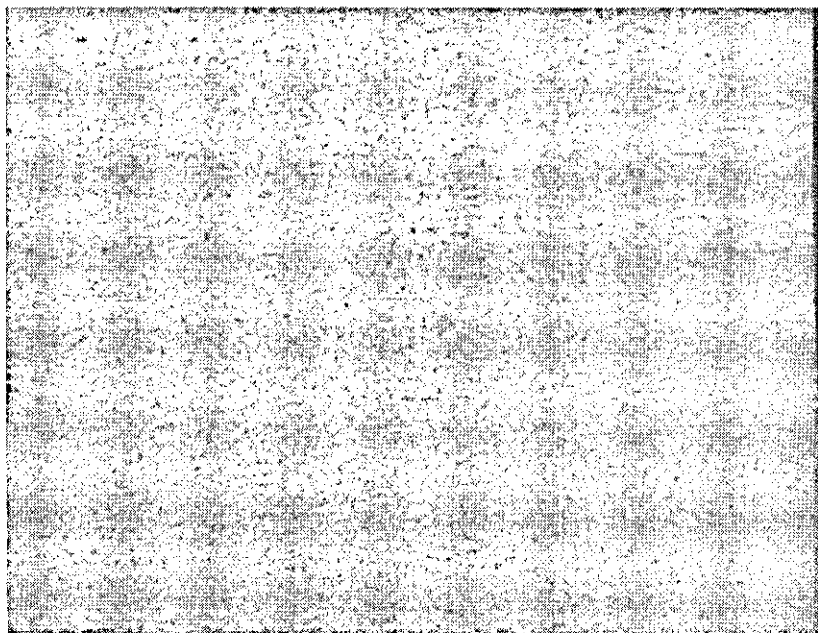
×200

creep damage in the neck region

Conclusions

Type IV failure

h

FOURCRACK creep specimen failure examination (KA1392/5)

Micro Number	PTC Ref.	Test Ref.	Temp. °C	Stress MPa	Est. Dur.	Final Dur.	Elong. %	R. of A. %	Failure
03/118 03/119	KA1392/5 (1#,2#)	02/068	650	75	400	359	2.31	18.07	Type IV

P91 N & Temper, . MR02/027B Welded with Metrode
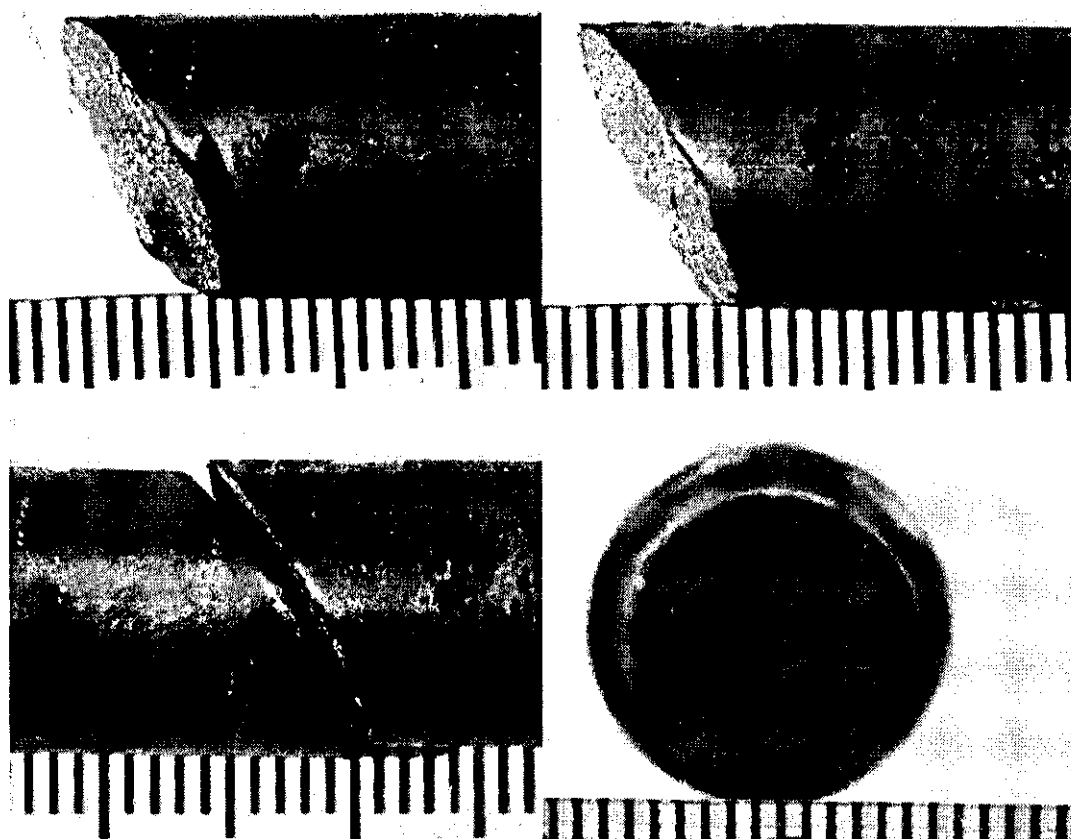
Macroexamination

Length of specimen halves (longer half + shorter half)(mm): 58 + 52
Distance from the fracture to other surface defect/s (mm):   none

Low mag. photograph (optical stereomicrograph) of the two specimen halves and the fracture surface/s, alongside a ruler.

Comments: 90 deg failure in centre of gauge length.

i
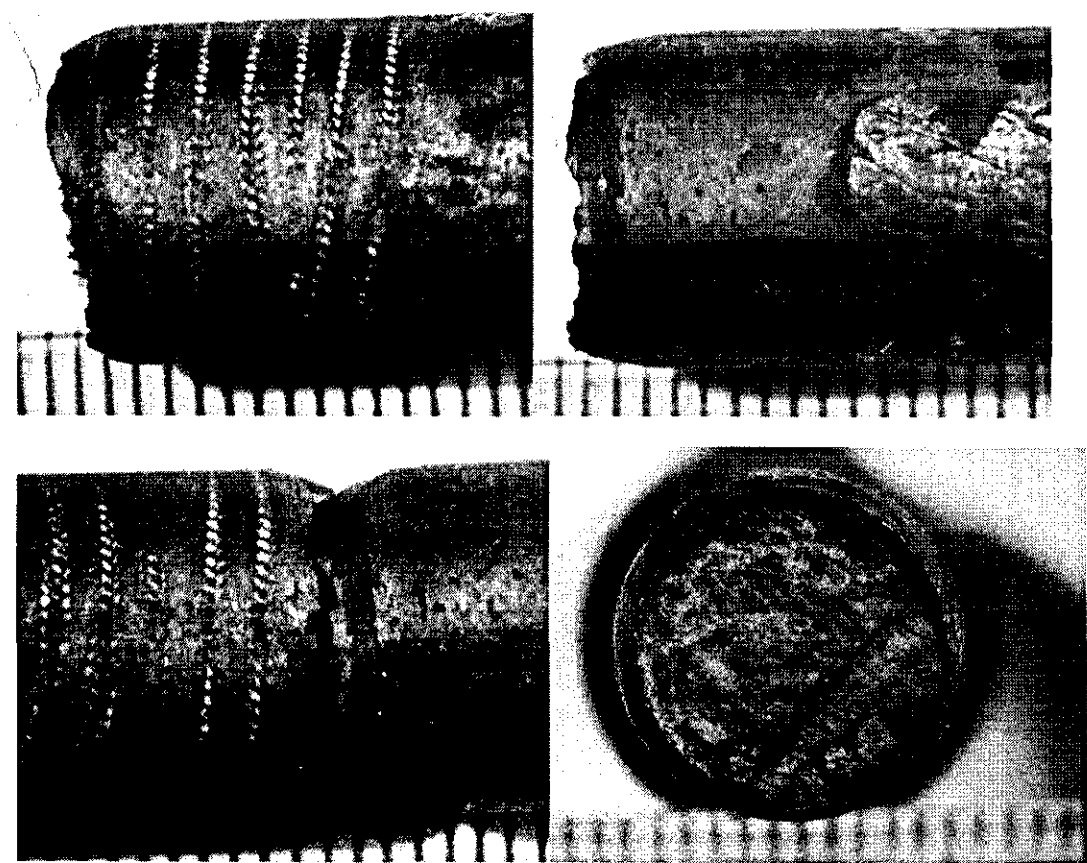
Sectioning and Microexamination

(Creep specimen width in this view = 10.9mm)

Comments: Failure in HAZ . Some creep damages in HAZ.

Conclusions

Type IV failure

FOURCRACK creep specimen failure examination (KA1395/1)

Micro Number	PTC Ref.	Test Ref.	Temp. °C	Stress MPa	Est. Dur.	Final Dur.	Elong. %	R. of A. %	Failure
03/124	KA1395/1	02/016	650	75.0	2500	7050	3.77	11.85	WM

P122 (HCM12A) Forging/Weld
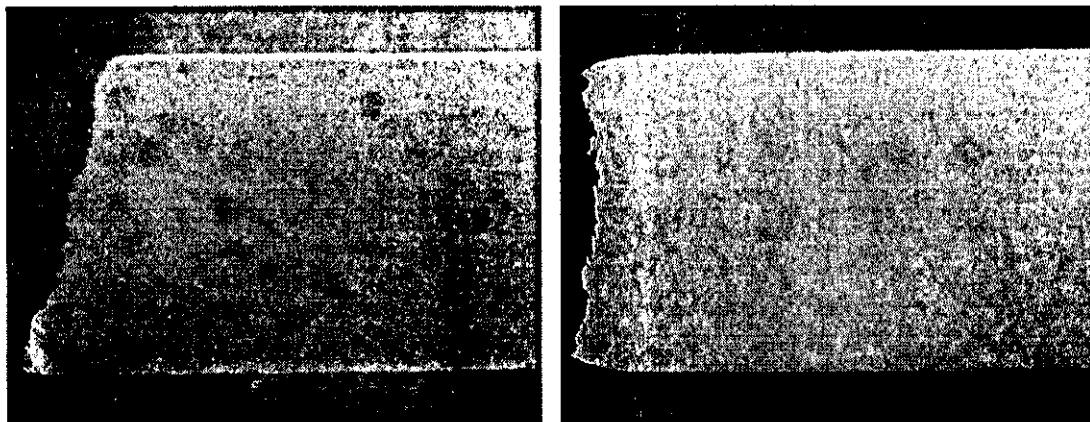
Macroexamination

Length of specimen halves (longer half + shorter half)(mm): 80 + 25
Distance from the fracture to other surface defect/s (mm):   none

Low mag. photograph (optical stereomicrograph) of the two specimen halves and the fracture surface/s, alongside a ruler.

Comments: 45 jagged failure, ¼ gauge length in weld metal.

Sectioning and Microexamination

(Creep specimen width in this view = 10.9mm)

Comments: Failure in weld metal.

Conclusions

Failure in WM

FOURCRACK creep specimen failure examination (1395/2)

Micro Number	PTC Ref.	Test Ref.	Temp. °C	Stress MPa	Est. Dur.	Final Dur.	Elong. %	R. of A. %	Failure
03/125 03/126	KA1395/2 (1#,2#)	02/012	625	105.0	3000	6129	1.49	3.16	Type IV

P92 (NF616) TWI Weld Test Plate W12

Macroexamination

Length of specimen halves (longer half + shorter half)(mm): 53+ 52
Distance from the fracture to other surface defect/s (mm):   none

Low mag. photograph (optical stereomicrograph) of the two specimen halves and the fracture surface/s, alongside a ruler.

Comments: 45 deg failure in centre of gauge length.

Sectioning and Microexamination
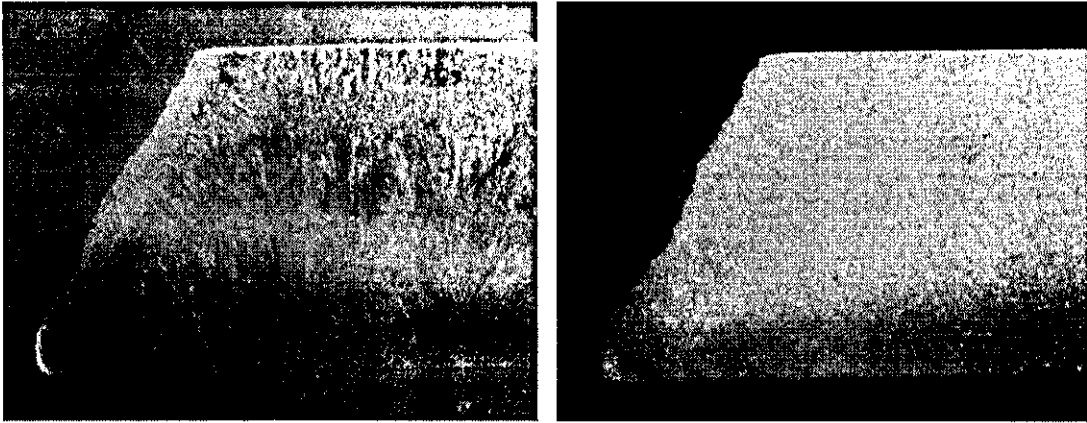
(Creep specimen width in this view = 10.9mm)

Comments: Failure in HAZ . No obvious creep damage in HAZ.

Conclusions

Type IV failure

FOURCRACK creep specimen failure examination (KA1395/3)

Micro Number	PTC Ref.	Test Ref.	Temp. °C	Stress MPa	Est. Dur.	Final Dur.	Elong. %	R. of A. %	Failure
03/127 03/128	KA1395/3 (1#,2#)	02/039	650	75.0	2500	5410	2.17	11.55	Type IV

P92 (NF616) Nippon Pipe M2W Electrodes
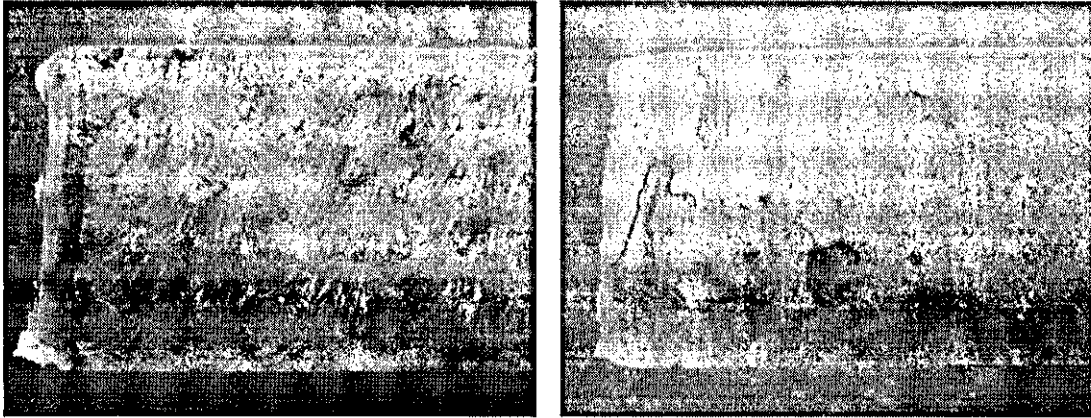
Macroexamination

Length of specimen halves (longer half + shorter half)(mm): 55+ 50
Distance from the fracture to other surface defect/s (mm):   none

Low mag. photograph (optical stereomicrograph) of the two specimen halves and the fracture surface/s, alongside a ruler.
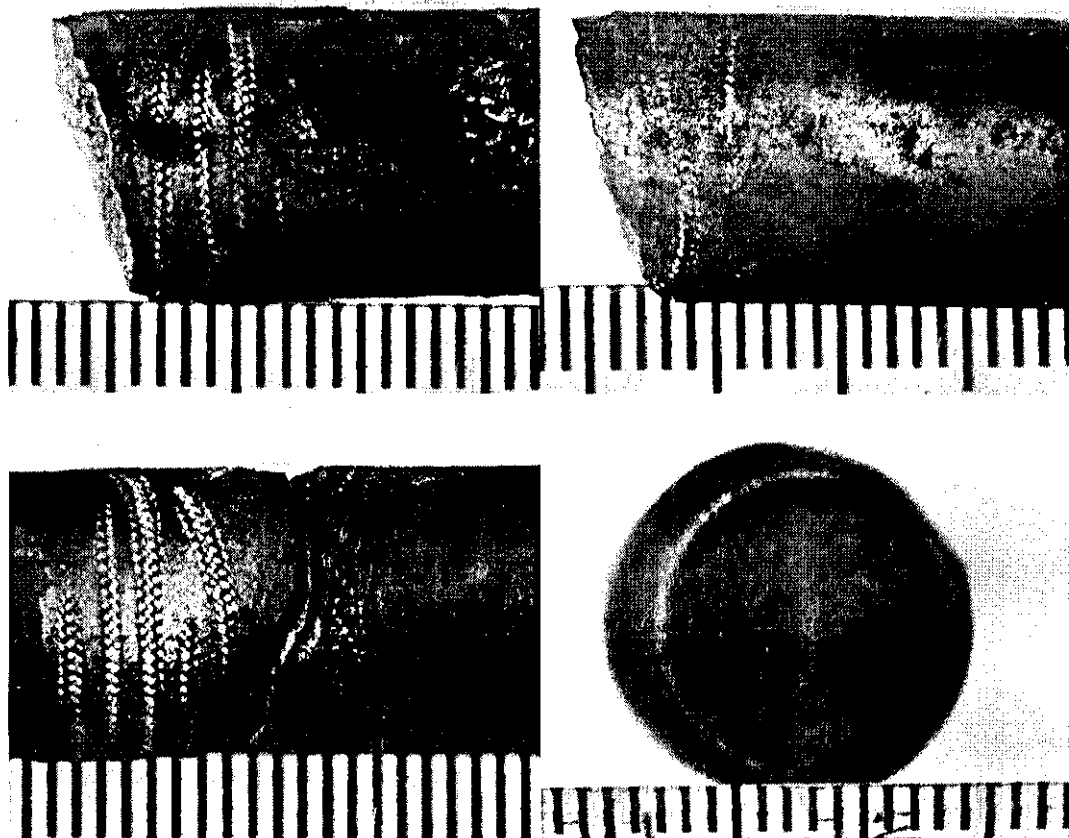
Comments: 45 deg failure in centre of gauge length.

Sectioning and Microexamination

(Creep specimen width in this view = 10.9mm)

Comments: Failure in HAZ . No obvious creep damage in HAZ.

Conclusions

Type IV failure

FOURCRACK creep specimen failure examination (KA1395/4)

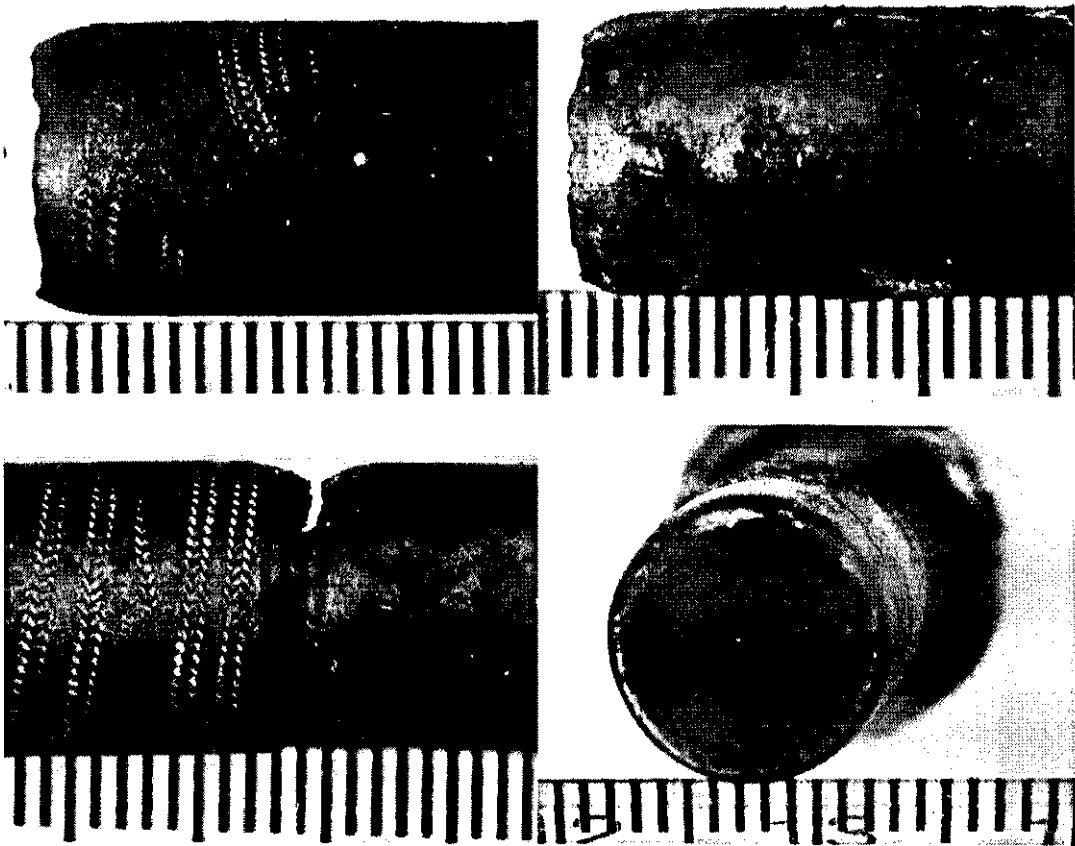| Micro Number	PTC Ref.	Test Ref.	Temp. °C	Stress MPa	Est. Dur.	Final Dur.	Elong. %	R. of A. %	Failure
03/129 03/130	**KA1395/4** (1#,2#)	02/080	600	105	4000	2222	3.97	14.32	Type IV

P91 As-Rec'd. MR02/027A Welded with Metrode

Macroexamination

Length of specimen halves (longer half + shorter half)(mm): 53+ 52
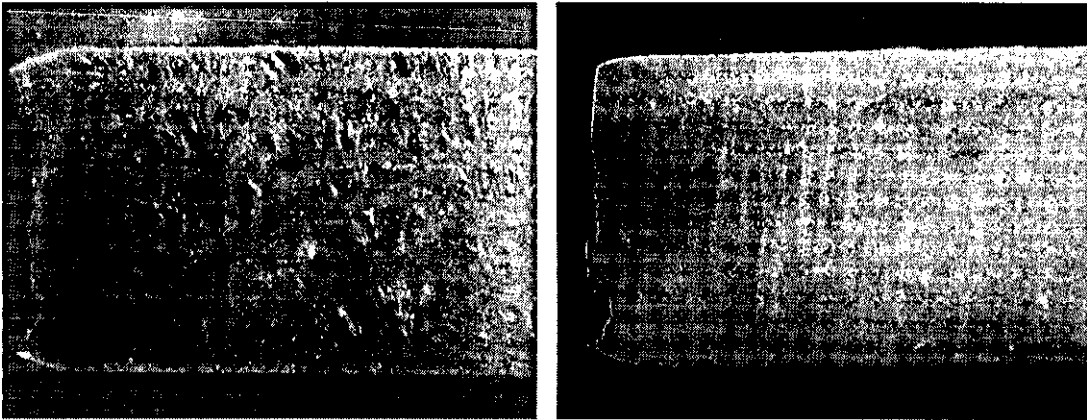Distance from the fracture to other surface defect/s (mm):   none

Low mag. photograph (optical stereomicrograph) of the two specimen halves and the fracture surface/s, alongside a ruler.


Comments: 90 deg failure in centre of gauge length.

Sectioning and Microexamination

(Creep specimen width in this view = 10.9mm)

Comments: Failure in HAZ. No obvious creep damage in HAZ.

Conclusions

Type IV failure

r
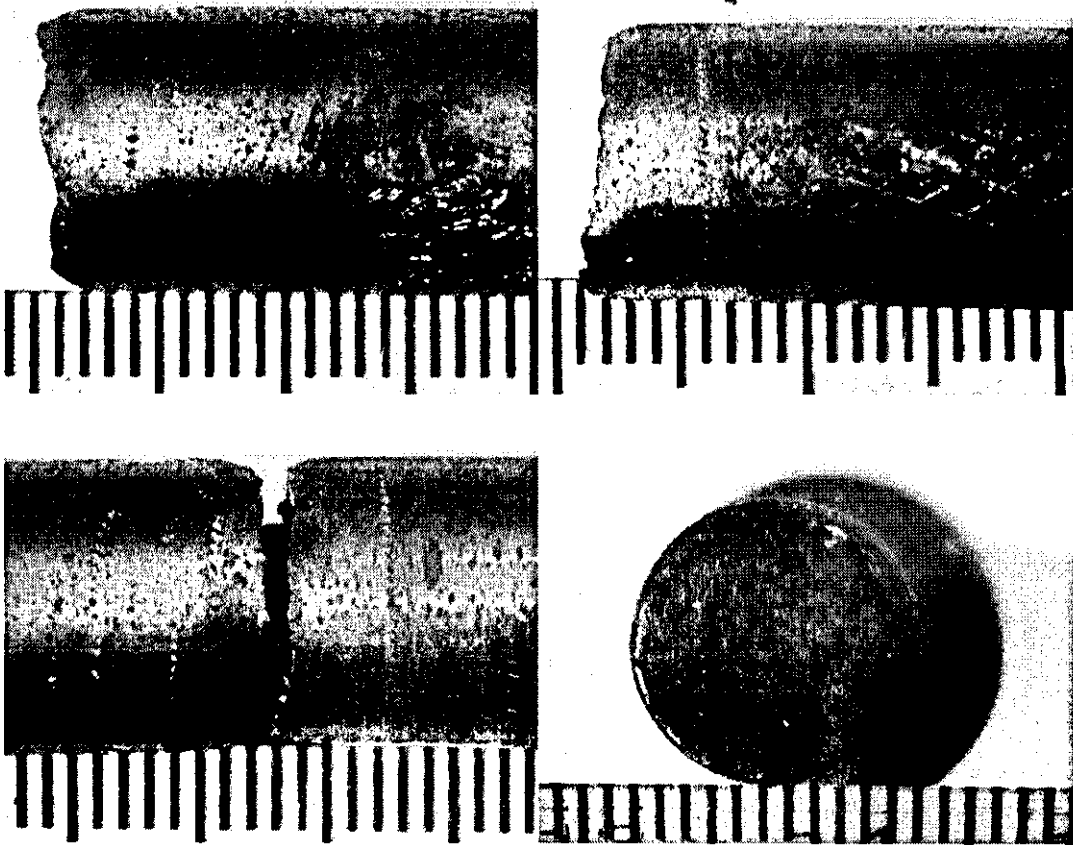
FOURCRACK creep specimen failure examination (KA1395/5)

Micro Number	PTC Ref.	Test Ref.	Temp. °C	Stress MPa	Est. Dur.	Final Dur.	Elong. %	R. of A. %	Failure
03/131 03/132	KA1395/5 (1#,2#)	02/077	635	75.0	1000	1246	3.06	15.30	Type IV

P91 As-Rec'd. MR02/027A Welded with Metrode

Macroexamination

Length of specimen halves (longer half + shorter half)(mm): 55+ 50
Distance from the fracture to other surface defect/s (mm):   none

Low mag. photograph (optical stereomicrograph) of the two specimen halves and the fracture surface/s, alongside a ruler.

Comments: 90 deg failure in centre of gauge length.

Sectioning and Microexamination

(Creep specimen width in this view = 10.9mm)

Comments: Failure in HAZ . No significant creep damage in HAZ.
Cavitation microcracks in the HAZ.

×200

Conclusions

Type IV failure

t
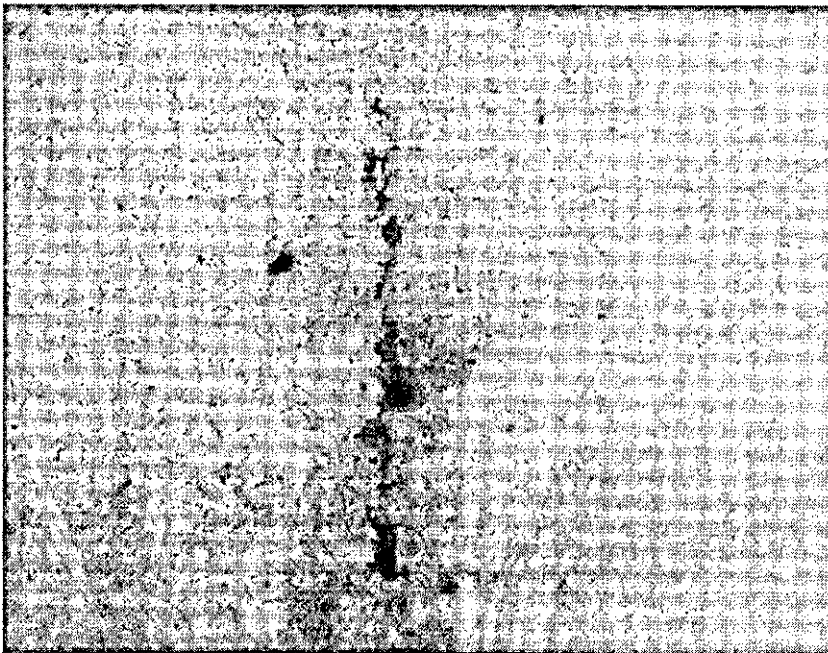
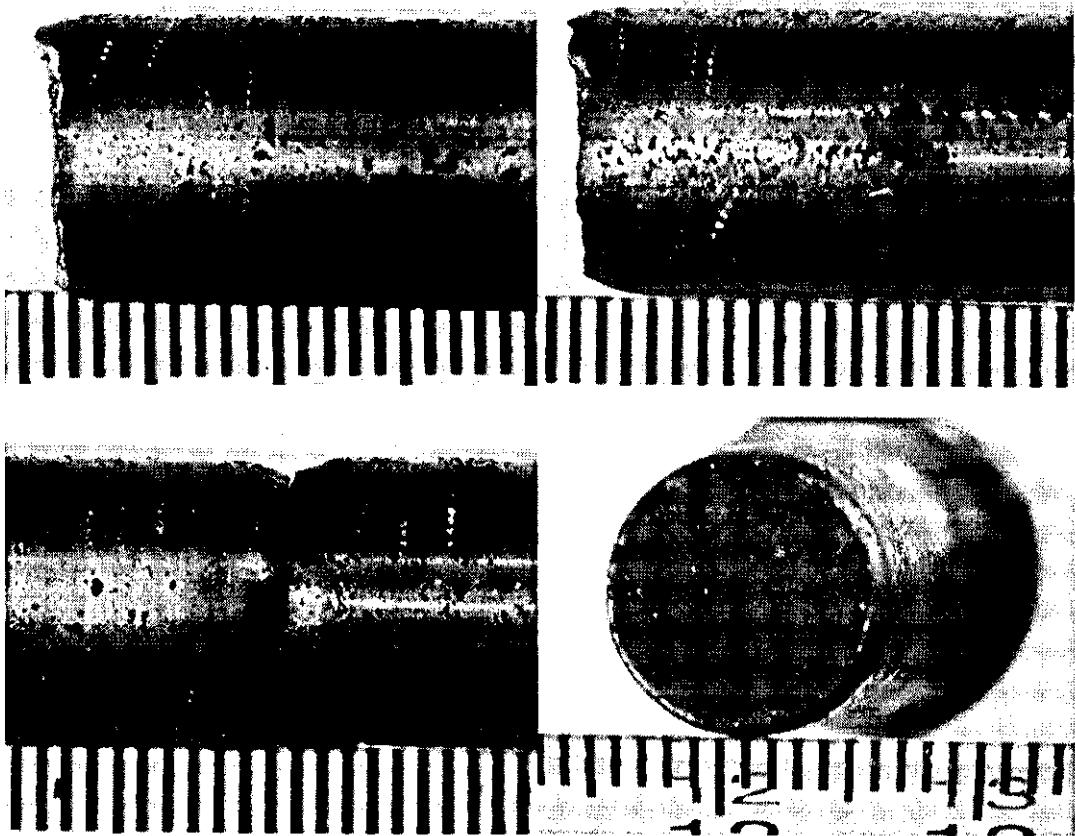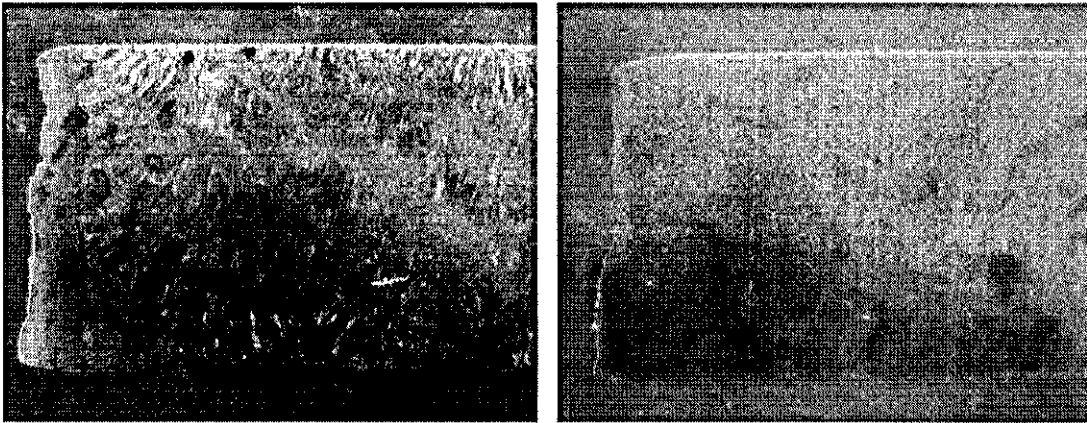## FOURCRACK creep specimen failure examination (KA1395/6)

Micro Number	PTC Ref.	Test Ref.	Temp. °C	Stress MPa	Est. Dur.	Final Dur.	Elong. %	R. of A. %	Failure
03/133 03/134	KA1395/6 (1#,2#)	02/081	600	105	4000	2176	3.01	15.47	Type IV

P91 N + Temper, MR02/027B Welded with Metrode

Macroexamination

Length of specimen halves (longer half + shorter half)(mm): 55+ 50
Distance from the fracture to other surface defect/s (mm):   none

Low mag. photograph (optical stereomicrograph) of the two specimen halves and the fracture surface/s, alongside a ruler.

Comments: 90 deg failure in centre of gauge length.

Sectioning and Microexamination

(Creep specimen width in this view = 10.9mm)

Comments: Failure in HAZ . No significant creep damage in HAZ.

Conclusions

Type IV failure

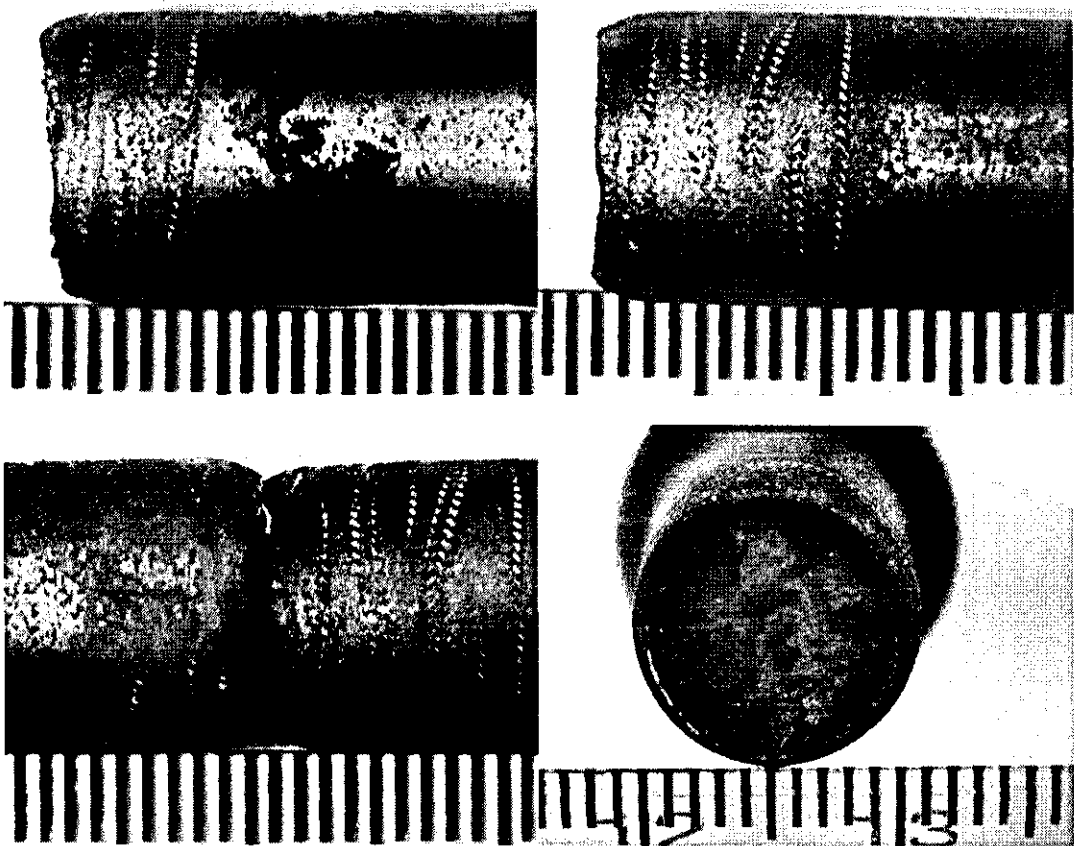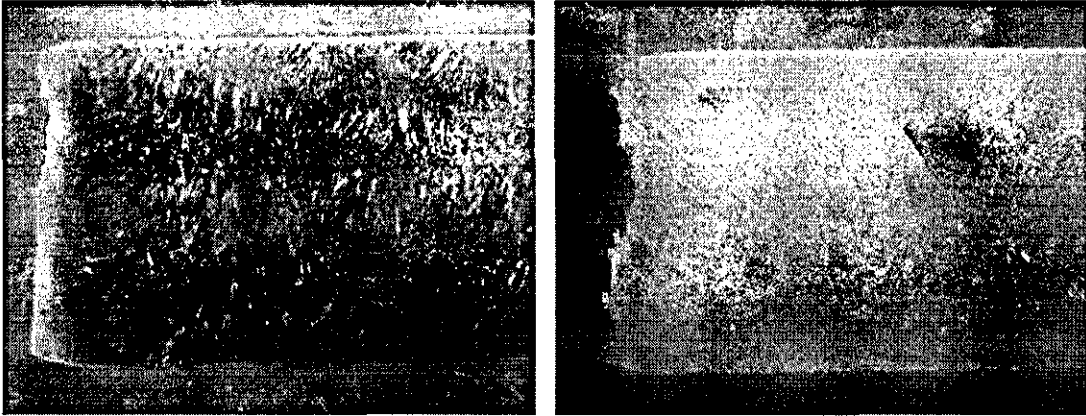**FOURCRACK creep specimen failure examination (KA1395/7)**

Micro Number	PTC Ref.	Test Ref.	Temp. °C	Stress MPa	Est. Dur.	Final Dur.	Elong. %	R. of A. %	Failure
03/135 **03/136**	**KA1395/7** (1#,2#)	02/078	635	75	1000	926	2.57	13.35	Type IV

P91 N + Temper, MR02/027B Welded with Metrode

Macroexamination

Length of specimen halves (longer half + shorter half)(mm): 53+ 52
Distance from the fracture to other surface defect/s (mm):   none

Low mag. photograph (optical stereomicrograph) of the two specimen halves and the fracture surface/s, alongside a ruler.

Comments: 90 deg failure in centre of gauge length.

Sectioning and Microexamination

(Creep specimen width in this view = 10.9mm)

Comments: Failure in HAZ . No significant creep damage in HAZ.

Conclusions

Type IV failure

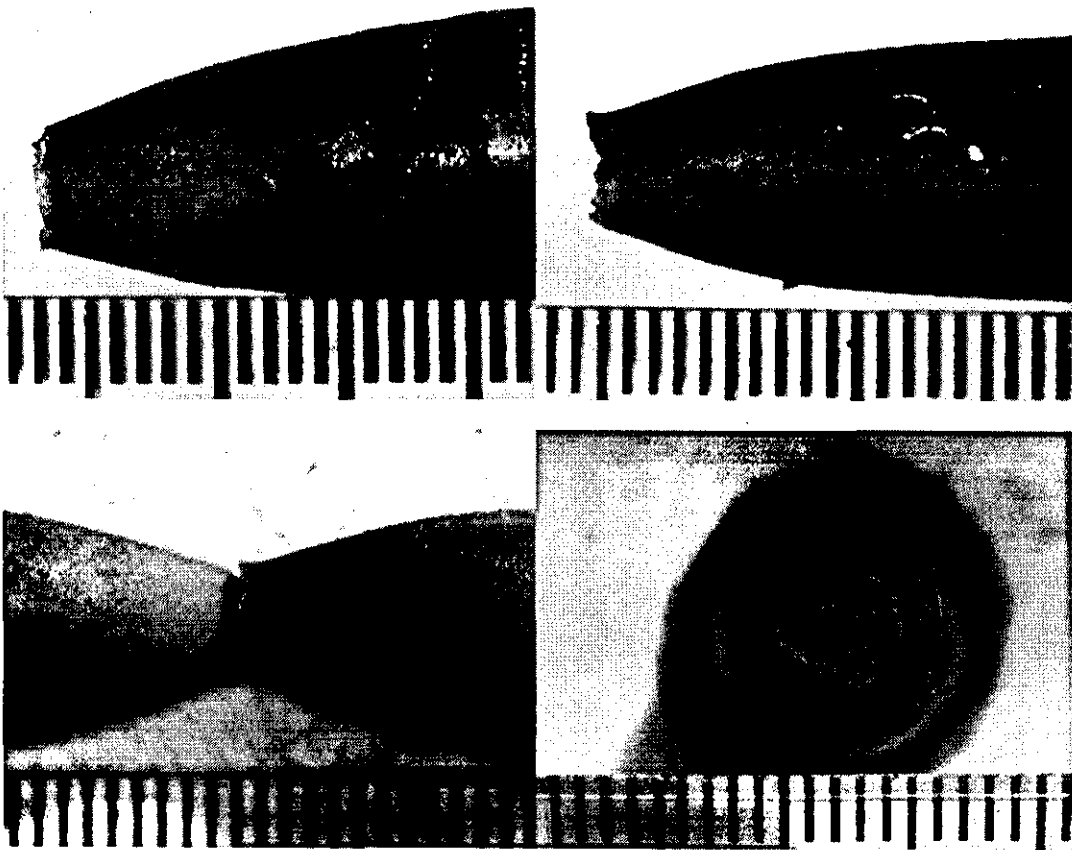## FOURCRACK creep specimen failure examination (KA1395/8)

| Micro Number	PTC Ref.	Test Ref.	Temp. °C	Stress MPa	Est. Dur.	Final Dur.	Elong. %	R. of A. %	Failure
03/137	KA1395/8	02/082	600	105	4000	2054	25.55	82.33	PM

P91 Aged, MR02/027B Welded with Metrode

Macroexamination

Length of specimen halves (longer half + shorter half)(mm): 70+ 52
Distance from the fracture to other surface defect/s (mm):   cup and cone in PM

Low mag. photograph (optical stereomicrograph) of the two specimen halves and the fracture surface/s, alongside a ruler.

Comments: cup and cone in parent material.

Sectioning and Microexamination

(Creep specimen width in this view = 10.9mm)

Comments: Failure in PM. No obvious damage in HAZ.

Conclusions

Failure in PM

FOURCRACK creep specimen failure examination (KA1395/9)

Micro Number	PTC Ref.	Test Ref.	Temp. °C	Stress MPa	Est. Dur.	Final Dur.	Elong. %	R. of A. %	Failure
03/138 03/139	KA1395/9 (1#,2#)	02/079	635	75	1000	1111	4.19	16.62	Type IV

P91 Aged, MR02/027B Welded with Metrode
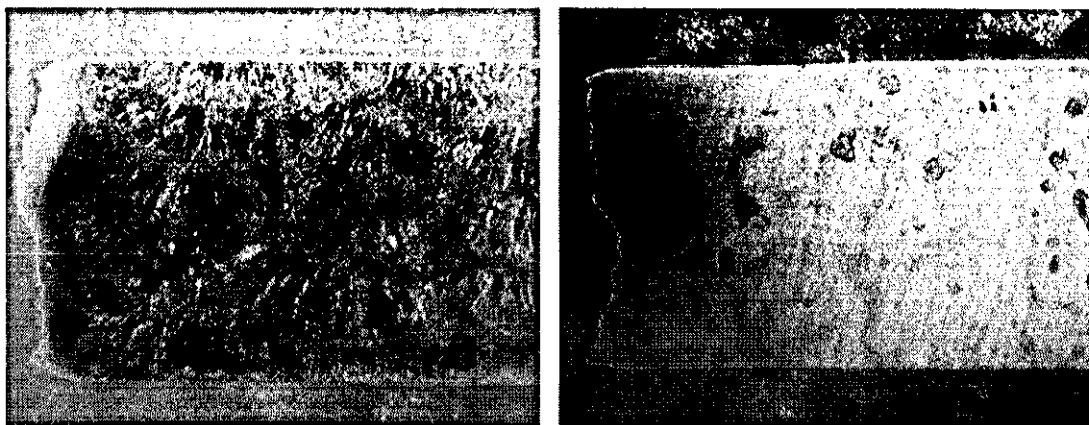
Macroexamination

Length of specimen halves (longer half + shorter half)(mm): 55+ 50
Distance from the fracture to other surface defect/s (mm):   none

Low mag. photograph (optical stereomicrograph) of the two specimen halves and the fracture surface/s, alongside a ruler.
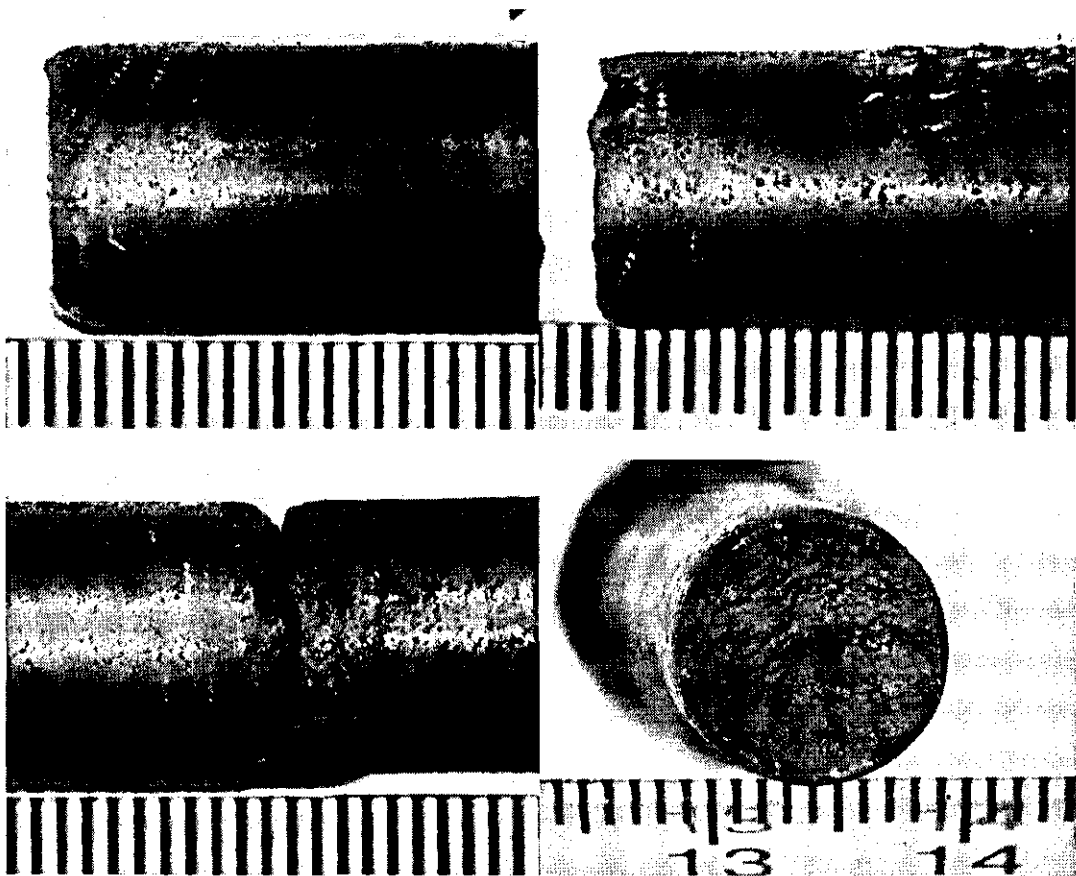
Comments: 90 deg failure in centre of gauge length.

Sectioning and Microexamination

(Creep specimen width in this view = 10.9mm)

Comments: Failure in HAZ . No significant creep damage in HAZ.

Conclusions

Type IV failure

## FOURCRACK creep specimen failure examination (KA1395/10)

Micro Number	PTC Ref.	Test Ref.	Temp. °C	Stress MPa	Est. Dur.	Final Dur.	Elong. %	R. of A. %	Failure
03/140 **03/141**	**KA1395/10** (1#,2#)	02/069	650	75	400	430	10.46	28.77	Type IV

P91 Aged, MR02/027B Welded with Metrode

Macroexamination

Length of specimen halves (longer half + shorter half)(mm): 55+ 50
Distance from the fracture to other surface defect/s (mm):   neck 5mm

Low mag. photograph (optical stereomicrograph) of the two specimen halves and the fracture surface/s, alongside a ruler.
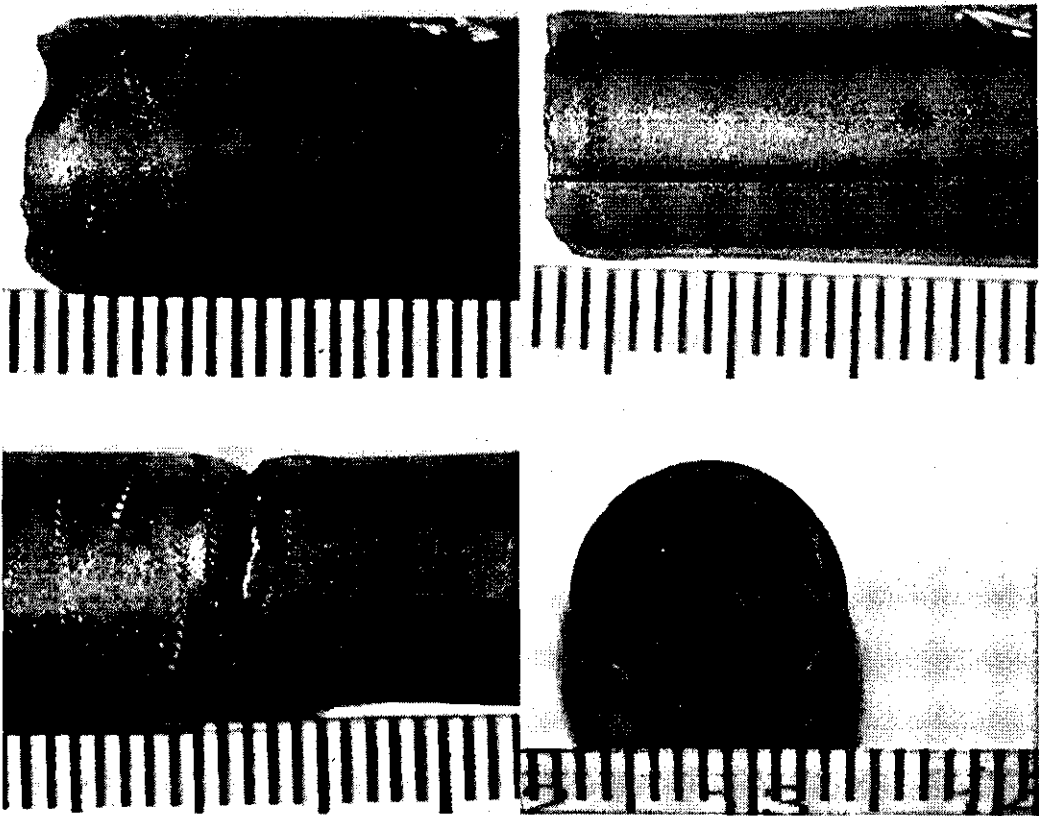
Comments: 90 deg failure in centre of gauge length.

Sectioning and Microexamination
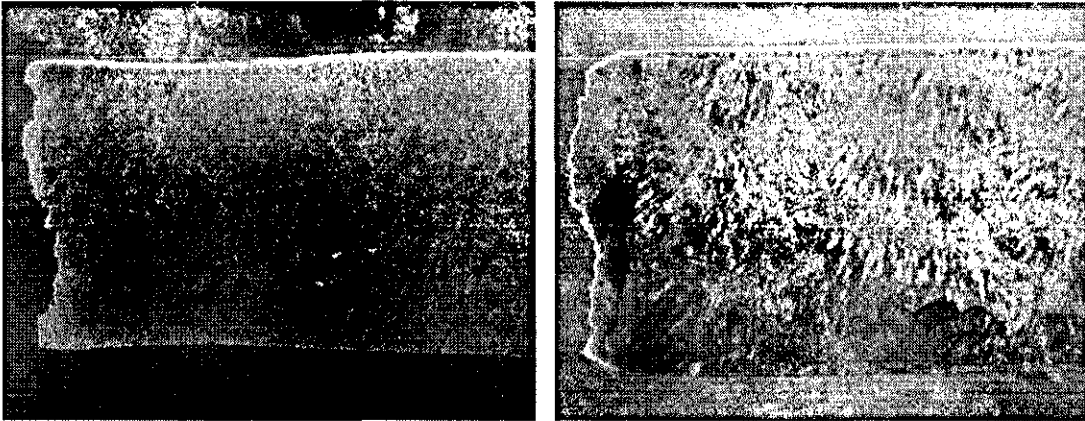
(Creep specimen width in this view = 10.9mm)

Comments: Failure in HAZ . No significant creep damage in HAZ. No obvious creep damage in the neck region.

Conclusions

Type IV failure

APPENDIX D: GRAIN BOUNDARY SEGREGATION (GBS) MODEL COMPUTER PROGRAMME (Matlab)

```
cg1=0.0002;
cg2=0;
cg3=0;
eb1=0.36*1.6*10^-19;
efv=1.4*1.6*10^-19;
Ts=1573;
T0=823;
k=1.3807*10^-23;
d=2*10^-9;
r=0.01;
thita=15;
ea=2.6*1.6*10^-19;
delta=0.05;
b=3*10^-5;
doc=1.7*10^-5;
em=1.63*1.6*10^-19;
doi=7.12*10^-5;
ei=2.68*1.6*10^-19;

figure(1): Cbnm/Cg-Ts
cbnmT=cg1*(eb1/efv)*((cg1*exp(eb1/(k*Ts)))/(cg1*exp(eb1/(k*Ts))))*exp(((eb1-
efv)/(k*Ts))-((eb1-efv)/(k*T0)));
C=cbnmT/cg1;
alfan=cbnmT/cg1;
te=r*k*Ts^2/(thita*ea);
dci=doc*exp(-em/(k*Ts));
dsi=doi*exp(-ei/(k*Ts));
tc=delta*b^2*log10(dci/dsi)/(4*(dci-dsi));
Ts=273;
for j=1:101
cbnmT(j)=cg1*(eb1/efv)*((cg1*exp(eb1/(k*Ts)))/(cg1*exp(eb1/(k*Ts))))*exp(((eb1-
efv)/(k*Ts))-((eb1-efv)/(k*T0)));
C(j)=cbnmT(j)/cg1;
Ts=Ts+13;
end
Ts=273:13:1573;
plot(Ts,C);
cbnmT,C(101);
xlabel('Ts, K')
ylabel('Cbnm/Cg')
```

```
figure(2): Cbn/Cg-t
cbnmT(1)=cg1*(eb1/efv)*(cg1*exp(eb1/(k*Ts(1)))/cg1*exp(eb1/(k*Ts(1))))*exp((eb1-
efv)/(k*Ts(1))-(eb1-efv)/(k*T0));
cbnmT(2)=cg1*(eb1/efv)*(cg1*exp(eb1/(k*Ts(2)))/cg1*exp(eb1/(k*Ts(2))))*exp((eb1-
efv)/(k*Ts(2))-(eb1-efv)/(k*T0));
cbnmT(3)=cg1*(eb1/efv)*(cg1*exp(eb1/(k*Ts(3)))/cg1*exp(eb1/(k*Ts(3))))*exp((eb1-
efv)/(k*Ts(3))-(eb1-efv)/(k*T0));
cbnmT(4)=cg1*(eb1/efv)*(cg1*exp(eb1/(k*Ts(4)))/cg1*exp(eb1/(k*Ts(4))))*exp((eb1-
efv)/(k*Ts(4))-(eb1-efv)/(k*T0));
alfan(1)=cbnmT(1)/cg1;
alfan(2)=cbnmT(2)/cg1;
alfan(3)=cbnmT(3)/cg1;
alfan(4)=cbnmT(4)/cg1;
dci(1)=doc*exp(-em/(k*Ts(1)));
dci(2)=doc*exp(-em/(k*Ts(2)));
dci(3)=doc*exp(-em/(k*Ts(3)));
dci(4)=doc*exp(-em/(k*Ts(4)));
cbnmT(1)=cg1*(eb1/efv)*(cg1*exp(eb1/(k*Ts(1)))/cg1*exp(eb1/(k*Ts(1))))*exp((eb1-
efv)/(k*Ts(1))-(eb1-efv)/(k*T0));
cbnmT(2)=cg1*(eb1/efv)*(cg1*exp(eb1/(k*Ts(2)))/cg1*exp(eb1/(k*Ts(2))))*exp((eb1-
efv)/(k*Ts(2))-(eb1-efv)/(k*T0));
cbnmT(3)=cg1*(eb1/efv)*(cg1*exp(eb1/(k*Ts(3)))/cg1*exp(eb1/(k*Ts(3))))*exp((eb1-
efv)/(k*Ts(3))-(eb1-efv)/(k*T0));
cbnmT(4)=cg1*(eb1/efv)*(cg1*exp(eb1/(k*Ts(4)))/cg1*exp(eb1/(k*Ts(4))))*exp((eb1-
efv)/(k*Ts(4))-(eb1-efv)/(k*T0));
alfan(1)=cbnmT(1)/cg1;
alfan(2)=cbnmT(2)/cg1;
alfan(3)=cbnmT(3)/cg1;
alfan(4)=cbnmT(4)/cg1;
dci(1)=doc*exp(-em/(k*Ts(1)));
dci(2)=doc*exp(-em/(k*Ts(2)));
dci(3)=doc*exp(-em/(k*Ts(3)));
dci(4)=doc*exp(-em/(k*Ts(4)));
t=0
for i=1:101
cbnt1(i)=cg1+(cbnmT(1)-cg1)*(1-
(exp((4*dci(1)*t)/(alfan(1)^2*d^2))*erfc((2*((dci(1)*t)^(1/2))/(alfan(1)*d)))));
cbnt2(i)=cg1+(cbnmT(2)-cg1)*(1-
(exp((4*dci(2)*t)/(alfan(2)^2*d^2))*erfc((2*((dci(2)*t)^(1/2))/(alfan(2)*d)))));
cbnt3(i)=cg1+(cbnmT(3)-cg1)*(1-
(exp((4*dci(3)*t)/(alfan(3)^2*d^2))*erfc((2*((dci(3)*t)^(1/2))/(alfan(3)*d)))));
cbnt4(i)=cg1+(cbnmT(4)-cg1)*(1-
(exp((4*dci(4)*t)/(alfan(4)^2*d^2))*erfc((2*((dci(4)*t)^(1/2))/(alfan(4)*d)))));
c1(i)=cbnt1(i)/cg1;
c2(i)=cbnt2(i)/cg1;
c3(i)=cbnt3(i)/cg1;
```

```
c4(i)=cbnt4(i)/cg1;
t=t+0.01
end
t=0:0.01:1;
plot(t,c1,'b-',t,c2,'r:',t,c3,'k-.',t,c4,'m--');
title ('GB concentration vs quenching time')
xlabel('quenching time, s')
ylabel('Cbn/Cg')
text(0.8,1200,'T1')
text(0.6,1500,'T2')
text(0.4,3000,'T3')
text(0.2,5000,'T4')


figure(3): Cbn/Cg-Ts
t=1;
Ts=273;
for j=1:101
cbnmT(j)=cg1*(eb1/efv)*((cg1*exp(eb1/(k*Ts)))/(cg1*exp(eb1/(k*Ts))))*exp(((eb1-
efv)/(k*Ts))-((eb1-efv)/(k*T0)));
te(j)=r*k*Ts^2/(thita*ea);
alfan(j)=cbnmT(j)/cg1;
cbnt(j)=cg1+(cbnmT(j)-cg1)*(1-
(exp((4*dci*te(j))/(alfan(j)^2*d^2))*erfc((2*((dci*te(j))^(1/2))/(alfan(j)*d)))));
C(j)=cbnt(j)/cg1;
Ts=Ts+14;
end
Ts=273:14:1673;
plot(Ts,C);


figure(4): Cbn/Cg-Ts with experimental data
t=1;
Ts=273;
for j=1:101
cbnmT(j)=cg1*(eb1/efv)*((cg1*exp(eb1/(k*Ts)))/(cg1*exp(eb1/(k*Ts))))*exp(((eb1-
efv)/(k*Ts))-((eb1-efv)/(k*T0)));
te(j)=r*k*Ts^2/(thita*ea);
alfan(j)=cbnmT(j)/cg1;
cbnt(j)=cg1+(cbnmT(j)-cg1)*(1-
(exp((4*dci*te(j))/(alfan(j)^2*d^2))*erfc((2*((dci*te(j))^(1/2))/(alfan(j)*d)))));
C(j)=cbnt(j)/cg1;
Ts=Ts+15;
end
Ts=273:15:1773;
plot(Ts,C);
```

C

```
xlabel('Quenching temperature,Ts')
ylabel('Cbn/cg')
text(1173,44,'*')
text(1373,98,'*')
text(1573,221,'*')
text(600,500,'- Model simulation')
text(600,450,'* Experimental')
cbnt(80)


figure(5): Cbn/Cg-Thita
thita=0;
for j=1:1001
cbnmT(j)=cg1*(eb1/efv)*((cg1*exp(eb1/(k*Ts)))/(cg1*exp(eb1/(k*Ts))))*exp(((eb1-
efv)/(k*Ts))-((eb1-efv)/(k*T0)));
te(j)=r*k*Ts^2/(thita*ea);
alfan(j)=cbnmT(j)/cg1;
cbnt(j)=cg1+(cbnmT(j)-cg1)*(1-
(exp((4*dci*te(j))/(alfan(j)^2*d^2))*erfc((2*((dci*te(j))^(1/2))/(alfan(j)*d)))));
C(j)=cbnt(j)/cg1;
thita=thita+0.02;
end
thita;
thita=0:0.02:20;
plot(thita,C);
xlabel('Cooling rate, K/s')
ylabel('Cbn/Cg')
axis([0,20,200,300])
text(15,265,'+')
text(0.1,278,'+')
text(3,230,'+ Experimental')
text(3,270,'------Model')


figure (6): Cbn/cg-(Ts, Thita)
thita=1;
for i=1:100
    Ts=273;
for j=1:100
cbnmT(j)=cg1*(eb1/efv)*((cg1*exp(eb1/(k*Ts)))/(cg1*exp(eb1/(k*Ts))))*exp(((eb1-
efv)/(k*Ts))-((eb1-efv)/(k*T0)));
te(j)=r*k*Ts^2/(thita*ea);
alfan(j)=cbnmT(j)/cg1;
cbnt(j)=cg1+(cbnmT(j)-cg1)*(1-
(exp((4*dci*te(j))/(alfan(j)^2*d^2))*erfc((2*((dci*te(j))^(1/2))/(alfan(j)*d)))));
C(i,j)=cbnt(j)/cg1;
```

```
Ts=Ts+20;
end
thita=thita+0.2;
end
Ts,thita
meshz(C);
colormap([1 0 0]);
xlabel('Quenching temperature,K')
ylabel('Cooling rate, K/s')
zlabel('Cbn/cg')
axis(1473,2273,0,20,0,10000)
```